THE ASSESSMENT OF TIME LAPSE MARINE CONTROLLED-SOURCE ELECTROMAGNETICS (CSEM) FOR DYNAMIC RESERVOIR CHARACTERISATION

Olarinre Salako

Submitted for the degree of Doctor of Philosophy

Heriot Watt University

Institute of Petroleum Engineering

December 2014

ABSTRACT

Marine controlled-source electromagnetics (CSEM) techniques can be used to detect subsurface resistivity anomalies to discriminate hydrocarbon filled reservoir from the water saturated sediments in pre-drill appraisal of seismic anomalies in hydrocarbon exploration. The governing physics of marine CSEM is electromagnetic induction/diffusion therefore it has poor structural resolution. Current time – lapse CSEM feasibility studies for reservoir monitoring assume that the intrinsic limitation of CSEM has little impact on the dynamic fluid discrimination, as more structural constraining information are available at a producing oilfield. However, basic resistivity model is used without rigorous rock physics model, and is thus lacking in dynamic reservoir characterisation. Recent efforts at utilising simulation models combined with rock physics for realistic water-flooding front did not include reservoir management issues. In this thesis, CSEM is presented from the perspective of a reservoir manager, the end – user of this technology. A review of various hydrocarbon production mechanisms and scenarios showed that water – related mechanisms are ideally suited for time lapse CSEM applications as a complimentary tool to seismic in reservoir monitoring because of the resistivity anomaly generated as water replaces hydrocarbon. Channelized turbidite system for the North Sea oilfield model is used, such that the laminar lithological arrangement of sand and shale indicates that a linear arithmetic summation of resistivities of shale and sand will be a good representative of electrical rock physics model. Using this electrical rock physics model, three hydrocarbon provinces are assessed for the technical risk of time lapse CSEM project, in similar manner as done in 4D seismic projects. The North Sea province has highest technical risk, followed by the Gulf of Mexico, while the West Africa province has the least technical risk. A simulation to electromagnetic (sim2EM) workflow is then incorporated into the simulation to seismic (sim2seis) workflow. The sim2EM workflow is used to first examine the impacts of overburden complexity and sea water resistivity stratification on CSEM data. It is observed that the structural impacts are more pronounced on the static CSEM images than on its dynamic images. Then, coupled forward modelling of inline CSEM data and seismic amplitude data from a 3D fluid flow reservoir simulator is performed. The simulator serves the dual purpose of common oilfield in which production is aided by water injection, and of an interpretational constraint involving correlation of CSEM and seismic anomalies with

injection and production activities at well locations (here called *dynamic well tie*). The time-lapse in-line CSEM amplitude change, modelled using dipole 1D, shows linear correlations of 64 to 68% with the change in water saturation. It is more responsive and consistently more linearly related to the change in water saturation than the seismic, despite the possible detrimental effects of reservoir heterogeneity. This is not surprising as seismic is responsive to a combination of changes in saturation and pressure. Coupled interpretation of seismic and CSEM modelled data show that time – lapse CSEM is a definite indicator of water saturation changes. For instance, when seismic softening due to rise in pressure masks increase in water saturation, or when seismic hardening due to pressure drop gives false increase in water saturation. The importance of brine mixing on the acoustic and electrical properties, during secondary and tertiary oil recovery, is examined. The seismic and EM rock physics are adjusted to cater for effective mixed brine resistivity, bulk modulus and bulk density, as functions of temperature and salinity for the injected and formation brines. Modelling of three scenarios of different combinations of injected and formation brines around the world, calibrated with a reference model in which brine properties were kept constant, indicate that EM is more responsive than the seismic, to the brine chemistry. Fluid flow modelling of sea water injection in the North Sea field shows that temperature effect is restricted to the vicinity of injector; while salinity effect travels farther from the injector along the water flooding front. The time-lapse EM could theoretically distinguish extreme brines. For instance, low salinity water injected into oil-wet reservoir with saline formation water; or moderately saline subsurface aquifer water injected into very saline formations of the Middle Eastern carbonates produced between -15 and 7% change in inline CSEM amplitude. In this thesis, 1D dipole forward modelling has generally highlighted values of EM in reservoir monitoring and management. Finally, repeat 3D EM data modelling produced time-lapse amplitude change of 0.3%, which is too small to be detected by the current CSEM acquisition. Thus, high precision EM field sensor will be required for practical application of 4D CSEM to reservoir monitoring. Only about 46% of this small 4D signature is interpretable for the change in transverse resistance of between -800Ωm^2 and -1050Ωm^2 (equivalent to resistivity reduction of between 13Ωm to 18Ωm). Broad qualitative information about the water flooded areas is provided, but fine detailed information about bypassed oil and early warning of water breakthrough could not be properly imaged.

DEDICATION

To those who have ever aided, and those who are aiding, my learning process – my teachers, lecturers and supervisors, mentors and role models (dead or alive), authors of books and materials which I have ever studied, and even my mates who have taught me one thing or the other. You have all inspired me in one way or the other to complete this work.

ACKNOWLEDGEMENTS

I sincerely thank the Petroleum Technology Development Fund of Nigeria for three years full scholarship. I appreciate further financial support received from the Edinburgh Time Lapse Project (ETLP). I am grateful to the Society of Exploration Geophysicist (SEG) for awarding me with the prestigious Ian Jack/BP/Amoco scholarships, twice (2012 and 2013).

I thank Prof Colin MacBeth – my primary supervisor, for the opportunity offered me to study in the ETLP – a world class reservoir geophysics research consortium. I appreciate his scientific guidance and encouragements which played vital roles in the achievement of this work. I thank Professor Eric Mackay for technical discussions on reservoir simulation. I enjoyed collaborative support with the Rock Solid Images (RSI). Special thanks to Dr Lucy MacGregor – the RSI Chief Technology Officer who facilitated this, including my visit to their office in Houston USA, where I spent two months working with their in-house software under her supervision. The results of this visit are reflected in Chapter 7. I thank my examiners – Dr Karen Weitemeyer and Prof Patrick Corbett, for useful feedback for improvement. I thank BP for supplying a North Sea oilfield reservoir simulation model. I appreciate the ETLP's sponsors (BG, BP, Chevron, ConocoPhilips, Eni, ExxonMobil, Hess, Ikon, Landmark, Maersk, Nexen, Norsar, Peroro, Petrobras, RSI, Shell, Statoil, Suncor, TAQA, TGS and Total) for supporting this research. Thanks to Schlumberger for the use of Petrel and Eclipse software. I thank all ETLP members during the period of 2010 – 2014 for general technical discussions and mutual assistances. I enjoyed the many 'lunch and learn' sessions. I am grateful to Dr Hamed Amini for the provision of simulator – to – seismic code, into which I incorporated electromagnetic forward modelling workflow. I appreciate the friendliness of all staff of the Heriot Watt Institute of Petroleum Engineering.

I am very grateful to my wife – Olawumi and my children for their understanding, especially when I was away in the US. Now, Emmanuel – my son will no longer ask me: "*Daddy, when are you finishing your PhD?*" I thank my mother and my mother–in–law for helping to look after my children in the course of this programme. I am eternally grateful to my parents who are my first set of teachers, and permanent teachers. All thanks to Almighty God – the Giver of life, for granting me life and ability to succeed with this PhD.

***Olarinre Salako**, December 2014*

DECLARATION

ACADEMIC REGISTRY
Research Thesis Submission

Name*:*	OLARINRE SALAKO		
School/PGI:	Petroleum Engineering		
Version: *(i.e. First, Resubmission, Final)*	Final	Degree Sought (Award **and** Subject area)	Doctor of Philosophy in Reservoir Geophysics

Declaration

In accordance with the appropriate regulations I hereby submit my thesis and I declare that:

1) the thesis embodies the results of my own work and has been composed by myself
2) where appropriate, I have made acknowledgement of the work of others and have made reference to work carried out in collaboration with other persons
3) the thesis is the correct version of the thesis for submission and is the same version as any electronic versions submitted*.
4) my thesis for the award referred to, deposited in the Heriot-Watt University Library, should be made available for loan or photocopying and be available via the Institutional Repository, subject to such conditions as the Librarian may require
5) I understand that as a student of the University I am required to abide by the Regulations of the University and to conform to its discipline.

* *Please note that it is the responsibility of the candidate to ensure that the correct version of the thesis is submitted.*

Signature of Candidate*:*		Date:	

Submission

Submitted By *(name in capitals):*	OLARINRE SALAKO
Signature of Individual Submitting:	
Date Submitted:	

For Completion in the Student Service Centre (SSC)

Received in the SSC by *(name in capitals):*			
Method of Submission *(Handed in to SSC; posted through internal/external mail):*			
*E-thesis Submitted (**mandatory for final theses)***			
Signature:		Date:	

TABLE OF CONTENTS

LIST OF TABLES

LIST OF FIGURES

LIST OF ABBREVIATIONS

AVO	Amplitude-Versus-Offset
AW	Aquifer Water
CC	Correlation Coefficient
CSEM	Controlled-Source Electromagnetic
CTD	Conductivity – Temperature – Depth
CW	Connate Water
DHI	Direct Hydrocarbon Indicator
DRI	Direct Resistivity Indicator
EAGE	European Association of Geoscientists and Engineers
EM	Electromagnetic
EOR	Enhanced Oil Recovery
GOC	Gas-Oil Contact
GOR	Gas/Oil Ratio
HED	Horizontal Electric Dipole
I	Injector
IOR	Improved Oil Recovery
IW	Injection Water
LoSal	Low Salinity Water
LWD	Logging While Drilling
MT	Magnetotelluric
NTG	Volume of sand in which fluid flows (porosity & permeability cut-off)
OOIP	Original Oil in Place
OOWC	Original Oil Water Contact
OW	Observation Well

P	Producer
PLT	Production Logging Tools
POWC	Produced Oil Water Contact
ppm	Part per million
PVT	Pressure-Volume-Temperature
RFT	Repeat Formation Tester
R_{sand}	Resistivity of clean sand (Archie's sand)
R_{sh}	Resistivity of intra-reservoir shale
RSI	Rock Solid Images
R_w	Resistivity of water
R_{we}	Effective resistivity of mixed injected-formation water
SAGD	Steam-Assisted Gravity Drainage
SD	Standard Deviation
S_e	Effective mixed injected-formation water salinity
SEG	Society of Exploration Geophysicists
Sim2EM	Simulator to electromagnetic modelling
Sim2imp	Simulator to impedance modelling
Sim2seismic	Simulator to seismic modelling
Sim2resist	Simulator to resistivity modelling
S_o	Oil saturation
S_w	Water saturation
S_{wc}	Connate water saturation
S_{wirr}	Irreducible residual water saturation
TDT	Thermal Decay Time
T_e	Effective mixed injected-formation water temperature
TM	Transverse Magnetic

TCS	Technical chance of success
TR	Transverse Resistance
UCSD	University of California San Diego
V_{sh}	Volume of intra-reservoir shale (V_{sh} = 1- NTG)
WAG	Water-Alternating-Gas
WD	Water Depth
WOR	Water/Oil Ratio
XBT	Expendable Bathy-Thermograph

LIST OF PUBLICATIONS

Part of this work is presented in the following publications:

(1) **Salako, O**., MacBeth, C., MacGregor, L., 2015. *Potential Applications of Time-lapse Marine CSEM to Reservoir Monitoring.* (Accepted for First Break Journal).

(2) **Salako, O**., MacBeth, C., MacGregor, L., E., 2015. *Effective Imaging of Reservoir Fluid Changes.* Madrid, 77th EAGE Conference & Exhibition incorporating SPE EUROPEC. (Abstract submitted for 4D Worskshop).

(3) **Salako, O**., MacBeth, C., MacGregor, L. & Mackay, E., 2013. *Potential Applications of Time-lapse Marine CSEM to Reservoir Monitoring.* London, 75th EAGE Conference & Exhibition incorporating SPE EUROPEC. Expanded Abstracts.

(4) **Salako, O**., MacBeth, C. & MacGregor, L., 2012. *Towards joint interpretation of CSEM Surveys with 4D Seismic for Reservoir Monitoring.* Copenhagen, 74th EAGE Conference & Exhibition incorporating SPE EUROPEC. Expanded Abstracts.

CHAPTER 1

GENERAL INTRODUCTION

1.0 Introduction

In order to effectively apply geophysics to monitor a producing hydrocarbon reservoir, a geophysicist requires a good understanding of the concepts of reservoir monitoring and production mechanisms from the viewpoint of a reservoir engineer or manager. The main reason for reservoir monitoring is to predict, as accurately as possible, the future behaviour or performance of a reservoir in order to enhance the recovery factor, so as to increase the oil reserve and thus extend the field life span. This is necessary, partly because of the need to meet the ever-increasing demands for fossil fuels, even as the campaign for alternative and renewable energy grows; and partly due to the high costs and risks associated with frontier exploration (Lumley 2004), which have now led to a growing need for what Fanchi (2006) described as "optimal conditions to maximize economic recovery of hydrocarbon from a 'prudently' operated field." The latter is particularly so, as it is believed that most of the easily accessible oils have been found and the next sets of hydrocarbon exploration activities are to be carried out in more challenging terrains that are politically volatile, environmentally unfriendly and requiring very high level of technical expertise.

Many of the energy companies now place as much priority on maximising the recoverability of the producing reservoirs as making new investment in exploration. To achieve this, different enhanced oil recovery (EOR) and/or improved oil recovery (IOR) methods have been employed and reservoir monitoring and management is now more robustly integrated. The emergence of 4D seismic in the last two decades has assisted in this direction as it has offered a synergistic approach to reservoir monitoring, whereby the reservoir engineers, reservoir geologists and reservoir geophysicists collaborate their efforts and expertise in monitoring and managing hydrocarbon producing reservoir. Seismic has remained the major geophysical tool in this context. The reasons for this include the successes recorded by the introduction of 3D seismic as against the earlier 2D seismic. This

provided the necessary motivation for repeat 3D seismic surveys, which is now termed 4D seismic or time-lapse seismic. Another reason is the huge research investment geared towards improved understanding and applicability of 4D seismic in making reservoir management decisions. Most importantly, seismic techniques have traditionally been the geophysical methods of choice in the oil and gas industry, as it offers high vertical and inter-wells horizontal resolution images of subsurface structures.

However, despite all its qualitative strengths at determining movement of fluid contacts, faults transmissibility, mapping of bypassed and compartmentalised oil which constitute the targets for infill wells, among others applications; separation of pressure and saturation changes with 4D seismic alone still remains a herculean task and subjects of much research work. This is because both the pressure and saturation changes combine together to produce 4D seismic response, and sometimes there are leakages between the fluid-saturation change and pressure change (Landrø 2001; MacBeth et al. 2006). These leakages pose challenges to qualitative and quantitative interpretation. Also accurate estimation of these dynamic reservoir properties is necessary in order to make reservoir management decision on possible well intervention and developmental plan. Therefore, some of the recent 4D seismic researches are geared towards making separation of changes in pressure and saturation possible, to further enhance interpretation and history matching the engineering simulation model.

Among other limitations of 4D seismic applicability are the difficulties of obtaining measurably high enough time-lapse signals with respect to noise, due to long time scales, in stiff and low porosity carbonate rocks such as seen in the Middle Eastern reservoirs (Dasgupta & Jervis 2009). Alternatively, pilot micro-seismic field trials conducted by Dasgupta & Jervis (2009) in Saudi Arabia have shown that passive seismic has a good potential for monitoring carbonate reservoir. There is also problem of very small change in elastic properties that are associated with seismic monitoring of injected water displacing medium or heavy oil at deep offshore environments, such as seen offshore Brazil and China, where the injected water and the oil being displaced have similar densities (Manrique & Campanella 2006). In addition, the recent low salinity (LoSal) water injection technology for enhanced oil recovery requires differentiating, on the basis of salinity differences, between the injected and formation waters. Also, time lapse seismic have not

been applied to monitoring reservoirs undergoing polymer injection (an example of chemical EOR), probably because this EOR mechanism may not produce detectable time-lapse seismic signal (Johnston 2013). Even with the integration of conventional well–scale reservoir surveillance techniques used by the reservoir engineers to validate 4D seismic analysis and interpretation; these limitations in applicability still exist. Therefore, there should be other geophysical tools that will either compliment time-lapse seismic or serve as an alternative to it in reservoir monitoring. One such tool is time-lapse Controlled-Source Electromagnetic (CSEM) method.

Integration of different but complimentary datasets is a usual phenomenon in applied geophysics, particularly in hydrocarbon exploration and appraisal. Commonly, different geophysical methods have different inherent ambiguities, non-uniquenesses and limitations in characterising different subsurface geological targets of interest. In oil and gas exploration and production, the goal of any integrated geophysical approach is to determine, as most effectively as possible, the reservoir and fluid properties, by utilizing differing strengths while reducing the ambiguities, risks and uncertainties associated with each of the methods. Therefore, it is very important for a geophysicist to know the strengths and weaknesses of the different methods within the context of the project at hand, so as to enable him or her to use the right combination of methods for the job at hand (MacGregor 2011). For instance, gravity and magnetic methods have been routinely used in the frontier hydrocarbon exploration to obtain regional reconnaissance information such as thicknesses of sedimentary layers overlying the basement rock, stratigraphical and structural configuration of the sediments and other features that could be favourable to the generation, migration and accumulation of hydrocarbon into a trap. This is possible because different subsurface lithological and structural configurations produce varying potential field strengths that are detected and measured at the surface as anomalous density (gravity) and magnetic susceptibility (magnetic). Information obtained from these potential field methods is then used to constrain more localised 2D and 3D high resolution seismic surveys to adequately image and map the subsurface structures and identify possible hydrocarbon traps as drilling targets.

Now, within the last fourteen years, Controlled-Source Electromagnetic (CSEM) method, which measures resistivity structure, has proved to be an excellent complimentary method to seismic in the pre-drill de-risking of hydrocarbon leads such as in a chalk reservoir (e.g. MacGregor 2011) and in clastic reservoirs (e.g. Hesthammer et al. 2012). Usually, resistivity logs are the only reliable hydrocarbon indicators at the well locations, but there are requirements to have a better understanding of the vertical and horizontal distribution of the fluid content within the subsurface structure. Also, it is necessary to discriminate resistive hydrocarbon from the conductive saline water prior to the very expensive drilling operation. These require a surface geophysical method that is sensitive to the resistivity contrast. Such method is the CSEM. The ability of the CSEM methods to provide the distribution of anomalous resistivity signal has been utilised in identifying hydrocarbon saturated reservoir, and this has helped in ranking prospects provided from seismic interpretation before making decisions on the drilling operations. This has significantly reduced the occurrence of drilling dry holes, particularly when the seismic direct hydrocarbon indicator is due to low gas saturation or shallow residual gas leakage caused by a failed trap (e.g. Moser et al. 2006). However, CSEM still depends largely on the seismic and well log information to overcome its limitations in terms of structural and vertical resolution. Also, for the fact that it is only sensitive to subsurface resistivity structure, not directly to fluid saturation distribution; it is usually calibrated against well logs for an improved interpretation and prospect appraisal (e.g. MacGregor et al. 2012). Therefore, it cannot stand alone as an exploration tool. Successes and disappointments of CSEM applications in the Barents Sea are recorded in (Kjølhamar et al., 2014; Carstens 2014).

Based on the successes of this joint exploration approach, it has been suggested that integration of CSEM with seismic in the production phase of the reservoir may provide more benefits in monitoring fluid saturations. In specific terms, it is believed that fluid substitution due to water injection and hydrocarbon production activities over two or more calendar periods could produce measurable time-lapse resistivity anomaly that could be detectable at the surface using time-lapse CSEM surveys. In addition, at this stage in the oilfield life cycle, there is a better understanding of the reservoir and more information are available from different sources to constrain structural deficiency of CSEM and to aid time-

lapse interpretation (MacGregor 2011). Table 1.1 shows the reduction in risk associated with CSEM interpretation as the life cycle of the field progresses from frontier exploration to monitoring and management stages.

Stage in the field life cycle	Seismic availability?	Well availability?	CSEM Interpretation risk	Remark
Frontier Exploration	None	None	Very high	Data difficult to interprete
Exploration	Sparse 2D, probably 3D	None or limited	High and model dependent	Detection of thin resistor possible
Appraisal and Development	3D	Several	Moderately low	Fluid discrimination possible
Monitoring and Management	Several 3D or 4D (Engineering simulator also available)	Many	Low	Monitoring of production - induced change in water saturation possible.

Table 1.1: *Reduction in the technical risk involved in CSEM interpretation as a function of the life cycle of an oilfield and availability of complimentary data from other sources (Modified from MacGregor 2011).*

Integrating CSEM into reservoir monitoring workflow is important as 4D seismic data analysis alone has not been enough to separate the saturation effect from the pressure effect explicitly. Equally important is role the time-lapse CSEM could play in secondary and tertiary hydrocarbon recovery processes involving distinguishing injected brine from the formation brine based on the dependence of resistivity on salinity and temperature. Generally, in cases where there are no acoustic impedance contrasts, there might be good possibilities that there would be a resistivity contrast to justify time-lapse CSEM surveys, for instance in water-flooding of heavy oil.

This thesis explores the possibility of integrating CSEM in reservoir monitoring and addresses other practical engineering and EOR issues, like temperature and salinity variations associated with water injection, and how they impact on the time-lapse CSEM measurements and interpretation. The thesis assesses CSEM for dynamic reservoir characterisation, especially in terms of how it might compliment 4D seismic.

1.1 Objectives of this research

The four main innovative objectives of this research are as follows:

(1) Extension of the concepts used in 4D seismic technology to assess time-lapse marine CSEM surveys for practical reservoir monitoring. This involves establishment of an engineering consistent electric rock physics model that will cater for the temperature and salinity variation during water injection. It also entails assessment of technical risks that may be involved in time-lapse CSEM project, through a screening study similar to 4D seismic. This is done using three hydrocarbon producing provinces.

(2) Incorporation of simulator to EM modelling workflow into the simulator to seismic workflow for feasibility studies of time-lapse CSEM in reservoir monitoring. This has brought about coupled interpretation of time-lapse CSEM and 4D seismic modelled data, in order to qualitatively separate the saturation and pressure effects due to production and injection activities. This interpretation is consistent with the production history, calibrated with information at well locations.

(3) Examination of the practical effects of changes in temperature and salinity during secondary and enhanced oil recovery involving brine mixing, on the time-lapse CSEM and 4D seismic monitoring. This highlighted CSEM unique potential as a complimentary reservoir monitoring tool, especially where change in fluid properties induces little or no change in the elastic properties, to warrant 4D seismic application in brine tracking.

(4) Insights into 4D CSEM data modelling and analysis. Various issues involved in making 4D CSEM possible.

First, let us look into the fundamentals and history of the controlled-source electromagnetic methods.

1.2 Fundamentals of Marine Controlled-Source Electromagnetic methods

James Clark Maxwell in his *Treatise on Electromagnetism*, first published in 1873 (*unabridged republication of the third edition of 1891 is referenced here*, Maxwell 1954), gave the mathematical formulation of the laws governing the behaviours of electromagnetic fields in a conducting material. The mathematical formulation is expressed in the four Maxwell's equations as written below:

$$\nabla \times H = j + \frac{\partial D}{\partial t} = c \tag{1.1}$$

$$\nabla \times E = -\frac{\partial B}{\partial t} \tag{1.2}$$

$$\nabla . B = 0 \tag{1.3}$$

$$\nabla . D = q \tag{1.4}$$

Equations (1.1) and (1.2) are the Maxwellian vector equations. Equation (1.1) indicates that the vector magnetic field (H) arises from the summation of the conduction current (j) and the time (t) varying displacement current (D), while equation (1.2) shows that the electric field (E) results from the time varying magnetic induction field (B) and that the electric and magnetic induction fields act in opposite directions. Equations (1.3) and (1.4) are the Maxwellian scalar equations. Equation (1.3) represents the Gauss's law of non-existence of magnetic charges. In other words, the only source of magnetic induction field (B) is electrical current. Equation (1.4) represents a direct agreement with the Coulomb's law, which shows that the electric charges (q) are the source of electric displacement current (D).

The electric field (E) and electric displacement current (D) are related by:

$$D = \varepsilon E \tag{1.5}$$

Also, the vector magnetic field (*H*) and magnetic induction field (*B*) are related by:

$$B = \mu H \tag{1.6}$$

Equations (1.5) and (1.6) are known as the constitutive equations, where ε and μ are the dielectric constant (permittivity) and the magnetic permeability, respectively. More information about Maxwell's equations and their implications could be obtained in (Zhdanov 2009).

The total current density (J) is the summation of conduction currents (J_c) and displacement currents (J_d). This is expressed in terms of electric fields as:

$$J = J_c + J_d = \sigma E + D \tag{1.7}$$

Where σ is the electrical conductivity of the material, which is the reciprocal of electrical resistivity (R)

The Maxwell's equations form the basis for the application of geophysical electrical methods, and in particular the electromagnetic methods, to investigate inhomogeneous conducting earth. The electromagnetic methods could be categorised into passive (natural sourced) and active (artificially induced source) methods and the surveys could be done airborne (aeromagnetic), onshore (land), or offshore (marine). There are two main electromagnetic techniques applied to offshore exploration, namely the Marine Magnetotelluric (MT) and the Marine Controlled – Source Electromagnetic (CSEM) methods. Marine MT method utilises natural telluric current source, while Marine CSEM method uses high powered artificially induced current source for which power, frequency, and relative positions of source and receiver are all controlled (Constable & Srnka 2007).

The electric field displacement term in Equation (1.7) led to the discovery of radio waves and broadcasting technology (Zhdanov 2009). However, at MT and CSEM frequencies, the displacement currents are negligibly small, thus they are simply ignored. Therefore, Equation (1.7) becomes:

$$J = \sigma E \tag{1.8}$$

Figure 1.1 illustrates the CSEM survey. The frequency domain CSEM requires deep water to avoid shallow water airwave phenomenon which tends to attenuates source energy into the air (Andreis & MacGregor 2008).

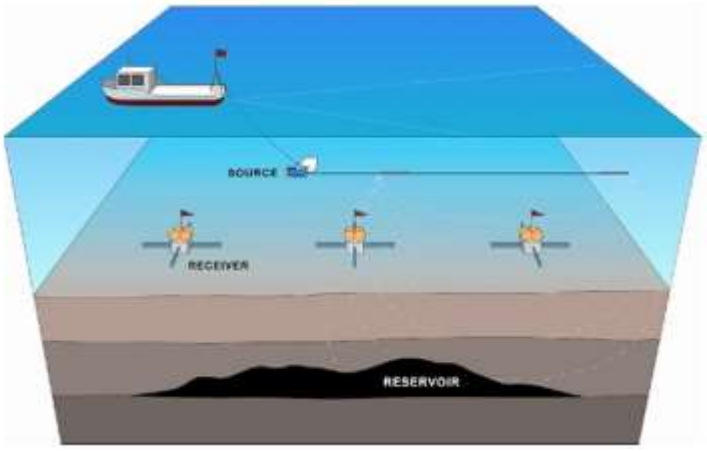

Figure 1.1: *Simple schematic illustration of horizontal electric dipole CSEM survey. The EM signal is emitted by the dipole source, about 100 – 200m long, towed 25 – 100m above the seafloor. The source induces high energy electromagnetic field into the subsurface (e.g. hydrocarbon reservoir) by transmitting up to 1000A (at a frequency 0.1Hz) current. The returning electric and magnetic fields are recorded by the seafloor receivers, from which the subsurface resistivity anomaly is indicated. Naturally generated magnetotelluric electric and magnetic measurements could also be recorded by the same seafloor receivers.*

The most important concept in any EM method is skin depth, as it determines the depth of penetration of the electromagnetic field into the earth. The concept determines the frequency of the electromagnetic source energy in relation to the resistivity and depth of the conducting overburden in the CSEM surveys. EM energy decays exponentially in conductive rocks over a distance given by the skin depth. The skin depth is therefore defined as the distance over which an electromagnetic field propagating through a conductive earth has been reduced by the factor of $1/e = 0.3678794411$ (Constable 2010; Zhdanov 2009). Skin depth (Z_s) is expressed mathematically in terms of conductivity (σ) and frequency (f) as:

$$Z_s = \frac{500}{\sqrt{\sigma f}} \tag{1.9}$$

In terms of resistivity (R) and time period (T), skin depth (Z_s) is expressed as:

$$Z_s = 500\sqrt{RT} \tag{1.10}$$

Equations (1.7) and (1.8) show that the depth of penetration of an electromagnetic field is increases with smaller frequency and larger resistivity. Therefore, a highly conductive overburden can significantly attenuate the electromagnetic source energy before it reaches the target resistive hydrocarbon reservoir (Zhdanov 2009). On the other hand, magnitude of the CSEM anomaly due to resistive reservoir becomes larger with a less resistive background structure, such that a much lower frequency is required to compensate for the attenuation. This explains the reason behind low frequency source used in frequency domain marine CSEM methods, in order to penetrate as far as the depth to the reservoir (MacGregor & Tomlinson 2014). Even at this, intrinsic structural resolution of CSEM anomaly is usually poor, and the depth of investigation is usually shallower than that of seismic.

1.3 History of Marine Controlled-Source Electromagnetic (CSEM) Methods

Historical backgrounds of marine controlled source electromagnetic (CSEM) methods are well documented in the open literature (majorly in Constable & Srnka 2007 and Constable 2010). Constable (2010) gave a good chronological order of the development of electromagnetic methods. While focusing on the ten years of practical applications of marine CSEM in hydrocarbon exploration, he closely linked historical development of marine CSEM with that of the marine magneto-telluric (MT). This is because the two methods are quite similar in terms of seafloor measurements of electric and magnetic fields, which are due to subsurface resistivity variations (see Figure 1.1). Even nowadays, MT data are still routinely collected during the CSEM surveys; they only require receivers which are sensitive to the passive natural EM fields within the subsurface and the induced electric and magnetic fields from the transmitter (e.g. in Eidesmo et al. 2002; Weitemeyer et al. 2006).

While CSEM involves measurement of both vertical and horizontal electric and magnetic fields due to vertical and horizontal flow of induced current; the Magnetotelluric method, on the other hand, involves measurements of only the horizontal component of the electric and magnetic fields due to the natural flow of telluric currents which are mostly generated in the horizontal plane within the earth (e.g. Cagniard 1953; Constable & Srnka 2007; Constable 2010).

1.3.1 Earlier applications – the link between MT and CSEM

Since the 1920s, marine electromagnetic methods have been developed mainly for military intelligence and defense applications and it has continued to be used for these objectives until the present day. Ship guidance, vessels and submarine cables detection were made possible with the aid of electric and magnetic fields generated by the alternating current (AC) marine electromagnetic methods (e.g. Drysdale 1924). The first use of EM methods for hydrocarbon exploration occurred in the former Soviet Union. It was in the form of MT consisting mainly of magneto-variational and gradient studies or towed electrokinetograph measurements (Fonarev 1982, in Constable 2010).

The MT method has been used onshore since the 1950s (Vozoff 1972) and offshore since 1980s (Key et al. 2006) as an imaging tool for mapping geologic structure as part of a routine in exploration activities. Marine MT, though earlier considered to be of limited use in the offshore hydrocarbon exploration (Chave et al. 1991), has been found to be commercially useful on the continental shelves for petroleum exploration (Constable et al. 1998; Hoversten et al. 1998). MT is particularly good at mapping salt deposits, volcanic and carbonates which are challengingly blind to the sharp imaging eyes of the seismic methods, but it cannot be used as a single method for hydrocarbon exploration because MT currents mainly flow horizontally and are mostly invisible to the thin sub-horizontal resistive formation (Constable & Srnka 2007). Thus, the MT technique lacks the ability to delineate the presence of thin resistive horizontal layers of hydrocarbon saturated rocks. However, it is capable of offering an independent estimation of the background resistivity structure, with which the CSEM data could be normalized in order to improve the CSEM signal due to the thin hydrocarbon resistors. Also MT data can be used to remove any

unwanted incremental resistivity effect at shallow depth that could be confounding deep seated anomalous resistivity targets in the radial field (Ellingsrud, et al. 2002; Eidesmo, et al. 2002).

1.3.2 Academic efforts and the development of Horizontal Electric Dipole (HED)

Subsequent developments of marine MT and marine CSEM soundings were driven by academic objectives to investigate the oceanic lithosphere, mantle and active spreading centres. As at early 1960s, Charles Cox and Jean Filloux had developed the first deep seafloor equipment for MT and CSEM soundings. They mobilized these electric and magnetic fields recorders into water depths of about 1 to 2 km offshore California. By 1965 they had deployed the same receivers into 4km water depth at about 650m distance from the shore. Although this later attempt did not produce concurrent measurements of seafloor electric and magnetic fields, but by calibrating both fields against the land magnetic field records, a seafloor MT response was produced. Full descriptions of this first set of recording instruments are well documented in Filloux (1967) and Cox, et al. (1971).

Bannister (1968) was probably the first to recommend the horizontal electric dipole (HED) array, which is now used in marine CSEM measurements today because of its theoretical and practical advantages (Constable & Srnka 2007). Bannister presented the theory of frequency-domain marine CSEM, seafloor-to-seafloor determination of sub-seabed distribution of resistivity by using a dipole transmitter to artificially generate and transmit electric current into the subsurface and dipole receiver to measure the resulting EM fields at the seafloor. His recommendation of the HED configuration was informed by the need to reduce the resulting errors due to the observed noise associated with the movement or vibration of magnetometers in the earth's main fields. Earlier, Brock-Nannestad (1965) had proposed a vertical gradient method which is quite similar to the MT method, and much later Coggon & Morrison (1970) proposed a comparatively high frequency vertical magnetic dipole source for characterization of shallow structures. Probably unaware of the Bannister's publication, Charles Cox of the Scripps Institute of Oceanography, University of California San Diego (UCSD), independently presented an HED CSEM sounding technique as an appropriate tool for delineating resistive subsurface geological layers (Cox

1980). However, in addition to this similar work to that of Bannister, Cox recognized that the transverse magnetic (TM) mode of propagation of the horizontal electric dipole is the most effective in terms of offering vertically transmitted electric fields in the poorly conducting rocks. This TM mode, otherwise called the radial mode is now employed in the hydrocarbon exploration. Cox (1981 in Constable 2010) expanded on the concept of marine CSEM with his deep-sea experiment carried out in 1979, which was motivated by the need to replace the relatively high frequency energy lost to magnetotelluric fields with a deep-towed artificial current transmitter in studying the shallow and resistive parts of the oceanic lithosphere. This radial mode transmission of horizontal electric dipole is utilized in my research for the reservoir monitoring purpose. Both electric and magnetic fields, amplitude and phase responses, are considered.

A comprehensive review of the HED EM instrumentation and its improvement in relation to the marine environment, where it is deployed, is given in Constable (2013). The EM modelling performed in this thesis utilized the HED method. MacGregor & Tomlinson (2014) recently provided a good tutorial on the methods and practice of marine CSEM, which includes a brief description of different CSEM acquisition techniques, with specific focus on the HED method and its suitability for oil industry application.

It is noteworthy that Martin Sinha and his group at the University of Cambridge, in the mid-1980s, also developed a marine CSEM system quite similar to that of the Scripps at UCSD but with a very important improvement in its transmitter antenna; which being neutrally buoyant, allows the deep-towed transmitter to be "flown" above the seafloor at about 100m high (Sinha et al. 1990). This improved equipment, which was first used in 1987 and 1988, enhanced academic studies over areas of tectonic activity, such as rough terrain of mid-oceanic ridge axis, that were the main geological targets of interest during this period. The approach later proved to be of desirable application in hydrocarbon exploration (Constable & Srnka 2007).

One of the fairly recent academic works includes a collaborative Cambridge/Scripps experiment which marked the first 2D inversion of real data (MacGregor et al. 2001). They conducted a comprehensive study which involves interpretation of a low resistivity

anomaly from marine CSEM survey, as diagnostic of the hot and/or saline fluids penetrating the crust at a site of extensive hydrothermal activity in the Valu Fa Ridge at the Lau Basin. They observed that the very low resistivity signatures could not have been caused by abnormally high porosity because there is no corresponding effect on the seismic velocity. Earlier collaborative studies involving the Cambridge and the Scripps groups are the Reykjanes (MacGregor et al. 1998) and the East Pacific Rise (Evans et al. 1991 in Constable & Srnka, 2007). Chapter 6 of this thesis examines this idea of temperature and salinity effects on the CSEM measurements and interpretation within the context of brine mixing in the reservoir, during secondary and tertiary hydrocarbon recovery.

Between 1984 and 1998, Nigel Edwards and his team at the University of Toronto performed several works on the modeling of time-domain EM (e.g. Edwards & Chave 1986 and Edwards 1997) and on the application of an adapted land magneto-metric resistivity technique, which uses a vertical low-frequency electric transmitter hanging from the ship to the seabed, in the marine environments (e.g. Edwards et al. 1985). Cheesman et al. (1988) also deployed a horizontal magnetic dipole-dipole time domain system. Although, these two time-domain techniques, unlike the deep-water frequency-domain horizontal electric dipole system, lack the deep propagation required for hydrocarbon detection; but they are still currently used for other geophysical surveys (Evans et al. 2002 in Constable & Srnka, 2007). Several other academic works on Marine CSEM and MT since 1970s are reviewed in publications like Palshin (1996), Constable (1990) and Baba (2005).

1.3.3 Application to hydrocarbon exploration: Industry involvement

Resulting from these academic studies, the potential of using marine CSEM for hydrocarbon exploration in the deep-water terrains has been well identified (Chave et al. 1991). Several factors did not permit its commercial application for hydrocarbon exploration. These factors include: (i) frequency domains CSEM requires deep water to avoid shallow water airwave effect; but the few number of offshore exploration activities then, were mainly done in the shallow waters of around 300m; (ii) challenges of computational ability and scarce electronic/digital data acquisition system; and (iii) industry focus on the just emerged and growing 3D marine seismic methods (Constable, 2010).

Another longer term concern stated by Constable (2010) is the fact that many companies that have commissioned CSEM surveys cannot make the best use of the data. This is because there is a shortage of skills and tools to integrate CSEM results with data from other sources, such as seismic and geological data. In other words, CSEM acquisition technology was growing faster than the development of interpretation tools. This thesis aims to partly address such concern, especially in terms of time-lapse reservoir monitoring, which involves integration with seismic and production information at well locations using fluid – flow simulation models.

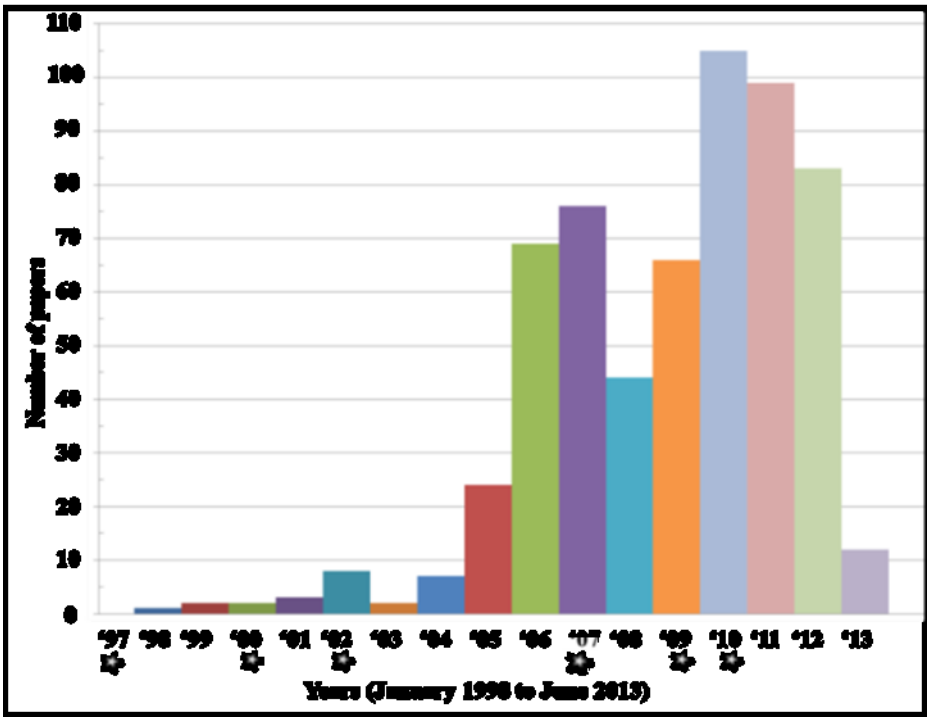

Figure 1.2: *Number of publications per year on marine CSEM between January 1998 and June 2013 at SEG and EAGE conferences, and in journals such as The Leading Edge, Geophysics, First Break, Geophysical Prospecting and others, totalling 603. The stared years are of particular interest. See text for detail (sourced from the SEG website).*

Between January 1998 and June 2013, there have been about 603 papers on CSEM research cutting across different areas of interest (sourced from Society of Exploration Geophysicists website). The numbers of papers on CSEM per year are as shown in Figure 1.2. Common to all the years under review are the developments of forward modeling and inversion algorithms (1D, 2D, 2.5D and 3D), joint inversion with seismic and/or MT,

acquisition and processing, all of which are still ongoing. Up until 2000, publications on CSEM have only been centered on the results of academic studies (e.g. Cox 1981; MacGregor et al. 1998); whereas when compared with seismic development timeline, as at 1997, technical risk involved in a 4D seismic project was already been assessed (Lumley et al. 1997).

The two major companies involved in the early industrial interests in marine CSEM are Exxon (now ExxonMobil) and Statoil. By performing a number of experiments involving numerical and physical modelling; Exxon, in the early 1980s, was able to scope-out a field test using naval minesweeper and towed electric sensors that were still under a developmental stage at Scripps. However, those factors mentioned earlier hampered further work (Constable & Srnka 2007). Around the late 1990s, deep marine exploration started at water depths of about 1000m in the Gulf of Mexico, and production in such terrain commenced in the early 2000s when marine technologies such as tension-leg platforms were developed. It was during this period that the industry started showing a more committed interest in marine CSEM (Constable 2010). ExxonMobil resumed its work on EM, this time, carrying out investigations into 3D CSEM survey design, data acquisition and processing, inversion and interpretation which culminated in field trial tests, around late 2001, carried out off Scotland and West Africa (Constable & Srnka 2007).

Earlier in late 1999, a review of Statoil's internal research on numerical and analog modelling showed that for a controlled-source EM amplitude signature of a hydrocarbon filled subsurface layer to be detectable, such target should not be too small relative to its burial depth, and the water depth should be significant enough to suppress the airwave effect which tends to create destructive interference with the desired signal. Statoil affirmed that if such conditions are met, then, the signal of such a model containing the oil layer will be a factor of 2 to 10 different from the non-oil saturated layered model (Constable & Srnka 2007). Based on realistically practicable parameters used, such as frequency, range, antenna length and power; the experimental signals obtained were above the noise floor threshold and this result sufficiently encouraged Statoil to embark on a full-scale field trial survey, carried out offshore Angola in November 2000 (Constable & Srnka 2007). This project, initially described as seabed logging, was done in collaboration with Scripps Institute of

Oceanography and the Southampton Oceanography Centre (comprising the group formerly at Cambridge) (Constable & Srnka 2007). The results are documented in the papers between 2000 and 2002 (e.g. Eidesmo et al. 2002 and Ellingsrud et al. 2002). These efforts by Statoil and Exxon marked the beginning of using CSEM as a new method for remote sensing and identification of hydrocarbon – filled layers in deep offshore terrains.

1.3.4 Fourteen years after the first field trial

About fourteen years after these field trial of Angola (Eidesmo et al. 2002), there have been many reported cases of successful applications of CSEM as a pre-drill de-risking tool, which in many cases have helped to update seismically interpreted hydrocarbon leads, confirming them to be either highly resistive hydrocarbon saturated commercial sweet spots or low resistivity non-commercial residual oil or gas, thereby significantly increasing drilling success rates (e.g. Moser et al. 2006). In other words, this has greatly reduced the drilling of dry holes which are very much more expensive offshore than the additional cost of a CSEM survey. Hitherto, the seismic method is the major surface exploration tool for both hydrocarbon trap mapping and direct hydrocarbon indication (DHI). However, there have been cases of dry holes occasioned by the false DHI or bright spot interpretation from seismic data alone, which are normally caused by lithological changes, fizz water or low gas saturation (Moser et al. 2006). Now, CSEM provides direct resistivity indicator (DRI) between the hydrocarbon and the formation water. However, its inability to structurally constrain the target depth and the possibility of the presence of non-hydrocarbon resistive subsurface features require that CSEM data be interpreted along with seismic data. Thus, CSEM is best used as a pre-drill appraisal tool, to obtain complimentary fluid information to that obtained from seismic data. There are many examples in the open literature, of integrated interpretation of CSEM and seismic data with well log calibrations, in which porosity and saturation are jointly inverted and/or interpreted (e.g. MacGregor et al. 2012; MacGregor 2011; Moser et al. 2006; Harris & MacGregor 2006; Constable & Weiss 2006; Hoversten et al. 2006 among others). There have also been recent pilot works on the application of marine CSEM to detect shallow gas-hydrate (e.g. Weitemeyer et al. 2006). The majority of publications between 2002 and 2006 focused mainly on the exploration applications of CSEM in conjunction with seismic. It is worth mentioning that during this

period, compared with seismic, 4D seismic was already been tested for quantitative interpretation to estimate pressure and saturation changes (MacBeth, et al., 2006). As at 2004, the thoughts of the possibility of time-lapse CSEM application in reservoir monitoring witnessed two patent registrations, one on May 25 (Strack 2004) and the other on June 24 (Constable 2004) the same year. Several papers have since then been written to examine the sensitivity of time-lapse CSEM in reservoir monitoring (e.g. Lien & Mannseth 2008; Orange et al. 2009; MacGregor & Cooper 2010; Andreis & MacGregor 2011; Lien 2013) and CO_2 monitoring (e.g. Bhuyian et al. 2012; Zhdanov et al. 2013). Interestingly, as at 2009, permanent sensors technology is already making 4D seismic technology possible on land. This shows that the emerging time-lapse CSEM can take advantage of the advances in the emerged and growing 4D seismic technology.

1.3.5 Rebirth of CSEM: Research future

MacGregor & Tomlinson (2014) identified four reasons, among others, responsible for the sudden fall in the CSEM applications in the oil industry around 2007, they are: (a) Failure of CSEM results to provide expected business values; (b) Infancy of CSEM acquisition and interpretation, especially in terms of poor understanding of anisotropy and integration with other geophysical dataset (seismic and well logs); (c) Placement of unrealistic ability on CSEM technology, due to potentially large market; and (d) Hampered market growth due to competition in patenting of the relatively new technology in the oil industry. However, MacGregor & Tomlinson (2014) concluded that CSEM is still a good source of resistivity information, and that if CSEM data are properly acquired and interpreted, the resistivity information could assist in reservoir characterization to determine rock and fluid properties. Earlier, Constable (2010) had identified four clear research directions in which CSEM technology is already going, they are: (i) addressing the airwave problem associated with shallow water depth, which has restricted the application of frequency-domain CSEM to deep water environment (e.g. Andreis & MacGregor 2008); (ii) application of time-domain methodology; (iii) the development of continuous profiling tools and; (iv) the use of CSEM for monitoring the hydrocarbon producing reservoir, which has many published feasibility as reviewed in Chapter 2. Another area significant to the future development of EM

technology in the oil and gas industry is the ability to jointly acquire 3D/4D EM with the 3D/4D Seismic data in one go. This will save time and money in acquisition.

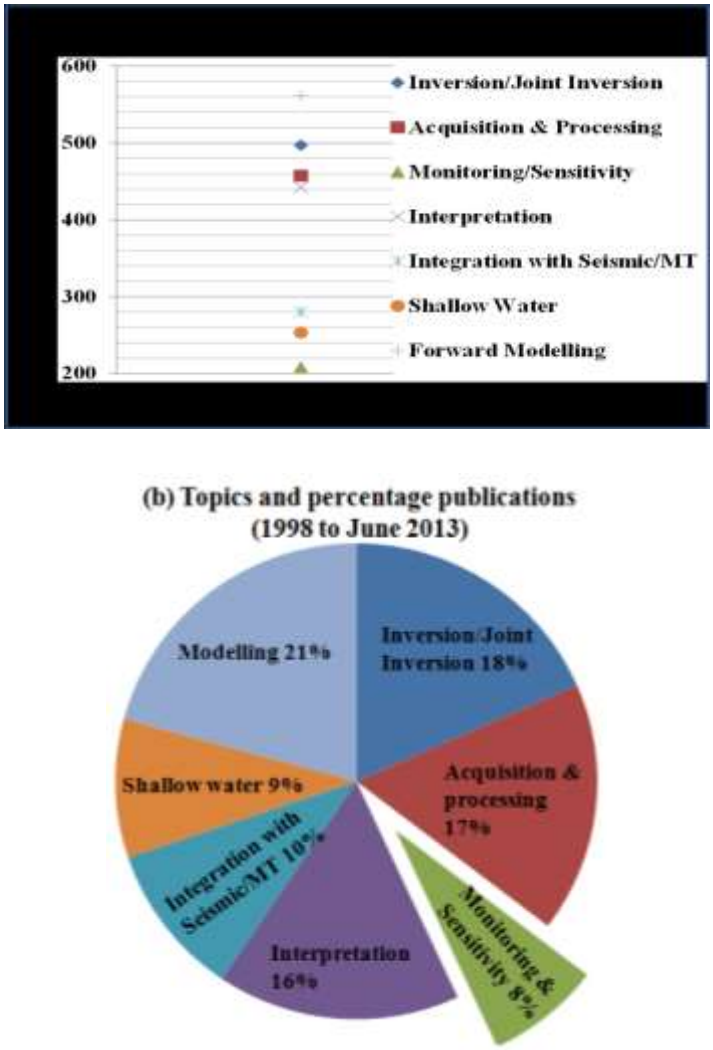

Figure 1.3: (*a) Number of papers versus topics on marine CSEM between January 1998 and June 2013 covering SEG and EAGE conferences abstracts, The Leading Edge, Geophysics, First Break and Geophysical Prospecting and other Journals. Most of the papers incorporate forward modelling and inversion. (b) Only 8% of these publications focus on the sensitivity of time-lapse CSEM in reservoir monitoring (informaion sourced from the website of the Society of Exploration Geophysicists, 1996 - 2013).*

Also, it will encourage joint analysis and interpretation to make the best use of the two geophysical datasets. In line with this vision, EAGE in its January 2014 edition of the *First Break* reported that the PGS recently succeeded in conducting a 'full scale simultaneous

acquisition of towed-streamer EM and 2D seismic data using Geo-streamer' in the Fastnet and Celtic Sea basins offshore Ireland (EAGE, 2014). Since 2010 when I started this work, much research effort has been made to fine tune the sensitivity studies of time-lapse CSEM in reservoir monitoring, incorporating fluid flow reservoir simulator for realistic fluid fronts (e.g. Shahin et al. 2010; Liang et al. 2011; Salako et al. 2012; Liang et al. 2012; Shahin et al. 2012; Salako et al. 2013). Some of these papers are reviewed in Chapter 2 to highlight the knowledge gaps. Figure 1.3 shows the distribution of publications according to the number and percentage of topics covered within the years under review. It is observed from Figure 1.3 that apart from research on shallow water investigation and integration with seismic, more work is still needed on time-lapse CSEM applications to reservoir monitoring. This is another justification for this research, which focuses on the practical application of CSEM surveys in reservoir monitoring during hydrocarbon production and water injection.

1.4 The thesis outline

In order to achieve the objectives set-out in section 1.1, this thesis is written into eight chapters. The other seven chapters are as outlined below:

Chapter 2: This chapter reviews available literature on the feasibility studies of time-lapse CSEM in reservoir monitoring. This is done in order to: (i) establish the knowledge gaps that are in line with the four innovative objectives set out above; and (ii) move away from the usual simple model time-lapse CSEM sensitivity studies, to a more practical dynamic characterization of reservoir properties. Reservoir monitoring and management, from the engineering perspective, is then introduced for the benefit of readers who are purely EM geophysicists. Various reservoir production driving mechanisms are briefly reviewed in order to establish the production histories where CSEM surveys could play an excellent complimentary role to 4D seismic. Finally, the challenges involved in this research and its contribution to the body of knowledge are stated in this chapter.

Chapter 3: Borrowing from similar concepts in time-lapse seismic, this chapter assesses the technical risks that might be involved in any time-lapse CSEM project. To achieve this,

and to further justify the practical need for CSEM surveys; using well logs, the value of resistivity as an electric property is assessed and compared with the elastic properties such as V_p/V_s ratio and P-impedance, in terms of their sensitivities to lithology and change in saturation during fluid substitution. This required, first, a review of the electrical rock physics (mainly Archie's clean sand model and its shale-inclusive derivatives), which relates some of the petrophysical properties of the reservoir with resistivity, in terms of practical reservoir monitoring. Then, a fluid flow consistent rock physics, which gives considerations to temperature and salinity variations in the reservoir undergoing seawater or low-salinity water flooding, is proposed. Finally, three petroleum provinces, namely the North Sea, Gulf of Mexico and the West Africa are assessed in terms of rock physics and geological parameters, production mechanisms, and time-lapse CSEM response, acquisition and repeatability. Their various risk indices are scored, ranked and interpreted. Here, the first objective of this research is achieved.

Chapter 4: Reservoir simulator to electromagnetic modeling workflow is established. The dipole 1D CSEM modelling code, by Key (2009), is used for the simulator to electromagnetic modelling. The workflow is incorporated into the usual 1D convolutional modelling of seismic data from the reservoir simulator. The impacts of sea water resistivity stratification and overburden complexity on the time-lapse CSEM measurement is assessed. This is done using a synthetic model built based on a North Sea oilfield. The second objective is partly achieved in this chapter.

Chapter 5: Detailed feasibility study in order to determine the detectability and interpretability of time-lapse CSEM in reservoir monitoring, using 1D EM modelling. A real North Sea simulation model is used in this forward modeling. The joint forward modelling workflow established in Chapter 4 enables time-lapse CSEM and time-lapse seismic modelled data to be compared in terms of their sensitivities to change in water saturation. It also enables coupled interpretation of time-lapse EM and 4D seismic modelled dataset for a more robust dynamic reservoir characterization. This particularly led to the qualitative separation of dynamic changes in reservoir, changes in pressure from the changes in water saturation. The assumption here is that images produced by 1D EM modelling of 3D reservoirs, as against 3D EM modelling, provide the best possible datasets to interpret time-lapse CSEM in reservoir monitoring. This assumption is removed in

Chapter 7, where 3D EM modelling result is presented. Also assumed in this chapter are constant temperature and salinity between the injected and formation waters, a situation applicable to re-injection of produced water. This latter assumption is also removed in Chapter 6. Here, the second objective of this research is fully achieved.

Chapter 6: The effects of salinity and temperature in time-lapse CSEM are examined. Different sources of injected water are reviewed, and how each of these sources might impact on salinity and temperature are discussed. In particular, the effects of changes in temperature and salinity during secondary and tertiary recovery are assessed using numerical modelling with salinity and temperature tracking facilities. Time – lapse CSEM and 4D seismic responses were compared for three scenarios of brine injections at different geographical locations. The third objective is achieved in this chapter.

Chapter 7: Having established some of the applications of time-lapse CSEM in reservoir monitoring using 1D modelling, this chapter examines full 3D repeated modelling using integral solution of Maxwell's equation (a code provided by RSI), to assess the 4D feasibility studies using both an hypothetical homogeneous and a heterogeneous synthetic simulation models built based on the North Sea oilfield. Several parameters are considered and tested in the 3D sensitivity studies. Second derivative of CSEM amplitude as a function of the receiver range is tested as an appropriate attribute to constrain signal resolution, for both homogenous and heterogeneous models. This chapter also looks into the importance of 3D survey acquisition strategy, whereby the tow lines are set parallel to the direction of maximum expected anomaly, as maybe predicted from the engineering simulation model. The chapter leads to conclusions and recommendations for future works.

Chapter 8: The summary of this work, conclusions and recommendations for further studies are documented in this chapter. Here, it is advised that the next logical step to continue this research is to carry out repeated 2D or 3D simulator-grid-constrained inversion of modelled CSEM data to generate transverse resistance or resistivity distributions for the baseline and monitor surveys. Within some level of non-uniqueness of inversion process, this should allow the interpretation to be carried out at the rock and fluid physics scale, if the property distributions for both baseline and monitor surveys, could be recovered.

CHAPTER 2

RESERVOIR MONITORING AND CSEM

An EM geophysicist requires a fair knowledge of the fluid flow simulation modelling in order to enable him/her discuss with a reservoir engineer, the potential of time-lapse EM as a complimentary tool to time-lapse seismic for reservoir monitoring. This is on the assumption that they both understand the strengths and weaknesses of time-lapse seismic. In other words, time-lapse EM application should be driven by practical engineering needs.

2.0 Review of literature on time-lapse CSEM sensitivity studies

The possibility of collecting time-lapse CSEM surveys for reservoir monitoring focusses on the intuitive hypothesis that the intrinsic problem of depth resolution in exploration application could have minimum impact in reservoir monitoring application. This is because there are additional information from well log and production data. Also, the depth to top reservoir, the reservoir interval where injection and production activities are taking place are all known. Thus, the problem is more constrained in reservoir monitoring than in exploration (see Table 1.1). However, there is still the issue of lowered signal when monitoring localised changes in resisitivity along the flooding fronts due to fluid substitution, as against the large regional signal expected in the exploration setting (Lien & Mannseth 2008; Black & Zhdanov 2009). It is therefore important to examine the detectability, interpretability and repeatability of time-lapse CSEM signal through synthetic modelling, as a preparatory step before carrying out field data acquisition just as it is now a *de rigueur* to do such feasibility studies even in the 4D seismic monitoring technology.

Presently there are no reported field examples of marine time-lapse CSEM data acquisition and interpretation (Johnston, 2013), but several sensitivity studies have been done. These involve forward modelling and inversion of time-lapse electromagnetic (EM) data to examine its applicability to reservoir monitoring. The studies are done either directly by using basic – representative models (Orange et al. 2009) or by using reservoir analogue (Andreis and MacGregor 2011).

For the basic models, an arbitarily assigned resistivity of the model is perturbed and the resulting EM response is forward modelled and then compared with the original EM response before the perturbation. This approach is a quick way of examining the detectability and repeatability of the EM to resistivity changes and changes in the various parameters like seawater depth and resistivity, overburden thickness and resistivity and other parameters involved in the real life field situation (e.g. in Orange et al. 2009; Lien 2013). However, the approach is insufficient to assess the interpretability of time-lapse CSEM for dynamic reservoir characterisation because the reservoir heterogeneity and fluid flooding fronts are not considered in this simple model. There is also a method, in which the end-points or single-valued resistivity for 100% hydrocarbon saturated rock or for 100% water saturated rock or mixed saturations (e.g. 50% water, 50% oil) are calculated using the rock physics, though the spatial variation in resistivity, which is the reality, is not accounted for (e.g. Andreis and MacGregor 2011). On the other hand, using reservoir analogue models and incorporating changes in fluid saturation enhances assessment of interpretability of the time-lapse CSEM modelled data in addition to the detectability. This approach, which has started gaining popularity since 2011 (e.g. Shahin et al. 2010; Liang et al. 2011), is closer to the reality expected in the field. It requires the use of fluid flow simulator which provides models of time- and spatially- varying reservoir properties. This is the method adopted and refined in this thesis for enhanced dynamic reservoir characterisation (Salako et al. 2012 and 2013).

There are several examples in the literature to illustrate the time-lapse CSEM feasibility, covering hydrocarbon production and water injection monitoring, CO_2 sequestration, borehole-to-surface EM monitoring, inter-well time-lapse CSEM tomography, land CSEM

monitoring, and the fluid flow simulation models driven time-lapse CSEM modelling. Some of these examples are described below.

Lien & Mannseth (2008) applied a 3D integral equation to numerically model the time – lapse EM effect of changing parameters, such as resistivity, flooding distance, sub-seafloor depth, target thickness and source frequency. They also examined the impact of measurement and modelling errors and the importance of optimal transmitter location. They used an initial basic oil-model of 100m thick reservoir with resistivity of 100Ωm, buried 1000m below the seafloor. The reference model setup contains seawater depth and resistivity of 1000m and 0.33 Ωm respectively, and background water-saturated rock with resistivity of 1Ωm. A dipole transmitter, with a length of 100m, transmitted a current of 1000A at 0.1Hz. They concluded that the CSEM method can detect the time-lapse changes in resistivity, which in reality could be inferred for saturation change. They conclude that the modelling errors due to misrepresentation of background conductivity (reciprocal of resistivity) is time invariant and could cancel out in the time-lapse CSEM measurements. This is an over-simplification of the repeatability issue, as in reality, it is necessary, though difficult, to have a good way of compensating for the oilfield infrastructure which could impact the monitor modelled data. Also, they showed that only the field components of the transverse magnetic mode of EM wave propagation should be considered in order to avoid artifacts that may result from the weak background fields. They stressed the importance of optimal source location such that the vertical source-receiver separation is not too short to avoid a situation whereby the data is dominated by the wave which has mainly propagated between the highly conducting seawater and the receiver. Also the separation should equally not be too long to avoid airwave dominated data. Equally important is the horizontal source-receiver distance, which they considered optimum at 1000m.

Orange et al. (2009) examined, using 2D finite element approach, time-lapse CSEM sensitivities to the various simplified scenarios of water flooding (e.g. basal and lateral) in a 2D basic model (both single and stacked reservoirs). The initial basic model used is 5km long and 100m thick, with resistivity of 100Ωm, buried in a 1Ωm homegenous overburden at 1000m below the seafloor. The seawater depth and resisitivity are 1500m and 0.33Ωm respectively. They showed that although time-lapse CSEM signals are small for the

different flooding scenarios, they are measurable and could be useful to characterise subtle changes in reservoir geometry if extra efforts are made to attain a high degree of survey repeatability with only allowable non-repeatable noise of 5%, or better still between 1% to 2% relative repeatability error. Of particular interest is their suggestion that the time-lapse change in CSEM response could depict the dynamic change in the fluid geometry as the reservoir is being produced. They also modelled several other factors such as near-surface inhomogeneities, time varying seawater resistivity and repeatability errors in transmitter geometry and receiver locations, all of which could affect the time-lapse CSEM measurement of a producing reservoir. It was argued that precise placement of the receiver, away from the near surface resistive bodies is important for repeat surveys. This is because the impact of the near surface body is significant when the source is located directly over the body. In order to compensate for the varying seawater resistivity so that the time-lapse CSEM response could reflect the change in reservoir, they suggested measurement of seawater resistivity as a function of water depth, using conductivity-temperature-depth probe at the time of CSEM surveys. Finally they noted that permanent monitoring, in which the transmitters and receivers are fixed to seafloor monuments – as done for gravity monitoring at Sleipner (mentioned in Johnston 2013), will enhance data repeatability.

Zach et al. (2009) reported relative electric field amplitude anomalies of between 30% - 50% for 3D time-lapse CSEM modelling of a large reservoir (10 km x 10 km). They perturbed an initial model of 50Ωm maximum resistivity, which was an analogue of the inverted 3D resisitivity cube from the 3D CSEM data acquired at the Troll oil field. They concluded that, with 5% repeatability error of the current marine CSEM technology, production and water injection activities could be monitored and that different realistic flooding patterns could be distinguished from one another, up to about 10% electric field amplitude anomaly. They mentioned that with the current level of accuracy of receiver orientation and future possibility of permanent seafloor monument, as suggested by Orange et al. (2009), time-lapse CSEM will be possible. Nonetheless, it is noted that non-repeatability issues are likely to be dominated by source navigation, which includes source altitude above the seafloor, source tilt at an angle from the towline, source path offset which could vary due to inconsistent source-receiver distance along the towline and source feathering.

Black & Zhdanov (2009) included the complicating effect of inhomogeneous background conductivity, sea bottom bathymetry and the presence of a salt dome structure with resisitivity as high as 30 Ωm into their sensitivity studies. All of these could significantly distort the EM response from a hydrocarbon reservoir. An homogeneous resistive oil reservoir model of 100 Ωm was laterally flooded with conductive water of 0.5 Ωm, from the right towards the left direction, and EM measurments were made at four positions along the x-direction as the oil is replaced with water progressively (i.e. X = 14.0, 12.8, 11.6, and 10.4 km) as shown in Figure 2.1 (from top to bottom image respectively).

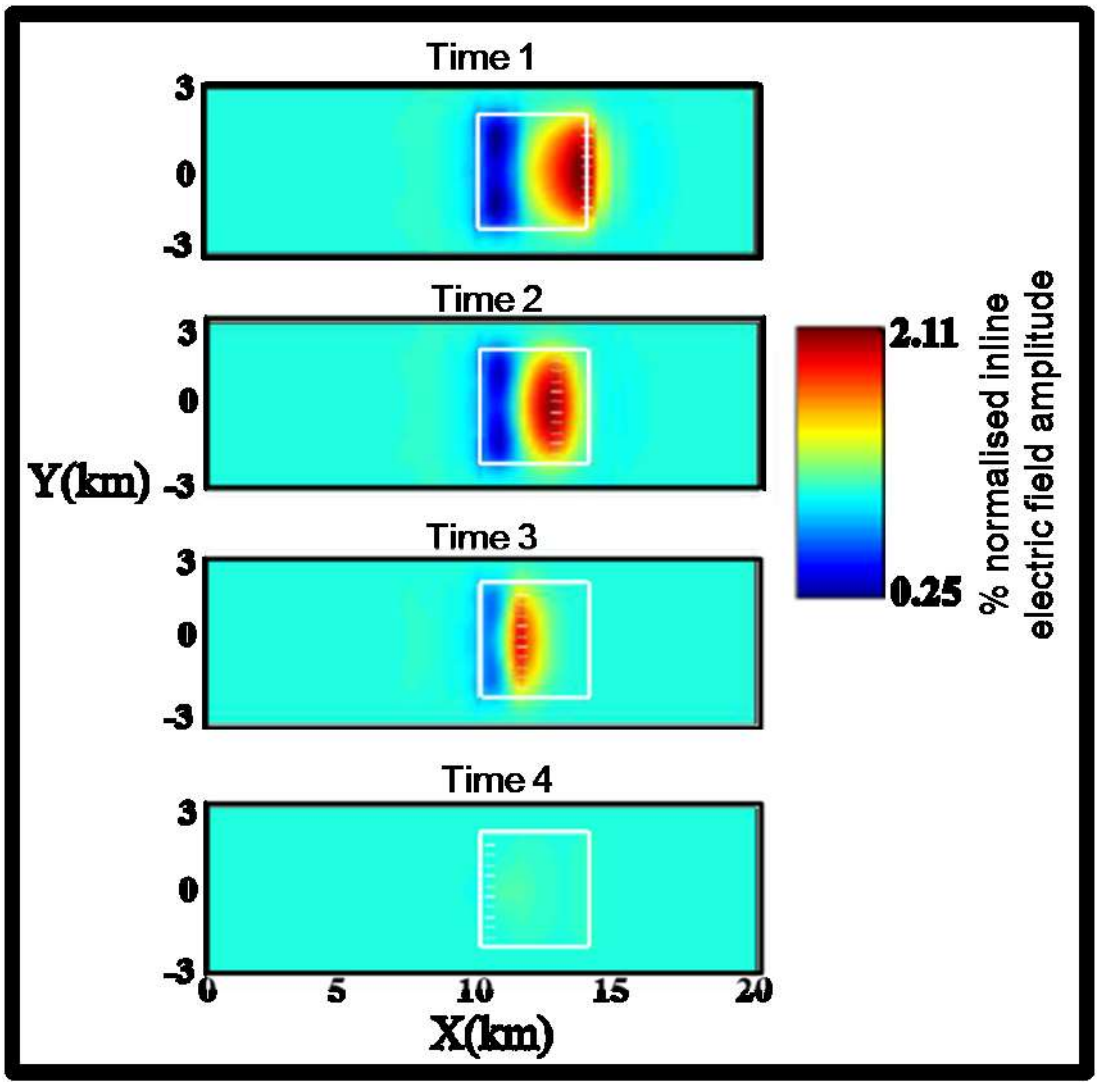

Figure 2.1: *Inline fields normalized by background at 0.3 Hz transmitting frequency. Within the white square box, the oil-water contact movement from right hand side to the left hand side could be observed in addition to the location of the remaining hydrocarbon. (Black & Zhdanov 2009).*

The total in-line electric field component, among other EM field components measured, normalised by the total background fields, show the oil-water contact movement towards the left, as the flooding progresses.

All of these sensitvity studies demonstrate a measurable time-lapse CSEM signal attributable to change in resistivity-thickness (transverse resistance) induced by possible saturation changes during production and injection activities. However, they all made an assumption of a sharp waterfront, which is unrealistic, as there are no sharp water movement in reality. Figure 2.2 shows a schematic cross-section of lateral water flooding in a canonical model with sharp time-lapse water front, and a more realistic model with irregular time-lapse water front.

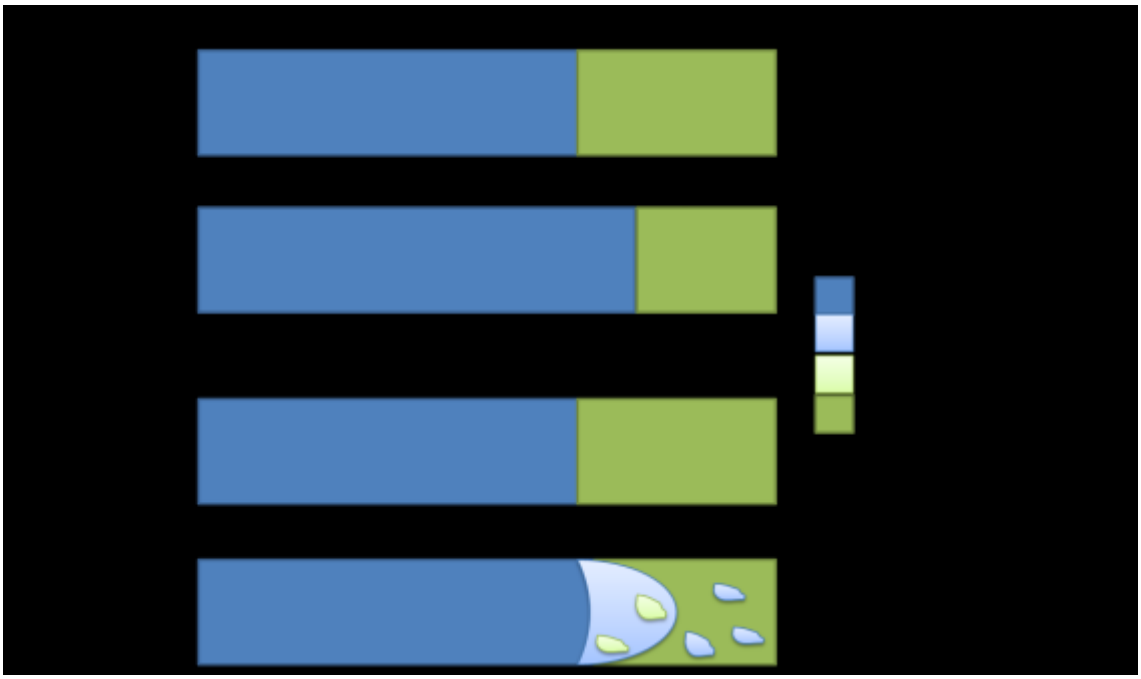

Figure 2.2: *Schematic diagram for: (a) A simple basic model (b) A more realistic model. See section 2.2 for more detail on production mechanisms.*

The fact that these studies did not include electrical rock physics model also make it difficult to assess time-lapse CSEM technology for dynamic reservoir characterisation. Moreso, most of the basic model examples used are 100m thick, but in reality, reservoirs are usually between 10m to 60m thick or even thinner.

Andreis & MacGregor (2011), went further to present second-order derivative of normalised EM amplitude with respect to source-receiver range as a good attribute for time-lapse CSEM analysis. Using Archie's electrical rock physics model for clean sand (Archie 1942), and obtaining the required parameters from the well logs, they calculated the resistivity of a synthetic model of a North Sea gas reservoir, at full gas saturation, to be 100 Ωm. A 3D channelized anticlinal model was embedded in a 1D inhomogeneous background with an average resistivity of 2 Ωm, between the depth of 1970 m and 2060 m below the sea surface with 500 m water depth. The model, which has varying lateral thickness, is about 60m thick at the upper part of the channel and covers an area of 7 km (length) by 1.7 km (width). Their modelling was based on an assumption that 22% residual gas saturation is left after a production process, which drops the initial reservoir resistivity to 8.2 Ωm. They performed 3D EM modelling to demostrate the 'sophistication' of this EM attribute, using three frequencies 0.3 Hz, 0.9 Hz and 1.5 Hz for the baseline model and 1.5 Hz as the optimum frequency for the time-lapse model. They postulated that the second-order derivative EM attribute is a good qualitative interpretation tool for depicting the edges of resistive bodies, where the measured fields are expected to change in reservoir monitoring (see Figure 2.3). However, they noted that, for this time-lapse CSEM attribute to be applied in reality; good survey repeatability achieveable through permanent installation (as earlier proposed by Zach, et al. 2009 and Orange et al 2009), and high signal-to-noise ratio through extensive stacking and spatial filtering technique are both required. Even with all of these measures, environmentally-related time-lapse changes like a 2°C change in ocean water temperature could produce 2% change in conductivity, which will significantly impact on the very small time-lapse change in the reservoir.

Andreis & MacGregor (2011) presented 2D inversion result which uses a priori constraints derivable from seismic and well logs data, whereby 3D baseline and monitor modelled CSEM datasets are separately inverted for 2D resistivity maps from which resistivity difference map is obtained. Figure 2.3 summarises their findings. They concluded that this inversion process will 'correctly account' for the time-lapse changes associated with environmental conditions and survey geometry, thus reducing the repeatability requirement which *ab initio* is difficult to achieve with current marine CSEM acquisition technology; just as it will also help in time-lapse quantitative reservoir characterisation. Their CSEM

inversion involving seismic structural constraint and well logs for resistivity calibration can be considered to be a good step towards the possibility of full 3D CSEM inversion. Such that simulator-grid and rock physics could provide robust structural and property constraints, to obtain 3D resistivity cubes for both baseline and monitor surveys, from which difference maps could be obtained. However, a better understanding of simulator-driven CSEM forward modelling incorporated with seismic is necessary, first, in order to assess the possibility of coupled interpretation of timelapse CSEM and seismic data for full dynamic reservoir characterisation.

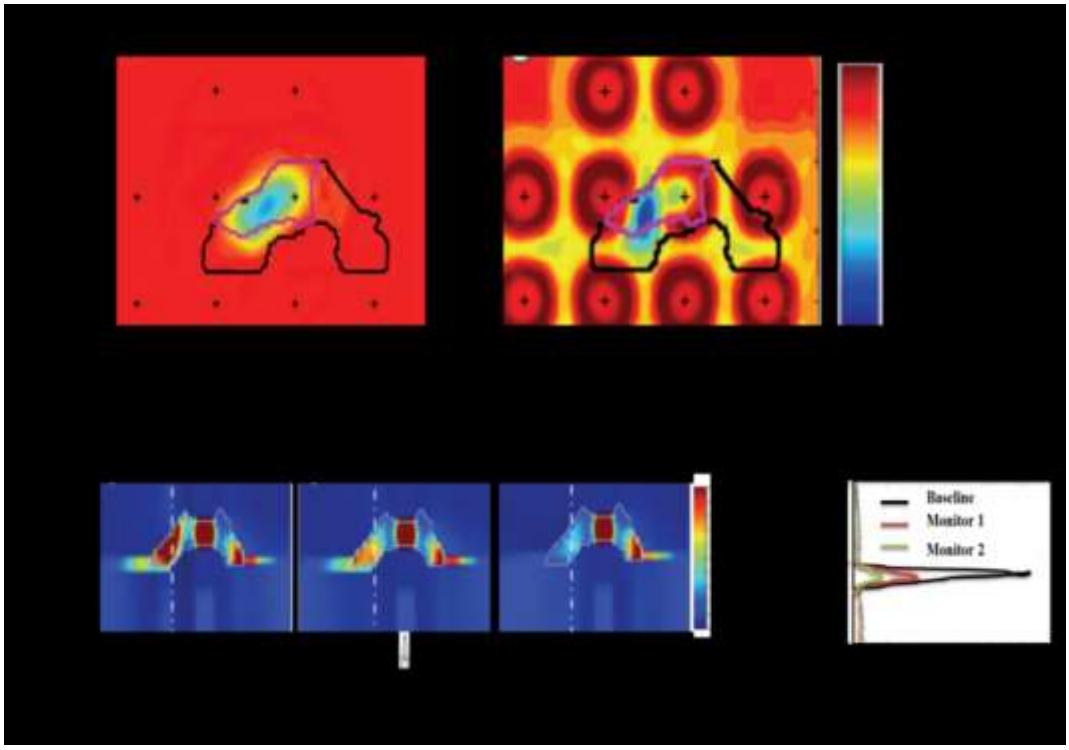

Figure 2.3: *(a) Time-lapse CSEM Second derivative attribute map, registering the anomaly within the magenta-coloured outline (left panel). The right panel shows the negative impact of 2% time-lapse change in conductivity on the same time-lapse attribute anomaly shown in the left panel. Black outline describes the horizontal footprint of the full channel and the black crosses are the source positions. (b) Recovered resistivity maps from the 2D inversion of CSEM data for the baseline, monitor 1 (after first stage of production) and monitor 2 (after second stage of production) respectively from bottom left to right. To the extreme right, is the resistivity profile from each inversion at the location indicated with white dotted line on the figures to the left (Andreis & MacGregor 2011).*

Lien (2013) carried out, using two approaches, simultaneous joint inversion of seismic amplitude-versus-offset (AVO) and CSEM data to obtain electric conductivity and P-wave velocity. The first approach utilizes Gassmann (Gassmann 1951) and Archie (Archie 1942) equations, to relate the elastic and the electric rock physics together, in order to jointly invert seismic AVO and CSEM datasets for a common model parameter – the fluid saturation. This rock-physics driven approach was earlier used by Hoversten et al. (2006). It involves common model parameters which share sensitivity to both datasets at the flooded zone. Lien (2013) successfully tested the approach on CO_2 injection. In order to ascertain the robustness of this process, results of single seismic inversion, single CSEM inversion and joint inversion of seismic and CSEM inversion were compared. The joint inversion yielded best and most stabilized estimate of CO_2 saturation, with a fairly good correlation to the original shape and size of the plume. Lien stated that this method could be applied to reservoir monitoring as well, especially as the aim of the reservoir monitoring is to identify a transition zone, where fluid saturation change has occurred in the reservoir. This led to the second approach called structure-coupled joint inversion, which focuses on the structural coupling of the two datasets. The method is beneficial in situations whereby the rock physics model of either of the seismic or CSEM is not well-known. Using cross-gradient method earlier proposed by Gallardo & Meju (2003) to impose structural similarity between the two datasets, Lien (2013) applied this method to water flooding scenarios.

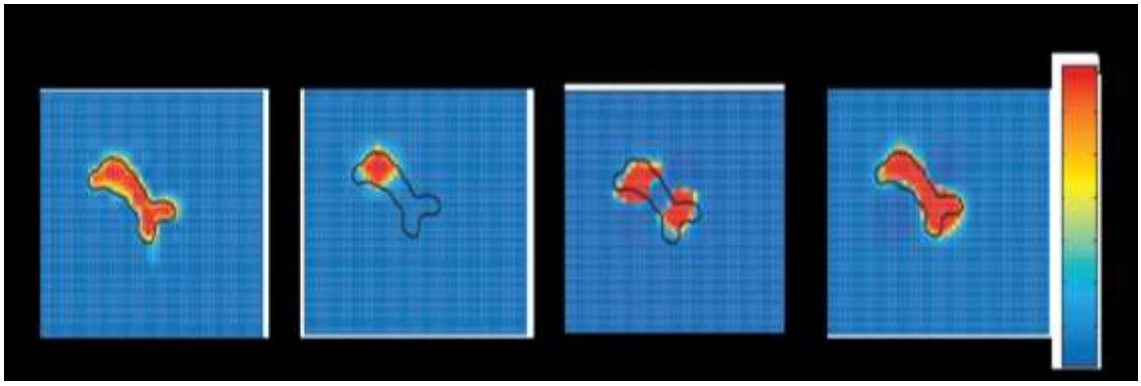

Figure 2.4: *Structurally-coupled joint inversion of CSEM and Seismic data produces conductivity map in 'd', which is more representative of the size and shape of true solution in 'a', much more than CSEM inversion alone in 'c'; 'b' is the initial representation of the model (Lien 2013).*

Their results in Figure 2.4 show that inverted conductivity image from CSEM data, structurally coupled with seismic, produce better representation of the true flooding front than inverting CSEM data alone. This further highlights the importance of seismic in structurally constraining CSEM inversion as earlier done by, among others, Andreis & MacGregor (2011).

Among many other examples of time-lapse surface CSEM sensitivity studies is that of Bhuyian et al. (2012), where 3D finite-difference algorithm, in time domain, was used to forward model time-lapse CSEM data. They assessed the effects of depth, lithology, reservoir geometry and the change in CO_2 saturations, and concluded that it is possible to apply CSEM technology to monitor subsurface CO_2 storage. Their conclusions were based on the fact that many potential carbon capture sequestration (CCS) sites are built in comparably shallow reservoirs where CSEM resolution is relatively high.

In all of these recent publications reviewed above, there is no significant connection between the geology (static reservoir properties) and engineering (dynamic reservoir properties) on one side and the CSEM (geophysical) response to change in reservoir production on the other side. Sharp flooding front is assumed in most of the examples. Therefore, in this research, an engineering simulation model is incorporated into the feasibility studies of time-lapse CSEM for reservoir monitoring. This approach provides realistic fluid (water and oil) flooding front and helps address challenges of interpreting the modelled data for dynamic changes in the reservoir.

There are few examples of time-lapse CSEM sensitivity studies incorporating fluid flow simulation model and the rock physics.

Ziolkowski, et al. (2010) published modelling results of synthetic time-domain EM surveys over the North Sea Harding field. Using Archie's rock physics model for clean sand and the fluid flow simulation, they calculated the resistivity distribution of the reservoir and then applied a 3D integral equation to forward model EM data; and subsequently employed a 1D inversion. They used well log to determine model resistivities, which gives values in excess of 1000 Ωm for the gas-bearing portion of the reservoir at 1700 m depth, and 1-3 Ωm

resistivity for the water bearing sediments. They specified the background resistivity to be 1 Ωm. Considering the baseline and two production periods (oil production and the gas cap), at five years interval; they were able to evaluate the potential of multi-transient EM repeatability for hydrocarbon detectability and reservoir monitoring in an offshore environment with water depth less than 200m. They concluded that the production-induced time-lapse changes in reservoir resistivity would be observable provided that a signal to noise ratio of the order of 100 (i.e. 40 dB) is achieved. Also they stated that, due to the mismatch between the collated 1D inversion of CMP gathers, which assumes infinite layering in the *x*- and *y*- directions, and the 3D target; the values of recovered resistivities (say 1.5 Ωm) is very low compared to the true resistivities (say 1200 Ωm). However, the 1D inversion defines the reservoir edges fairly well.

Liang, et al. (2011) utilised synthetic fluid (water and oil) flow reservoir simulator and Archie's rock physics model, to generate a realistic water front in their studies. They used a 3D finite-difference algorithm to forward model the CSEM response. Their fluid flow simulation model assumes an offshore oil reservoir buried 1000 m below the seafloor, in 1500 m water depth. The rectangular reservoir used in the lateral flooding experiment, has a dimension of 6 km by 6 km by 100 m, gridded to 60 by 60 by 1. They concluded that, in confirmation of the earlier works, inline electric and transverse magnetic EM fields produced adequate sensitivity to changes in resistivity due to oil production and water injection. However, they stated that time-lapse CSEM interpretation is not a straightforward process, inversion resistivity maps would aid interpretation. They later presented, in Liang et al. (2012), joint inversion of CSEM and production data. With an assumption that the salinity and temperature of the injected water is equal to that of the formation water, they carried out forward modelling and constrained inversion to improve the interpretation of time-lapse CSEM. They examine the CSEM forward responses and inversion results for production time of 10 years and 50 years, and concluded that the joint production and CSEM inversion approach can provide additional quantitative interpretation to the sensitivity studies of identifying fluid movement from the horizonal electrical and magnetic fields.

Shahin, et al. (2012) simulated a poorly consolidated shaly sandstone model, populated with petrophysical properties, generated using Gaussian geostatistical distribution. They obtained all the engineering data for flow fluid, such as capillary pressure, relative permeability, and PVT (pressure, volume, and temperature) properties of reservoir fluids from Killough (1995). The dual water rock physics model was used because it has the advantages of being constant with the dispersed clay model, and almost all the required parameters could be computed directly from the well logs. They calculated the resistivity distribution of the fluid saturated shaly sand, with the highest hydrocarbon resistivity value of 10 Ωm, which is very small. However, the reservoir thickness of 300 m results in a 3000 Ωm^2 transverse resistance, which makes the reservoir suitable for this sensitivity study. This is because CSEM is actually sensitive to the transverse resistance rather than the resistivity per se (Constable & Weiss 2006). The model dimension used is 2200 × 600 × 350m, and with a grid size of 10 × 10 × 10 m, they have 220 × 60 × 35 number of cells in the *x*- , *y*- and depth directions. Using two injectors at the corners and one producer in the middle of the 2D reservoir, they applied 2.5D parallel adaptive finite element algorithm to forward model time-lapse CSEM data for three production time steps (zero, five, and ten years). The time-lapse CSEM show 1-5% and 5-10% anomalies for 5 years and 10 years of water injection respectively, which they said could be detected with careful application of the current acquisition technology. They warn that at a short production interval (of less than 1 year), time-lapse CSEM may not be detectable. They advised that future work on forward modelling should incorporate both the electrical and elastic properties of reservoir rocks such that aid possible joint inversion of seismic and CSEM data for better reservoir monitoring.

These previous studies showed that CSEM sensitivity to fluid substitution could be employed to monitor hydrocarbon production and water injection activities, and that inversion processes include constrained joint inversion with seismic, could aid better qualitative and quantitative interpretation of saturation changes. However, there has not been any screeening study to assess possible risks involved in time-lapse CSEM project. Chapter 3 of this thesis addresses this in detail. It is worth mentioning that the aim of every dynamic reservoir characterisation is not only to monitor change in saturation but also to obtain pressure information, and to locate possible areas for infill drilling. There is an

interplay between saturation changes and pressure changes. For instance, in hydrocarbon production, water injection is usually performed for both pressure support and hydrocarbon drainage toward the producers (wells). Equally, whenever there is a pressure drop due to primary oil production, gas comes out of solution and it impacts on the original gas saturation condition of the reservoir. It is worth examining if time-lapse CSEM could detect such a gas exsolution effect. Even in CO_2 sequestration, pressure builds-up due to heterogeneity of the reservoir could have impact on the rock volume available for CO_2 storage (Grude, et al., 2013).

Thus, for hydrocarbon reservoir monitoring, coupled interpretation of time-lapse CSEM and 4D seismic data with information from the fluid flow simulation model is needed. Such coupled interpretation requires, first, the combination of electric and acoustic models in the forward modelling of time-lapse CSEM and 4D seismic responses. This will help in ascertaining if CSEM is truly more sensitive to fluid saturation changes than seismic. Thus, integration with seismic should not only be based on the need for structural constraint for CSEM inversion, but also for dynamic reservoir characterisation, because CSEM is not sensitive to pressure change while seismic methods are. All of the above point to the fact that time-lapse CSEM is not a standalone method for reservoir monitoring, not only in terms of its inherently poor resolution of reservoir depth, but also in terms of engineering practicality of reservoir monitoring. The workflow for coupled modelling is described in Chapter 4, while interpretation of modelled dataset is addressed in Chapter 5.

Additionally, none of the papers reviewed above gives consideration to the processes involved in the oil recovery, they all assume the same temperature and salinity conditions for both the injected water and the formation water. In seismic monitoring, with the exception of steam injection, such assumption may be valid, but in time-lapse CSEM studies, they may not. For instance, injection of cold sea water means the temperature and salinity of injected water should not be the same as those of the *in situ* water, which gives differing water resistivities. This concept and its potential application in brine tracking are further examined in Chaper 6.

Other forms of time-lapse EM in the literature include borehole-to-surface EM (BSEM) method. Zhdanov et al. (2013) presented a (BSEM) method, in which the sources of EM field are placed within the borehole, close to the reservoir, in order to increase sensitivity and resolution of the EM signals. They tested this method through synthetic forward modelling and inversion for CO_2 injection monitoring at the Kevin Dome sequestration site in Montana USA. They were able to recover the original resistivity of the formation and concluded that since the CO_2 plume can be reasonably recovered from the resistivity images at different times with different CO_2 volumes, saturations and radii; then monitoring CO_2 sequestration can be possible with 3D inversion of the BSEM data. They however concluded that practical evaluation of the technique is necessary. Figure 2.5 shows the comparison between their true resistivity models and recovered resistivity models from inversion of BSEM data, at the same depth of 1.125 km for the different phases of CO_2 injection, and for the plume radii ranging from 1 km to 2.5 km. The inverted resistivity models recovered the true model fairly well and the shape and dimension of the plume increases as the sequestration progresses.

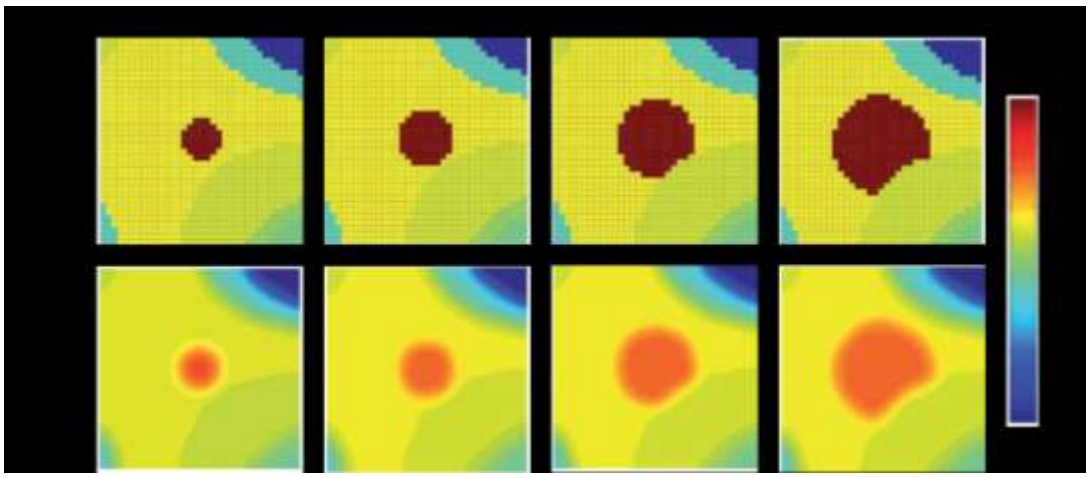

Figure 2.5: *Time-lapse comparison between the true resistivity models (top row) and recovered resistivity models (bottom row) from 3D inversion of BSEM model data, at the same depth of 1.125 km for the different phases of CO_2 injection, for the plume radius increasing from 1 km to 2.5 km. We can see the recovered resistivity models mimicking the increasing shape and size of the plume (Zhdanov et al. 2013).*

Earlier, Marsala et al. (2011) had presented the results of a first pilot field test of borehole-to-surface EM technology in Saudi Arabia. Through data processing in frequency domain,

and 1D and 3D constrained inversion in frequency domain; they obtained resistivity maps of the carbonate reservoir, from the BSEM dataset. They also obtain induced polarization maps, which they combined with resistivity maps to produce fluid distribution maps. They concluded that this method has demonstrated its capability to identify oil and water bearing reservoir layers, which makes it useful in reservoir monitoring. In addition, they claimed the method can also be used for exploratory purpose to diagnose the seemingly non-diagnosed areas.

Cross-well EM monitoring technology has also been suggested, and there are several examples for different geological settings in the open literature, such as the one described by Mieles et al. (2009) for carbonate reservoir in Oman; and the one represented by Wilt et al. (2005) for a low permeability, marine shale (diatomite) reservoir.

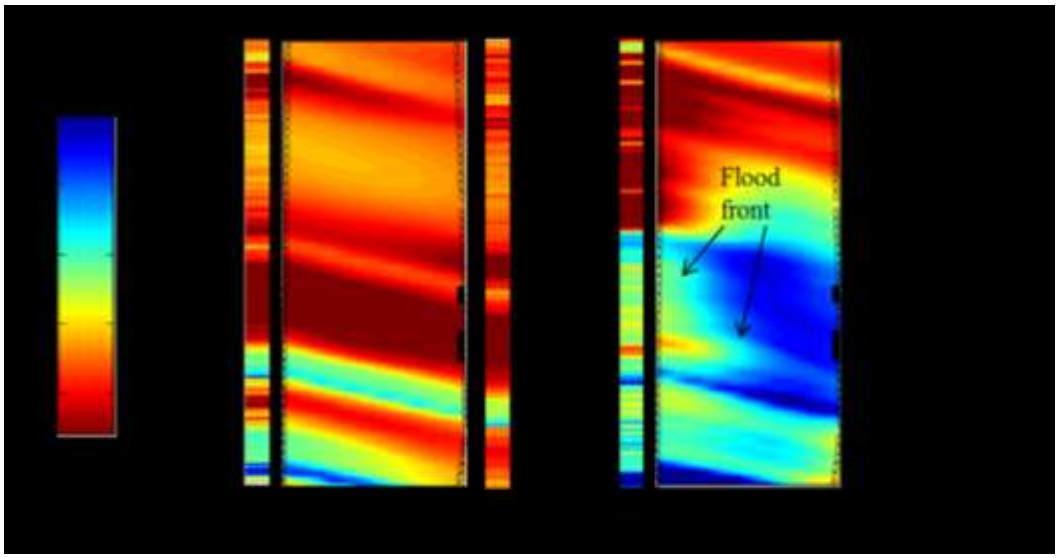

Figure 2.6*: Time-lapse resistivity images obtained from pilot cross-well CSEM measurements. Left image: pre-water flooding resistivity profile. Right image: post-water flooding resistivity profile after one year of water flooding. IW is the injection well. OW1 and OW2 are observation wells before and after water injection respectively. The observation and injection wells are 67m apart, with a vertical coverage of 140m. We can observe the water flooding front away from the points of injection (on the right hand side) (Mieles, et al. 2009).*

In these two examples, water injection processes were monitored through reservoir scale resistivity mapping by inverting modelled cross-well electromagnetic or pilot data. Figure

2.6 shows the results of pilot inter-well time-lapse CSEM measurements by Mieles, et al. (2009), both for pre-water-flooding (left) and one year post-water-flooding (right). The flooding front is clearly shown on the resistivity profile on the right hand of Figure 2.6. This method works well in open holes or fibre-cased wells. It could also be used in chromium steel cased - holes or by placing the EM field receivers inside the steel casing. However, both chromium and steel casing attenuate EM signals, thus limiting the separation and frequency of measurement. In addition, they state that interpreting saturation or porosity changes from these resistivity changes, in reality, may not be simple.

Similar to cross-well EM monitoring is the recent advance in logging while drilling (LWD). This is a real-time formation evaluation, whereby transient EM is used to obtain ultra-deep and azimuthal resistivity reading, formation strike direction and distance to different sub-surface interfaces for geo-steering purposes. This information has helped in controlling drilling direction and proper placement of producing well for optimum oil recovery.

Suggestions for land time-lapse CSEM surveys have also been made because of the possibility of better repeatability of source and receiver positions, as against the offshore acquisition. The problem of airwave, being the main EM signal on land, presents a major challenge for reservoir monitoring on land. Wirianto, et al. (2010) presented a feasibility study of land CSEM monitoring in which they suggested that proper survey design, involving the positioning of a source in a vertical well, could enhance onshore application of time-lapse CSEM for reservoir monitoring.

It can be opined that for 4D EM technologies to become commercialized as reservoir monitoring tools, two broad requirements need to be met: (i) good quality 4D EM signal and properly registered inversion derivatives (e.g. transverse resistance and resistivity difference maps); (ii) dynamic reservoir characterization driven by engineering concepts (making the best use of the good quality repeat EM data). The second requirement (ii) depends on the first (i), which is why much research effort by the EM community has been dedicated to this aspect of technological improvement. However, it is equally important to develop skills in making the best use of the good quality repeat EM data whenever the

anticipated improved acquisition; processing and inversion technologies have made them available. Interpretational skills, especially in terms of coupling information from time-lapse EM with 4D seismic and validating with activities around the injection and production wells to make reservoir management decision are similarly very important.

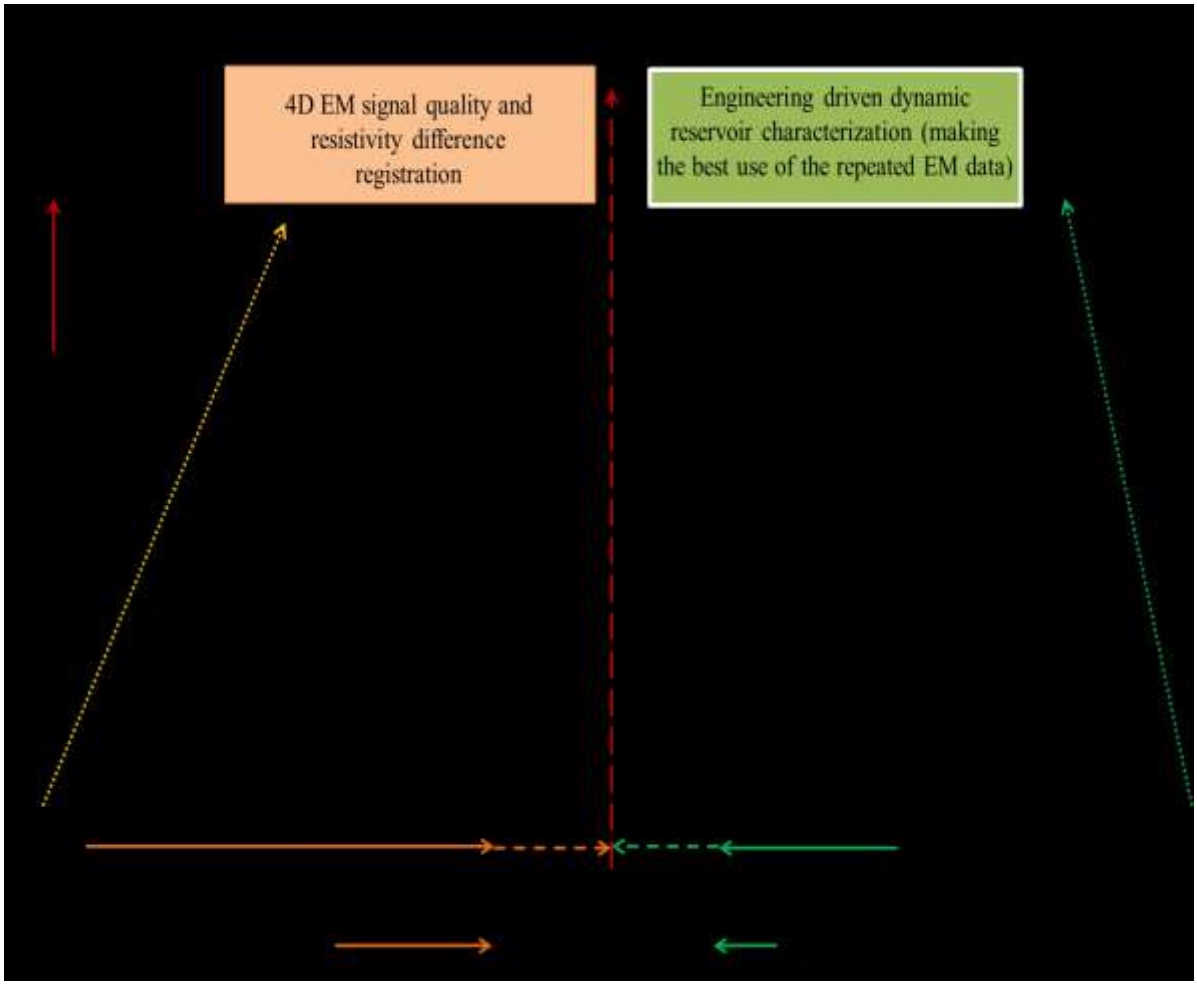

Figure 2.7: *Elements of technological improvement required to commercialize time-lapse EM in reservoir monitoring. On the left hand side are the development required to improve 4D signal quality and resistivity difference registration. On the right hand side are the required improvements in interpretational technology. The requirements for good quality 4D EM signal and ability to jointly obtain repeated EM and Seismic dataset will enhance our ability to make the best business use of the repeated EM data. This thesis largely sits on the right hand side of this Figure.*

Figure 2.7 summarises the major elements of technological improvement required to commercialize time-lapse EM in reservoir monitoring. In order for the two requirements to be met together, research activities have to progress in both directions and the time-line to

achieve this is largely unknown as it depends on various factors such as investment in EM research, business motivation, available alternative technologies.

There are two fundamental assumptions in this work.

First is that we have a good quality repeat EM signal (or its resistivity derivatives through EM inversion), thus we are required to analyze, interpret and examine its values in terms of its complimentary or alternative roles to time-lapse seismic in reservoir monitoring. Although 1D dipole EM modelling does not represent 3D subsurface reality, it presents to us a good quality EM signal, which we hoped for, with improvement in acquisition and processing technology (left hand side of Figure 2.7). Second is that we can eventually acquire repeat EM datasets simultaneously with repeat seismic datasets over the same producing field (topmost element on the left hand side of Figure 2.7), thus we are also required to interpret the two dataset for dynamic reservoir characterization.

These two assumptions justify the choice of using 1D EM modelling and reservoir simulation model in this research. The reservoir simulation model provides common platform for obtaining simultaneous time-lapse EM and seismic dataset with good level of survey repeatability (maybe through permanent sensors). It is therefore necessary to study the concepts of reservoir management and fluid flow simulation, as these will help in understanding subsequent chapters.

2.1 Introduction to reservoir management and fluid flow simulator

The main philosophy behind this research is to extend the successes recorded with the application of marine controlled-source electromagnetic (CSEM) in hydrocarbon exploration phase, to hydrocarbon production monitoring and reservoir management phase in the life cycle of a field. In order to do this, it is imperative for a CSEM expert to have a fair understanding of reservoir management, fluid flow simulation modeling and the mechanisms involved in hydrocarbon production, all of which lie largely in the engineering domain. This is because, the interpretation of time lapse CSEM data and its integration with 4D seismic data should be, at least for now, consistent with the prediction obtained from

the engineering simulator. Such consistency will provide the basis for extra information in updating fluid flow simulator, whenever an acceptable level of CSEM surveys repeatability is achievable.

Reservoir management, in this context, is the application of earth sciences and reservoir engineering expertise to safe optimization of hydrocarbon recovery. Such optimization process is a continuous interaction between all available datasets which help in decision making throughout the life cycle of a field (Saleri, 2005). In simple term, management of reservoir entails proper allocation of resources in order to achieve economic hydrocarbon recovery at a minimized capital investment and reduced operational cost (Thakur, 1996). Usually, obtaining optimum recovery and at the same time reducing the operational cost, which are the two-in-one expected outcome of sound reservoir management, is a difficult task requiring managers to coordinate and integrate the inputs from geoscientists, engineers, economists and every other professionals involved in the decision making process (Fanchi, 2006; Thakur, 1996).

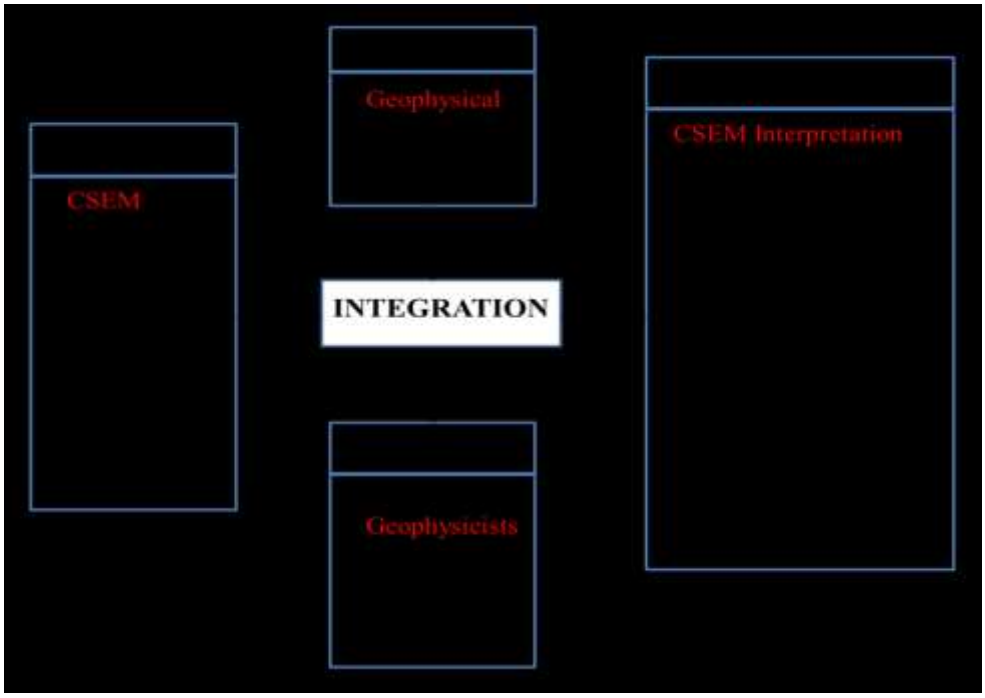

Figure 2.8: *Reservoir management approach showing integration of geoscientific, engineering and financial data, tools and the people (further modified from Thakur, 1996; originally from Satter, et al., 1994). CSEM is now being examined for geophysical application in this integrated approach.*

Reservoir management is therefore, a multidisciplinary job. Figure 2.8 describes the different people involved in using integrated technologies and tools to acquire required datasets for numerical simulation and reservoir management. This research examines the possible applications of CSEM interpretation in reservoir monitoring as highlighted in this integrated reservoir management approach.

The major reason for reservoir management, from the business point of view, is to generate different realizations of cash flow predictions and to determine the most prudent option in terms of economic returns (Thakur, 1996). In doing this, knowledge of production profile and price forecast are required. While the price forecast could be offered by the economists or financial experts, getting the production profile requires detailed technical reservoir description using geological, petrophysical and geophysical techniques, and reservoir engineering simulation model (Fanchi, 2006; Thakur, 1996; Craig Jr, et al., 1977). Thus, geophysical techniques are now playing roles throughout the life cycle of a field. In particular, reservoir monitoring is now largely an integration of conventional reservoir surveillance data and information obtained from the interpretation of time lapse seismic data. This thesis explores the possibility of obtaining additional value by including CSEM in this integration scheme.

The tools for technical reservoir description, characterization and production monitoring are called reservoir models. Generally speaking, there are two main models in petroleum geoscience and engineering. We have the static model for reservoir characterization, which is built with inputs from the geologists, geophysicists and petrophysicists. It is popularly called the geologic model and it contains basic reservoir properties, such as porosity, net-to-gross (NTG), faults, barriers and baffles and permeability distribution across the field in finely gridded cells of several million. We also have the dynamic model for reservoir monitoring and management, otherwise called engineering simulation model or fluid flow reservoir simulator.

The fluid flow simulation combines three fundamental laws governing fluid motions in porous media, they are: (i) the conservation of mass, (ii) momentum, and (iii) energy. The fluid flow simulator is built by up-scaling the geologic model to a coarser-gridded

simulation model and populating this with hard engineering data, e.g. pressure, fluid volumes produced and injected, temperature, measured production and injection rates, produced water/oil ratio, saturation, viscosity, transmissibility, densities, salinities and other necessary data relating to the reservoir, its fluid content and the fluid injected. The up-scaled petrophysical properties and these engineering data are all needed to solve the numerical problems of fluid flow within the reservoir, involving several equations on material balance. The up-scaling of the geologic model is required in order to reduce the computational time of the simulation process which generates several outputs of reservoir dynamic properties at every time step. The dynamic reservoir model is the main tool used in monitoring hydrocarbon production and injection activities, and in predicting future performance of the reservoir. This aids in strategic planning of reservoir production intervention and management (Fanchi, 2006; Iqbal & Satter, 2010). Fluid flow simulator has been described as a consensus model and a point of contact between many professionals, supplying different input datasets, right from the preparatory stage and throughout the life cycle of the field (Fanchi, 2006; Craig Jr, et al., 1977).

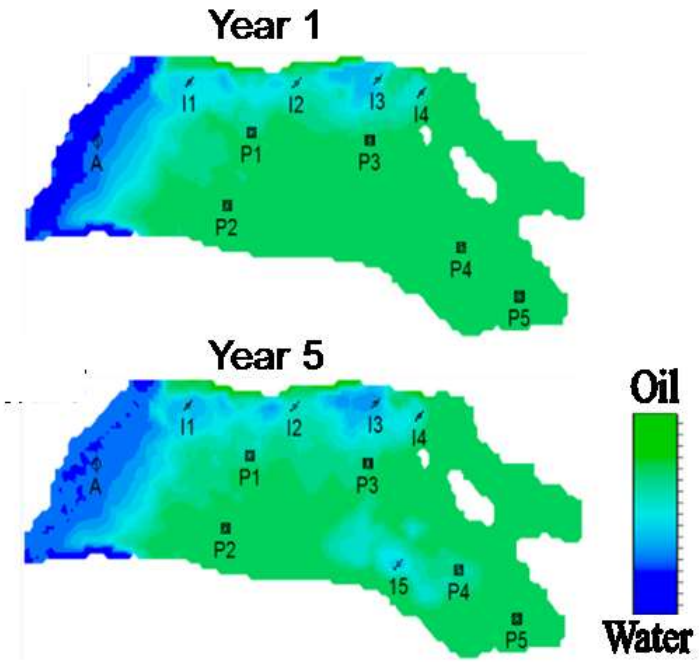

Figure 2.9*: An example of a reservoir simulation model. Here, production is aided by lateral aquifer drive (water source labelled A) and water injection. The open injectors are labelled I1, I2, I3 and I4 while the open producers are labelled P1, P2, P3, P4 and P5. Here we have two phase fluid saturations, water saturation (in blue colour) and oil saturation (in green colour).*

Therefore the accuracy of the reservoir simulator to forward predict the performance of hydrocarbon reservoir depends on the amount of data available from these various professionals. The performance prediction generally improves with time as more datasets are available. Figure 2.9 shows typical examples of maps derived from reservoir simulation model in a two phase fluid flow, where oil production is aided by both lateral aquifer drive and water injection. The movement of waterfront is such to drive oil towards the production wells. It is observed from Figure 2.9 that the oil/water is not a sharp boundary. Injector I5 was not there at year 1, several factors could have influenced the decision to drill water injector 15 after year 1 before year 5.

It is worthy of mentioning the popular saying that 'all models are wrong' by default but 'some are useful.' This is why fluid flow simulation models are continually updated as more data are available. Also noteworthy is the fact that all reservoirs are heterogeneous and such heterogeneity should be properly captured as much as possible in the simulation models. Johnston (2013) mentions that all reservoirs are not just only heterogeneous, they are also more heterogenous than we originally think and even as we study the reservoirs, we will futher understand that they become much more heterogenous. In other words, as we progressively populate the model with more information from different sources at any given time, the reservoir model is still considered to be wrong yet more useful with less uncertainties because we now understand the model better. So, the more volume of information available to build the model or update the model, the less "wrong" and more representative of reality is the model.

Therefore, as much as the intention of this work is to examine the possible applications of CSEM in reservoir monitoring, the approach has to be engineering based, using both the sythetically built and industry-supplied updated (and modified) reservoir simulation models as the focus of our attention. Reservoir engineers, who are at the centre stage of reservoir monitoring and management, recognize the importance of geology and geophysics in predicting reservoir performance. Thus, they seek large quantity of high quality data from the geoscientists in updating the reservoir models in a process called history matching. Geoscientists also stand to gain feedback on that information earlier provided from the results of numerical simulation and history matching carried out by the reservoir engineers

(Thakur, 1996). This interactive synergistic process has led to what is now known as 'closing the loop' between the engineering and 4D seismic information. Ultimately, this is where time-lapse CSEM technology should aim!

Much before the advent of 4D seismic, engineers used conventional methods for reservoir surveillance through which they predict reservoir performance. Jack (1998) and Johnston (2013) mentioned some of these methods, which also provide hard data to populate simulation model: (i) well testing on production and injection wells, wellhead pressure or down-hole pressure measurements and pressure-interference tests are all done to obtain information on pressure changes during production and injection activities. Except for a high pressured reservoir, a large pressure drop is not desirable, engineers especially want to keep the production pressure above the bubble point pressure, below which there will be gas ex-solution in an oil reservoir; (ii) records of fluid production and injection rates at well locations. Engineers keep these records to control, say, water cut at production well; (iii) produced water/oil ratio (WOR) and gas/oil ratio (GOR). Production engineers desire low WOR and GOR; (iv) repeat neutron thermal decay time (TDT) logging to determine water saturation behind casing in production wells. This is done to control water production while increasing oil production rate; (v) repeat formation tester (RFT) to indicate reservoir pressure at different depth locations; (vi) tracer injection either with water or gas and monitoring such tracers at production wells; (vii) production logging tools (PLT) to measure fluid density, water cut etc.

Many of these tools provide information only in the vicinity of well locations and this also partly accounts for the uncertainty in reservoir simulation model which makes use of the information from these conventional tools. Even the tracer injection and production logging tools, which offer information across the reservoir volume, do not capture lateral reservoir heterogeneity. This is the major reason for integrating time lapse seismic into reservoir monitoring to serve as a complimentary source of valuable inter-well information (Johnston, 2013). It is hoped that interpreting time lapse CSEM modelled data would offer more inter-well information about change in water saturation, to compliment time-lapse seismic information.

2.2 The mechanisms of hydrocarbon production: putting time-lapse CSEM and seismic into perspective

It is imperative for a CSEM expert to have a good knowledge of how hydrocarbon is produced from the reservoir. Such knowledge is helpful in the interpretation of time-lapse CSEM, and coupled interpretation with 4D seismic. This is because the recovery mechanism has a closed link with the production history, in terms of pressure and saturation changes, which geophysical interpretation seeks to unravel from the time-lapse anomaly.

Hydrocarbon production could proceed by a primary mechanism aided by natural energy, which is a resultant energy derived from the force of gravity, capillary pressure, viscosity and inertia forces. If the energy generated naturally within the reservoir is high enough, it can provide the primary driving force for hydrocarbon production. Examples of primary production mechanisms are: (a) aquifer-water drive, in which hydrocarbon production energy is derived from external aquifer due to slight expansion of water as a result of pressure reduction in reservoir. Recovery in aquifer-water drive could be as much as 40% to 80% of original oil in place (OOIP); (b) gas-cap drive is common in thick reservoirs where steeply dipping large gas cap, in communication with the oil zone, expands as pressure drops. Recovery due to gas cap expansion could range between 30% and 60% of OOIP; (c) solution-gas drive, usually occurs in horizontal thinly-bedded oil reservoir, in which there is no initial gas cap but a drop in pressure below bubble point causes gas ex-solution, which then aids oil flow. Recovery of this type is usually low, up to 25% of OOIP (Johnston 2013).

Figure 2.10a, b and c show schematic diagrams of aquifer water, gas-cap and solution-gas drives respectively. In Figure 2.10a, there is bypassed oil at both flanks of the reservoir. No water is produced yet as the producer well is completed far above OOWC and there is no early water breakthrough. In Figure 2.10b, some gas is produced with oil and there is un-drained oil behind the new gas-oil contact (GOC). In Figure 2.10c, gas comes of solution due to pressure drop below bubble point. Some of the free gas is produced. The aquifer is inactive in Figure 2.10b and c, though in some situations there may be combination of

either of the two gas drives with the aquifer drive. Fluid displacement depends on the heterogeneity of the reservoir, which is not taken into account for simplicity. It may be impossible for time-lapse CSEM to identify each of solution-gas drive and gas-cap drive mechanisms, notwithstanding it can easily identify aquifer-water drive. This is because resistivity is not a good indicator to differentiate between gas and oil, but it is an excellent indicator to discriminate oil from water for aquifer water drive.

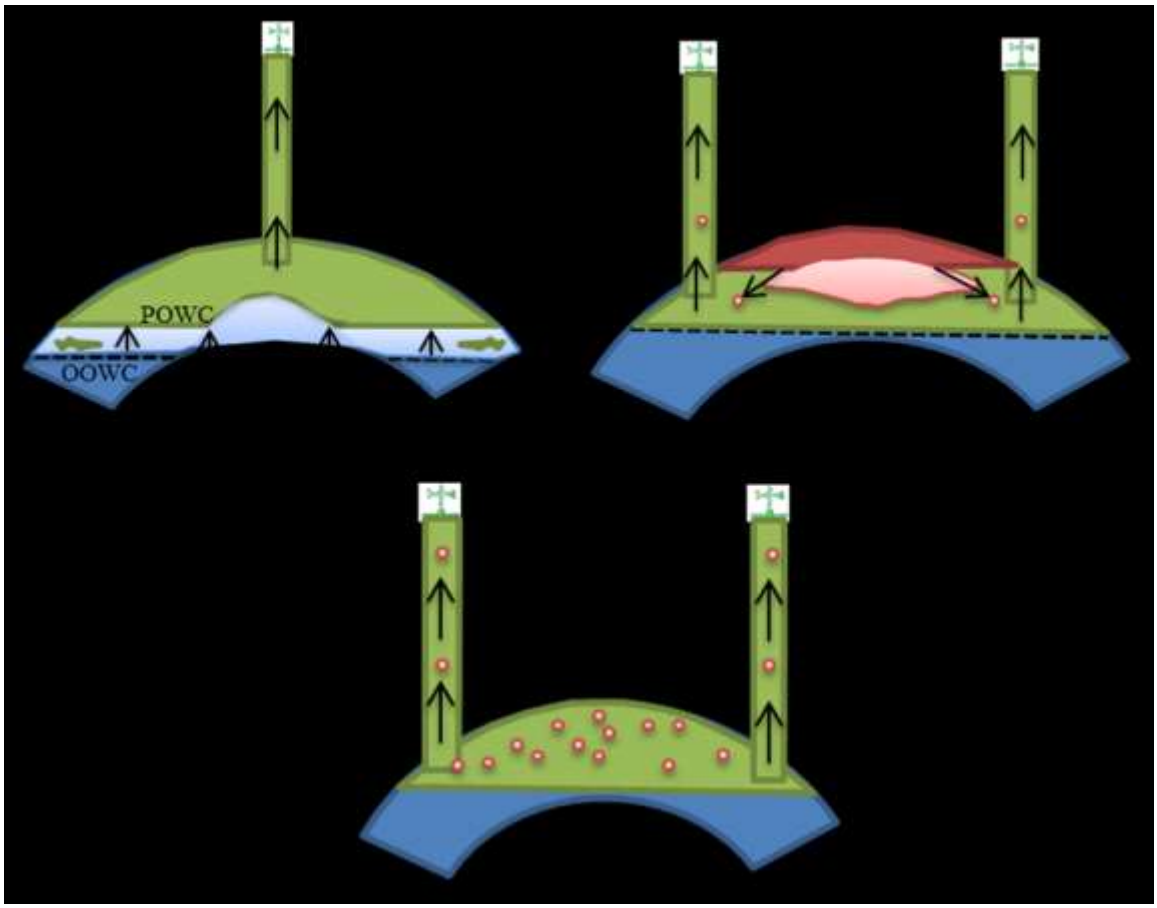

Figure 2.10: *Production by natural energy (a) Expanding aquifer-water (in blue) driving oil upward to the producer well, the original oil-water contact (OOWC) has moved to the produced oil-water contact (POWC) due to water displacing oil (in light blue). (b) Expanding gas-cap drive (in red) driving oil downward towards the producer well. Gas (in light red) is displacing oil down-dip. (c) Solution gas drive in which evolved mobile gas moves freely upward to form secondary gas cap which provides energy for oil production. See Table 2.1 for summary of time-lapse EM and 4D seismic responses.*

Whereas, 4D seismic can identify solution-gas and gas-cap drives due to contrasting densities and bulk moduli between oil and gas. Table 2.1 summarizes the expected responses of time-lapse EM and 4D seismic to primary production mechanisms, and their related reservoir management issues. Since EM seems to be insensitive to gas-oil displacement, it can potentially be used to discriminate confounding fluid effects (between water and hydrocarbon) as well as to separate the change in saturation from the change in pressure in 4D seismic.

We also have secondary production mechanisms involving fluid (water or gas) injection, which is usually applied whenever the primary energy becomes insufficient. Water injection is a popular secondary mechanism because water is usually readily available, especially in the offshore environment. Coincidentally, CSEM surveys are also popular for marine application as the airwave phenomenon is reduced offshore. A good reservoir candidate for water injection will be one with a weak aquifer support, and this presents good resistivity contrast for time-lapse CSEM detectability, as injected water displaces gas or oil within the reservoir pore spaces. Depending on the reservoir condition and production objectives, displacement can be lateral, in the case of lateral flooding; or vertical, in the case of basal flooding; or both.

Generally speaking, water injection is usually done within the reservoir oil-leg for the reason of effective oil drive and maintenance of pressure. Intuitively, however, for a thin reservoir, where there is a lithological continuity between the aquifer and the oil-leg, but the pressure support is insufficient to drive the oil, water injection could be done from the aquifer to support the oil drive so as to avoid early water breakthrough at the production well. Figures 2.11a and b show both types of water injection, within the aquifer and within the oil-leg respectively. In Figure 2.11a, the original oil-water contact (OOWC) has moved to the produced oil-water contact (POWC) due to water displacing oil (in light blue). There is bypassed oil near the centre of the reservoir. Injection below the OOWC helps to delay water breakthrough and it is more effective in sweeping the oil to the producer, than the injection into the oil leg. In Figure 2.11b, injection above the OOWC results into un-drained trapped oil (behind the injector) and un-swept bypassed oil (distal to the injector).

Primary Mechanisms	Production History	Time-lapse EM Response	4D Seismic Response	Reservoir Management Issues
Aquifer water drive	Expansion of external aquifer due to pressure depletion	Hardening (drop in resistivity) due to water displacing oil within the reservoir or due to water breakthrough at the producer	Hardening due to water displacing oil within the reservoir or due to water breakthrough at the producer	Locate bypassed oil and channeling along low permeability paths
Gas cap drive	Gas cap expansion due to pressure drop	No signal (no resistivity contrast between oil and gas)	Softening due to gas displacing oil within the reservoir or due to increased GOR at the producer	Identification of undrained oil
Solution gas drive	Gas coming out of solution due to pressure drop below the bubble point.	No signal (no resistivity contrast between oil and gas)	Softening due to the combination of pressure decline and gas coming out of solution usually in the proximity of producers	Identification of barriers and baffles, isolated and bypassed compartments

Table 2.1: *Summary of time-lapse EM and 4D seismic expected responses to primary production mechanisms (described in Figure 2.10) and the reservoir management issues.*

In terms of time-lapse geophysical signals, both seismic and EM could produce measurable signals to water injection. For time-lapse seismic, we expect hardening due to increased acoustic impedance (density and velocity) as water replaces oil, and if the pressure effect has minimal impact on the seismic signal, usually away from the injector. However, there may be a situation whereby time-lapse pressure-up (softening) signal, during water-flooding, is higher than the water sweep (hardening) signal, such that the former masks the latter. In such situation, imaging both signals with 4D seismic alone becomes challenging, and water movement would not be qualitatively monitored. This is the situation when time-lapse CSEM data could serve complimentary role of unmasking saturation effect from the pressure effect.

For consistency of terminologies and enhancement of coupled interpretation, time-lapse EM hardening and softening are defined in terms of 4D seismic hardening and softening definitions. Time-lapse EM hardening is therefore defined as a situation when conductive saline water replaces resistive oil; or when more saline more conductive (less resistive)

injected water displaces less saline less conductive (more resistive) *in situ* water. Time-lapse EM hardening due to water replacement of oil is, thus, more common than one due to water replacing water. Time-lapse EM softening, on the other hand, is defined as a situation when resistive oil replaces conductive saline water. This condition is not common in reality. EM softening is more probable when less saline less conductive (more resistive) injected water displaces more saline more conductive (less resistive) *in situ* water.

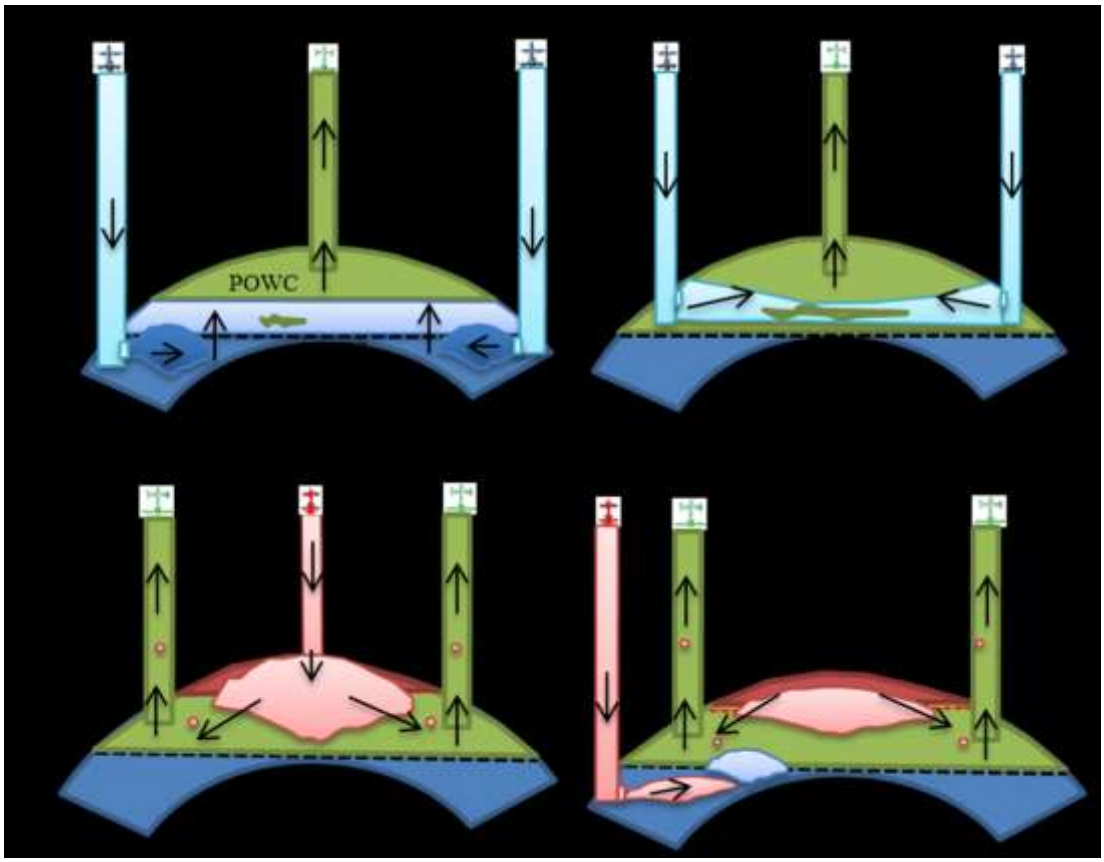

Figure 2.11: *Examples of secondary production mechanisms (a) Water injection into the aquifer causing both lateral and upward expansion of the aquifer near the injector (in blue), thus driving oil mostly upward to the producer well (b) Water injection into the oil leg, causing mainly lateral sweep of the oil towards the producer well. (c) Gas re-injection into the gas cap to avoid gas cap shrinkage and to maintain pressure. (d) Gas re-injection into the aquifer, this helps originally inactive aquifer to become supportive to the gas cap in driving the oil toward the producer well.*

Time-lapse EM hardening effect of water replacing oil is seen from the drop in resistivity, as conductive water replaces resistive oil. This seems to be a definitive way of illuminating change in water saturation, as EM is blind to pressure effect. Figure 2.12 shows a classical

example of such situation. Similar example is shown in Chapter 5 for coupled interpretation of time-lapse CSEM and 4D seismic modelled data.

Another type of secondary recovery is gas injection. Gas could be re-injected into the gas-cap to prevent shrinkage of the gas-cap, and to maintain reservoir pressure and support production. Produced gas could also be re-injected into anywhere in the field. The latter is usually done in order to meet the regulatory requirement to prevent gas flaring, but could also help to prevent gas-cap shrinkage if injection is done into the gas-cap for down-dip displacement of oil towards producing wells (Johnston 2013). Time-lapse seismic provides excellent signatures for gas injection, displacing of oil or water. Intuitively, whereas time-lapse CSEM might not identify injected gas displacing oil; it can identify resistivity contrast between the injected gas and the aquifer water. Figures 2.11c and d show both gas injection, into the oil-leg and aquifer respectively. Table 2.2 summarizes the expected responses of time-lapse EM and 4D seismic to secondary production mechanisms (mainly water injection and gas injection).

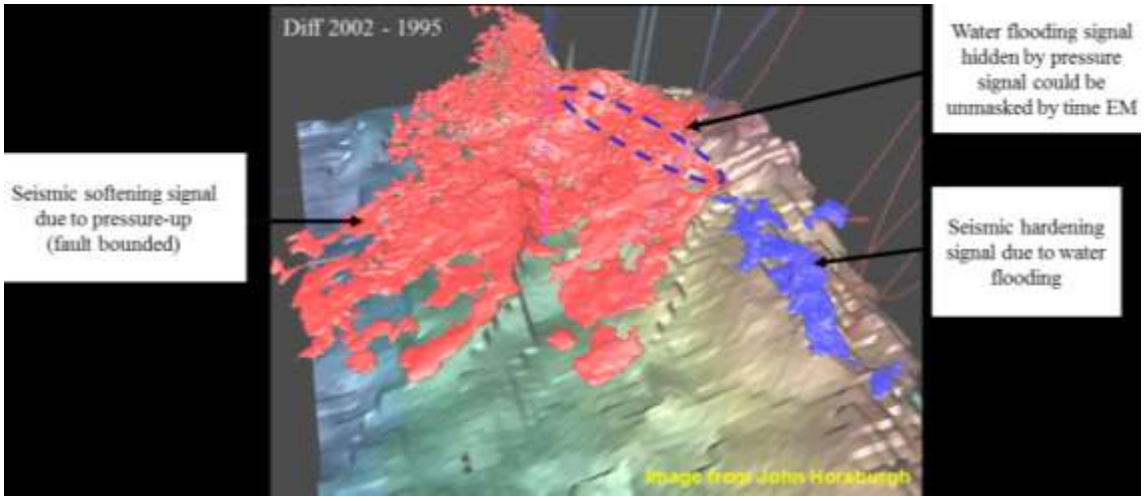

Figure 2.12: *Example of hidden water saturation signal in a 4D seismic attribute difference cube, which could possibly be illuminated by time-lapse EM. Fault bounded pressure-up softening signal (red) is stronger than the fluid signal at the top right hand section (with blue dotted circle), where the water sweep hardening signal from the bottom right (blue) extends (Staple 2006, in MacBeth, 2013)*

Secondary Mechanisms	Where in the reservoir?	Production History	Possible Time-lapse EM Response	4D Seismic Response	Reservoir Management Issues
Water Injection	Water leg (where connate water saturation is high)	Injected water pushing the aquifer/formation (connate) water to drive the oil. Both connate water banking and oil banking occur.	Magnitude depends on the salnity and temperature contrasts between the injected and formation waters (connate water banking signal). Hardening (lowered resisitivity) due to water driving oil (oil banking signal).	Injected water may not be seen differently from formation water. Hardening due to water replacing oil. Softening due to increased pressure near the injector wells can mask the signal due to change in saturation	(i) Location of bypassed oil. (ii) Determination of sweep efficiency and water evolution. (iii) Siting of in-fill oil producer well(s)
	Oil leg (where connate water saturation is low	Oil immiscibly displaced by injected water	Hardening (lowered resisitivity) due to water driving oil. Substantial signal expected	Hardening due to water replacing oil will be high. Softening due to rise in pressure near the injector wells can mask the signal due to saturation change	
Produced Gas reinjection	Gas leg	To maintain or raise pressure, avoid gas-cap decline and boost oil recovery as oil is displaced by gravity downdip	No resistivity contrast. No timelaspe EM signal	If pressure is maintained, the softening signal will be mainly due to gas displacing oil downdip. Increased pressure may reinforce the softening	(i) Early monitoring due to high mobility of gas (ii) Optimum production plan to minimize gas production and recycling (iii) Location of bypassed oil. (iv) Siting of in-fill oil producer well(s)
	Oil leg	To maintain or raise pressure and displaced oil laterally or downdip	No resistivity contrast. No timelaspe EM signal	Softening due to gas displacing oil. Rise in pressure near injector may reinforce the softening.	
	Water leg	To fulfill regulatory requirement of preventing gas flaring (just like injecting anywhere within the reservoir). To support pressure from the aquifer in driving oil updip.	Softening (increased resistivity) due to gas driving water. Substantial signal expected	Softening due to gas displacing water. Rise in pressure near injector may reinforce the softening.	

Table 2.2: *Summary of time-lapse EM and 4D seismic responses to secondary production mechanisms (described in Figure 2.11) and the reservoir management issues. Since EM seems to be insensitive to gas-oil displacement and pressure change, it can potentially be used to discriminate confounding fluid effects, and to separate the effect due to the change in saturation from the effect of change in pressure, in 4D seismic.*

We also have enhanced oil recovery, a form of improved oil recovery (EOR/IOR), which involves a process or combination of processes aimed at producing more hydrocarbons from the reservoir, usually, after utilizing primary and/or secondary recovery processes. In some other cases, enhanced oil recovery is the only mechanism of producing the reservoir, such as viscous heavy oil reservoir. Examples of enhanced oil recovery are described below, with the possible geophysical implications:

(a) Low-salinity water injection: it is a relatively new enhanced oil recovery mechanism which is used to recover oil in a highly oil-wet reservoir (Seccombe et

al. 2010). As described in Table 1.2, while time-lapse seismic may consider 'water' to be 'water' with constant properties, irrespective of whether it is injected or in situ (connate or aquifer) water; time-lapse EM, on the other hand, has tendency to distinguish injected water from the in situ water due to the salinity and temperature difference that may exist between the two kinds of waters. Thus, time-lapse CSEM could be applied to monitor low-salinity water injection, and this is assessed in Chapter 6.

(b) Chemical recovery: this includes the use of surfactants, and polymer flooding to prevent the loss of fluid into the high permeability zones, thus aiding effective oil sweep towards the producer. There is no example of time-lapse seismic monitoring of chemical flooding, especially polymer flooding, in the literature to date. This is probably because time-lapse seismic signal of polymer flooding, for instance, will be too small to detect (Johnston 2013). However, time-lapse CSEM might be able to detect polymer flooding because of the salinity contrast between the saline formation water, pre-injected fresh (low-salinity) water and the polymer solution.

(c) Miscible-gas-injection which includes CO_2 injection, where injected CO_2 mixes with the *in situ* oil to reduce viscosity and interfacial tension, thus making oil more mobile (Iqbal & Satter 2010). CO_2 injection is also done mainly for carbon sequestration. Time-lapse seismic response to CO_2 flooding is complex because of the difficulty in identifying the miscible zone which may not have acoustic impedance contrast to the un-swept oil zone. Notwithstanding, the presence of free CO_2 gas in the swept region behind the miscible region, called 'slug', could be detectable due to acoustic impedance contrast between the CO_2 (in the swept zone) and the miscible region (Johnston 2013). Time-lapse CSEM sensitivity to CO_2 has so far only been modelled for CO_2 sequestration, usually within the aquifer, rather than for hydrocarbon recovery.

(d) Water-alternating-gas (WAG), which helps to improve mobility ratio between the displacing phase and the oil (Iqbal & Satter 2010). Water-alternating-gas has a combination of production histories for gas and water injections, thus the time-lapse

seismic and CSEM responses may complement each other to reflect the timing of each of the gas and water injections.

(e) Thermal recovery such as cyclic steam stimulation, continuous steam flooding, steam-assisted gravity drainage (SAGD) (Iqbal & Satter 2010). All thermal recovery systems aid production of the heavy oil by reducing its viscosity and resistance to flow. 4D seismic is an excellent tool for monitoring thermal recovery, especially steam injection, as heating of viscous oil can usually result in significant 4D signals due to a large acoustic impedance contrast. It is not likely that time-lapse CSEM can offer any usefulness in thermal recovery process. This is because steam is expected to be highly resistive, as it contains negligible or no ions, thus it will assume similar electric properties as the oil.

2.3 Main challenges of this work

The main purpose of this work is to carry out simulation driven forward modelling to assess potential practical applications of time-lapse CSEM to reservoir monitoring. This also involves coupled forward modelling of time-lapse CSEM and seismic to examine integrated interpretation. Therefore, the main challenges are to simulate hydrocarbon production and injection activities, with different scenarios of water injection, and then establish a work flow for this joint modelling. However, since there is no time-lapse CSEM data, interpretations will be based on modelled data alone, using the simulation models and well information for validation.

Although, 4D CSEM modelling is discussed in Chapter 7, assessment of practical application of time-lapse CSEM to reservoir monitoring is done using less complex 1D CSEM modelling of a more complex 3D reservoir model incorporating rock physics consistent with fluid flow. This is based on the assumptions mentioned earlier in section 2.1. Table 2.3 summarises the approaches used in this work, within the context of the various other approaches used in the literature. The scope of this work is limited to forward modelling, as a robust understanding of forward modelling will later enhance constrained inversion and repeat surveys design.

	Elements	Increasing Level of Complexity	Occurrence in Literatures	What is used in this thesis	Remark
1	MODEL	Canonical	Still common		Real reservior simulation model permits integration with reservoir engineering
		Synthetic Simulation Model	Since 2010	X	
		Real Reservoir Simulation Model	Not sure	X	
2	ROCK PHYSICS	No Rock physics	Still common		Both lithology and engineering elements are important for good interpretation
		Archie's model	Now common		
		Shaly Sand model	Few	X	
		Engineering Consistent	Not available	X	
3	PRODUCTION MECHANISMS AND EOR	No consideration	Common		Consideration will help determine where best could time-lapse CSEM be suitably applied
		Considered	Not available	X	
4	FORWARD MODELLING	1D Dipole	No longer common	X	3D Modelling is the way to go, but 1D modelling is quick and could offer reconnaissance information.
		2.5D/3D Integral Algorithm	Now common	X	
		Finite Difference Algorithm	Now common		
5	INTERPRETATION OF MODELLED DATA	Sensitivity studies	Common	X	The final aim is to combine 4D CSEM and 4D Seismic datasets with production and injection activities at well locations for reservoir monitoring and management
		Well activities driven	Not available	X	
		Coupled with 4D Seismic	Not available	X	
6	INVERSION (1D, 2D, 3D)	Well constrained	Common		The scope of this thesis is limited to forward modelling. The better our understanding of forward modelling, the better we are able to constrain the inversion process and interpret the datasets. Simulator grid constrained inversion seems to be the way to go.
		Joint with Seismic (structural constrained)	Common		
		Simultaneous with Seismic (joint properties)	Common		
		Simulator grid constrained inversion	Not available		

Table 2.3: *Summary table of approach used in this work in relation to what are available and what are not available in the literature.*

2.4 Contributions of this work

This thesis serves as a reference for future time-lapse CSEM data interpretation and coupled interpretation with time-lapse seismic data for reservoir monitoring. It contributes to knowledge in the areas of potential applications of CSEM in monitoring some selected water-related oil production or recovery mechanisms. The robust workflows for 3D simulator-to-resistivity and the 1D resistivity-to-electromagnetic forward modelling will be useful for future work in terms of quick time-lapse CSEM screening and feasibility studies. The time-lapse 3D resistivity-to-electromagnetic modelling in chapter 7 is the foundation to future work on 3D EM inversion, where simulator-grid will be used for structural constraint. The established joint forward modelling of 4D seismic and time-lapse EM from a common platform of fluid flow simulation model will not only help the inversion process in future, it will also aid the analysis and interpretation of simultaneously acquired seismic and EM datasets, which is an emerging technology.

CHAPTER 3

ELECTRIC ROCK PHYSICS AND TECHNICAL RISK ASSESSMENT

"Do you think it will work?" The answers could range from optimistic to pessimistic: "Yes, it should be great or could be risky or no, that will never fly or the even worse answer, give us $100,000 to do a complete feasibility study and we'll get back to you in a few months" Lumley et al. (1997).

The statements quoted above relate to technical risk assessment of a time-lapse seismic project, at its infancy and even now when 4D seismic is a well-matured technology. The substances of the statements are equally true for time-lapse EM, which is still very much an on-going research tool. Electric rock physics will play a key role in answering the main question: Do you think time-lapse EM could work?

3.0 Introduction

Electric rock physics is the bridge linking the petrophysical properties of subsurface rock and fluid (geology), and the electric and magnetic fields measured at the surface as signals (geophysics). Many available electric rock physics models, which are improvements on the original Archie's clean sand model (Archie 1942), have only sought for lithological consistency. This chapter proposes an electric rock physics model that is both lithological and fluid - flow consistent, for reservoir monitoring. In this model, the EM sensitivity to resistivity of shale, brine temperature and salinity are accounted for, in response to brine mixing during fluid injection. The model is used to carry out a time-lapse CSEM screening study.

The time-lapse CSEM screening study is borrowed from the 4D seismic screening for technical risk assessment. The quotation above, from Lumley et al. (1997), indicates the complexity of time-lapse seismic at the early stage of its application to reservoir monitoring, and the importance of reconnaissance investigations. Even nowadays, with improved data acquisition and processing technologies coupled with sophisticated analysis software; there are still challenges in terms of qualitative and quantitative interpretation of 4D seismic. Thus preliminary model studies are essential at the beginning of every 4D project. More importantly, different geological terrains and oilfield development conditions require that risk assessment be done to know if 4D seismic will work in a particular setting or not, before investing into 4D data acquisition. Screening and feasibility studies help in accomplishing this "risk assessment" objective. Both studies also aid in prioritizing projects according to business objectives by ranking the "technical chance of success" (TCS) for several projects. This is especially true for a portfolio containing a number of oilfields in different geological terrains, where reservoirs are subjected to different type of recovery mechanisms. Such ranking help in making business decision as to which field will offer the best return on investment in a 4D project.

Screening and feasibility studies draw on the knowledge of reservoir geology, rock and fluid physics, reservoir production driving mechanisms and fundamentals of geophysics to assist in analyzing and answering several technical and business questions in planning 4D seismic project. Johnston (2013) summarizes some of the important questions hoped to be answered with screening and feasibility studies such as: (a) Can time-lapse seismic work in this reservoir and under this production mechanism? This includes details on the magnitude of 4D difference, detection and resolution of the 4D signals, concerns on acquisition and processing, and the optimum timing of repeat surveys. (b) What are the benefits? For instance, in terms of the reservoir management, well intervention, production and injection volume control etc. (c) In terms of priority in a portfolio of fields, which field have the highest TCS and could bring highest returns with less investment?

All of these will enhance clear communication of expected outcomes to the management. For instance, "give us $100,000 to do a complete feasibility study and we will get back to you in a few months*"* is definitely a costly answer to the simple question "do you think it

will work?" Possibly, no manager would approve such request, without having clear and easily understandable information about business impact of time-lapse project, with some initial uncertainties attached the information! Therefore, it is important to have a quick, less laborious and less costly 4D screening study first before a more costly feasibility study, to evaluate the most important reservoir and seismic parameters that will impact the technical chance of success of a 4D project. This way, the simple question "do you think it will work?" could be answered timely and cheaply. This is why this concept is important to be incorporated into the time-lapse CSEM technology.

There are few differences between screening and feasibility studies. Although they are both useful reconnaissance measures prior to making decision on 4D projects. However, while assets screening offers quick, less detailed spreadsheet information about each of the major reservoir properties, elements of rock and fluid physics and seismic responses, most of which are independent of one another. Feasibility study, on the other hand, combines all of these items together in a more detailed analysis involving the use of reservoir simulator and rock physics model in the forward calculation of time-lapse seismic response. Sometimes, well log data cross-plots may also be included. Table 3.1 shows the summary of a full description of 4D screening and feasibility studies, and their differences as reconnaissance tools in reservoir monitoring project. It is worth noting that forward calculation of time-lapse seismic response from the simulator is not only a feasibility tool; it is also helpful in 4D seismic data interpretation and updating of simulation models. The fact that 4D screening could be done, and should be done much early in the life of a field, during exploration and appraisal, justifies the need to develop a technique for screening an asset for the possibility of a time-lapse marine CSEM project. This is about thinking ahead, about the possible factors that could impact on the repeated CSEM surveys.

Lumley et al. (1997) are the first set of people who introduced screening for time-lapse seismic project. They developed a technique of assigning numerical scores to various reservoir and seismic parameters that are important to examining the technical chance of conducting a successful time-lapse project.

Difference	Quick 4D Asset Screening	Detailed 4D Feasibility study
Stage in the life of field	• Early during exploration • Field Appraisal	• Later during field development • Production and injection
Tools/Data needed	• Regional geologic information • Core data/well logs (cross-plots) • Key rock, reservoir and seismic properties • Planned recovery mechanism	• Information at well locations • Production mechanism/history • Reservoir simulator • Rock and fluid physics • Existing seismic data (if available)
Items Estimated	• Changes in reservoir properties • Changes in elastic properties	• Changes in reservoir properties • Changes in elastic properties • Change in 4D response (Attributes)
Effort required/What it entails	• Low effort/quick • Scoring of each properties • Summing of scores	• High effort /detailed/time consuming • Simulator to Seismic modelling • Parameterisation and well calibration
Presentation of results	• Spread sheet of technical risk	• Maps of reservoir properties • Maps of Seismic modelled data
Type of questions answered	• What is the TCS in each field? • Is 4D seismic application possible? • Any need for further study?	• Is the 4D response detectable? • Is it interpretability? • Is 4D seismic application possible? • Optimum timing for repeat survey? • Is existing data good for baseline? • What repeatability efforts are required?

Table 3.1: *Description of the similarities and the differences in 4D screening and feasibility studies as reconnaissance tools for time-lapse seismic project*

The assigned numerical scores are tabulated into what they called "4D – technical – risk spreadsheet". They considered four geological provinces, namely Indonesia, Gulf of Mexico, West Africa and the North Sea in an increasing order of risk, to demonstrate this technique. Although, Marsh et al. (2003) later introduced a rapid method of calculating oil/brine coefficient of reflectivity for 4D technical assessment; nonetheless, the spreadsheet approach is still the most popular in the industry.

While adopting the technique by Lumley et al. (1997) into developing time-lapse CSEM screening methodology, it is noted that the engineering requirements in terms of the production driving mechanisms and how they might impact on the rock physics should be included in this study. Therefore, the rest of this chapter will address the rock physics and the modification that incorporates production and injection activities. The Chapter will also address the value of resistivity as an electrical property compared with elastic properties in

terms of time-lapse sensitivity to the change in fluid saturation. Then, assessment and numerical scoring of the various technical indices for time-lapse CSEM will be done. Finally, this risk assessment will be interpreted for three chosen hydrocarbon provinces, namely the Gulf of Mexico, West Africa and the North Sea.

3.1 The electric rock physics models

The main function of the electric rock physics is to enable us to calculate the resistivity of the reservoir model, which will then serve as a major input to forward model the EM response. Here, a brief review of the different forms of electrical rock physics is carried out.

3.1.1 The shaly sandstones resistivity models

Archie's model described in Appendix 1 assumes that the reservoir rocks are homogeneous clean sandstones, which are electrically neutral, and that only the formation water within the pore spaces is electrically conductive. In reality, homogeneous clean sandstone hardly exists. Most reservoir rocks, particularly clastic reservoirs, contain shale component which has mobile ions – carrying clay minerals as its important constituent. Thus the shale component has higher conductivity than the sand component, and this implies marginal increase in the overall conductivity of the fluid-saturated shaly sandstone clastic reservoir. So, apart from the effects of shale on the reservoir quality in terms of lowering porosity and permeability, shale is equally important in terms of the overall electrical properties of the reservoir rock which has direct effect on the determination of the fluid saturation. Therefore, Archie clean sand model becomes insufficient for shaly sandstone reservoir, as it does not cater for this effect and could lead to under-estimation of resistivity and, consequently, a reduced estimation of hydrocarbon saturation which has an economic implication.

However, in terms of time-lapse measurements for reservoir monitoring, the assumption of no change in lithology between pre- and post- production activities, for a non-compacting reservoir, could be safely applied and could make Archie's equation (Archie 1942) fairly applicable to study change in resistivity due to change in fluid saturation (see equation A1.1

in Appendix 1). This condition indicates that even if the static model is wrong, the dynamic change in resistivity may still be correct since there is no change in lithology (Lien & Mannseth 2008). Perhaps, this is the reason many previous works on time-lapse CSEM sensitivity studies have utilized the simple Archie's equation, coupled with the fact that the electrical property of shale is difficult to characterize.

However, it is equally important to evaluate the initial resistivity model properly before the examination of the change in resistivity. This is because the magnitude of the initial resistivity could exert a limiting value on the possible magnitude change in resistivity due to change in fluid saturation, even though there is no change in lithology. In other words, the higher the initial resistivity value, the higher the limiting value for possible change in resistivity due to fluid substitution. In relation to time-lapse CSEM response, initial baseline signal should be detectable enough, before time-lapse signal could be detectable. If the initial resistivity value of the reservoir in contrast to the conductive background is too small to be detectable by CSEM, then there is a possibility that the time-lapse CSEM anomaly may not be detectable.

Thus, there is a need to adequately represent the shale content of the reservoir in the electrical rock physics, and a good number of equations have been developed for shaly sandstone reservoirs. These equations, which are various modifications to Archie's equation, are dependent on the nature of shale distribution within a reservoir rock, which could be laminated, structural or dispersed based on the geological environment, among other factors. Figure 3.1 b, c and d show pictorial representations of laminated, structural and dispersed shale distribution respectively. Most of the shaly sandstone model equations have been developed with the assumption that shale exists in any of these specific geometric forms or in their combination. Common among these equations is Waxman-Smits model (Waxman & Smits, 1968). It considers ion diffusion which causes cation exchange in the double layer surrounding the clay particles. Several modifications to the Waxman-Smith model also exist, and one of such is Dual-water model (Best, et al., 1980; Clavier, et al., 1984). The dual water model takes into consideration the bound water, which could lead to additional porosity and saturation in shale. It also allows differing values of formation water resistivity for the free and bound waters, due to the difference in salinity and temperature in the sand and shale components of the shaly sand rock. Both

Waxman-Smith and Dual-water models are specifically good at modelling dispersed clay distributions (Shahin, et al., 2012).

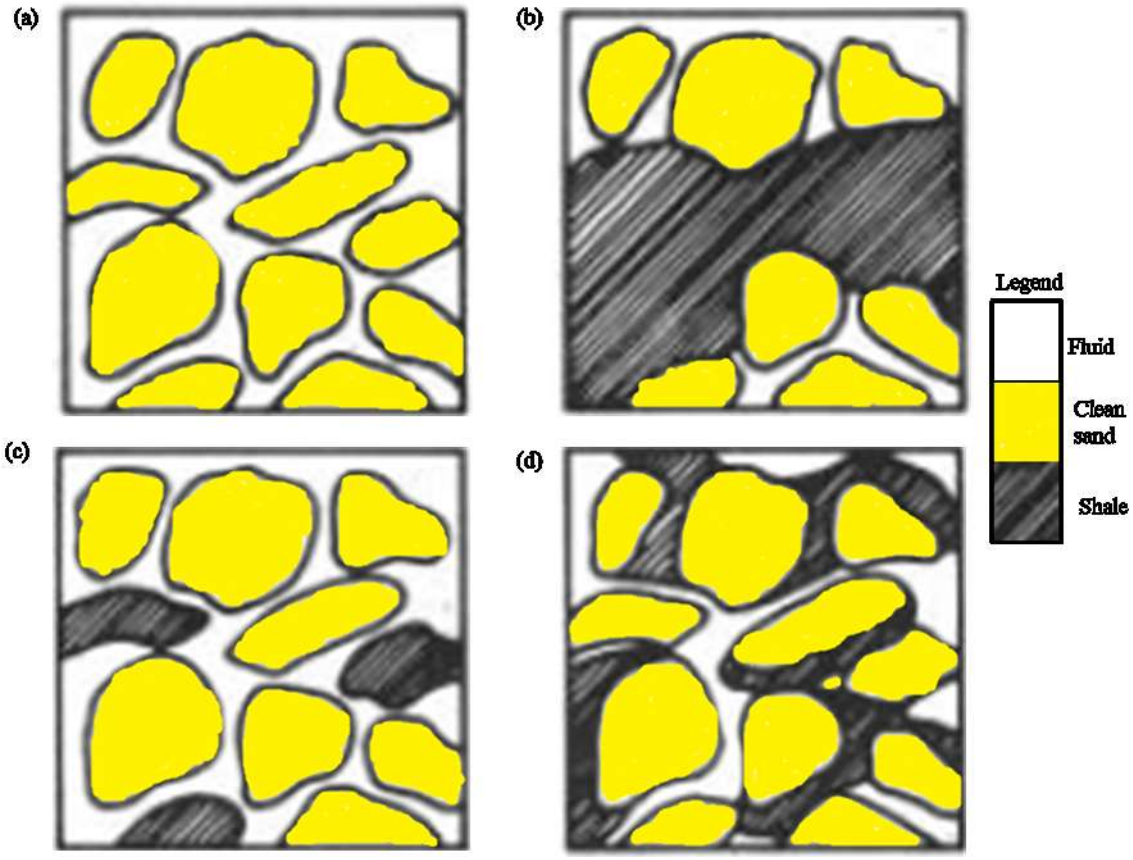

Figure 3.1: *Pictorial representations of: (a) Clean sand without shale, Archie's model is applicable (Appendix 1). (b) Laminated shale distribution where shale laminae are distributed between the layers of sand. (c) Structural shale distribution where shale nodules are distributed in the formation matrix. (d) Dispersed shale distribution where shaly minerals are dispersed throughout the sand, causing fractional filling of the pore spaces in between the sand, and thus reducing the effective porosity and permeability (Crain 1986).*

Among other shaly sand models are Simandoux model (Simandoux 1963), and Indonesian model (Poupon & Leveaux 1971) which worked well for Indonesian geological environment. More comprehensive information about the various kinds of equations for shaly-sand electrical rock physics could be obtained in Worthington (1985) who described thirty shaly sand model equations, and in Doveton (2001) who gave nine selected model equations from numerous collections. The fact that all of these equations reduce to the

Archie fundamental equation, as shale content tends to zero limiting value, lends credence to the fact that none of the shaly sand models could be said to be 'absolutely correct', but each is useful within a particular geological setting. After all, *'all models are wrong but some are useful'*.

Therefore, various forms of shaly-sand model equations take this general basic form of conductivity (reciprocal of resistivity) summation (Simandoux 1963; Worthington 1985; Doveton 2001):

$$\frac{1}{R_t} = \frac{\Phi^m S_w^n}{aR_w} + X \quad ; \tag{3.1}$$

where the first term on the right-hand-side is the fluid-saturated clean sand conductivity (basically Archie's formula), and the second term 'X' is the intra-reservoir shale conductivity. The shale term may be relatively simple or complex. It depends on the volume of shale (V_{sh}), the resistivity of shale (R_{sh}), the shale surface bound water saturation (S_{wsh}) and the shale porosity (Φ_{sh}) among other parameters. It may be treated either independent of, or dependent on, the clean sand term depending on the clay distribution as shown in Figure 3.1.

3.1.2 Fluid flow consistent shaly sandstones resistivity models

(a) Effective resistivity for mixed lithologies

If we assume that the shale porosity is not effective to fluid flow, thus (Φ_{sh}) is negligible, and that water saturation due to bound water on the shale surface (S_{wsh}) is negligible. Then, the X term becomes only a function of volume of shale (V_{sh}) and resistivity of shale (R_{sh}), and the only porosity we have is the effective sand porosity rather than a total porosity. This is in agreement with the 'inactive cells' assumption, usually made by the reservoir simulation engineers in treating shales in the fluid flow simulator, in order to enhance the material balance for good fluid flow. The engineers simply consider shale and other low capacity lithologies as not present in the simulation model! Of course, in perforating both

producer and injector wells, the drilling and well completion engineers are always careful to locate high *NTG* sand sections. However, while shale may be 'inactive' to fluid flow, it is not electrically neutral. Therefore, in the process of modelling resistivity from the fluid flow simulator, the *X* term should still be considered in terms of the shale volume and resistivity. The anisotropic arrangement between sand and shale has a significant impact on resistivity estimation.

Generally, there are two forms of anisotropic arrangement of sand-shale lamination (Klein 1993; Tabanou, et al. 1999; Tsili & Sheng 2001), such that a layered sequence of sand and shale could be represented by either of these equations:

$$R_t = (1 - V_{sh})R_{sand} + V_{sh}R_{sh}, \tag{3.1a}$$

$$\frac{1}{R_t} = \frac{1 - V_{sh}}{R_{sand}} + \frac{V_{sh}}{R_{sh}} \; ; \tag{3.1b}$$

In the simulation model, the shale volume (V_{sh}) is defined in terms of net-to-gross (*NTG*) as:

$$V_{sh} = 1 - NTG \quad ; \tag{3.1c}$$

NTG in this case is the effective volume of sand, the medium through which the fluid flows. It is the volume ratio of sand which permits fluid flow to the total volume of constituent lithologies (sand, shale, carbonate, cement etc). It is the gross sand with porosity and permeability cut-off as defined in the engineering simulation model. It is applicable to time – lapse CSEM modelling because this is where resistivity changes due to fluid substitution is expected to be large.

Equation (3.1a) is an arithmetic average, which gives the total estimate of resistivity for a vertically arranged sequence of sand and shale layers. It is the summation of the product of the volume ratio and resistivity of each lithology. Since the volume ratio takes value from zero to one, then this vertical resistivity estimate is controlled by the more resistive sand layer, especially for a high *NTG* reservoir. Equation (3.1b) is the harmonic average which approximates the total horizontal resistivity, with a parallel arrangement of sand and shale

layers. Here, the less resistive shale layer dominates. In both equations, R_{sand} is the Archie's true resistivity for clean sand reservoir, while R_{sh} is the resistivity of intra-reservoir shale which could be fairly estimated from well logs by taking the average value of deep resistivity measurements within a thick section of intra-reservoir shale.

The choice of which of the equations (3.1a and b) should be used depends on factors such as the nature of the reservoir and the sensitivity of EM acquisition configuration within the reservoir unit, and the extraneous conditions (such as water depth and overburden structure). Equation (3.1a) is employed to model the CSEM data in this thesis, as it is consistent with the available North Sea turbidite channelized reservoir simulation model. The reservoir contains beds of sandstones intercalated with thin layers of shales in a laminated arrangement, such that the reservoir can be represented by lithological resistors in series as shown in Figure 3.2. Also, my CSEM modelling utilized inline horizontal electric dipole (HED) source and receiver instrumentation. In this modelling, the pseudo vertical resistivity within the resistive reservoir is preferentially measured by the purely radial propagation of electromagnetic field (Ramananjaona, et al. 2011; Brown, et al. 2012). Although within the overburden, the inline geometry is sensitive to both the vertical and horizontal components of resistivity, the vertical resistivity is more significant (MacGregor & Tomlinson 2014).

Thus for N layers of sand and M layers of shale in a reservoir where each layer has its *NTG*, sand resistivity (R_{sand}) and shale resistivity (R_{sh}), then equation (3.1a) becomes:

$$\sum_{1}^{N+M} R_t = \sum_{1}^{N}(NTG.R_{sand}) + \sum_{1}^{M}\left[(1-NTG).R_{sh}\right] \quad ; \tag{3.2}$$

In the fluid flow simulation model, 3-dimensional reservoirs are normally gridded into a number of cells. Each cell, denoted by the *i*, *j*, *k* space position, is assigned with specified reservoir properties values (porosity, water saturation, net-to-gross, etc). Thus, by re-writing equation (3.2) in terms *x*, *y*, *z* number of simulation cells and the properties in each of the cells, we have:

$$\sum_{i=1,j=1,k=1}^{x,y,z}\left[R_t\right] = \sum_{i=1,j=1,k=1}^{x,y,z}\left[NTG.\frac{aR_w}{\Phi^m S_w^n} + (1-NTG).R_{sh}\right]; \tag{3.3}$$

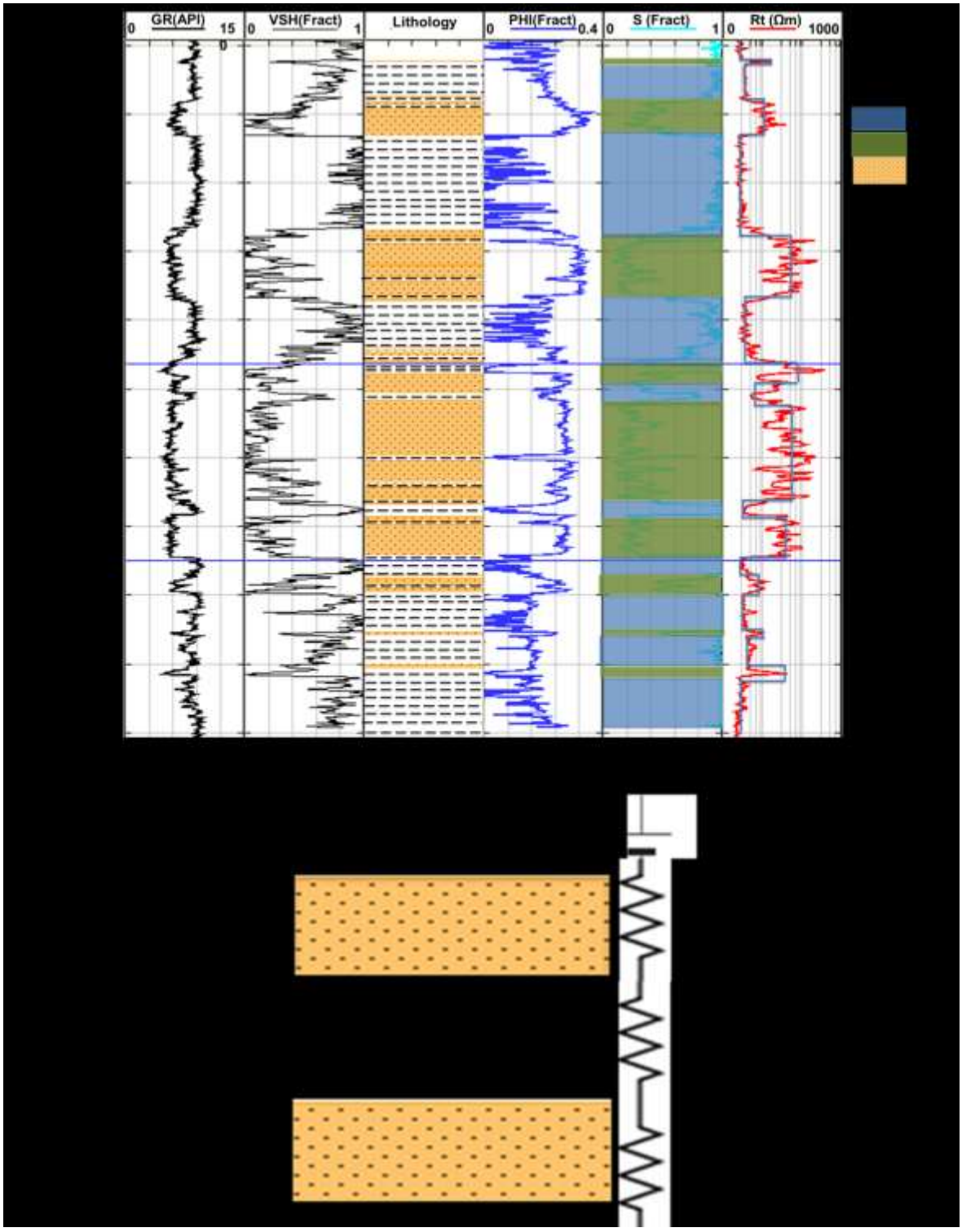

Figure 3.2: *(a) A suite of logs showing laminar lithological distribution within the channelized turbidite reservoir from which lithology and fluid condition are calibrated for subsequent simulation modelling; (b) Total resistivity of the reservoir containing sand and shale layers arranged in series, as a function of the net-to-gross* (*NTG*)*, resistivity of saturated-sand* (R_{sand}) *and resistivity of intra-reservoir-shale* (R_{sh}).

With equation (3.3), 3D resistivity distribution of the reservoir could be calculated, and assuming that we are dealing with a non-compacting reservoir, where only change in water saturation is causing change in resistivity during oil production and water injection activities, then we can forward model the time-lapse CSEM response and relate it with change in saturation, either directly or by first inverting for change in resistivity. Equation (3.3) has been calibrated at the well location, and it is found to be consistent with the in situ R_t for the North Sea field example under consideration. It is applied in Chapters 4 and 5 for the 1D CSEM modelling and in Chapter 7 for 3D integral forward modelling of the CSEM responses respectively.

(b) Effective resistivity for mixed fluid

As mentioned earlier, EM is not able to determine the change in oil saturation from the change in gas saturation, since there is no resistivity contrast between oil and gas. *This is rather a blessing than a curse*, as we shall see in Chapter 5. In time lapse CSEM, we are monitoring change in water saturation rather than change in oil saturation. This is because oil contains extremely negligible or no mobile ions, thus it conducts negligible or no electricity that could be monitored with electric and magnetic field propagation. Moreover, while we measure the resistivity of liquid water (R_w), we hardly measure the resistivity of liquid oil which is almost infinite. Crain (1986) gave about 10^9 to $10^{16}\Omega$m for the resistivity of oil.

Therefore, at reservoir scale, we can only track changes in water saturation as water replaces oil in the pore space. It is also worth-noting that during either aquifer drive or water injection, '*water is not just water.*' We could have aquifer water mixing with connate or formation water, or injected water mixing with formation water, or the three (injected, aquifer and formation) waters mixing together if there is aquifer coning during water injection. These waters could have different salinities and temperatures, thus creating an 'R_w' regime within a pore space different from those of individual waters. Thus, for a dead oil reservoir containing no initial gas cap, within the oil-leg, the saturation equation A1.3a in Appendix 1 will be:

(a) For the baseline case,

$$S_o = 1 - (S_{wirr} + S_{fm}) \quad ; \tag{3.4a}$$

'S_{wirr}' is the irreducible connate water saturation. It is the non-movable minimum water saturation. It typically ranges between 0.15 and 0.3 within the reservoir oil leg, with attendant high *in situ* oil saturation (S_o). Connate water is usually defined from the capillary pressure curves. It is determined along with relative permeabilities of water (K_{rw}) and oil (K_{ro}) from the special core analysis. In the simulation model, S_{wirr} is normally specified along with K_{rw}, K_{ro} and water-oil capillary pressure '*c'*. Within the reservoir pore space partly saturated with connate water and partly saturated with oil, the $K_{rw} = 0$ and $K_{ro}=1$, and capillary pressure is at its maximum value. 'S_{fm}' is the movable water saturation within the formation, and usually higher than the value of connate water. The presence of movable formation water means $K_{rw} > 0$ and $K_{ro} < 1$. Formation water could be produced with oil, but as more formation water is produced, there will be a point whereby the water becomes immobile and K_{rw} tends to *0*, this is the point where we have $S_{fm} = S_{wirr}$.

Apart from the alteration in the relative permeability and capillary pressure, the only electrical properties that could be used to distinguish between the formation and irreducible connate waters are temperature and salinity. Although it could be fairly assumed that, since the two waters co-exist within the same subsurface lithology and depth location, the temperature and salinity conditions of the two waters in a particular reservoir will be the same, especially when they are in equilibrium. Thus, in terms of the electrical rock physics, '*formation water is formation water*', but only when it becomes immobile, it becomes irreducible connate water. Thus equation (3.4a) could just be rewritten as:

$$S_o = 1 - S_{fm}; \tag{3.4b}$$

If at all there will be any *in situ* variation in temperature and salinity, it would possibly be due to lithological variation within the reservoir with different salt concentration and thermal conductivity, or differential proximity to the subsurface salty formations and salt domes or a source of high temperature and thermal conductivity, or a more fresh water or a more saline water is intruding from nearby subsurface environment into the reservoir. In such situation, we would have varying *in situ* R_w values and this introduces uncertainty into

production induced dynamic changes. Thus, except for a reservoir known to be located within an area with such physical occurrences, it is a reasonable assumption to assign constant average value of R_w for all the cells in the baseline reservoir simulation model.

(b) For the monitor case:

(i) If we have natural aquifer drive, the remaining oil saturation (S'_o) within a pore space will be:

$$S_o^{'} = 1 - (S_{fm}^{'} + S_{aq}) \ ; \tag{3.5a}$$

'S_{aq}' is a measure of the amount of subsurface water either below the original oil water contact in the reservoir, or in an external structure fully saturated with water (no oil), that has travelled into this pore space which was originally partly or fully saturated with oil. Mass conservation within the pore space dictates that $S'_o < S_o$. Likewise the new formation water saturation (S'_{fm}) is less than the original formation water saturation (S_{fm}), such that the aquifer water saturation in equation (3.5a) is equal to the combined produced oil and water saturations. This is expressed as:

$$S_{aq} = (S_o - S_o^{'}) + (S_{fm} - S_{fm}^{'}) \quad ; \tag{3.5b}$$

The first and second terms in brackets on the right hand sides are produced oil and produced water saturations respectively, and they are function of the volumes produced, obtainable from the simulation model. If there exist temperature and salinity differences between the aquifer and the formation waters, then we can separate the three fluids (oil, formation water and the aquifer water) based on resistivity contrasts. However, for aquifer water drive to be effective, apart from the expansion of aquifer water due to sudden pressure drop in the oil which creates pressure gradient, lithological continuity between the aquifer and the reservoir is equally important. In this case, there might be little or no contrast in salinity and temperature to warrant R_w contrast to separate the formation water from the aquifer water.

(ii) For water injection within the oil-leg, where there is no aquifer water coning:

$$S_o^{'} = 1 - (S_{fm} + S_{winj}) \quad ; \tag{3.6a}$$

'S_{winj}' is a measure of the amount of surface water external to the reservoir, obtainable from different sources depending on availability, proximity to the oilfield or according to the choice of recovery mechanism (further discussed in Chapter 6). Apart from re-injected produced water, different injected waters have differing salinity and temperature conditions from those of the original formation water. So, just like in aquifer drive, we can separate the three fluids (oil, formation water and the injected waters) based on resistivity contrasts, and we can express injected water saturation in terms of produced oil and water saturation as:

$$S_{winj} = (S_o - S_o^{'}) + (S_{fm} - S_{fm}^{'}); \tag{3.6b}$$

In this case, except for re-injection of produced water, R_w value varies dynamical with the reservoir as water injection proceeds. This should be captured in the simulation model.

(iii) For water injection within the aquifer, where there is aquifer water conning, both the aquifer water and the injected water mix with the formation water in the process of replacing oil:

$$S_o^{'} = 1 - S_{fm} + S_{aq} + S_{winj}; \tag{3.7}$$

Similarly, each of the four fluids, especially the three waters (formation water, aquifer and the injected waters) can be tracked based on R_w contrasts, if there exist salinity and temperature contrasts among them.

In general, produced water in the three monitor cases may not be only the formation water but a mixture of different waters involved. However, our most concern is the interaction of the waters and oil within the pore spaces in the reservoir. We can then use this interaction to identify where we have no change in reservoir resistivity, which could be diagnostic of either water or oil or lithology. Also, where the resistivity has dropped could be diagnostic of water replacing oil, and an indication of water injection efficiency. Interpretation of this information will require validation by *dynamic well-tie* (i.e. proximity to the injector or

producer) as shown in Chaper 5. In situations whereby contrasting values of salinities and temperatures of waters involved could produce significant change in resistivity, and in turn a measurable change in CSEM, then we could distinguish between two or among three waters. This could offer additional information about water evolution within the reservoir over a period of time that could help in reservoir management (Salako, et al. 2013) . This is discussed further in Chaper 6.

It is now established that different waters interact dynamically within a producing reservoir, and that varying salinity (S) and temperature (T), thus water resistivity (R_w), are the only electrical rock and fluid physics parameters we can use to track various waters involved. The only exception is when both the injected water and formation water have similar conditions, such as natural aquifer drive or sometimes with produced water injection. Therefore, a general form of equation connecting R_w with both S and T is required. Such equation will provide an engineering consistent representative value of R_w in a simulation cell, at any particular reservoir location (pore space) and time, as production and injection activities proceed.

Most empirical relationships usually measure R_w either as a function of T at a particular value of S, or as a function S at a particular value of T. For instance, the reference for sea water salinity is about 35grams per litre, equivalent to 35,000 parts per million of $NaCl$ solution, if only Na^+ and Cl^- ions are present (e.g. in Constable et al. 2009). Becker, et al. (1982) gave a linear expression between water resistivity (R_w in Ωm) and water temperature ($T°C$) as:

$$R_w = [3.0 + 0.1T]^{-1} \ ; \tag{3.8}$$

The accuracy of equation (3.12) is considered to be low, say between 3 to 5% for typical sea water temperature. Constable et al. (2009) modified a cubic equation of Perkin & Walker (1972) which is considered to be more accurate between 0° and 25°C. The modification, in equation (3.9) sought improved accuracy for temperatures ranging between 0° and 200°C.

$$R_w = [2.903916(1 + 0.0297175T + 0.00015551T^2 - 0.00000067T^3)]^{-1} \ ; \tag{3.9}$$

Equation (3.9) provides a measure of varying sea water resistivity between the sea surface (at temperature of say, 5° and 30°C) and the seabed (at temperature of say, -5° and 3°C) depending on the seasonal changes, geographical location, sea water depth and the point of measurement referenced to the thermocline depth range. This variation is captured in Figure 3.3. Constable (2013) used this equation to describe the importance of sea water temperature and resistivity in marine CSEM instrumentation, modelling and data acquisition. This is equally important in time-lapse marine CSEM, as repeat surveys could be acquired at different season of the year with differing temperature depth condition. However, this equation gives no consideration to varying sea water salinity as a function of depth. This is not applicable within the reservoir context where different waters of different salinities and temperatures mix together.

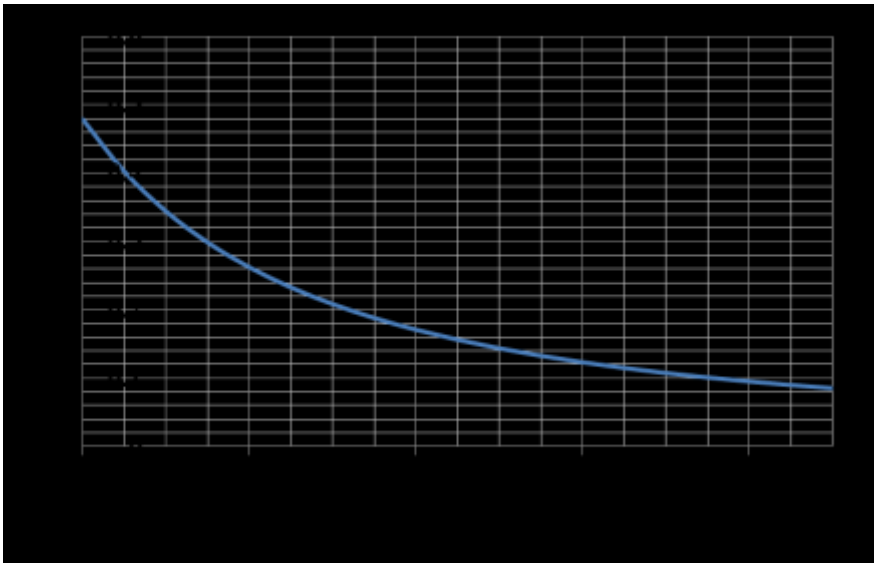

Figure 3.3: *Sea water resistivity as a function of temperature. This is drawn using Equation 3.9 above (originally Perkin & Walker 1972, modified by Constable et al. 2009).*

If we have effective temperature and salinity for the mixed waters within a pore space at a particular production and injection time step, we could then obtain effective R_w for the pore space. The popular Arp's formula (e.g. in Tiab & Donaldson, 2004) enables an unknown R_w to be calculated from a known R_w given the temperature values (in °C) for the two cases. This formula is applicable to a wide range of temperature and salinity values, but salinity value must be constant for the two cases.

$$R_w(@T_1°C) = R_w(@T_2°C) \times \frac{T_1 + 21.5}{T_2 + 21.5} \quad ; \tag{3.10}$$

Equation (3.10) does not allow varying salinity to be incorporated. The relationship between R_w and salinity (S in *ppm* of NaCl solution) at room temprature (23.88°C = 75°F) has been established in many publications (e.g. Dresser Atlas Inc.1982; Tiab & Donaldson, 2004). This is given as:

$$R_w(@T = 23.88°C) = 0.0123 + \frac{3647.5}{S^{0.955}} \quad ; \tag{3.11}$$

Liang, et al. (2012) combines equations (3.10) and (3.11) together to produce a single equation, relating R_w to varying T and S as:

$$R_{we} = \left(0.0123 + \frac{3647.5}{S_e^{0.955}}\right) \times \left(\frac{82}{1.8T_e°C + 39}\right); \tag{3.12}$$

R_{we}, S_e *and* T_e are the effective reservoir water resistivity (in Ωm), effective salinity (in equivalent *ppm* of *NaCl* solution), and effective temperature (in °*C*) respectively. The first term on the right hand side is only valid at room temperature, thus creating two temperature conditions in the equation. The popular Schlumberger log interpretation chart provides several curves based on Arp's emperical formula (equation 3.10), where R_w values are obtained for a wide range of temperatures between 10°*C* to 200°*C*, for various fixed salinities values between 200*ppm* and 280,000*ppm* of *NaCl* solution. This is the most commonly used chart in the petrophysics community.

Crain (1986), proposed an equation which replicates this chart as much as possible:

$$R_{we} = \left(\frac{400{,}000}{(1.8T_e^{\circ}C + 32) \times S_e}\right)^{0.88} \quad ; \tag{3.13}$$

Comparing equations (3.12) and (3.13) as shown in Figures 3.4 and 3.5; it could be observed that for every pair of salinity and temperature, the value of water resistivity is higher for equation (3.13) than for equation (3.12).

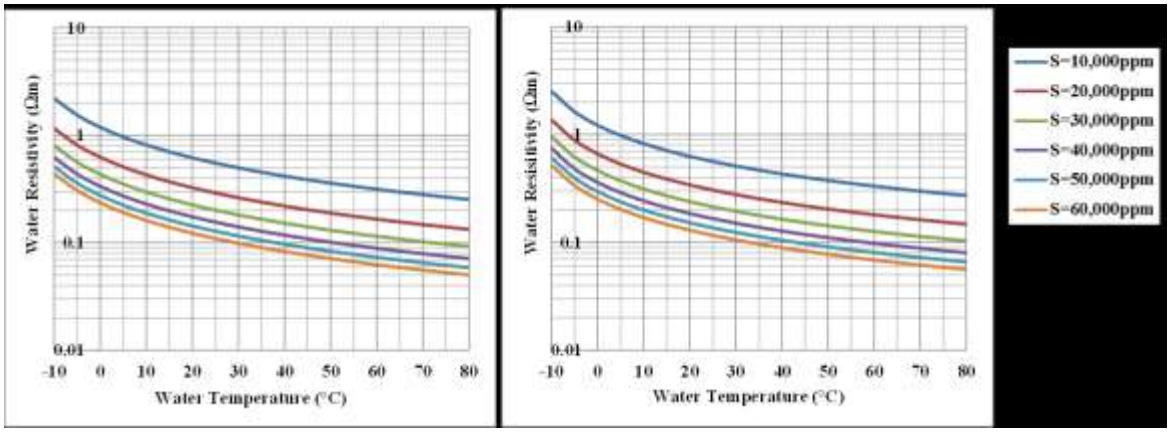

Figure 3.4: *Water resistivity versus temperature as different salinity values using: (a) equation 3.12 proposed by Liang, et al. (2012) which is a combination of popular Arp's formula and equation given by Dresser Atlas Inc (1982); and (b) equation 3.13 proposed by Crain (1986), which is consistent with the Schlumberger log interpretation chart.*

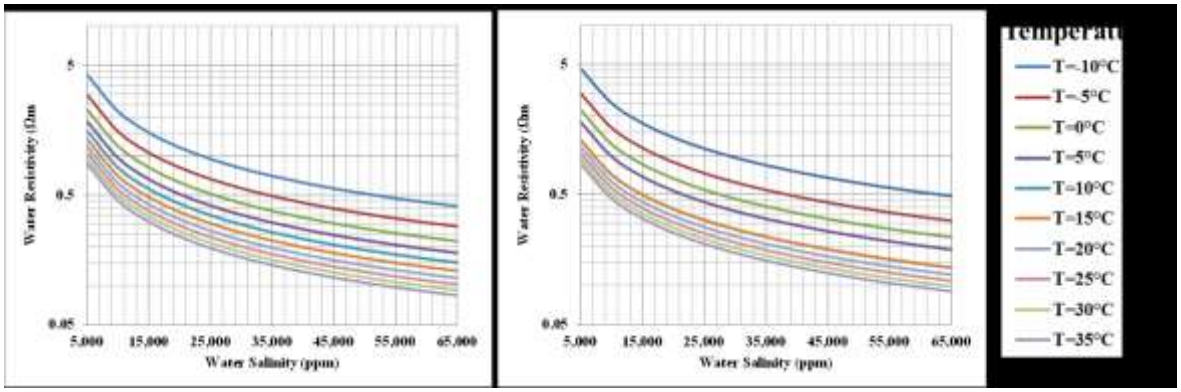

Figure 3.5: *Water resistivity versus salinity as different temperature values using: (a) equation 3.12 proposed by Liang, et al. (2012) which is a combination of popular Arp's formula and equation given by Dresser Atlas Inc (1982); and (b) equation 3.13 proposed by Crain (1986), which is consistent with the Schlumberger log interpretation chart.*

This disparity in water resistivity, of between 0.05 and 0.3Ω*m*, calls for caution in choosing which of the two equations should be used in forward modelling for tracking salinity and temperature. Although Liang, et al. (2012), in using equation (3.16), ignored the diffusive mixing of formation and injected waters by simulating instantaneous isothermal and salt concentration of the mixed water; but this equation is found to be inadequate for estimating a baseline effective R_{we}. For instance, in the North Sea oilfield example, where the baseline reservoir (water) temperature is given as 58°*C*, and formation

water salinity is given as 18,000 *ppm* equivalent of *NaCl* solution (e.g. in Martin & MacDonald, 2010); equation (3.12) gives a baseline formation water resistivity of 0.1871 Ω*m* while equation (3.13) gives 0.2026 Ω*m*. Now, for time-lapse measurements, a 0.0155 Ωm difference in water resistivity may cause erroneous interpretation. The industrial operator of this oilfield used average water resistivity of 0.2 Ω*m* corrected to 58°C reservoir temperature. This places a good level of confidence on equation (3.13) for electrical tracking of effective temperature and salinity of water in a reservoir being produced by water injection.

Now combining equations (3.3) and (3.13) together, we have a fluid flow consistent equation which provides R_t for each cell in the simulation model as:

$$R_t = a.\frac{NTG}{\Phi^m S_w^n}\left(\frac{400{,}000}{(1.8T_e^{\circ}C+32)\times S_e}\right)^{0.88} + (1-NTG)R_{sh} \quad ; \quad (3.14)$$

Other issues relating to thermal interaction, essentially cooling, between fluids and rock, and the fluid salinities addition (salinization and desalinization) for the application of equation (3.14) are discussed in Chapter 6, where the equation is applied to assess CSEM applicability in monitoring of some selected EOR mechanisms.

3.2 The value of resistivity

Resistivity logs, especially deep resistivity tools that offer true formation resistivity, remain the most reliable tools in obtaining the saturation profile with respect to depth at well log scale. At the well log scale, we can examine the value of resistivity as an electric property by comparing it with the fundamental elastic properties like density, P-wave and S-wave velocities, and their derivatives in terms of their time-lapse sensitivities to fluid substitution.

Using another North Sea suite of wireline logs shown in Figure 3.6, deflection of resistivity log (in track 3) to the right (value of 10Ωm to 15Ωm) between depth interval 2206m and

2226m is interpreted as oil sand, which is shown with the separation between the green (oil) and blue (water) curves on the saturation profiles (in track 4).

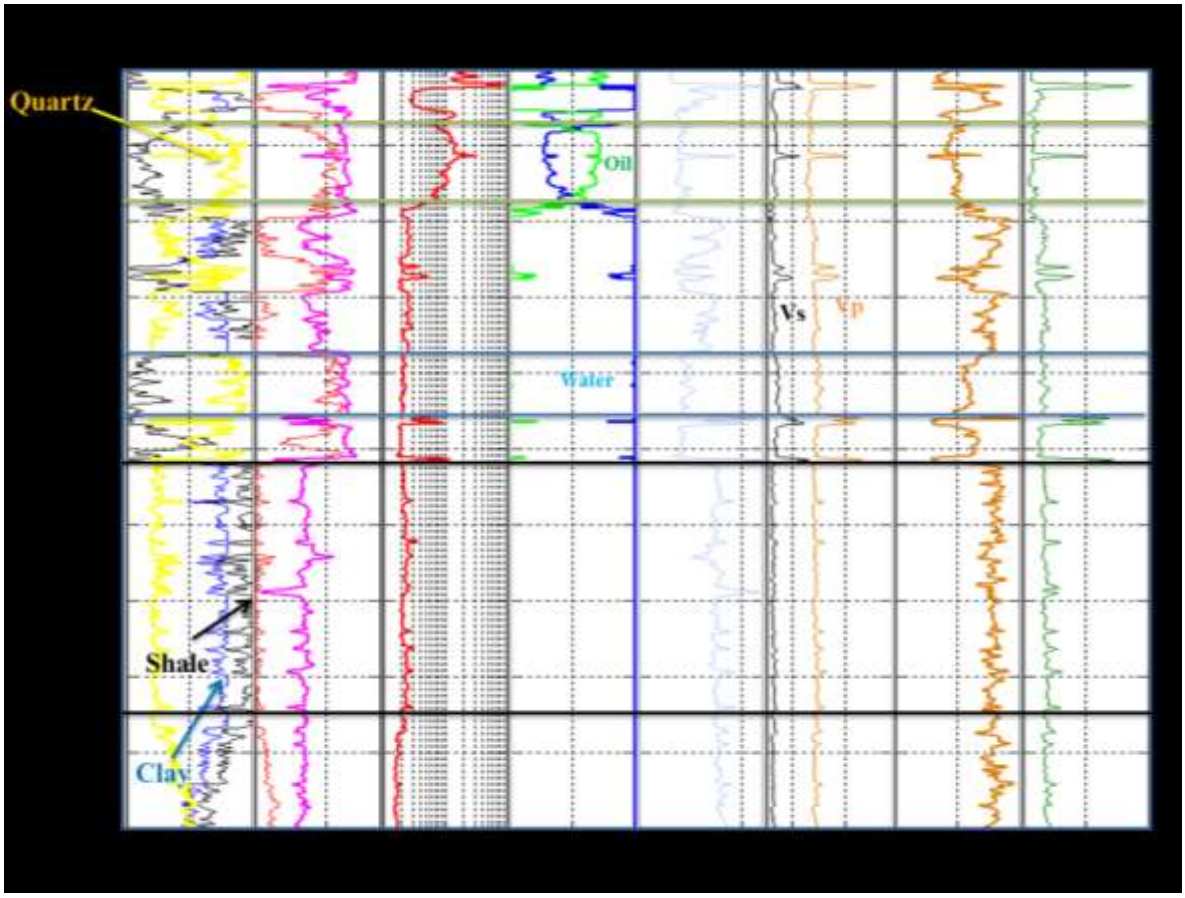

Figure 3.6: *An example of a suite of well logs for a North Sea field, where oil sand, water sand and shale are interpreted at depth intervals 2206m to 2226m, 2265m to 2280m and 2294m to 2360m respectively, to demonstrate the value of resistivity as a better fluid discriminator as compared with the elastic properties.*

There is a high fraction of quartz minerals at this interval, which is an indication of high NTG sand as shown by the separation between the yellow (quartz, about 80%) and the black (shale, about 20%) curves, and absence of blue (clay) curve on lithology profiles (in track 1). Similarly, depth intervals 2265m to 2280m and 2294m to 2360m are interpreted as water sand and shale respectively. Whereas density log, P-wave velocity (V_p) and S-wave velocity (V_s) logs, calculated V_p/V_s ratio and P-impedance logs in tracks 5, 6, 7 and 8 respectively show some indications of porosity and lithology variation; they all show little or no indication of fluid variation. To investigate this further, in static sense, cross-plots of

the elastic properties and resistivity are obtained for each of the interpreted intervals of oil sand, water sand and shale.

For the three cross-plots in Figure 3.7, it could be deduced that V_p/V_s ratio is the best lithological discriminator with about 10.6% increase from water sand to shale, followed by P-impedance with about 4% increase from water sand to shale, although with some overlapping.

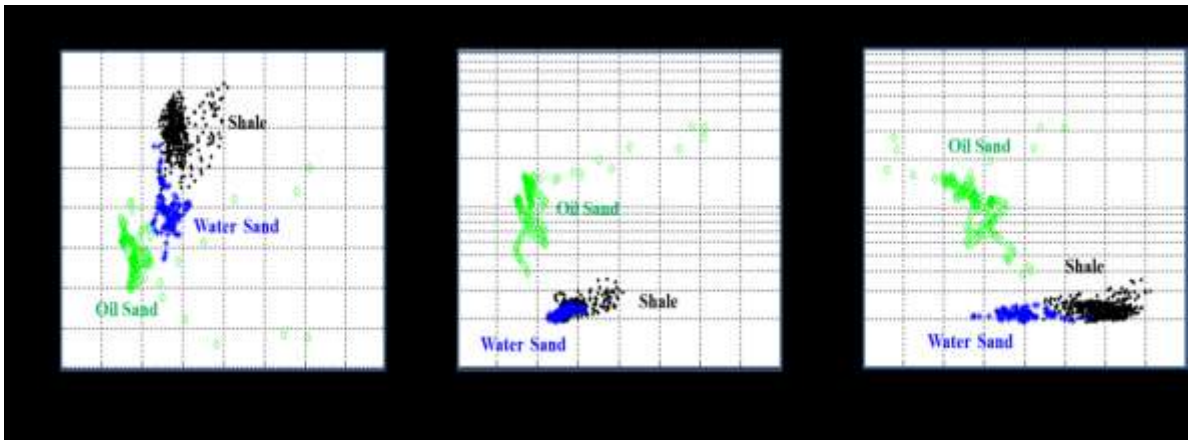

Figure 3.7: *Cross plots of elastic properties and resistivity for oil sand, water sand and shale interpreted from figure 2.1; (i) V_p/V_s ratio versus P-impedance, (ii) Resistivity versus P-impedance, and (iii) Resistivity versus V_p/V_s ratio.*

It is observed that resistivity shows no visible change from water sand to shale. However, in terms of static fluid discrimination, V_p/V_s produced an increase of 5.6% magnitude from oil sand to water sand making it the least fluid discriminator; P-impedance produced an increase of 15.5% magnitude from oil sand to water sand; whereas resistivity produced a decrease of 80% magnitude from oil sand to water sand making it the most sensitive fluid discriminator.

In order to demonstrate the dynamic value of resistivity, in terms of the reality of hydrocarbon production and water injection, combined elastic (Gassmann, 1951) and electric (Archie 1942) fluid substitution is carried out. This is done by replacing 5%, 10% and 15% of oil with water to demonstrate three different stages of oil production and water injection. Figure 3.8 shows the cross-plots and the summary table of calculated percentage

changes in V_p/V_s, P-Impedance and resistivity for these percentages of fluid substitution. There is a general movement of signals from oil sand (green colour) towards water sand (blue) as more oil is replaced with water.

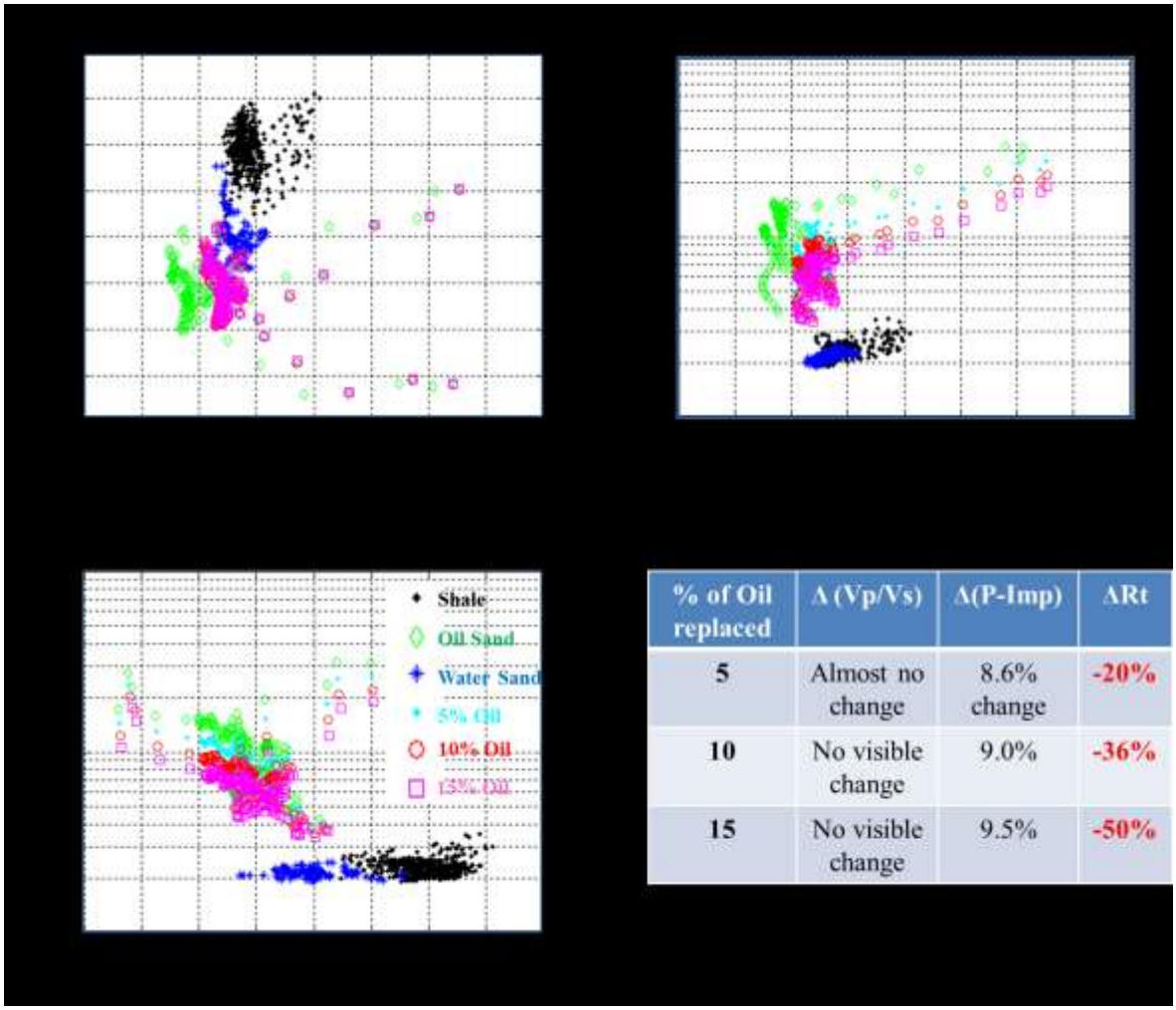

% of Oil replaced	Δ (Vp/Vs)	Δ(P-Imp)	ΔRt
5	Almost no change	8.6% change	-20%
10	No visible change	9.0%	-36%
15	No visible change	9.5%	-50%

Figure 3.8: *Cross plots of elastic properties and resistivity properties to demonstrate fluid substitution. For oil sand, in Figure 2.2, combined Gassmann and Archie fluid substitution is done for 5%, 10% and 15% oil replacement with water; (i) V_p/V_s ratio versus P-impedance; (ii) Resistivity versus P-impedance; (iii) Resistivity versus V_p/V_s ratio; and (iv) Summary table of calculated percentage changes elastic (V_p/V_s) and electric (Resistivity) attributes.*

For V_p/V_s ratio, which earlier showed good lithological discrimination, there is almost no change between different percentages of fluid substitution, thus making it a poor elastic attribute for dynamic fluid discrimination. P-impedance shows some positive anomalous responses to the changes in saturation, positive because water has higher acoustic

impedance than the replaced oil. The initial 5% oil replacement with water in the oil sand produced 8.6% change in P-impedance. The subsequent 10% and 15% fluid substitution resulted in 9.0% and 9.5% changes respectively, in the P-impedance. This means there is no proportionality between the percentage of oil replaced with water and the change in P-impedance response. Resistivity on the other hand, produced negative anomalous change as the resistive oil is being replaced with conductive water. For 5%, 10% and 15% oil replacement, there are -20%, -36% and -50% changes in resistivity respectively.

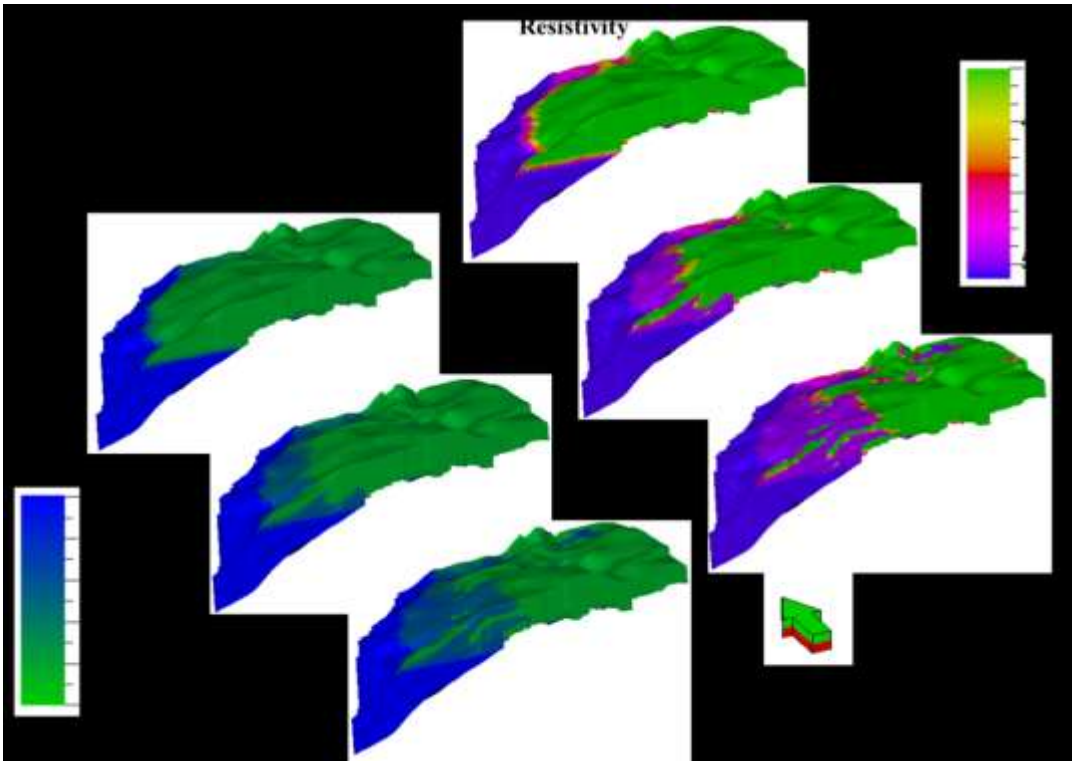

Figure 3.9: *Water saturation distribution and the corresponding calculated resistivity for the baseline (1998) and two monitors (2001 and 2004) 3D reservoir models. This demonstrates a good visual correlation between the water saturation and the resistivity models (simple Archie equation is used with no reference to temperature and salinity).*

These changes are big and they show a good level of correlation with the percentage fluid substituted. It is now certain, at least at well logs scale, that resistivity has a good value, and better value when compared with elastic attributes, for dynamic fluid substitution. Now at reservoir scale, the value of resistivity is examined by calculating the 3D resistivity distribution using Archie's equation (3.1). Porosity and water saturation are obtained from

the engineering simulation model of the North Sea reservoir. The supplied R_w value (temperature corrected) of 0.2 Ωm is used. Other Archie's constants 'a=1' and 'n=2'are assumed for clastic reservoir. The R_o value within the water-leg (where $S_w \approx 1$) is measured from the well log data to be 2.04 Ωm at 'Φ = 27.5%'. Using Equation 3.2, 'm' is calculated to be 1.8. Figure 3.9 above shows the images of water saturation and the 3D resistivity distributions calculated for the baseline (1998) and the two monitor (2001 and 2004) models. Obviously, the resistivity models have good visual correlation with water saturation models. It will be desirable to transform this to spatial and dynamic variations in CSEM surface measurements.

3.3 General overview of the assessment and screening indices

Although resistivity has shown some values as shown above, it is still important that various technical issues should be assessed before embarking on marine CSEM measurements for reservoir monitoring. This assessment, here called time-lapse screening, will provide reconnaissance information to ascertain the level of risk involved with the project before actual field surveys. There are a few numbers of indices that should be considered in any time-lapse CSEM technical risk assessment and screening exercise. Here, they are categorized into three subsets. The first subset is the engineering-consistent rock and fluid physics, which contain indices relating to the elements of rock and fluid physics. These are the reservoir and fluid properties that have bearing on the spatial and time varying resistivity value of the reservoir, as production and injection activities progress. Assessment of these factors involves interplay between the geological parameters and the production mechanisms. The second subset is the physical state of the reservoir rock, the surrounding rock and the extraneous elements of the earth that could impact on the EM signal. The third subset is EM response itself, the various features of the static and time-lapse EM response which should either render the data interpretable or non-interpretable. All of these will determine the technical chance of success of time-lapse CSEM project. Table 3.2 gives the summary of these three subsets of the assessment indices. The contribution of some of the assessment indices, to the technical chance of success in a time-lapse CSEM project, can be examined using Equation (3.18).

Category	Sub-category	Assessment Indices	Remarks
Engineering consistent rock and fluid physics	Main dependent variables	Change in resistivity (ΔRt, *in* Ωm)	**Model parameterisation Major parameters that determine detectability**
		Time interval (Δt)	
	Reservoir rock properties	Compaction factor (a)	
		Porosity exponent (m)	
		Saturation exponent (n)	
		Net-to-gross *(NTG)*	
		Porosity (Φ)	
	Fluid properties	Formation & injected waters resistivity (*Rw, in* Ωm)	
		Formation & injected waters temperature (*T, in* $^{\circ}C$)	
		Formation & injected waters salinity (*S, in ppm*)	
		Initial water saturation (Sw)	
		Change in water saturation (ΔSw)	
Physical states	Sea water conditions	Sea water depth (*in metre*)	**Model parameterisation Survey plan and strategy Repeatability Detectability**
		Sea water resistivity (*in* Ωm)	
	Overburden conditions	Depth to the top of reservoir unit (*in metre*)	
		Overburden resistivity structure (*Robd vs. depth*)	
	Target conditions	The reservoir unit thickness (*in metre*)	
		Several stacked reservoirs	
		Other resistive subsurface structures	
EM signal response	Forward modelling (1D and 3D)	Optimum frequency (*in Hz*)	**Detectability Survey plan & startegy Repeatability Interpretability**
		Resolution	
		Signal magnitude	
	Forward modelling and Inversion (1D 2D, 2.5D and 3D)	Fluid contact visibility	
		Inverted resistivity recovery	
		Predicted change in resistivity	
		Predicted change in transverse resistance	

Table 3.2: *Indices used in time-lapse CSEM reconnaissance screening studies. The indices are grouped into three main categories with subcategories in each group. Each subcategory contains some assessment indices which are discussed independently in detail.*

Assuming that the bulk reservoir resistivity only changes as a function of change in water saturation due to production and injection activities over a period of calendar time, and that the intra-reservoir shale is not contributing to the fluid flow; then, we can use the chain rule to express a small change in resistivity over a period of time to be equal to the product of the change in resistivity with respect to change in water saturation, and a small change in water saturation over the same period of time.

Thus, equation (3.18) becomes:

$$\frac{\Delta R_t}{\Delta T} = NTG.\frac{-n.a.\left\{\frac{400000}{Temp \times Sal}\right\}^{0.88}}{S_w^{n+1}.\Phi^m}.\frac{\Delta S_w}{\Delta T} \quad ; \tag{3.19}$$

Interestingly, the shale term has been eliminated in the rate of change. Now, using equation (3.19) and some scientific intuition, let us discuss each of the assessment indices under each category, and how they could be determined.

3.3.1 Assessment of the indices of the engineering-consistent rock and fluid physics

Perhaps the primary set of indices that should be given priority consideration in time-lapse CSEM screening is the rock and fluid physics parameters, incorporating production mechanisms. As described in Table 3.2, this category is subdivided into three sub-categories namely the main dependent variables, the reservoir rock properties and the fluid properties. They constitute the major factors to determine the detectability of the intra-reservoir time-lapse changes, and should be properly parameterized in EM forward modelling. Some of them could be assessed directly from equation (3.19).

1. **The main dependent variables**

   i. *'ΔR_t' (in* **Ωm***)*, the change in resistivity due to fluid substitution is the main reservoir parameter which determines whether repeat CSEM survey should be

conducted or not. The larger its value, the more assuring will be the technical chance of success, in terms of detectability, and even in terms of interpretability when the EM field data are inverted. For successful frequent monitoring, we desire a detectable and rapid change in resistivity over a short period of time, say a few months. Water-flooding, using saline sea water for instance, into the oil leg of a high permeability and high porosity reservoir will lead to a significant change in resistivity within a short period of time. High permeability and porosity will together enhance fluid flow and provide enough room for fluid substitution to take place, which will subsequently lead to high change in resistivity, enough to warrant repeat EM survey.

ii. *'ΔT'*, this is the time between CSEM surveys, say baseline and the first monitor surveys. This time depends on the rate of production and injection activities, and the geological nature of the reservoir. In other words, how often (in time) does the change in detectable resistivity occur to warrant a repeat CSEM survey?

Both *'ΔR_t'* and *'ΔT'* depend on other indices, and they are referred to as the dependant variables in this context, as they could not be determined on their own, without giving considerations to other variables. The minus sign in equation (3.19) indicates that we are generally dealing with a reduced resistivity in the time-lapse electric rock physics, as the water displaces oil. Although there are few exceptions to this, when a more resistive fluid displaces a more conductive fluid, as we shall see later in Chapter 5. In such cases, the minus sign becomes positive.

2. The reservoir rock electric parameters

These parameters have been extensively discussed in open literature (e.g. Archie 1942; Worthington 1985; Donaldson & Siddiqui 1989; Sharma, et al., 1991; Mavko et al., 1998; Doveton 2001) in terms of the static rock physics. Here, they are discussed more, in terms of their time-lapse impacts.

i. **The compaction factor**, ***'a'***: It could be determined empirically from laboratory experiment on core sample. It is usually assumed to be equal to 1. This assumption could indicate that the reservoir is not undergoing differential compaction due to production, which is consistent with our earlier assumption above. Thus, except we are dealing with a compacting reservoir, the tortuosity factor plays no significant role in EM reservoir monitoring.

ii. **The porosity exponent or cementation factor**, ***'m'***: Rock matrix itself is assumed to be electrically non-conductive, thus porosity exponent indicates how much of the pore network within the reservoir rock increases the resistivity. It could also be determined from core experiment, and it usually takes value between 1.3 and 2 depending on the degree of consolidation of the reservoir rock. Low value of cementation factor means the reservoir is less consolidated, thus better permeability and porosity, which enhances fluid flow and fluid substitution. Shahin et al. (2012) have the awareness of this fact, thus they used different cementation factors for different geological facies, in calculating their resistivity model. On the other hand, from Equation 3.18, the fact that the cementation factor is an index of the porosity, and that the porosity is measured in fraction, makes high value of cementation factor desirable to achieve high initial resistivity, even though its value does not have any time-lapse effect, except for compacting reservoir. The high initial resistivity in this case will be lithological indicative, rather than fluid indicative. A value of 2 is usually assigned to cementation factor for most consolidated rock, though its value for a particular reservoir could be determined from special core analysis (SCAL) or by using Equation A1.2 (see Appendix 1) in combination with values of variables obtained from the well logs at reservoir location of interest.

iii. **The saturation exponent**, ***'n'***, could be deceptively considered to be a fluid property rather than being a reservoir rock property. It models the presence of other fluids within the rock pore spaces. Thus, it is a function of the fluid-

wettability of rock, which is defined as the relative wetness of the rock surface by water and oil. In order words, saturation exponent depends on the rock's preferential adhesive affinity to a particular fluid rather than the other. The value of saturation exponent ranges from less than 2.0 for a highly water-wet rock to more than 8 for a highly oil-wet rock (Donaldson & Siddiqui, 1989). In fact, Sharma et al., (1991) gave as high as 9.5 for a substantially oil-wet rock. Thus, Saturation exponent plays an important role in hydrocarbon reserve estimation (Corbett, 2010). Figure 3.10 shows the relationship between the wettability of a rock and saturation exponent for Elgin sandstone.

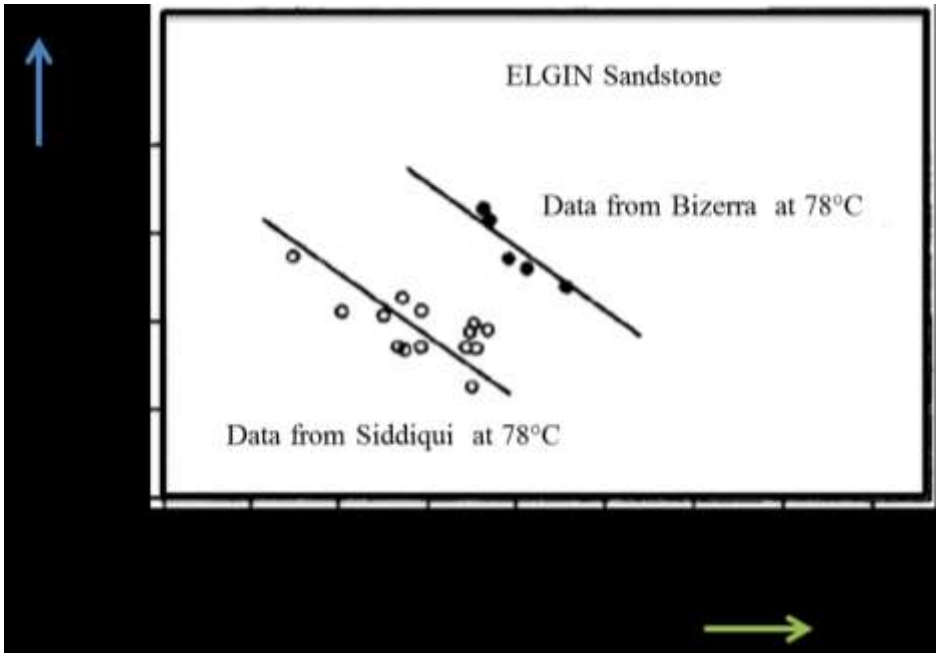

Figure 3.10: *A plot of an empirical relationship between wettability index and saturation exponent for some chosen sandstone formations at a given temperature, showing increasing trends of water-wetness of rock and oil-wetness of the rock respectively on the y- and x-axes (modified from Donaldson & Siddiqui 1989).*

We usually assume that most rocks are more water-wet than oil-wet, with a saturation exponent of a value of 2. This assumption may not be valid for some rocks, for instance rocks in the Arctic regions such as seen in Endicott field in the Alaskan basin, where it has been recorded that hydrocarbon reservoirs are more oil-wet, thus requiring a tertiary EOR using the low-salinity water injection to recover the high saturation residual oil (Seccombe

et al. 2010). For an oil-wet rock, the adhesive force between the rock and the oil is very high and this will make it difficult for water, especially saline sea water, to drive the oil towards the producer during water flooding. So, for an effective fluid substitution, we desire a strongly water-wet reservoir rock with a low value of saturation exponent.

iv. **Net-to-gross (NTG)** is the volume of net sand lithology as a fraction of the total volume of rock matrix. It is the effective sand volume, through which the fluid flows. The higher the value of NTG, the closer the reservoir model to a clean sand model, with good porosity and permeability. Such high NTG with attendant good fluid substitution aids high change in resistivity. High NTG also means lower effect of shale conductivity, thus a relatively high initial resistivity value. Reservoir scale NTG is usually obtained from quantitative interpretation of 3D seismic data, calibrated with well information. Thus in terms of dynamic EM, engineering definition of NTG as pertaining to fluid flow and fluid substitution, such that resistivity changes can be aided, applies.

v. **Porosity (Φ)**: High porosity is desirable for sufficient fluid saturation. It indirectly aids fluid flow. Although high porosity tends to lower the initial resistivity value, thus lowering the EM response with respect to the background structure (Ellis & Keirstead, 2011) as shown in Figure 3.11. This is considered to be an initial lithological effect which limits the room for change in resistivity. However, within an oil leg in a highly porous reservoir, the initial resistivity value may still be significantly large due to high initial oil-saturation. This is more of fluid-related resistivity than lithology-related. Moreover high porosity within the oil-leg presents a large room for fluid substitution, allowing for enough possibility for water to displace oil, thus producing large change in resistivity. The assumption that the reservoir is non-compacting means the porosity is not reducing with production, and thus the lowering resistivity is not driven by lithology, but by fluid substitution. Therefore, high porosity is still desirable, especially within the oil-leg of the

reservoir, where fluid substitution is most effective in engineering sense. Reservoir scale porosity is usually obtained from quantitative interpretation of 3D seismic data, calibrated with well information.

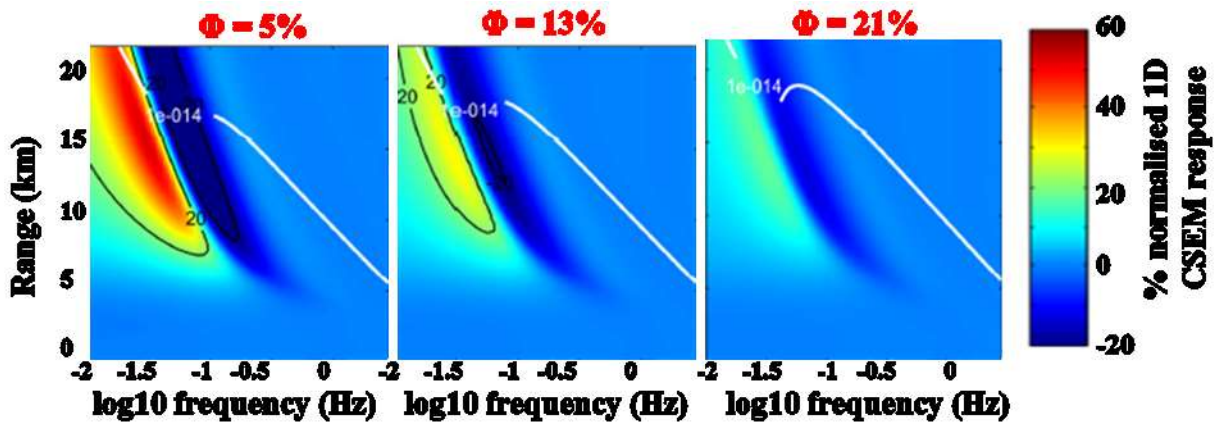

Figure 3.11: *1D EM responses normalized with background for three reservoirs having similar properties except porosity. The responses are plotted as a function of source-receiver range and frequency respectively on the y- and x-axes. At 15km range and 0.3Hz frequency (Log10 frequency = -1.5), for instance, as the porosity increases from 5% to 13% to 21%, the EM response decreases from about 60% to 35% to 15% (Ellis & Keirstead, 2011).*

3. The Fluid Properties

i. **Water resistivity** (R_w *in* Ωm): This, originally, is the formation water resistivity. In reservoir monitoring sense, it is the water resistivity, which is the resistivity of a combination of formation water (which could be either aquifer water or connate water or irreducible water depending on the area of interest within the oilfield) and the injected water of different kinds. Usually R_w is obtained from the formation water sample or from the SP log. However, in terms of reservoir monitoring, this static value may not be valid, because as injected water mixes with the formation water, the value of R_w changes spatially and dynamically for a period of time, depending on the salinity and temperature condition of the injected water relative to that of the original formation water. For conventional purpose, similar temperature and salinity are desired for both injected and formation water, but this can only be obtained if we re-inject the produced water. Unfortunately, the produced

water could only be re-injected after a significant period of water injection from other sources. Also, the produced water is usually not of sufficient volume for re-injection, thus additional water is sourced elsewhere. This complicates the value of R_w, which should be determined based on the values of resultant temperature and salinity of the mixed water in the reservoir, as a particular spatial field location and time. Whatever may be the case, water resistivity is always lower than the resistivity of oil, and this difference in resistivity will always produce anomalous signature whenever there is a fluid substitution. An additional value with proper measurement of R_w is that it helps in distinguishing between the injected water and the *in situ* reservoir water, which enhances the study of the evolution of water. This may be important in monitoring the efficiency of water injection, and especially in low salinity water injection for enhanced oil recovery.

ii. **Formation and Injected waters temperatures** (***T*** *in* $°C$): As described under the water resistivity, resultant temperature of the mixed reservoir water is important to determining the value of R_w. Even for produced water re-injection, the temperature of the injected water will still be slightly lower than that of the in-situ reservoir water. For seawater injection, especially during winter season in some part of the world, we expect to see high difference in temperature. However, as we shall see later in Chapter 5, injected water temperature tends to equilibrate fast to assume the subsurface temperature, as injected water moves away from the vicinity of injection well and get heated towards the production well. Thus, temperature effect is most pronounced near the injectors. Although lowered temperature due to cold water injection has tendency to increase the resistivity of water, thus reducing the anomalous signature. However it does not affect our ability to monitor oil displacement with water injection, as the anomaly is still expected to be large enough to be detectable.

iii. **Formation and Injected waters salinity** (***S*** *in ppm*): Also as described under the water resistivity, resultant salinity of the mixed reservoir water is

important in determining the value of R_w of the reservoir. For produced water re-injection, the reservoir salinity value is expected to be fairly constant. However, adding more water from other sources to the produced water to raise the required volume of injected will impact on the salinity of the reservoir water. Not only that, mixing of water with different salinity values may cause production related issues like formation of 'mineral scales' around the wellbore and even within the reservoir over a period of time. The mineral scale has the tendency to restrict fluid flow. Salinity mixing is an irreversible mass summation and it depends on the initial salinity values of the constituent waters (injected and formation). Thus, its effect is more pronounced than temperature, even away from the injectors. Whether it will raise or lower the resultant R_w depends on the difference between the salinities of waters involved. If the injected water has higher salinity than the formation water, then the injection process will lower the resultant R_w and vice versa. In any case, our ability to monitor change in saturation due to oil displacement during water injection is not impeded.

iv. **Initial water saturation (S_w)**: A direct look at Equation (3.19) shows that low initial water saturation enhances high change in resistivity of the fluid-saturated rock. Thus, we need to know which leg of the reservoir we are injecting into. Within the oil leg, the initial S_w is equivalent to irreducible water saturation (S_{wirr}). Here, the oil saturation could be as high as 70% to 90% while the water saturation is only about 10% to 30%. This means, water injection into this leg to drive oil towards the production well will raise the water saturation significantly, thus high change in resistivity (R_t). However, water injection into the aquifer for pressure support can only produce change in resistivity within the aquifer, based on the contrasting salinity and temperature. However, as the injected water pushes the aquifer, and the aquifer pushes the oil towards the production well, we can expect change in resistivity due to aquifer water replacing the oil. Generally speaking, low initial S_w is desirable, and this is only possible within the oil leg.

v. **Change in water saturation** (ΔS_w): Simply put, from Equation (3.19), the higher the change in water saturation, the higher the change in resistivity. High change in water saturation is achievable either by injecting into the oil-leg, or by basal or lateral aquifer drive causing oil displacement.

3.3.2 Assessment of the indices relating to the physical state

This category of assessment indices are divided into three sub-categories, namely the sea water, overburden and target conditions as described in Table 3.2. It is important to parameterize these indices appropriately during EM forward modelling as they have bearing on survey planning and strategy, repeatability and detectability.

1. Sea water condition

i. **Sea water depth** (**in** *metre*): The water depth should be significantly deep enough to suppress the air wave effect, which tends to have destructive interference with the desired EM signal. Figure 3.12 shows that better EM responses are obtainable for deeper sea water.

ii. **Sea water resistivity** (**in** Ω*m*): Conductive sea water will aid good transmission of source current into the subsurface. Usually, a low sea water resistivity of 0.3Ωm is normally assumed. However, due to temperature gradient and possible variation in salinity within the sea water column, sea water resistivity may vary from the sea surface to the seafloor. Seasonal variations in weather also have impact on the seawater condition. In order to minimize model error in EM forward modelling and preparation for actual field survey, sea water condition should be properly represented taking into consideration the time of the year for both baseline and monitor surveys.

2. Overburden condition

i. **Depth to the top of reservoir unit** (**in** *metre*): The deeper the overburden depth to the top of reservoir, the lower both the baseline and time-lapse EM

responses. A shallow reservoir generally produces better anomaly than a deep seated reservoir. In CSEM modelling, the depth to top reservoir is considered from the sea surface, which combines the water depth with the overburden thickness. While large sea water depth is preferable, shallow overburden is desirable. This is examined in detail in Chapter 6 using 3D modelling.

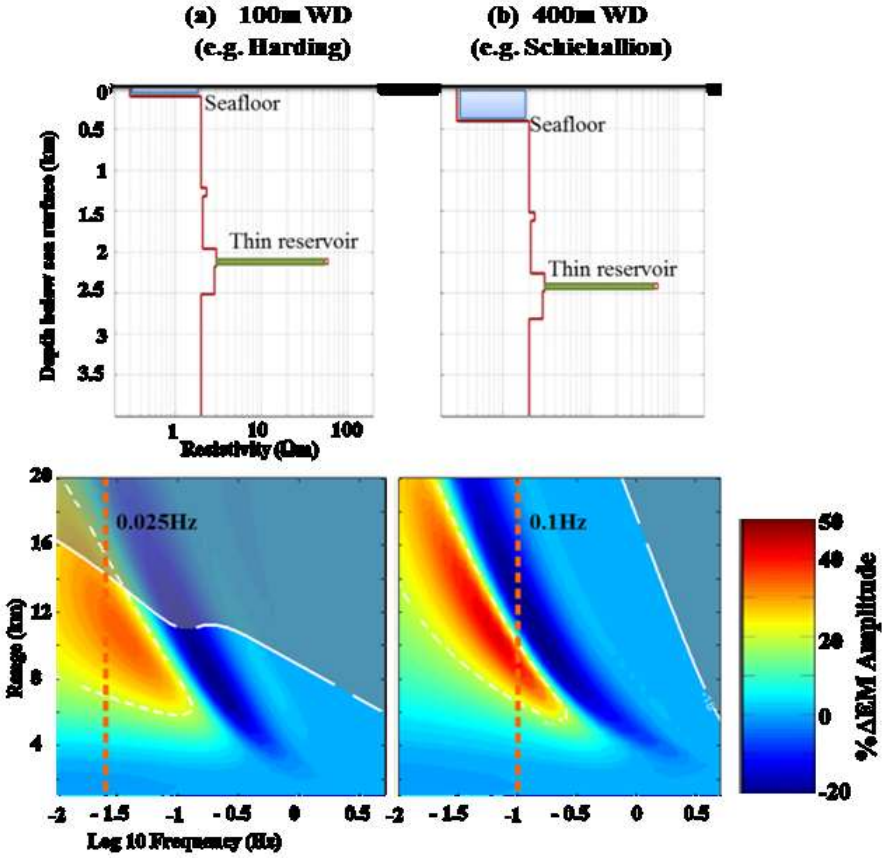

Figure 3.12: *Comparison of 1D EM responses normalized with background for two examples of water depth conditions with similar subsurface properties. The responses are plotted as a function of source-receiver range and frequency respectively on the y- and x-axes. The resistivity of thin reservoir, located 2km below the seafloor, is 60Ωm. (a) The sea water depth is 100m as seen in Harding field , thus the signal is generally low and visible at a rather low frequency of 0.025Hz. (b) The sea water depth is 400m as seen in Schiehallion field, thus the intermediate signal obtained at a moderate frequency of 0.1Hz.*

ii. **Overburden resistivity structure**: Overburden resistivity (R_{obd}) as a function of depth (*depth*) has direct impact on both the baseline and time-

lapse EM signatures. A relatively simple overburden, with almost constant low resistivity profile will enhance the EM anomaly of the thin resistive reservoir. Also, since there is no production phenomenon that could cause a change in the overburden resistivity structure, for a non-compacting reservoir, then for the same low resistivity simple overburden profile the time-lapse response will be better delineated than for a more complex varying high resistivity overburden profile. This is examined in detail in Chapter 6 using 3D modelling.

3. Target condition

i. **The reservoir unit thickness (in *metre*):** Naturally in geophysical measurement, the thicker the target section, the better the anomalous response with respect to the background. If the resistive reservoir unit is thick enough, and not too small relative to its burial depth, the relative signal of the anomaly compared to the host rock will be measurable. A thick reservoir will also support good fluid substitution, which will enhance significant resistivity change.

ii. **Several stacked reservoirs:** The presence of overlying resistive reservoir will produce an 'add-up' amplitude effect on the underlying reservoir. For baseline EM measurement, the combined response will produce higher amplitude with respect to the 1D background structure than when there is no shallow resistor. However, in the time-lapse domain, if the deeper reservoir is produced, the shallower reservoir acts to increase the background structure with respect to the time-lapse difference signal due to fluid substitution occurring in the deeper reservoir. Therefore, the time-lapse response becomes lower than the situation when there is no shallower reservoir. Similar situation occurs, even if the overlying resistive body is not a hydrocarbon reservoir, but a resistive lithological material like basalt. In case of simultaneous production from stacked reservoirs, there is a dilemma

of separating the contributory effect of each reservoir to the overall time-lapse EM signal.

3.3.3 Assessment of the indices relating to the EM response

This category of assessment indices are divided into two sub-categories, namely forward modelling and a combination of forward and inverse modelling as described in Table 3.2. All of these indices contribute to the examination of detectability, survey plan and strategy, and most importantly they determine repeatability and interpretability.

1. **Forward modelling (1D and 3D)**

   i. **Optimum frequency** (**in** *Hz*): The higher the optimum EM frequency, the better both static and time-lapse EM signals. High frequency is a function of overburden structure and sea water depth as shown in Figure 3.12, and in Chapter 6. A shallow overburden and deep water depth will enhance high optimum frequency, and better signal. 1D forward modelling is a quick way of obtaining optimum frequency with which real field EM data are acquired.

   ii. **Resolution:** Generally speaking, EM resolution of the reservoir with respect to the background is poor. This is due to the diffusive nature of the EM field, but the resolution can be improved with extra effort in survey acquisition. High optimum frequency, thick reservoir unit, deep sea water, less confounding overburden resistive structure coupled with optimum survey geometrical configuration will enhance EM resolution.

   iii. **Signal magnitude:** The higher the resistivity contrast between the reservoir and the host background rock, and/or between pre-production and post-production within the reservoir; the higher the magnitude of the static and time-lapse EM signals respectively.

2. **Forward modelling and Inversion (1D and 3D)**

i. **Fluid contact visibility:** Visible change in the fluid contact, either directly from the EM difference maps or from the inverted resistivity difference maps is an important indicator of change in saturation due to production and injection activities. Low visibility of fluid contact means we cannot identify change in saturation. High porosity, less consolidated shallow reservoir will yield better fluid contact visibility than a more consolidated low porosity reservoir.

ii. **Inverted resistivity recovery:** In order to enhance interpretation, especially as EM data resolution is always an issue of concern due to the diffusive nature of the electromagnetic field, thus inversion of the EM data to recover the resistivity image of the reservoir is important. The more constrained the inversion, the better the recovery of resistivity image (3D cube of 2D map) and less the degree of uncertainty in interpretation. Hopefully, in future, inversion could be constrained with the engineering simulation model (both grid and properties). Comparison of the calculated resistivity from the simulation model, with the inverted resistivity from the modelled EM data is important in this regard.

iii. **Predicted change in resistivity:** This is important as it will determine if the change is detectable. This is achievable either by forward calculation of resistivity and change in resistivity from the simulator using the rock physics, or by inversion of two set of modelled data obtained by forward modelling of simulator to electromagnetic data.

iv. **Predicted change in transverse resistance:** Ordinarily, EM is sensitive a combination of resistivity and unit thickness, otherwise called resistivity-thickness or transverse resistance. So, the predicted change in transverse resistance will help to determine if the proposed time-lapse EM surveys will yield a quantitative interpretable result. This can be determined in similar

ways as predicted change in resistivity, but taking into consideration the thickness of the subsurface layers involved.

3.4 Numerical scoring of important indices for three selected hydrocarbon provinces

Assigning numerical scores to all of these assessment indices is subjective. For instance, as important as the initial water saturation is, it is a function of the area of reservoir under consideration, and as such, could not be assigned a single value. However, some of the indices have been considered for direct numerical scoring, for three selected hydrocarbon provinces, namely the West Africa, the Gulf of Mexico and the North Sea. These indices are not exclusive, but are among the important assessment elements in screening time-lapse EM project. The guide to risk assessment score card in Figure 3.13 shows colour and the corresponding scores based on the *degree of relative proximity* to the ideal value expected for low risk. Colour 'green' and a score of '3' are assigned to an index with value closest to the expected ideal value, such that the index constitutes very low risk. Colour 'orange' and a score of '2' are assigned to an index having value closer to the ideal value and thus of moderate risk. Finally colour 'red' and a score of '1' are assigned to an index with value close to the ideal value and thus of high risk.

RISK ASSESSMENT SCORE CARD GUIDE			
	Closeness to ideal value of the index		
Risk level for each idex	Closest	Closer	Close
Risk index	Low risk	Moderate risk	High risk
Colour			
Score	3	2	1

Figure 3.13: *Risk assessment score card guide. See text for full description.*

For typical range of values, numerical scores are assigned to fifteen (15) assessment indices in order to compare the three chosen hydrocarbon provinces as shown in Figure 3.13. These typical ranges of values only offer workable information for screening and ranking of the three provinces for possible time-lapse EM project. Various fields in each of the

provinces will have differing values which could assist to rank fields in a portfolio of projects in a particular province.

			HYDROCARBON PROVINCES			
SUB-CATEGORY	**ASSESSMENT INDICES**	**IDEAL**	**WEST AFRICA**	**GULF OF MEXICO**	**NORTH SEA**	**REMARK**
Reservoir properties	Cementation factor (*m*)	Low	Low	Moderate	Moderate	**West Africa**
	Saturation Exponent (*n*)	Low	Low	Low	Low	
	Oil wetness of the rock	Low	Low	Low	Low	
	Net-to-gross *(NTG)*	High	Moderate	Moderate	Low	
	Porosity (Φ)	High	26 to 30	21 to 34	16 to 23	
	Reservoir thickness (*in metre*)	High	15 to 45	30 to 45	4 to 12	
Formation water properties	Formation water Salinity (*ppm*)	High	40,000	190,000	200,000	**Gulf of Mexico and North Sea**
	Formation water Temperature (℃)	High	79	80 to 82	60 to 101	
	Formation water Resistivity (℃)	Low	0.08	0.02	0.02	
Sea water conditions	Sea water depth (*in metre*)	Deep	1,000 to 1,600	400 to 1,500	74 to 1,000	**West Africa**
	Sea water resistivity (*in* Ω*m*)	Low	Low	Low	Low	
Overburden conditions	Overburden ave. resistivity (in Ωm)	Low	Low	Low	Low	**West Africa**
	Depth to top reservoir (*in metre*)	Shallow	1,200 - 2,500	2,000 - 2,400	1,800 - 3,169	
EM	Optimum frequency (*in Hz*)	High	0.25 - 0.625	0.1 - 0.2	0.02 - 0.1	**West Africa**
	Survey repeatability	High	Low	Low	Low	
Total score for selected indices			39	38	31	
Technical chance of success (based on selected indices)			87	84	69	
Technical risks (based on selected indices)			13	16	31	

Figure 3.14: *Numerical scoring of some selected risk assessment indices for the West Africa, Gulf of Mexico and North Sea hydrocarbon provinces (Lumley, et al. 1997; Ellingsrud, et al. 2002; Ellis & Keirstead 2011; Figure 3.12 and some intuitive assignment of values). See text for full description.*

3.5 Interpretation of the technical risks for selected hydrocarbon provinces

Using Figure 3.13, it is observed that for reservoir properties, sea water and overburden conditions, and the EM, the West Africa province obtain highest passing scores, followed by the Gulf of Mexico, with the North Sea coming last. However, for formation water properties, the North Sea province has the highest mark followed by the Gulf of Mexico, with the West Africa coming last. In terms of reservoir properties and overburden conditions, all of the indices are favourable to West Africa province because of its relatively young geology (e.g. Tertiary Niger Delta), whereas the North Sea provinces are mostly of old geology, typically Permian and Jurassic ages. The Gulf of Mexico geological age ranges from Late Triassic to Holocene, which is in-between the ages of the West Africa and the North Sea hydrocarbon provinces.

Younger sediments generally are less consolidated and more porous, occurring at relatively shallow subsurface locations than the older rocks that have undergone extensive burial, digenesis, compaction and consolidation, thus with less porosity. This why the West Africa and the Gulf of Mexico provinces have better scores than the North Sea province in terms of the reservoir properties and the overburden condition. Similarly, because the North Sea geology has undergone a long period of subsidence, it has higher values for the formation water temperature and salinity, than those of the Gulf of Mexico and the West Africa. This yields low water resistivity values for the North Sea province and makes it favourable to the formation water properties. In terms of the sea water condition, the high sea water depth in the West Africa province makes it most favourable in terms of preventing possible 'air-wave' phenomenon in EM survey. The factors relating to the reservoir properties and overburden conditions, coupled with the sea water depth are all responsible for scoring West Africa province higher than other provinces in terms of the EM assessment indices, particularly the optimum frequency.

Overall, the West Africa province shows the least risk, thus highest technical chance of conducting a successful time-lapse EM project. Coincidentally, Girassol, where the first CSEM application to hydrocarbon exploration was carried out is considered as a West African oilfield. However, it should be noted that although the probability of conducting a successful time-lapse EM in the North Sea is the lowest of the three provinces assessed, modelling works using a producing oilfield in the North Sea yielded promising results. Also, repeatability is a common problem with the three provinces and hopefully this could be addressed in future whenever EM data could be acquired simultaneous with seismic data, using permanent sensors.

CHAPTER 4

TIMELAPSE 1D CSEM MODELLING AND NON-REPEATABILITY

"PGS does first simultaneous EM and 2D seismic survey." – EAGE (2014).

4.0 Introduction

Integration of time-lapse CSEM with time-lapse seismic and fluid flow simulation model for reservoir monitoring and updating of engineering model will be possible, whenever the CSEM and seismic dataset are repeatedly acquired simultaneously either by towed streamers, or better by permanent sensors over a producing oilfield, with high level of repeatability. Repeat seismic acquisition technology has advanced, and this has enhanced qualitative time-lapse seismic interpretation; but CSEM data acquisition technology for exploration purpose, on the other hand, is still very much in its infancy. In fact, there is no record of repeat CSEM data yet (Johnston 2013). This is why feasibility studies should be geared towards a good understanding of the three fundamental elements namely: repeatability, detectability and interpretability involved in any time-lapse geophysical (in this case, seismic and EM) applications to reservoir monitoring.

Repeatability has to do with the degree of similarity between the repeat surveys. It is a function of how consistent the acquisition geometry is, for the repeat surveys; how similar is the processing algorithm and workflow employed in treating the repeat datasets. In the case of repeat CSEM surveys, additional factors beyond the acquisition geometry and processing algorithm are the impact of sea water properties (salinity, temperature) and the complexity of geological background structure (overburden and under-burden) on the electrical resistivity. Detectability, on the other hand, is the magnitude of time-lapse geophysical response to the dynamic changes in the reservoir properties. In other words,

can the production and injection activities induce changes in the elastic and electric properties of rock? If yes, are these changes in the properties enough to be detected at the surface by the geophysical method? Finally, interpretability has to do with how appropriately the time-lapse data can be integrated with geological and engineering data.

The dynamic change in reservoir has to first be detectable before one can make any meaningful interpretation of it. So also, a significant level of survey repeatability is a prerequisite to detectable time-lapse signal. Therefore, interpretability is dependent upon both detectability and repeatability for good technical chance of successful time-lapse geophysical monitoring of reservoir. Also, business objectives should equally be considered in making decision on repeat surveys. These three elements are described by Johnston (2013) for the seismic case. Figure 4.1 shows the relationship between these elements and the technical chance of success (TCS).

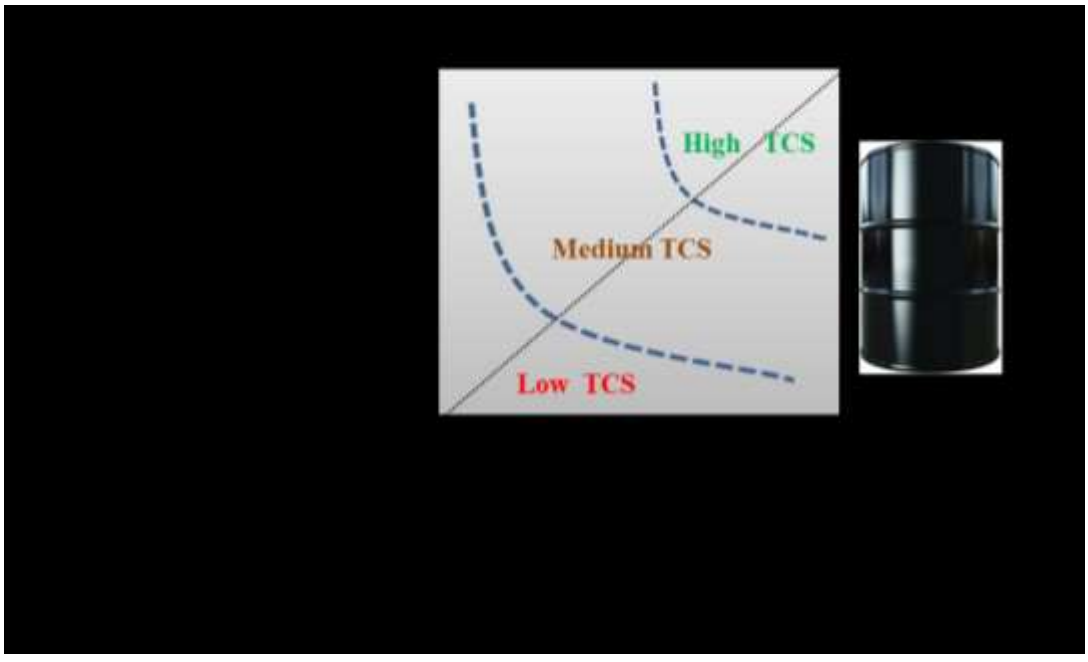

Figure 4.1: *Technical chance of success (TCS) and interpretability increase with increasing detectability and repeatability. Decision to conduct repeat survey is also driven by the business objectives in terms of what additional income (say in dollar per barrel) could be generated based on the value of information at the current oil price (adapted from Johnston, 2013).*

The main focus of this Chapter is to assess the impact of sea water properties variations and background complexity as elements of repeatability on the time-lapse CSEM survey results. Sea water properties variations and background complexity are very important in CSEM exploration (e.g. Ellis & Keirstead, 2011), and it is important to know how they affect time-lapse CSEM for reservoir monitoring. The uniqueness of this work is it is reservoir simulation driven. Thus, we first establish the workflow for the simulation to electromagnetic modelling, which is incorporated into the popular simulator to seismic modelling (e.g. Amini et al. 2012; Johnston 2013).

4.1 Methodology and workflow for coupled simulator to seismic and EM forward modelling

The methodology for the coupled simulator-to-seismic (sim2seismic) and simulator-to-EM (sim2EM) modelling requires integration of datasets obtained from different sources. One may either start from the geological model, or use an already made simulation model directly. Then, the static and dynamic reservoir properties are extracted from the simulator as input parameters to calculate 3D elastic and electric resistivity distributions for each time step, using the elastic and electric rock physics models. These processes are called sim2imp and sim2resist respectively. Both elastic impedances and electrical resistivity could then be visualized together for different time steps using a suitable tool like the commercial software, Petrel, or even Matlab.

Next is the CSEM modelling. Usually, our earth is viewed as a three dimensional feature, but in geophysical analysis, a one dimensional modelling could serve as a preliminary step in examining the sensitivity of geophysical tools to the earth properties of interest before embarking on the three dimensional modelling. 3D reservoir simulation is combined with 1D CSEM modelling here. Using Dipole 1D code of Key (2009), pseudo – logs of resistivity versus depth for all the *x*- and *y*- surface locations are extracted for each dynamic time step. The resistivity values from the wireline well logs are then used to calibrate the resistivity distribution within the reservoir, and to obtain probable background resistivity structure (overburden and underburden). For the seismic, pseudo – log extraction of the elastic impedance and convolution with Ricker wavelet are performed to obtain seismic

modelled data for different time steps. Amini et al. (2012) described sim2seis workflow in detail. The full workflow for coupled sim2seis and sim2EM is schematically described in Figure 4.2.

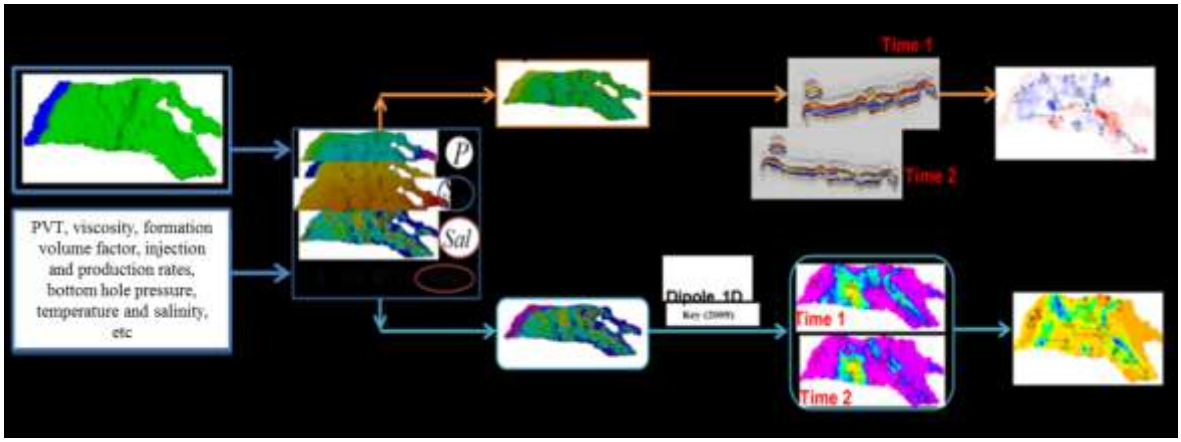

Figure 4.2: *A coupled workflow for simulation-to-seismic (sim2seis) and simulation-to-EM (sim2EM) modelling. The original sim2seis workflow, into which the sim2EM is embedded, is described by Amini et al (2012). Archie (1942) model is modified for the sim2resist while 1D dipole code of Key (2009) is used to run resist2EM modelling. Salinity and temperature are tracked in Chapter 6.*

4.2 3D synthetic reservoir: sim2resistivity and sim2EM modelling

Before we look into a more practical example of an industrial – built, history – matched and updated reservoir model in Chapter 5, it is important to consider a small, simple and geologically consistent model built using the properties of a North Sea oilfield. This offers a quick check on the EM forward modelling workflow. This is preparatory to the more complicated real field complicated example, where EM is integrated with seismic. In this section, a workflow involving geological modelling, petrophysical modelling and fluid flow reservoir modelling are followed step by step, as a combination of prerequisites to the EM forward modelling.

4.2.1 Geological and petrophysical modelling

The synthetic reservoir model under consideration is an analogue of a heterogeneous deep-water turbidite system on the UK continental shelf containing sand channels interbedded with shale layers. The 3D reservoir model has dimension 2025m by 2025m by 50m in the X, Y and Z directions, and the depth to the top reservoir is 1900m.

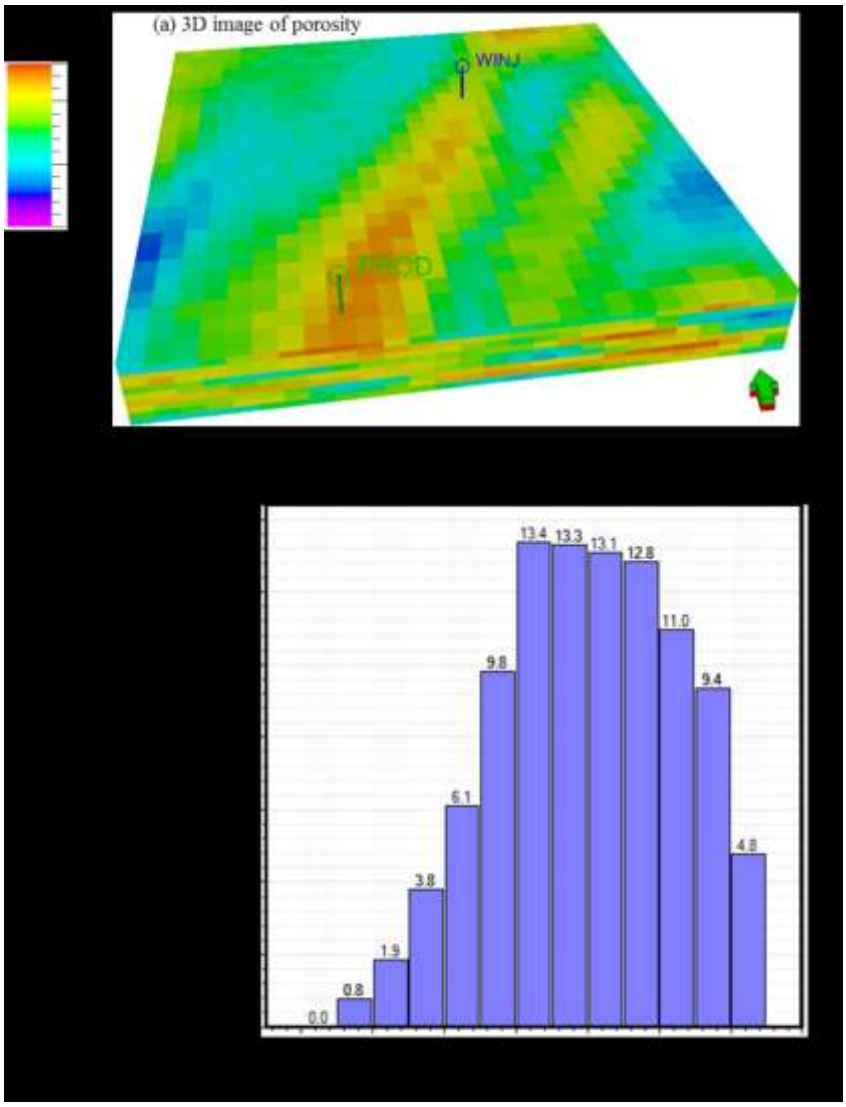

Figure 4.3: *(a) 3D Image of reservoir porosity showing the sandstone channels, with minimum and maximum values of 0.209 and 0.325 respectively. A water injector and an oil producer are situated at the opposite ends diagonally. (b) Histogram of porosity showing the percentage occurrence of the various porosity values. The highest proportion of porosity lies between 0.26 and 0.30.*

The reservoir is gridded into 27 by 27 cells in the X and Y directions, and 10 layers in the Z direction, making a total number of 7290 cells, with each cell having a dimension of 75m by 75m by 5m.

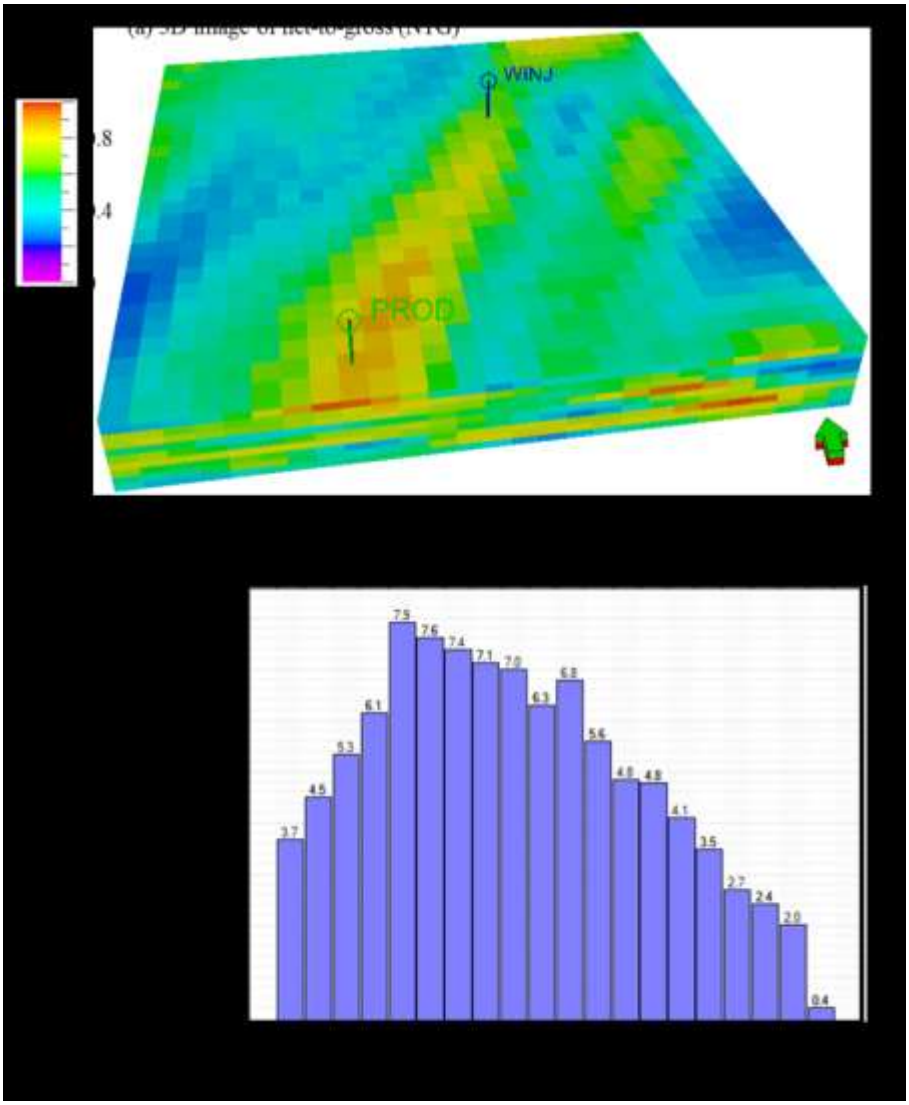

Figure 4.4: *(a) 3D Image of reservoir NTG showing the sandstone channels, with minimum and maximum values of 0.203and 0.98 respectively. (b) Histogram of NTG showing the percentage occurrence of the various NTG values. The highest proportion of NTG lies between 0.38 and 0.64.*

The model is populated with geologically consistent petrophysical properties using Gaussian geostatistical distibution functionalities in the commercial software (Petrel), which is a good distribution to model channelized sandstone reservoirs. Figure 4.3 and Figure 4.4 show the 3D image and histogram of porosity, and of net-to-gross (NTG) respectively. The sand rich channels have a porosity of between 0.25 and 0.30, and NTG of

between 0.7 and 0.9. The horizontal permeability along X direction is similar to that along Y direction, and it ranges between 90mD and 907mD. Along Z direction, the permeability is about ten times lower, that is, between 9mD and 99mD as shown in Figure 4.5.

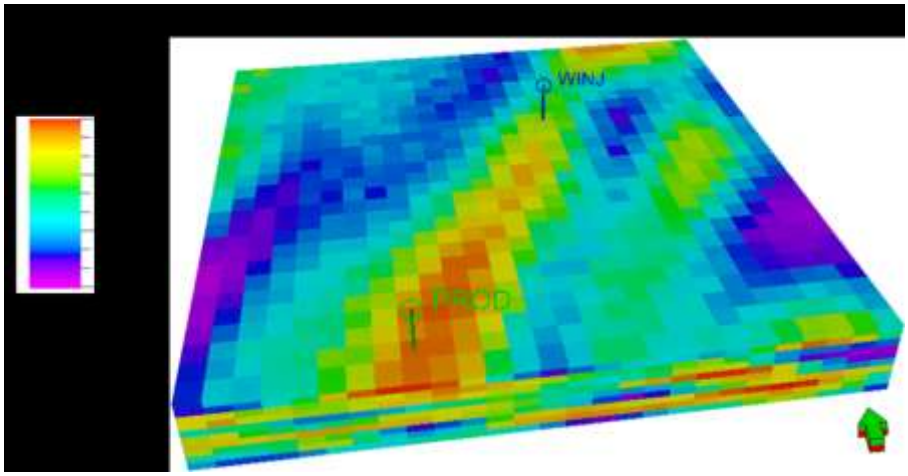

Figure 4.5: *3D Image of reservoir permeability showing the channels, with minimum and maximum values of 90mD and 907mD respectively. A water injector and an oil producer are situated at the opposite ends diagonally and there is no potential barrier to fluid flow in this direction. This distribution is similar for the x, and y directions, but ten times less magnitude for the z-direction.*

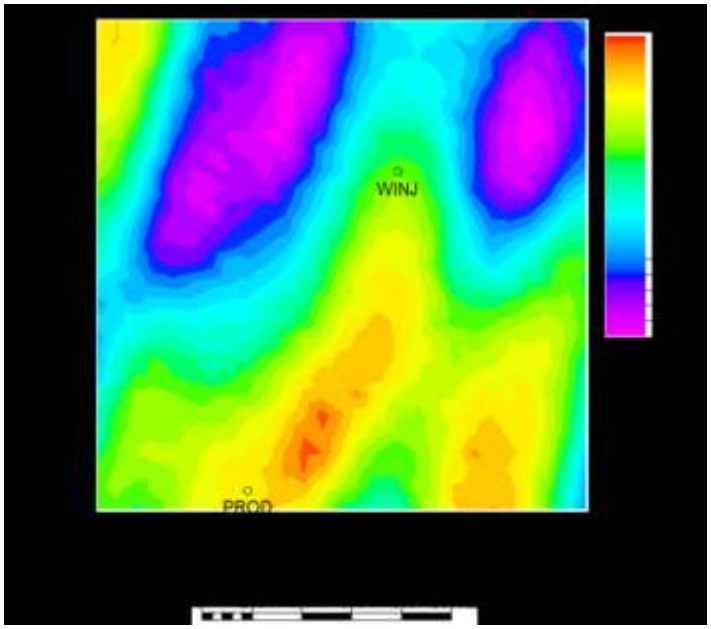

Figure 4.6: *2D map of porosity, with value ranging from 25% to 30% within the modelled oil leg of the reservoir. A water injector and an oil producer are situated at the opposite ends, diagonally, of the major high porosity sand channel.*

The reservoir model is built to demonstrate production in an oil leg with initial connate (irreducible or formation) water saturation of 0.18 (i.e. oil saturation of 0.82). As the reservoir has sufficient permeability, there is no barrier to fluid flow within the sand channels. The 2D map of reservoir porosity is shown in Figures 4.6. The net-to-gross maps looks the same as the porosity map.

4.2.2 Reservoir simulation modelling

The commercial finite difference reservoir simulator, Eclipse 100, is utilized to perform 3D fluid flow simulation of reservoir containing oil, soluble gas and water. This enhances practical realizations of oil production and water injection activities. The static geological model (grid and reservoir properties) is exported directly into the simulator without mathematical up-scaling, thus the original grid block and cell dimensions for the geological model are used for the fluid flow simulation modelling. The hard engineering data for the North Sea producing turbidite reservoir, such as the capillary pressure, relative permeability and the PVT properties supplied by an industrial sponsor, are borrowed for the synthetic fluid flow simulation. Water flooding and oil production are scheduled with one well each for ten years with a time step of one year. The pre-production baseline model stands for discovery in August 2012, while production and injection activities are simulated for monitor models from August 2013 to August 2022. The oil production well is completed within the high porosity, high NTG sand while the water injection well is placed at a far end from the oil producer (as shown in Figures 4.3, 4.4 and 4.5), within a less porous and lower NTG sand to enhance efficient oil sweep, and avoid early water breakthrough at the producer.

In this modelling, it is assumed that there is neither solution gas drive, nor aquifer support; thus oil production is mainly driven by water injection from inception. The bottom-hole pressure at the oil producer is 2850psia (see Figure 4.7a), this is assumed to be above the bubble point pressure of the reservoir. In order to avoid pressure drop at the producer and thus gas coming out of solution, water injection was initiated at pressure of 4150psia, which drops suddenly to 4000psia due to initial production at the producer.

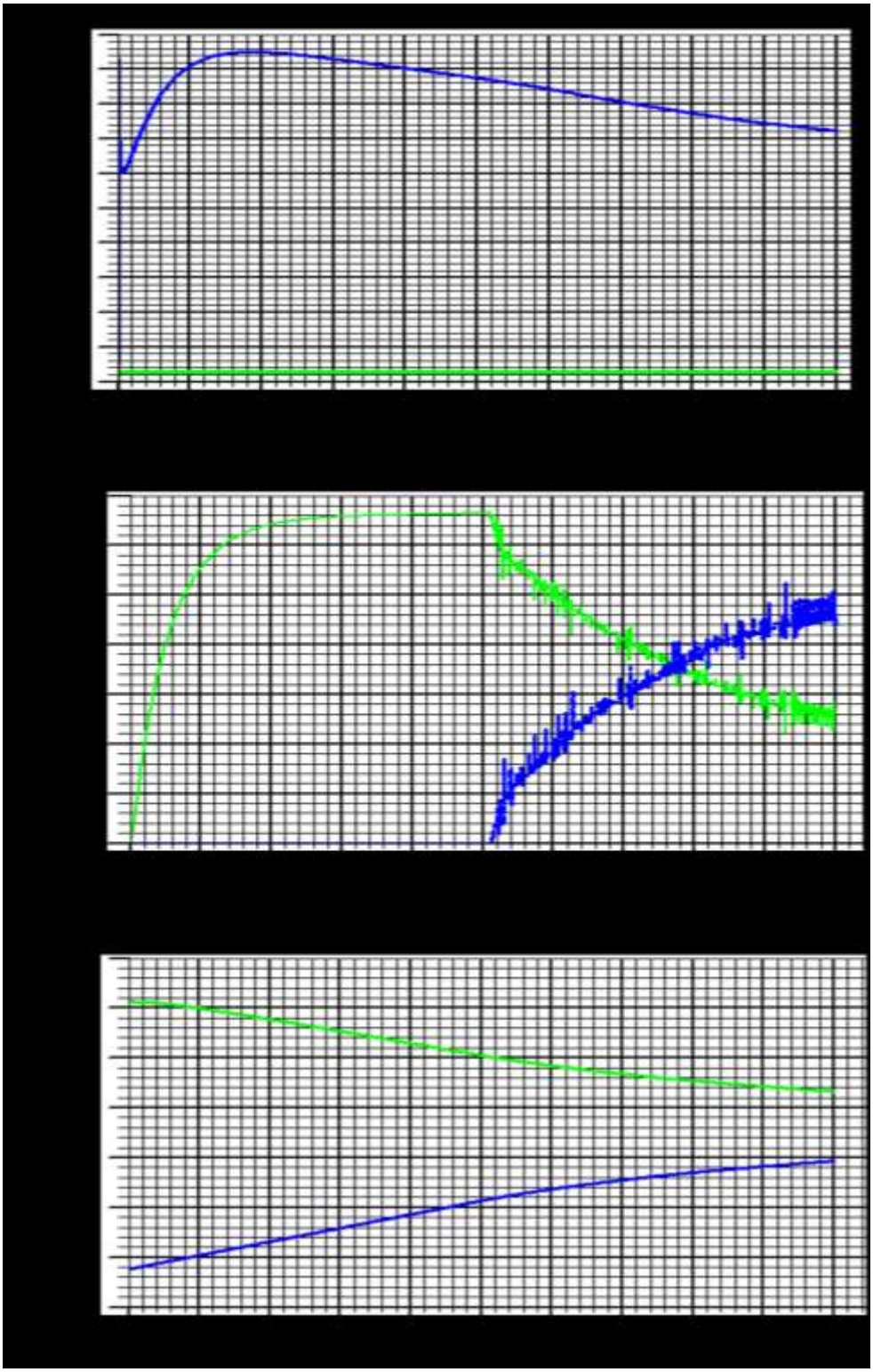

Figure 4.7: *(a) Well bottom-hole pressure for water injector and oil producer; (b)Field fluid production* and *(c)Field fluid in place, as a function of time. Water and oil are represented in colour blue and green respectively. See text for detail description of the graphs.*

The reservoir pressure is continually kept above the bubble point pressure. The pressure at the injector increased to about 4700psia for the first two years of production, and then gradually falls. However, during this period, the bottom-hole pressure at the injector is above 4200psia such that there is no gas ex-solution for the simulated period of production and injection activities. Oil production rate per day increases until after two years of production when it remains steady on a plateau for another three years before the production started declining, first a sudden drop, then a gradual decrease with time. During the first five years period, water injection proceeds but there were no water production at the producer. A sudden drop in oil production brought about water production at the producer, which increases until there is water breakthrough after five years (see Figure 4.7b). The field oil in place reduces, as the field water in place increases throughout the simulated period (Figure 4.7c).

4.2.3 Simulator to resistivity (sim2resistivity) modelling

Using the workflow described in Section 4.1 (the lower part of Figure 4.2), the 3D resistivity of the reservoir is calculated from the simulator using Equation (3.7) in Chapter 3. Standard Archie's constants a = 1, n = 2 and m = 1.8 for this field are used. It is worth nothing that the log section provided does not contain water saturated sand section, from which some of the Archie's parameters could be directly estimated. Formation water resistivity (R_w) is calculated to be 0.2Ωm within the area of interest in Figure 3.2 using Equation 3.13 and the values of temperature (58°C) and salinity (18,000ppm) at that location as given by the operator of the analogue oilfield. Figure 4.8 shows the 10 resistivity "depth-slices" for the baseline reservoir model, which ranges in value from 23Ωm to 48Ωm. However, we expect the CSEM to illuminate the cumulative effect of these resistivity slices at the surface, in form of transverse resistance as shown in Figure 4.9. The value of transverse resistance ranges between 1410 Ωm^2 and 1990 Ωm^2, which for the 50 m total thickness of the reservoir equates to bulk average resistivity of between 28.2 Ωm and 39.8 Ωm. On the other hand, the average background resistivity is 2.45Ωm (see Figure 4.12b) and the effective transverse resistance over the same 50m interval in the background is 122.5Ωm^2. Therefore, the reservoir has effective transverse resistances and

average resistivities that are considerably greater than those of the background values, thus making the reservoir layers anomalously resistive compared to the host background.

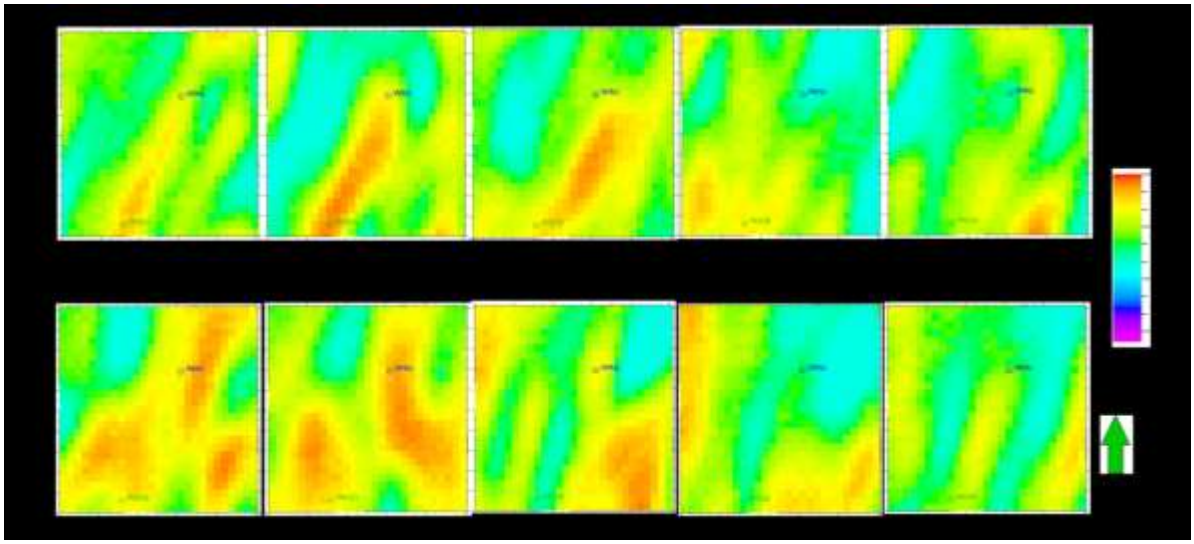

Figure 4.8: *Resistivity depth-slices for the baseline model showing the channels and the position of water injector and the oil producer. Slice 1(top left) is the shallowest 5m top layer while slice 10 (bottom right) is the deepest 5m bottom layer.*

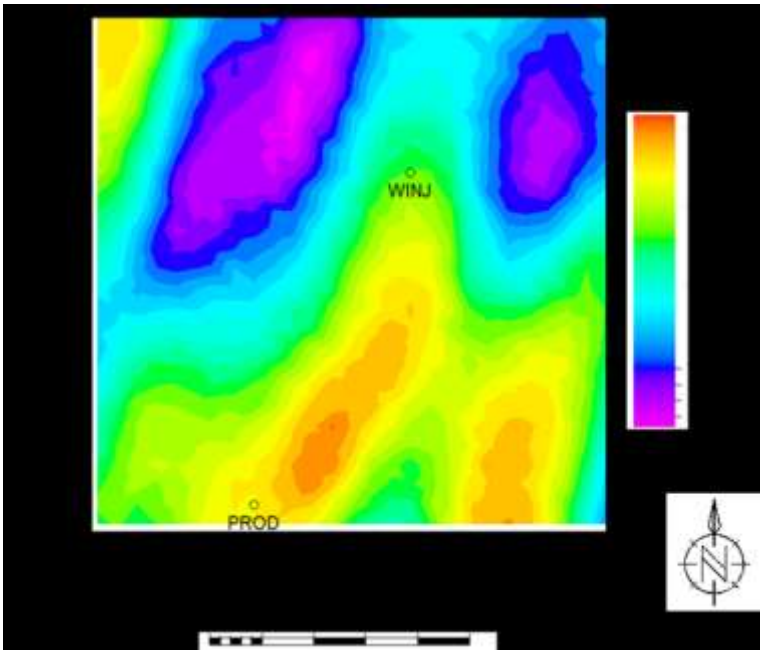

Figure 4.9: *Pre-production (baseline) map of transverse resistance for all the slices showing the oil filled high net-to-gross sand channels with high transverse resistance at the bottom, and the low net to gross channels at the top with low oil saturation. Water injector is inserted at the top to drive the oil towards the producer.*

4.2.4 Resistivity to EM (resistivity2EM) modelling

The modelling is based on the assumption of in-line CSEM acquisition geometry, which has the most sensitivity to reservoir structures. This is in agreement with the electric rock physics described in Chapter 3. In this geometry, the resulting signals are preferentially sensitive to the vertical resistivity of the reservoir, containing lamina layers of sands and shales. Parameterisation of the CSEM modelling involves accounting, as much as possible, for the resistivities and thicknesses of all the earth materials encountered by the EM source energy including the sea water, the background structure which consists of the overburden and the underburden, and the reservoir target itself. Figure 7.1a (Chapter 7) describes the process of pseudo-log extraction of reservoir resistivity-depth profile, which is fed into the Dipole 1D CSEM modelling code.

4.3 Discussion of non-reservoir features in EM modelling

Here, we first discuss the two main non-reservoir features (the sea water and the background structure) considered in forward modelling of EM from resistivity, as pertaining to non-repeatability of time-lapse modelled data.

4.3.1 The sea water resistivity profile

Variation in sea water resistivity with depth, and its seasonal fluctuation may have direct effects on the repeatability of time-lapse data. Sea water resistivity depends both on the salinity and temperature profiles with respect to water depth (WD). In an open sea, water salinity value varies negligibly except in Mediterranean region or in situation whereby fresh water is flowing into the sea (Constable 2013). Thus the salinity of the sea water could be assumed to be fairly constant with respect to water depth, say around 30,000ppm of *NaCl* solution for this example (as provided by the field operator's petrophysicist, for the injected sea water used in the analogue oilfield). This is unlike the temperature, which varies with water depth, especially for water depth less than one kilometer (Bertrand 2005; Constable 2013). Usually sea water temperature between the sea surface and the sea bed, is stratified into the mixed layer, thermocline section and deep layer, based on the vertical thermal

structure within the water column (Bertrand 2005). This stratification varies from one season to another (e.g. summer to winter) and from one geographical location to another (e.g. from the North Sea to the Meditteranean Sea). Bertrand (2005), while studying the effect of varying sea water temperature on the seismic wave velocity, gave a good account of this thermal structure. He stated that the thermal structure varies with the external influences such as the oceanic currents (or waves), solar energy radiation and wind. For instance, the higher the intensity of solar radiation during summer, the deeper the water column being heated up, due to deeper vertical penetration of the elevated temperature. Thus, the temperature generally reduces with depth resulting in a negative thermal gradient within the water column during summer. During winter, different thermal structure exists and this varies for different locations.

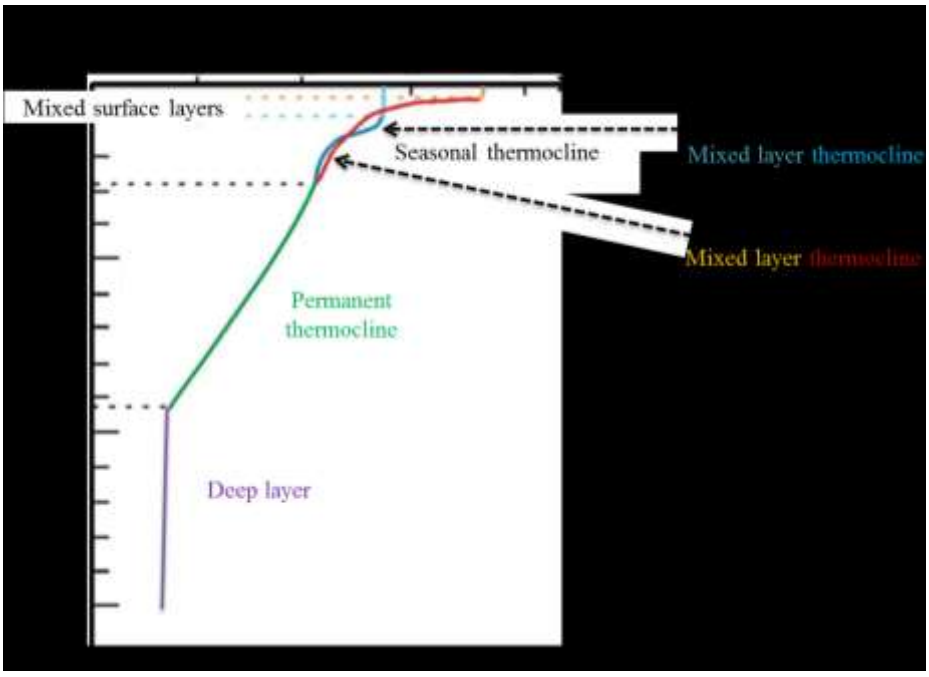

Figure 4.10: *Generalized temperature – depth profile for summer and winter seasons (from Bertrand 2005).*

However, there is usually a permanent thermocline section for both the summer and winter seasons as shown in the generalized example of thermal structure in Figure 4.10. Table 4.1 also shows examples of temperature – depth structure for Mediterranean Sea, East Atlantic and Shetlands where our field analogue is located, with an average water depth of 400m (Meadows, et al. 2005, Martin & MacDonald, 2010).

Table 4.1: *Temperature profiles for the Shetlands, East Atlantic and Mediterranean Sea (from Bertrand, 2005). The analogue field example in this thesis is located in the Shetlands, where there is no seasonal thermal gradient.*

Except in the mixed water layers and seasonal thermocline session, where there are some variations in thermal structure before the onset of permanent thermocline; there is no marked difference between the summer and the winter temperature profiles. The static vertical depth – temperature profile below seasonal thermocline is the same for both seasons.

Now, to establish static resistivity – depth profile, let us assume for simplicity that the repeat surveys are carried out every summer around the month of July/August when the average sea surface temperature is 15°C. Combining the Shetlands profile in Table 4.1 with various Equations in Chapter 3 relating temperature – salinity – resistivity, we can obtain the sea water resistivity profiles as shown in Table 4.2. Figure 4.11a shows the sea water temperature – depth profile while Figure 4.11b shows the comparison of Crain (1986)'s relation (equation 3.17) for the actual salinity of 30,000ppm in red coloured solid curve, and for a salinity of 35,000ppm in green coloured solid curve, with the relation proposed by Constable et al (2013) (equation 3.13) which is independent of salinity, in green coloured broken line. The disparity in these profiles calls for caution as to which of the equations should be employed to generate sea water resistivity – depth profile to be used in CSEM modelling.

			Crain (1986) @Salinity of 30,000ppm	Crain (1986) @Salinity of 35,000ppm)	Constable et al (2009)
	Water Depth (m)	**Temperature (°C)**	**Resistivity (Ωm)**	**Resistivity (Ωm)**	**Resistivity (Ωm)**
Water Surface	0	15	0.270144617	0.23587567	0.232914896
Mixed layer	20	7.5	0.339543999	0.29647145	0.27966353
Termocline section	120	6.96	0.346057991	0.30215912	0.283626499
	220	6.42	0.352844911	0.30808509	0.287683559
	320	5.88	0.359922676	0.31426501	0.291837799
Total Water depth	400	5.88	0.359922676	0.31426501	0.291837799
Average Resistivity			0.338072812	0.29518689	0.277927347

Table 4.2: *The modelled vertical resistivity profile (structure) of the sea water in the analogue field example(at the Shetlands area) for Crain's relation (1986) (equation 3.17) at salinities of 30,000ppm, and salinity of35,000ppm of NaCl solution, is compared with Constable et al (2009)'s relation which is independent of the salinity (equation 3.13).*

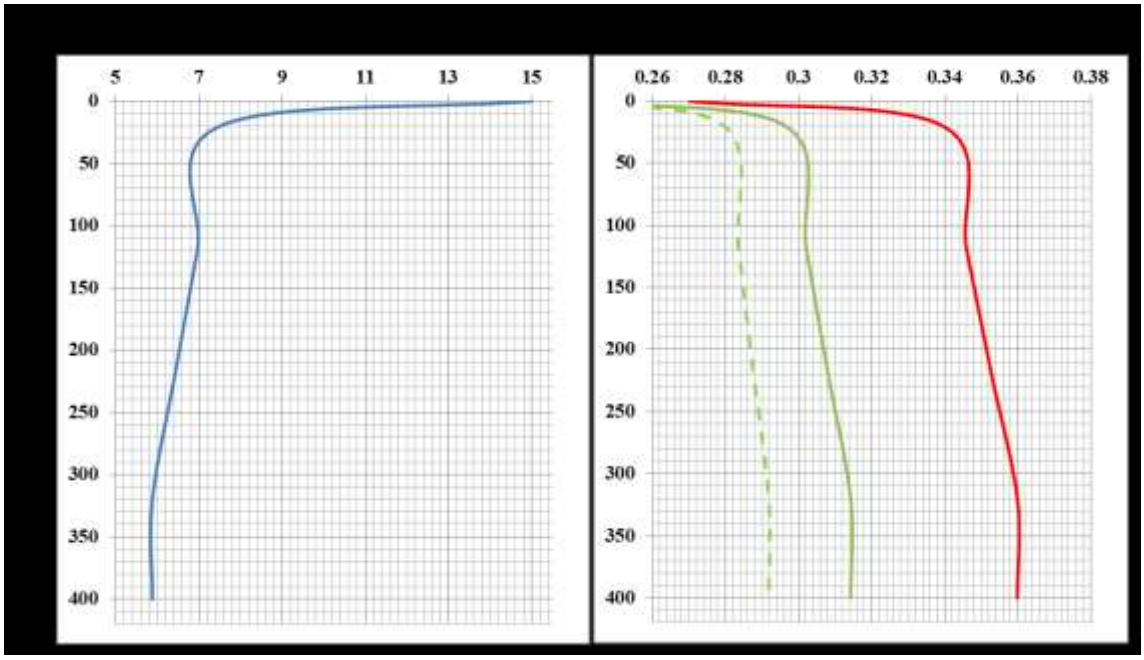

Figure 4.11: *(a) Sea water temperature profile characteristics of the project area; (b) Resulting sea water resistivity profiles. The solid red and green curves are obtained using equation 3.17 (Crain's relation, 1986) at salinities of 30,000ppm and 35,000ppm respectively, while the broken green curve is obtained using equation 3.13 (the salinity independent relation given by Constable et al. 2009).*

The salinity – independent equation of Constable et al (2009) is believed to have assumed the salinity of 35,000ppm of total dissolved solid (not *NaCl* solution equivalent, as we do not know the exact constituent ions). This is why the Crain's relation at salinity of 35,000ppm *NaCl* solution is closer to this profile than at 30,000ppm. The Crain's profile at salinity of 30,000ppm is used to parameterize the sea water resistivity structure as it is consistent with the petrophysical information within the reservoir section as supplied by the field operator. Conductivity – Temperature – Depth (CTD) data could also be obatined in real situation.

4.3.2 The background resistivity structure

In order to account for the background resistivity structure outside the reservoir, a resistivity profile as a function of depth including both the overburden and a section of the underburden is obtained from the resistivity log at a well location (from a vertical well). Ordinarily, in this 1D modelling, we require the vertical (interval) resistivity profile rather than the horizontal resistivity usually obtained from the resistivity logs in a vertical well-bore, but there is no other available source of information. This is because anisotropic (vertical and horizontal) resistivity measurements are rarely made, and even when they are made, it is usually restricted to the reservoir interval rather than the overburden and underburden sections (MacGregor & Tomlinson, 2014). Figure 4.12a shows the schematic profile describing both vertical and horizontal anisotropic resistivity measurements needed for full 3D modelling. 3D full inversion of CSEM dataset in the field or nearby field could provide an estimate of both measurements but this, unfortunately, is not available. Thus, for this modelling work, isotropic condition is assumed and that the vertical resistivity of the background structure could be fairly represented with the horizontal measurement from the resistivity log. Log measurement in the well starts from 1.12km below the sea bed, therefore between the seabed and the start of log measurement, an extrapolated value of 2Ωm is used. Figure 4.12b shows the actual profile of vertical interval thicknesses versus background horizontal resistivity measurement, referenced to the sea-surface. This background structure is assumed to be constant with time. Of course, except when there is an injection of conductive or resistive fluid into the overburden or there is a sudden change in overburden porosity due to compaction between the baseline and monitor surveys, we do

not expect any change to the background resistivity structure. The ten-layered, 50m thick synthetic reservoir section is inserted within the interval 1.9km and 1.95km below the sea bed (i.e. 2.3km and 2.35km below sea surface). We will now examine the impact of both the sea water resistivity stratification as against single resistivity representation of sea water, and the subsurface background resitivity structure on the qualitative interpretation of time-lapse CSEM modelled data.

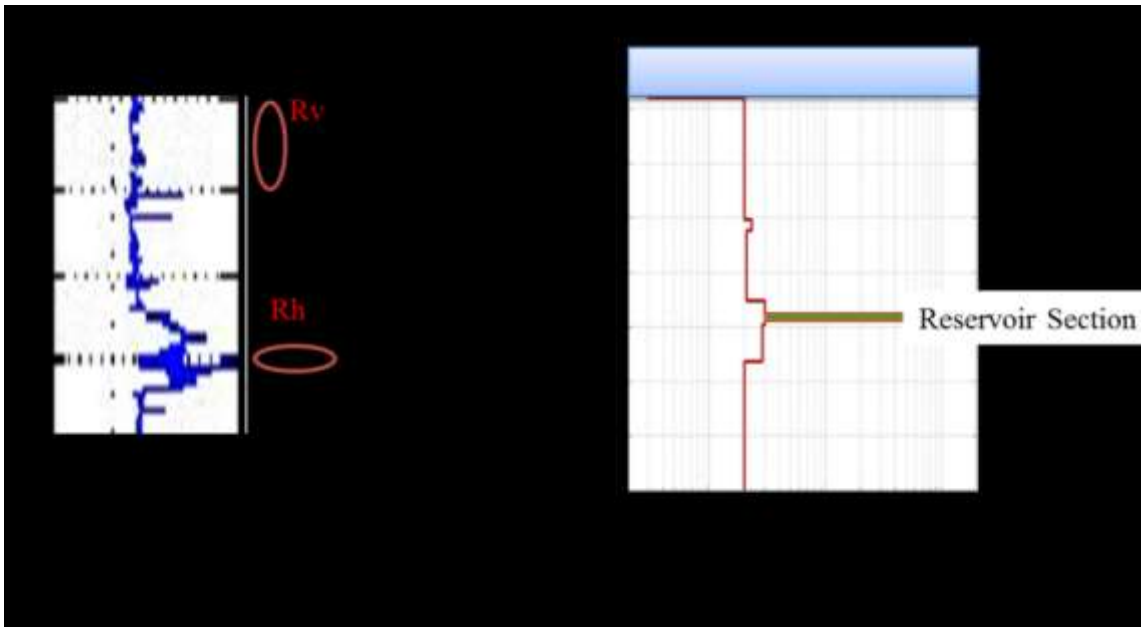

Figure 4.12: *(a) Schematic representation of ideal anisotropy measurement of vertical resistivity (R_v) and horizontal resistivity (R_h) required to properly parameterize the background resistivity structure for forward modelling of CSEM data; (b) Profile of background horizontal resistivity (R_h) versus vertical depth obtained from a resistivity well log of the analogue field example. Average background resistivity is 2.45 Ωm, while that of the reservoir ranges between 28.2Ωm and 39.8Ωm.*

4.4 The impact of seawater resistivity stratification and background resistivity structure on CSEM signal responses

Having established some facts about the sea – water resistivity profile and the background resistivity structure, we can now examine their non-repeatability impact on the illuminating eyes of time-lapse CSEM to monitor changes in water saturation in an oil producing reservoir undergoing water injection. To do this, we consider the synthetic model for pre-

production baseline (zero year), and two monitor models – 2 years and 5 years after oil production and water injection have proceeded. During these periods, water saturation is increasing due to water injection, and after 5 years of oil production, sudden drop in oil production coincided with the beginning of water production at the producer (see Figure 4.6b and c).

Four scenarios are modelled. First, is the real field situation with possible complications in the sea water and overburden structure. Second, is a situation with homogeneous sea water having an average single – resistivity value over the entire water depth (i.e. uniform thermal structure) but retaining heterogeneity in the subsurface background resistivity structure. The third scenario is a situation whereby the sea water resistivity is heterogeneous (i.e. non-uniform thermal structure) but homogeneous overburden and underburden structure. The fourth scenario is a situation whereby both the sea water and the 1D background structure are treated as homogeneous. All of these scenarios will also cater for our understanding of seasonal change in temperature, thus change in resistivity of sea water.

4.4.1 Scenario one: Complicated model

(a) Frequency-offset-signal analysis

Frequency-offset-signal analysis is an important step in any pre-survey planning and strategy for designing optimum field data acquisition for exploration purposes. It becomes more important for time-lapse studies because time-lapse signals are coming from a more localised region of the reservoir, and getting this signal requires optimum frequency and offset. This will assist further signal analysis, mapping and interpretation of field data, or modelled data in this case. To do this, we take resistivity - depth profiles from a location in the field where there is a change in resistivity between the pre-production and the post-production models. This location, at coordinate 1200 m on the X-axis and 975 m on the Y-axis, is shown with a black dot on the map of a monitor transverse resistance in Figure 4.13. The transverse resistance in this monitor (5 years after production) ranges between 180 Ωm^2 and 1990 Ωm^2 which is equivalent to average resistivity of between 3.6Ωm and 39.8Ωm for the 50m thick reservoir section. The lowest value of 3.6Ωm, for the water

flooded area, is still slightly higher than the background average resistivity of 2.45Ωm (i.e. 122.5Ωm^2 transverse resistance). Compare this with Figure 4.9 for the baseline map of transverse resistance and note the transverse resistance colour-bar scale graduation in the two Figures (i.e. 4.9 and 4.13). The lower limit of transverse resistance in the baseline model has reduced from 1410 Ωm^2 to 180 Ωm^2 in the monitor model due to water flooding, thus scaling the two models (baseline and monitor) on a similar colour-bar becomes impractical.

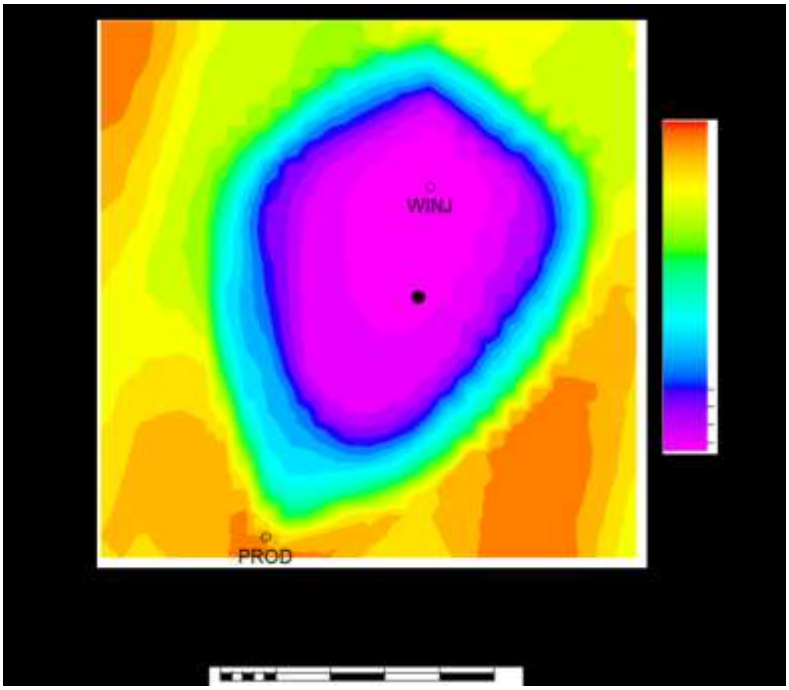

Figure 4.13: *Post-production (monitor) map of transverse resistance showing the location at which resistivity-depth profiles were taken for both the baseline and monitor models (the black dot at coordinate 1200m on the X-axis and 975m on the Y-axis). See text for detail.*

The resistivity profiles extracted at this location for the base and monitor models are shown in Figure 4.14. The baseline (pre-production) resistivity profile (green colour), which is between 28 Ωm and 44 Ωm, is about 7 to 11 times greater than the monitor (water-flooded) resistivity profile (blue colour), which is between 3 Ωm and 4 Ωm. So, we expect a significant change in the CSEM response between the baseline and monitor models. It is also worth-noting that water-flooded resistivity is still slightly higher than the background average resistivity of 2.45 Ωm.

The CSEM data are then forward modelled for the two resistivity profiles, with stratified sea water resistivity and inhomogeneous background resistivity structure parameterised into the model. The survey layout is such that the transmitter dipole is towed 25 m above the seafloor and parallel to the single receiver dipole deployed on the seafloor. The source – receiver spacing (offset) increases by 500m from zero up to 15 km. Sixteen transmitting frequencies at equal logarithmic interval between 0.01 Hz to 10 Hz inclusive were used.

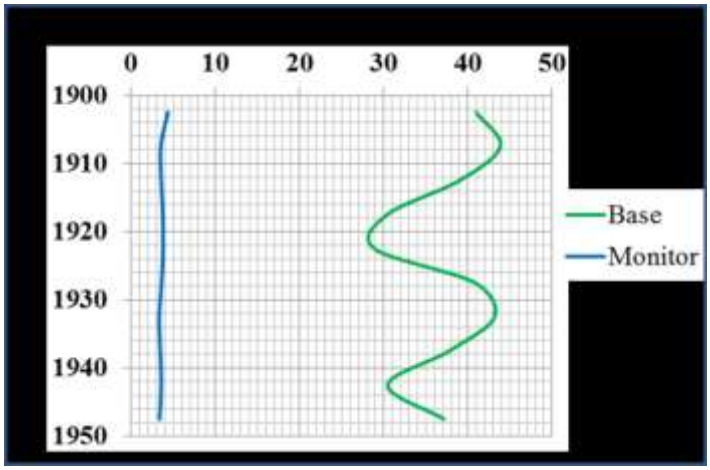

Figure 4.14: *Pre-production (baseline) and post-production (monitor) resistivity-depth profiles at the chosen surface coordinate 1200 m on the X-axis and 975 m on the Y-axis (indicated with black dot in Figure 4.13). See text for detail.*

Figure 4.15 shows the absolute EM amplitudes profiles, for an inline electric field, plotted against the logarithm of frequencies for some chosen offsets (between 5km and 11km at 1km interval), both for the baseline (continuous lines) and monitor (broken lines) models. The baseline signal is higher than that of the monitor as expected. Both signals are measurable and quite significant, they are recorded on the scale of 10^{-12} V/Am^2, and are much higher than the usual noise floor of between 10^{-14} V/Am^2 and 10^{-15} V/Am^2 for current CSEM acquisition technology (MacGregor & Tomlinson, 2014). This is important as both the baseline and monitor signals should first be detectable before we can carry out time-lapse analysis.

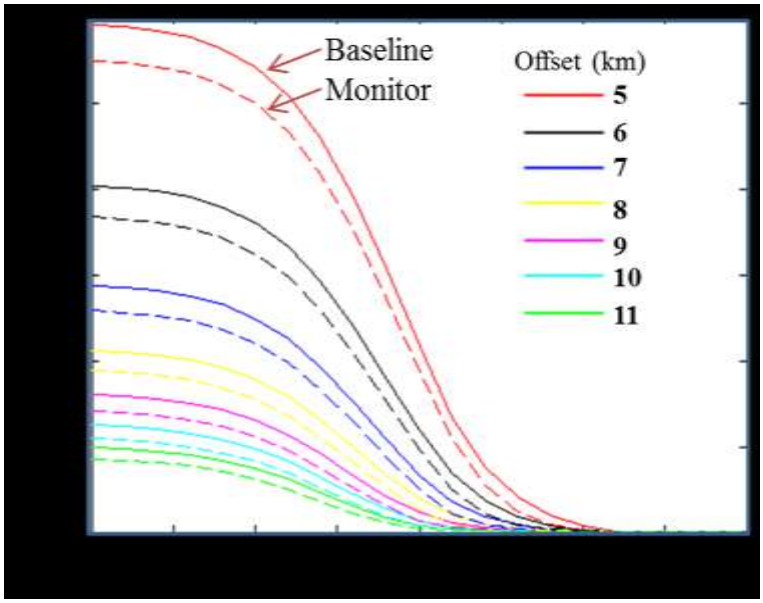

Figure 4.15: *Absolute EM amplitude for an inline electric field component, plotted as a function of log frequency, for some chosen offsets. Continuous lines represent the baseline profile, while the corresponding broken lines with similar colour represent the monitor model.*

The normalised percentage change in the EM amplitude between the monitor and the baseline data is calculated using Equation (4.1):

$$\Delta A_{EM} = 100 \times \left(\frac{A_{EM}^{Monitor} - A_{EM}^{Base}}{A_{EM}^{Base}} \right) \% \; ; \tag{4.1}$$

where ΔA_{EM} is the normalised percentage change in the EM amplitude for any chosen EM field component between the monitor and the baseline.

We can also look at the change in phase using Equation (4.2):

$$\Delta \phi_{EM} = \phi_{EM}^{Monitor} - \phi_{EM}^{Base} \; ; \tag{4.2}$$

where $\Delta \phi_{EM}$ is the phase change between the monitor and the base. These equations could also be applied between any two chosen monitors, and for any chosen EM field component.

The aim at this stage is to determine the optimum frequency-offset combination for time-lapse signal analysis. Thus, the normalised percentage change in the EM amplitude for an inline electric field component, is plotted as a function of logarithm-of-frequency and offset as shown in Figure 4.16a and b (essentially the same but interchanging the axes for better observation).

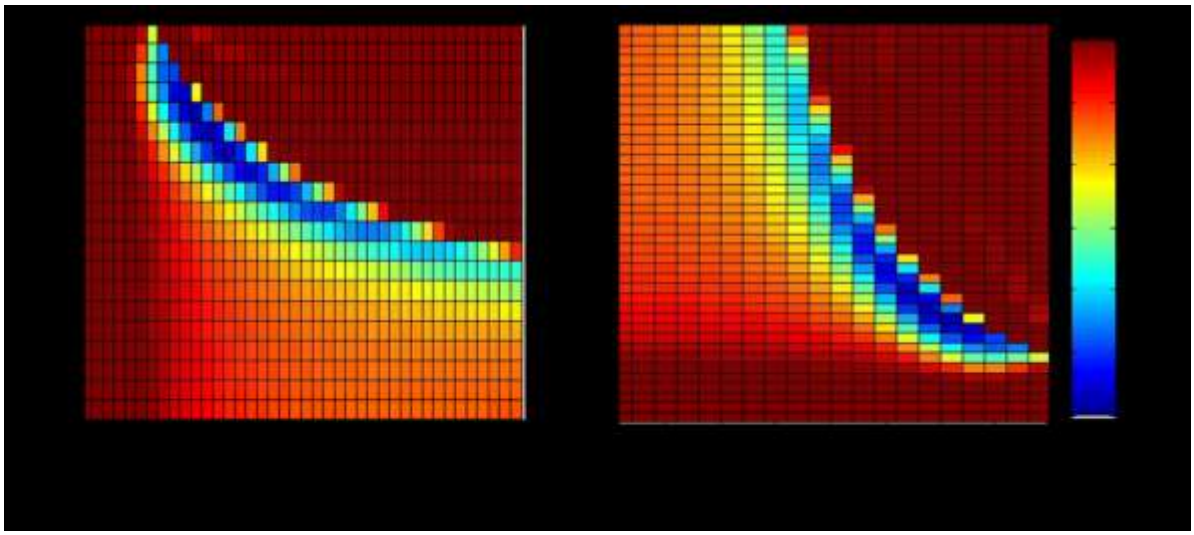

Figure 4.16: *Plot of percentage change in inline electric field amplitude between the baseline and monitor profiles (after 5years of production and injection), as a function of frequency and offset, for (a) offset on the x-axis while log frequency on the y-axis, and for (b) log frequency on the x-axis while offset on the y-axis.*

The amplitude change is as high as 60%, and substantially detectable with the current CSEM acquisition technology, with an expected non-repeatable noise of say, 5% (Constable, 2010). Although this encouraging 1D result is not consistent with the 3D situation as shown in Chapter 7. The negative change is an indication of conductive water replacing resistive oil, thus reducing the magnitude of electric field normalised with the current dipole (measured in V/Am^2). It could be observed from Figure 4.16a and b that, for logarithm-of-frequency below -1.1 (i.e. frequencies smaller than 0.08Hz), the signal strength and resolution are weak. Also, for offsets lower than 4km, there is no signal at all, just as the signal resolution and strength significantly fall beyond 14km offset. For optimum time-lapse analysis, we desire a frequency-offset combination that will offer good signal strength and resolution. However, there is usually a trade-off between signal strength and resolution, as several frequency – offset combinations could yield different

combinations of signal strength – resolution. Thus a balance has to be established, which is sometimes subjective.

As we know, a fairly long offset is likely to produce signal strength more representative of the deep-seated reservoir condition than the short offset which is more affected by the near surface structure; although we also need a reasonably high frequency that will help with good signal resolution. However, high signal strength for a deep-seated reservoir is usually accomplished with low frequency, as much of the high frequency would have been attenuated by the near surface heterogeneous and anisotropic structure. This means that the deep-seated reservoir with high signal strength at far-offset could suffer reduced signal resolution at low frequency. Visual inspection of Figure 4.16 indicates that any of the following frequency – offset combinations could be considered for further analysis: 0.1Hz – 10km, 0.2Hz – 9km, 0.3Hz – 8km, 0.4Hz – 7km, 0.5Hz – 6km, 0.6Hz – 5.5km and 0.1Hz – 5km.

(b) Analysis of 2D static EM maps

Using 0.2Hz – 9km as the optimum frequency – offset combination, the 2D maps of the EM amplitude of the entire reservoir model, comprising 729 one-dimensional depth-resistivity profiles, are generated for the inline electric field, vertical electric field and crossline magnetic field components as shown in Figures 4.17a, 4.18a and 4.19a respectively, for the baseline case. These images are visually inspected and compared with the baseline map of the transverse resistance (in Figure 4.9, which is now the 'b' part of each of the Figures 4.17, 4.18 and 4.19) in order to attempt static qualitative interpretation of the CSEM modelled data, before the time-lapse analysis. In Figure 4.17a, the channels are illuminated, though the vertical resolution is poor. They are more elongated than the actual length. The sea water resistivity stratification and the background resistivity structure combined together to mask the reservoir structure, and this causes poor registration of the resistive reservoir formation. Similar effects are observed in Figures 4.18a and 4.19a for the vertical electric and crossline magnetic components.

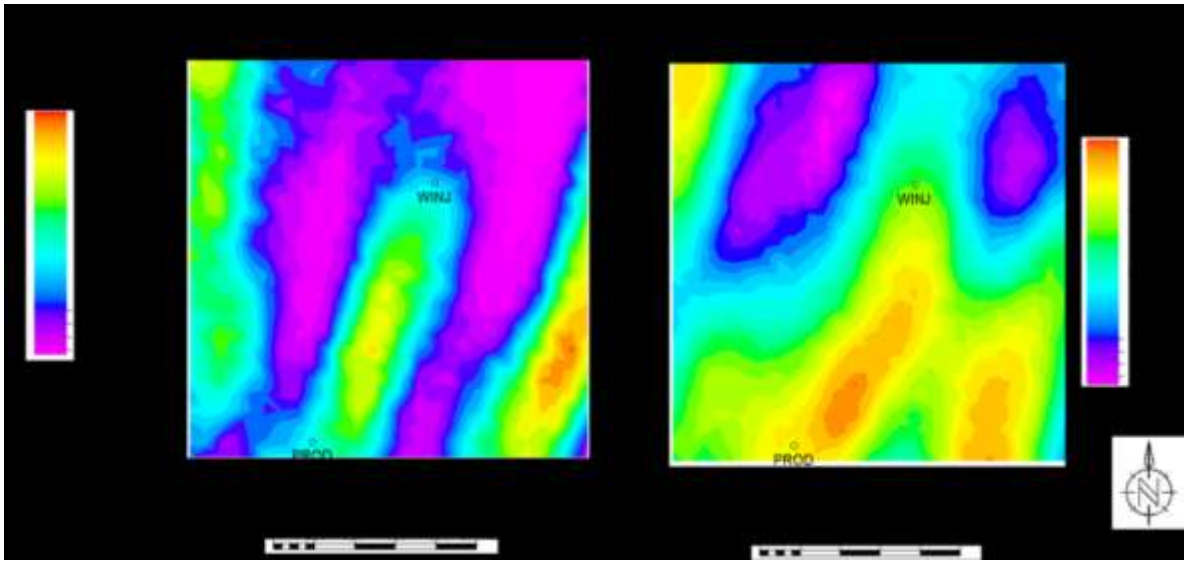

Figure 4.17: *(a) Baseline EM amplitude map for inline electric field at 0.2Hz frequency and 9 km offset. Both the sea water resistivity stratification and inhomogeneous background structure are incorporated in the model parameterization. (b) Pre-production map of transverse resistance (shown in Figure 4.9).*

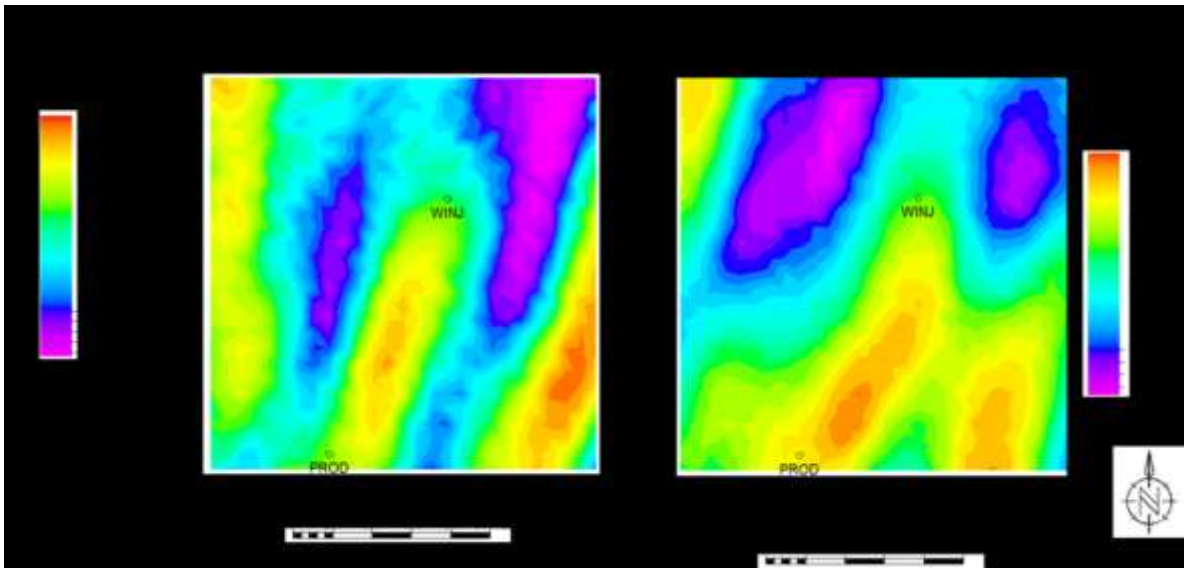

Figure 4.18: *(a) Baseline EM amplitude map for vertical electric field at 0.2Hz frequency and 9 km offset. Both the sea water resistivity stratification and background structure are incorporated in the model parameterization. (b) Pre-production map of transverse resistance (shown in Figure 4.9).*

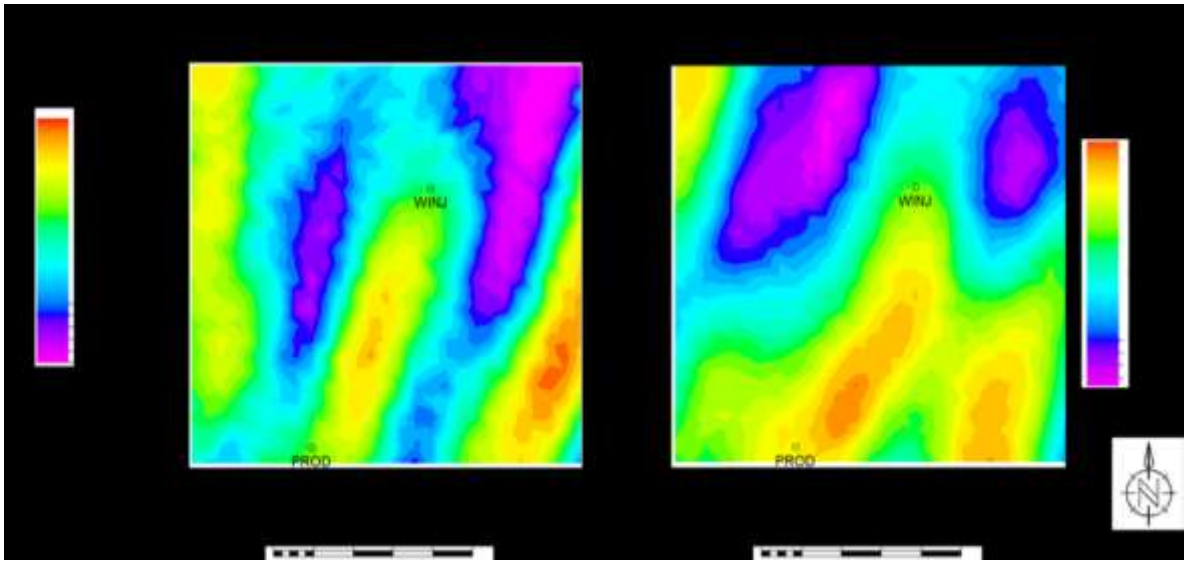

Figure 4.19: *(a) Baseline EM amplitude map for crossline magnetic field at 0.2Hz frequency and 9 km offset. Both the sea water resistivity stratification and background structure are incorporated in the model parameterization. (b) Pre-production map of transverse resistance (shown in Figure 4.9). These are visually inspected to attempt qualitative interpretation.*

4.4.2 Scenario two: homogeneous sea water with heterogeneous background

Now, let us assume an homogeneous sea water with an average resistivity value of 0.338Ωm over the entire water column, rather than the red-colored profile in Figure 4.11 earlier used. This will enable us to further understand the effect of sea water resistivity stratification. Here, we keep the background overburden and underburden resistivity structure the same as for the scenario one. Similar frequency – offset analysis for this parameterization shows that we can still use the combination of 2Hz – 9km as shown in Figure 4.16. Thus, we model the field reponses of the baseline model again, as shown in Figures 4.20 for the inline electric field component.

Comparing the two inline electric field components, Figure 4.20a (i.e. one with no sea water resistivity stratification) with Figure 4.17a (one with sea water resistivity stratification), it is observed that the over-all signal strength has reduced from the initial range of between 3.26 x 10^{-14} V/Am^2 and 3.82 x 10^{-14} V/Am^2, to a new range between 3.12 x 10^{-14} V/Am^2 and 3.4 x 10^{-14} V/Am^2. This in itself does not constitute a detectability problem as the measured value is still bigger than the noise floor.

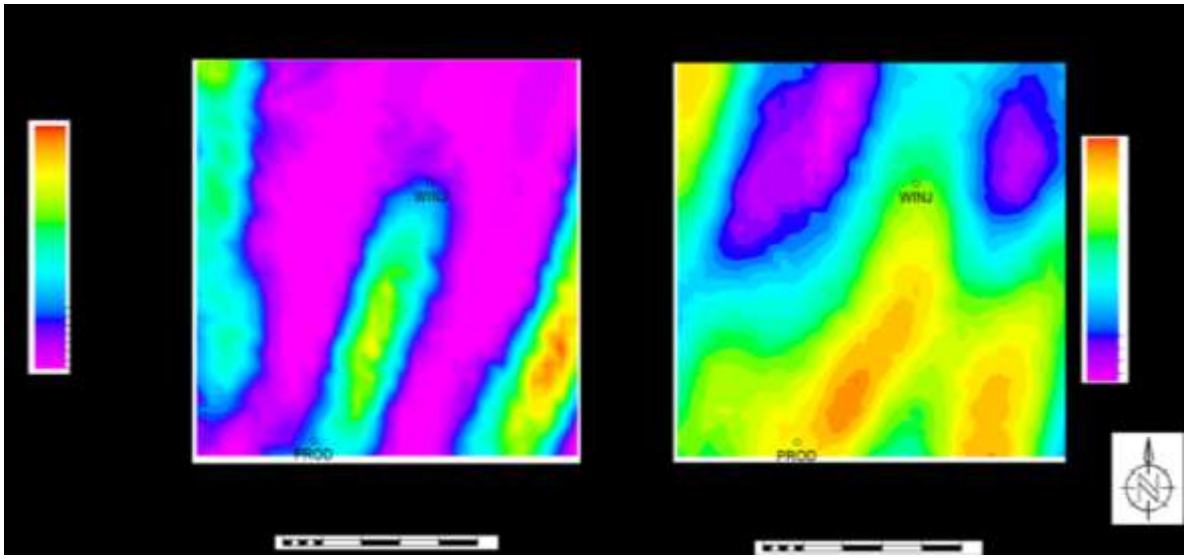

Figure 4.20: *(a) Baseline EM amplitude map for inline electric field at 0.2Hz frequency and 9 km offset. Homogeneous sea water with average resistivity is assumed, but background structure is incorporated in the model parameterization. (b) Pre-production map of transverse resistance (shown in Figure 4.9).*

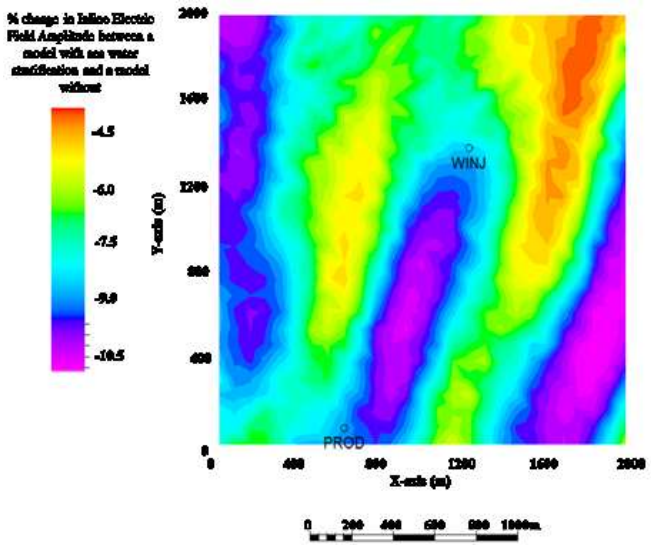

Figure 4.21: *Percentage change in inline Electric Field Amplitudes between a model with sea water resistivity stratification and a model without. This is the percentage difference between Figures 4.17 and 4.20*

However, inspecting Figure 4.20a and and 4.20b for similarity, it is observed that the resolution is still unacceptable for good qualitative interpretation. Taking a percentage drop in the signal strength (i.e. between Figure 4.20a and Figure 4.17a), it is observed as shown

in Figure 4.21, that making the sea water homogeneous has generally reduced the signal but the effect is small, about -3.9% within the low NTG sand which has low transverse resistance, than the effect in the high NTG sand bodies with -10.7%, which has high transverse resistance. For the vertical electric field and crossline magnetic fields component, similar drop in the signal strength is observed. In particular, the signal reduction in the vertical electric field is as high as -12.7% but this is more uniform for both the low and high NTG sand bodies. The crossline magnetic field is the least affected of the three field components, here the high NTG sand body is less affected by -2.3%, than the low NTG sand body with about -2.5%.

What has been shown here so far, is a map-based confirmation of similar work done by Orange et al. (2009) and Key (2009) among others. It can be inferred that the sea water resistivity stratification, rather than homogeneous assumption of single – valued sea water resistivity, reduces the measured signal. However, it has little or no impact on the signal resolution. In other words, the CSEM signature contains a portion relating to the sea water resistivity stratification. This indicates that the more the number of conductive layers (sea water column, in this case), the more the source energy penetrating the subsurface. This causes increased EM field perturbation not necessarily connected to the reservoir section.

A safe inference could be drawn from this analysis, that if we alter the sea water temperature profile during winter season, we should have a more resistive water which will invariably reduce the EM source energy penetration into the subsuface. However, measurement of sea water resistivity at any particular survey period could be easily incorporated into the CSEM studies. Sea water resistivity profile as a function of depth could be calculated from the temperature – depth profile obtainable using an expendable bathy-thermograph (XBT) or directly by using conductivity-temperature-depth sensor mounted on the EM transmitter during survey (Constable 2013). Having said that, what about the background resistivity structure? The fact that, with homogeneous sea water resistivity, the resolution is still largely poor means heterogeneity in the background resistivity structure could be more important to signal resolution than does the sea water stratified thermal structure. This leads us to the third scenario, in which we keep sea water

stratification, and assume homogeneous average resistivity values for both the overburden and the underburden.

4.4.3 Scenario three: Heterogeneous sea water with homogeneous background

If we insert the reservoir in-between an homogeneous 1 Ωm overburden and underburden, while retaining heterogeneity of the stratified sea water resistivity. We see a high resolution EM response as shown in Figure 4.22. Similar high resolution signals are obtained for the other field components. This indicates that the major uncertainty in CSEM modelling is the background subsurface resistivity heterogeneity, rather than the sea water resistivity variation due to thermal structure. The EM energy source is transmitted through the sea water through the seabed, and then into the subsurface down to the reservoir layers where the electric and magnetic fields are excited as the source energy is diffused onto the resistive reservoir. Thus the signal offers a clear image of the reservoir, which is very good for qualitative interpretation.

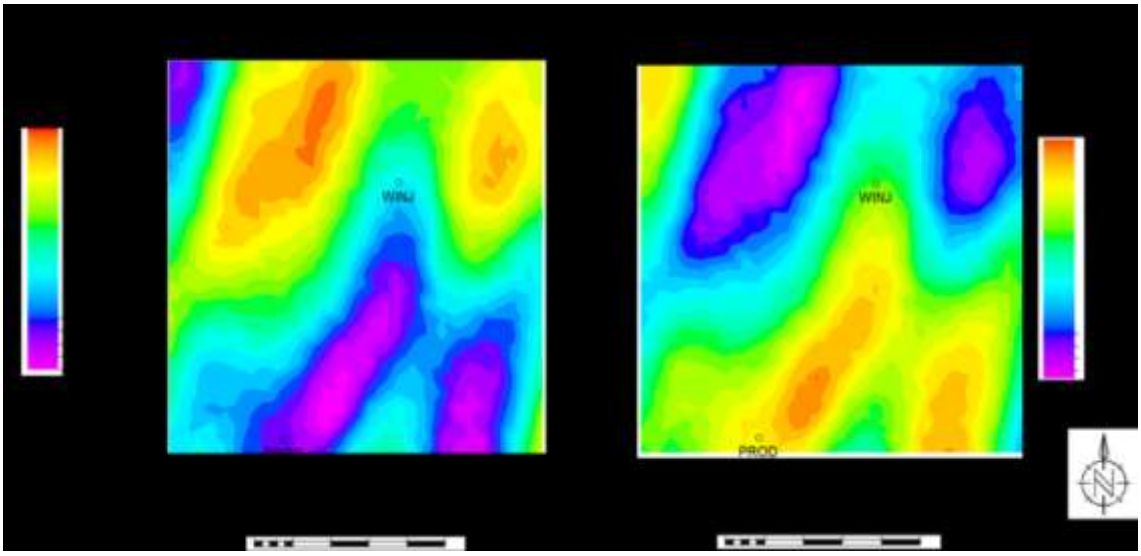

Figure 4.22: *(a) Baseline EM amplitude map for inline electric field. The sea water is stratified but background structure is considered as 1 Ωm conductor. (b) Pre-production map of transverse resistance (shown in Figure 4.9).*

Visual comparison of Figure 4.22a and Figure 4.22b show almost a perfect match for a very good qualitative interpretation. However, using average resistivities of 2.45 Ωm for the

overburden and 2.85 Ωm for underburden yields similar results, but with poor resolution, as shown in Figures 4.17 to 4.20.

4.4.4 Scenario four: Homogeneous sea water with homogeneous background

Before we examine how each of the previous scenarios impact on the detectability and interpretability of time-lapse CSEM responses to the change in water saturation; let us look at the last scenarios. Here, we have completely homogeneous sea water, and overburden and underburden structure. This is the common assumption in the EM community. We just need to adjust scenario three with an average sea water resistivity of 0.338 Ωm. The results brought about a significant improvement in the signal resolution, with all the three CSEM field components clearly showing the reservoir features when matched with the map of transverse resistance. The inline electric, the vertical electric and the crossline magnetic field components are shown in Figures 4.23a, b and c respectively.

The total signal strength is slightly reduced, as against scenario three, but the resolution is very good. Internal features as small as 20metres are seen, even though this is a 1D model. We have seen that non-reservoir background structure and sea water resistivity depth profile have effect on the CSEM measurement. While the sea-water resistivity profile mainly impacts on the signal strength, the background resistivity distribution are the major causes of poor structural resolution in CSEM measurement. This is apart from the effects due to the higher dimensions, as we shall see in Chapter 7. These effects are understood in the EM community usually with canonical model examples. Here, a more realistic simulator-driven map-based model has further confirmed this knowledge.

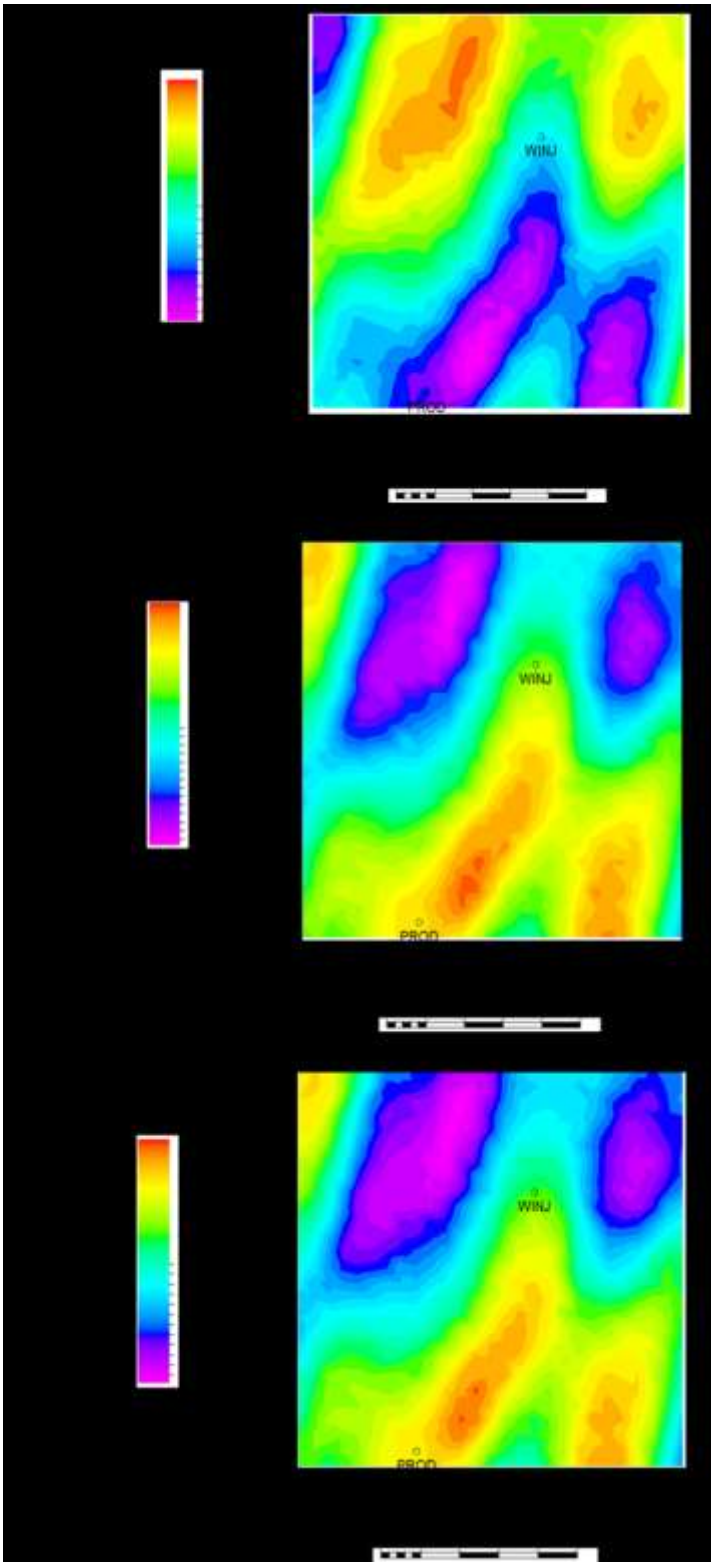

Figure 4.23: *Baseline EM amplitude maps for: (a) Inline electric field; (b)Vertical electric field; (c) Cross-line magnetic field. Both the sea water and background structure are considered to contain homogeneous resistivity with depth. They all match almost perfectly with the map of transverse resistance in Figure 4.9. It provides a very good qualitative interpretation of the channel sands.*

4.5 The impact on the time – lapse CSEM response

Let us now look at the impact of these complications on the time-lapse CSEM response. First, we look at the modelled data with heterogeneous background structure and sea-water resistivity stratification, as expected in real situation (i.e. scenario one in section 4.4.1). We consider the three components of the CSEM modelled data for the baseline and monitor surveys, and their time-lapse difference maps.

Figures 4.24 show the maps of transverse resistance, amplitudes of the inline electric field, vertical electric field and the crossline magnetic field responses respectively for the baseline and the two monitor models. The spatial variation in the baseline transverse resistance is lithological driven, as the water saturation at this stage is designed to be uniformly distributed. For the monitor maps, we see the water flooding front towards the producer at the bottom of the maps (Figure 4.24a). As earlier stated, when we compare the baseline amplitude images of the three CSEM field components (Figure 4.24b, c and d) with the base map of the transverse resistance (Figure 4.24a), we see that the pre-production and injection static anomaly are not properly positioned in the CSEM modelled data due to the non-reservoir complications. However, for the inline electric field (E_y) component in Figure 4.24b, we now see an increasing amplitude due to water injection in the monitor modelled maps, and this elevated amplitude does not only show the direction of the water flooding front, but it also shows the over-all shape of the flooded area from the baseline to monitor models. This is an indication that even though the internal resolution is not exactly perfect (when compared with Figure 4.24a), there is a reduced level of uncertainty in CSEM anomaly registration for time-lapse case, as against for the static case.

For the vertical electric field (E_z) component field in Figure 4.24c, water injection progressively drops the amplitude and this also shows the general shape and dimension of the flooded region of the reservoir model. These two CSEM electric field components are the most commonly measured, because the crossline magnetic field (B_x) component is believed to be more prone to noises (Constable 2013). Nonetheless, for completeness, we analysed the crossline magnetic field component, shown in Figure 4.24d, which shows

similar images as those of the inline electric field components and they both have better internal resolution of the flooded region, than the vertical electric field component.

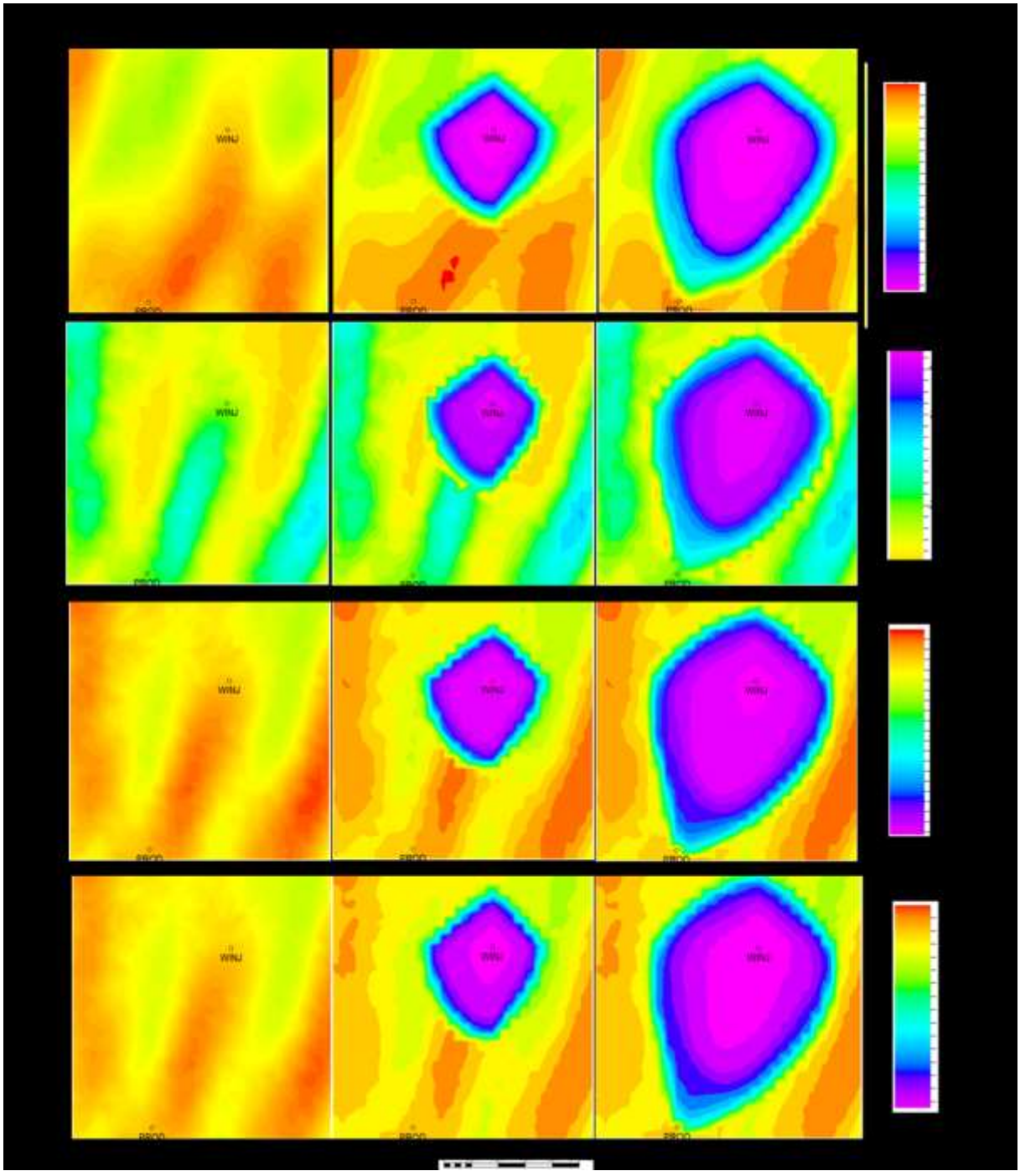

Figure 4.24: *Maps of (a) Transverse resistances; (b) Amplitudes of in-line electric field; (c) Amplitude of vertical electric field; (d) Amplitude of cross-line magnetic field for the baseline (pre-production) and the monitors two and five years after production and injection activities at 8km offset.*

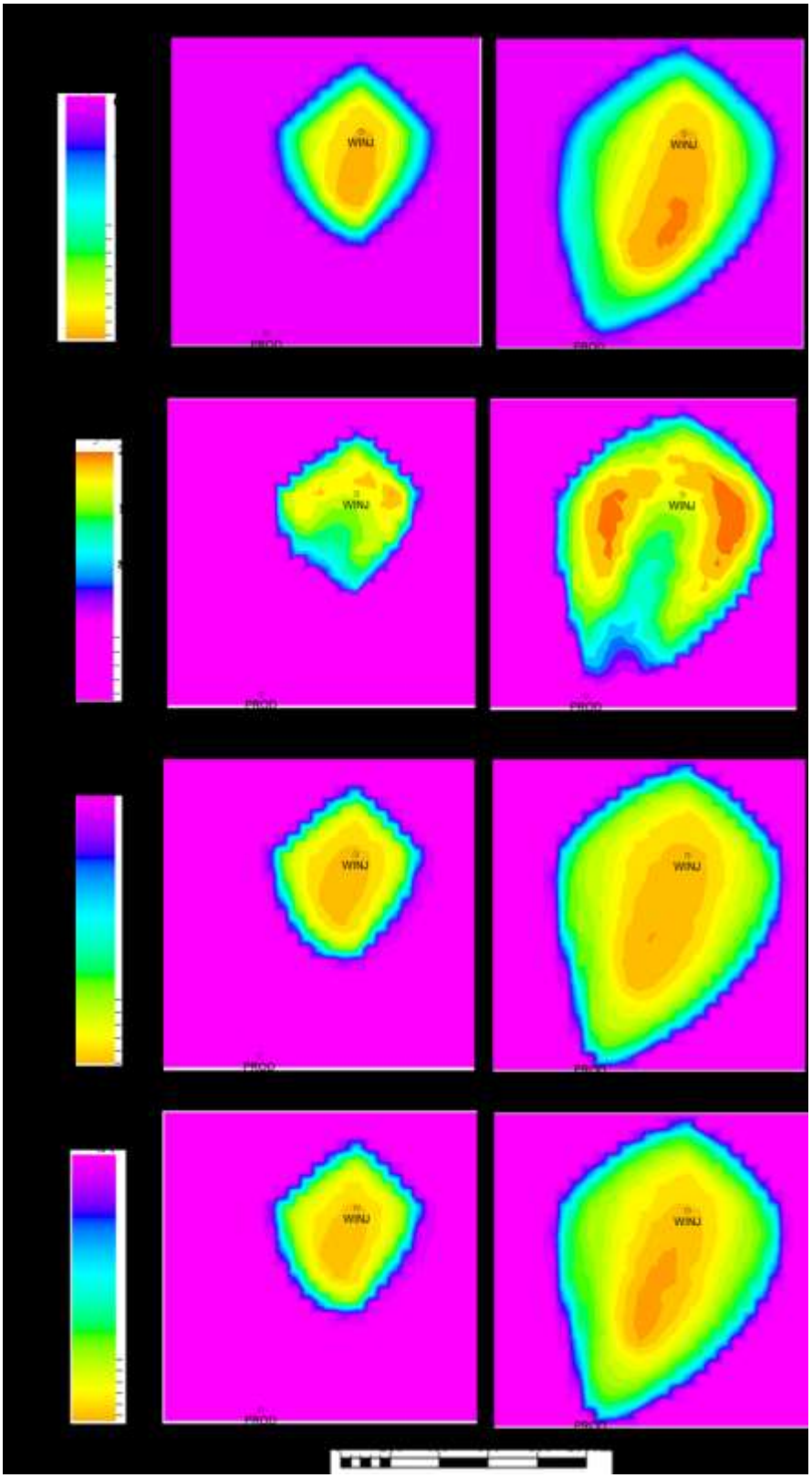

Figure 4.25: *Changes in (a) Transverse resistance; and amplitude (b) In-line electric field (ΔE_y); (c) Vertical electric field (ΔE_z) and (d) Cross-line magnetic field (ΔB_x) after 2 and 5 years of oil production and water injection activities at 8km offset.*

The next question we need to ask is: can time-lapse CSEM difference maps register the anomalous change in reservoir transverse resistance, due to change in water saturation, in the prescence of non-reservoir complications? To answer this, we compare the maps of changes in transverse resistance with the time-lapse CSEM difference maps for the inline electric, vertical electric and crossline magnetic fields respectively as shown in Figure 4.25. The negative change in transverse resistance (Figure 4.25a) indicates that conductive water is replacing resistive oil, thus reducing the over-all resistivity of the reservoir. The water movement is predominantly vertically directed from the injector to the producer. Comparing the maps of changes in the in-line electric field amplitudes (Figure 4.25b) with the maps of changes in the transverse resistance (in Figure 4.25a), we can observe that the inline electric field has a good resolution along W-E, but a poor resolution along the N-S trend of the reservoir model. This is such that the in-line amplitude change can not delineate the incursion of the water flooding front towards the production well, and early warning of water breakthrough could not be detected. This poor N-S resolution causes a symmetrical lateral resolution whereby two different values of changes in the transverse resistance produces similar value of change in in-line electric field amplitude. This is shown in a quadratic fit to the crossplot of ΔE_y versus ΔTR shown in Figure 4.26a. As expected, the amplitude change in the vertical electric field component has the highest magnitude, up to 55% (Figure 4.25c). The vertical resolution is very good but with lesser horizontal resolution. The crossplot of ΔE_z versus ΔTR in Figure 4.26b shows a very good correlation coefficient of 0.92 for the monitor 2, and 0.91 for the monitor 5, which is consistent with low standard deviation. Suprisingly, the crossline magnetic field produces a better resolution in the vertical direction than the inline electric field.

Comparing the change in crossline magnetic field (ΔB_x) with the change in transverse resistance (ΔTR) (Figure 4.25d), it is observed that for the monitor difference 2, the internal resolution of the gradation in ΔTR is delineated by the ΔB_x, but as the water flooding front advances, the resolution of the internal architecture of the reservoir is reduced. The crossplot of ΔB_x versus ΔTR in Figure 4.26c shows a very good correlation coefficient of 0.92 for the monitor 2, and 0.91 for the monitor 5, which is also consistent with low standard deviation. Thus, it is possible to estimate ΔTR from ΔB_x, particularly when ΔB_x is above absolute value of 15%, which means only the value of transverse resistance greater

than absolute value of 800 could be estimated with the level of uncertainty stated. This is similar to the crossplot of ΔE_z versus ΔTR, except that the vertical electric field has higher range of value of validity between about 30% to 55% (Figure 4.25b).

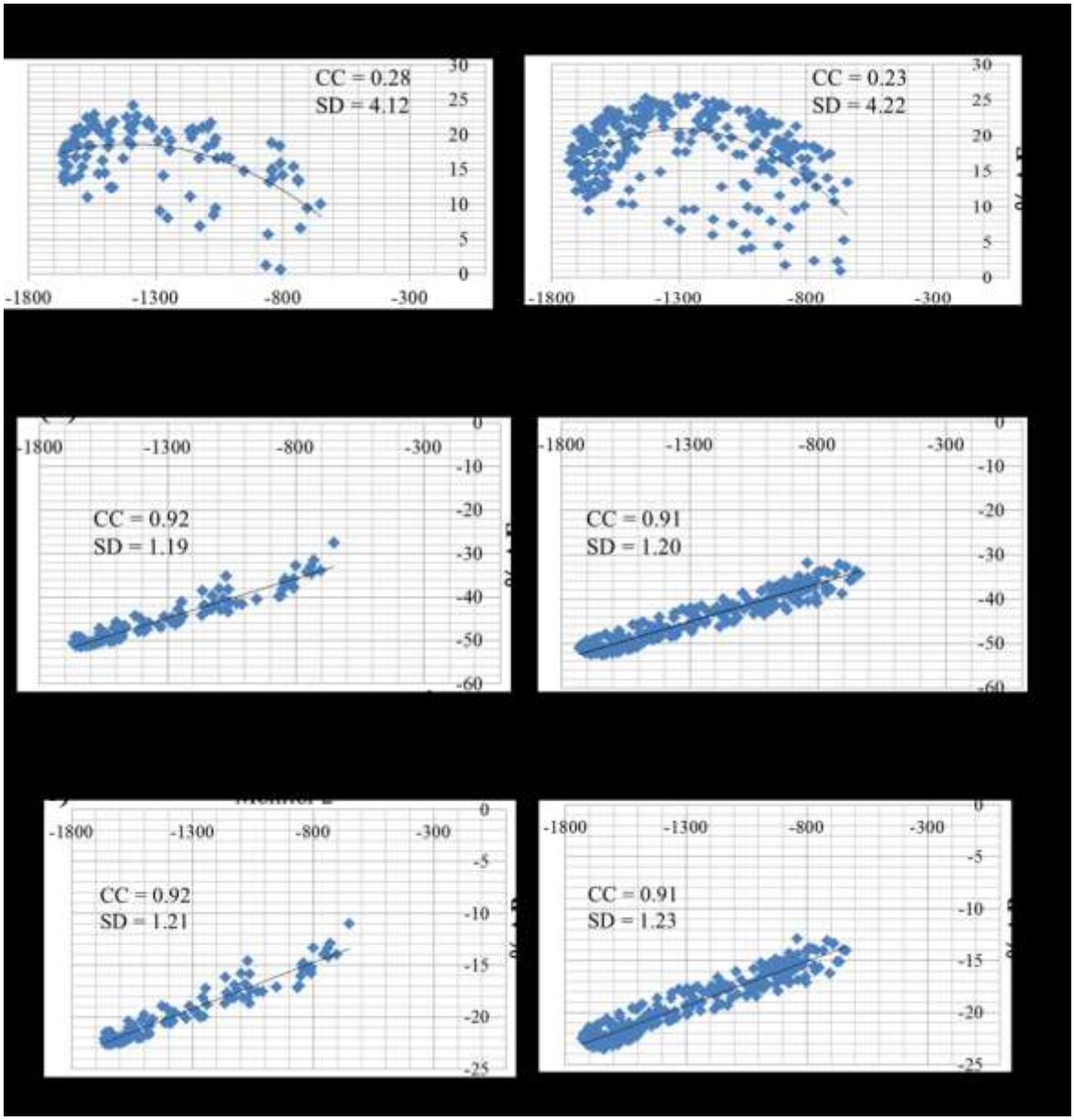

Figure 4.26: *Cross-plots of amplitude change in the: (a) In-line electric field (ΔE_y); (b) Vertical electric field (ΔE_z); and (c) Cross-line magnetic field (ΔB_x) versus change in transverse resistance (ΔTR) respectively, after 2 and 5years of oil production and water injection activities. CC is the correlation coefficient while SD is the standard deviation.*

However, with the complicated non-reservoir parameters, we still desire direct estimation of change in water saturation with the reservoir from the time-lapse CSEM. Luckily a good

linear relationship exists between the transverse resistance and the depth average water saturation as show in Figure 4.27. The depth average water saturation is a product of the net-to-gross, porosity and the water column thickness. This is an important reservoir attribute in estimating the remaining oil place.

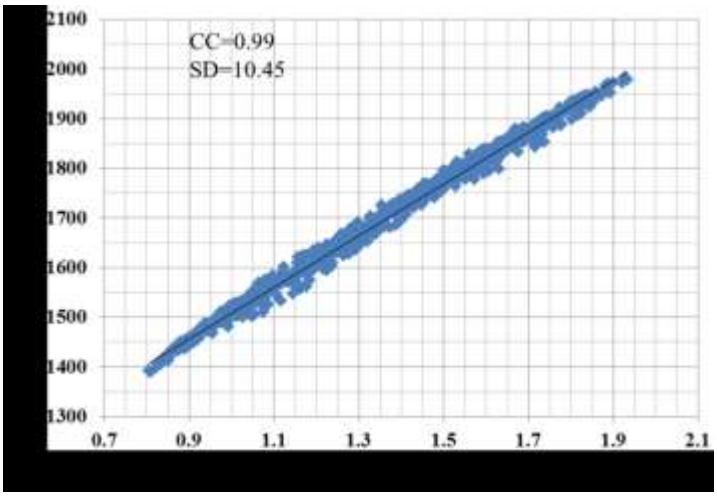

Figure 4.27: *Linear relationship between the transverse resistance and the depth average water saturation for the baseline model.*

4.6 Summary

Varying the degree of heterogeneity in the sea water, overburden and under-burden resistivity results in differing resolution and anomaly registration for the same reservoir target. The time-lapse CSEM analyses of a synthetic reservoir model in this Chapter have shown that intrinsically poor resolution of the CSEM is mostly restricted to static conditions resulting from inhomogeneous background structure. When the two cases of heterogeneous and homogeneous background were compared for dynamic analyses involving baseline and monitor models, it was observed and concluded that these have little or no impact on the dynamic registration of the changing resistivity within the reservoir. Therefore, change in resistivity could be interpreted for change in water saturation during production and injection activities. Although, the background heterogeneity has impact on the overall signal strength, change in the measured fields due to change in water saturation is still measurable by changes in the different CSEM components, in this 1D modelling. This is a good indication that the CSEM could serve a good purpose in monitoring changes

in water saturation, with a reduced level of uncertainty relating to resolution and anomaly registration due to complexity in the background structure. Two repeatability features have been considered here, other repeatability features that may affect detectability and interpretability are: the presence of near surface resistive materials, effect of stacked reservoirs, and repeatable survey geometry among others. Some of these have been extensively discussed in the open literature, but attempt is made in Chapter 7 to further examine some of these using 3D modelling.

CHAPTER 5

INTERPRETATION OF TIME-LAPSE CSEM MODELLED DATA

"The longer-term concern is that interpretation tools, particularly those that integrate CSEM results with other geophysical and geologic data, have lagged behind the data acquisition capabilities, and thus companies that have commissioned marine CSEM surveys, or are partners of companies that have, cannot always make the best use of the data." – Constable (2010).

"The joint modelling of the elastic and electrical properties of reservoir rocks will lead to the consistent forward modelling algorithm for joint inversion of seismic and CSEM data and is a topic for future research." – Shahin et al. (2010).

"However, increases in pressure near injector wells can mask 4D (seismic) signal that results from water sweep" – Johnston (2013).

*"Look at EM from the eyes of a practical reservoir manager." – Colin MacBeth***.**

5.0 Introduction

In Chapter 4, it was established that the sea water resistivity stratification and non-uniform background resistivity structure have no significant impact on our ability to detect and interpret time – lapse CSEM data for change in the reservoir. Now, the objective is to know how best could time-lapse CSEM data be integrated with time-lapse seismic for reservoir monitoring. Since time – lapse CSEM dataset are not available, foundation could only be

laid for the integrated interpretation by using datasets jointly forward modelled from the engineering fluid flow simulator. The main objective of this Chapter, therefore, is to "look at the EM from the eyes of a practical reservoir manager." The fluid flow simulator, in this case, serves a dual purpose of a '*common oil field*' where repeat simultaneous CSEM and seismic surveys have been carried out, and of a '*calibrating tool*' for integrated dynamic reservoir characterization.

Previous works on time-lapse CSEM sensitivity studies could be said to have examined detectability, even the recent ones that incorporated realistic fluid flooding front by using fluid flow simulator (e.g. Liang et al. 2011 and 2012; Shahin, et al., 2010 and 2012) did not look into the interpretability in terms of reservoir dynamic characterization. Although Liang et al. (2012) considered using CSEM as a proxy to assessing permeability as related to fluid movement during production, using joint inversion; yet most previous works that incorporated seismic, only used seismic to structurally constrain EM inversion (Andreis & MacGregor 2011). However, it should be noted that time-lapse EM cannot be a stand-alone tool for dynamic reservoir characterization, not only because of its intrinsic structural deficiency, but also because both saturation and pressure changes are involved in reservoir monitoring. Thus, the integration of CSEM and seismic with the fluid flow simulation model in reservoir monitoring should be driven by both the need to constrain EM inversion and the need to assist seismic in separating the dynamic reservoir properties. In fact, integration with the engineering simulation model will help reduce the emphasis on the structural constraint and place more emphasis on dynamic reservoir characterization, and much later updating of the simulation model (history matching).

Shahin et al. (2010) said "the joint modelling of the elastic and electrical properties of reservoir rocks will lead to the consistent forward modelling algorithm for joint inversion of seismic and CSEM data and is a topic for future research." Now, the future begins from here! As described in Chapter 2, both the production driving mechanisms and the production history result into the changes in saturation and pressure, and these are represented in a simulation model. The assumption is that both datasets have been acquired at the same calendar times in the same oilfield with good survey repeatability, such that their responses should be diagnostic of the production and injection activities. It is therefore

naturally instructive that if time – lapse seismic is as good as the time - lapse EM, in terms of their detectability and interpretability to the change in water saturation in the presence of change in pressure; one may then ask the question that, of what importance is incorporating time-lapse EM into reservoir monitoring?

The workflow described in section 4.1 is implemented using an industry supplied North Sea reservoir simulation model, thus no geological modelling was done here. In Chapter 3, where we performed time-lapse EM screening, the North Sea hydrocarbon province yielded highest technical risk of success. Therefore, if this integrated study could work in the North Sea, the assumption is that it should work in other provinces too, namely the West Africa and Gulf of Mexico. It is also assumed that the salinity and temperature of the injected water are equal to those of the formation water, a condition that is only approximately valid for produced water re-injection and later stage production situation whereby R_w is fairly constant due to re-injection of produced water. Direct comparison of CSEM and seismic is carried out, as regards to their relative sensitivities to the changes in the dynamic properties of reservoir, particularly in the presence of variable reservoir thickness, net-to-gross and porosity. Finally, integrated interpretation of time – lapse CSEM and time – lapse seismic modelled data is attempted, for dynamic reservoir characterization, using well activities in the fluid flow simulator to calibrate and validate the interpretation.

5.1 The North Sea producing oilfield

Having established, from a simple synthetic model, that time-lapse CSEM monitoring of changes in the water saturation is possible, even in the midst of complicated non-reservoir parameters, let us now look at a more complicated real reservoir simulation model of a producing oilfield undergoing water injection in the North Sea. Here, we shall be considering not only changes in water saturation, but also other dynamic reservoir parameters, namely changes in pressure and changes in gas saturation. Therefore, the first step in this integrated dynamic reservoir characterization is to carry out simulator – driven coupled forward modelling to generate both seismic and CSEM amplitudes changes and then compare them in terms of their sensitivities to the dynamic reservoir properties. The

second step is coupled interpretation of both repeat modelled dataset. Both steps will reveal the usefulness and limitation of CSEM in reservoir monitoring.

The deep-water oilfield, with water depth ranging between 350m to 450m, comprises tertiary turbidite sands with multiple stacked reservoirs. Reservoirs are buried between the depth of 1.5km to 2.3km below the seafloor. The reservoir porosity ranges from 25 to 30%, permeability is between 200 to 2000 millidarcy, and the pore compressibility used to simulate fluid flow is 7×10^{-6} psi^{-1}. The simulation model of this field and a vertical well log data are supplied by the operator. This model comprises 128 x 53 x 35 cells which covers two main reservoir sections, the top section covering layers with cells 1 to 16 in the z-direction is considered not to be producing, thus set as in-active in the simulation model, while the bottom sections between layers with cells 17 to 35 in the z-direction is the main producing target considered as the active part of the model. The field is about 6km long and 4km wide with the main reservoir unit thickness ranging between about 25 to 50m. The reservoir production and injection activities are simulated for 10 years, between 1998 and 2008 inclusive, thus covering the baseline and ten monitor surveys. The model is re-run using Eclipse simulator.

5.2 Reservoir simulator to resistivity and impedance modelling

The required parameters such as the irregular corner-point grid with average dimension of about 75m x 90m x 25m, static properties (e.g. porosity, net-to-gross) and dynamic properties (e.g. water saturation, oil saturation, gas saturation, pressure, etc) are extracted from the simulator to carry out resistivity and impedance modelling. For the resistivity modelling, the value of formation water resistivity (R_w) is estimated to be 0.2Ωm from the formation temperature of 58°C and formation water salinity of 18,000*ppm* using equation 3.17 described in Chapter 3. This R_w value is examined to be similar to the valued used by the operator in their field development. It is extremely difficult to locate fully water – saturated sand section within the depth of interest on the well logs provided. Therefore, a Picket plot of porosity versus resistivity in this section may not provide a reliable estimate of R_w to calibrate the calculated value. An average shale resistivity value of 2.8Ωm is obtained from the well logs at the depth of interest. Other standard constants used in

simulator to resistivity modelling are a = 1; n = 2 and m =1.8. The resulting baseline reservoir resistivity model is calibrated with the true resistivity log within the depth of interest as shown in Figure 5.1. There is a good correlation between the calculated resistivity and the well log resistivity measurement, with average value as high as 60Ωm.

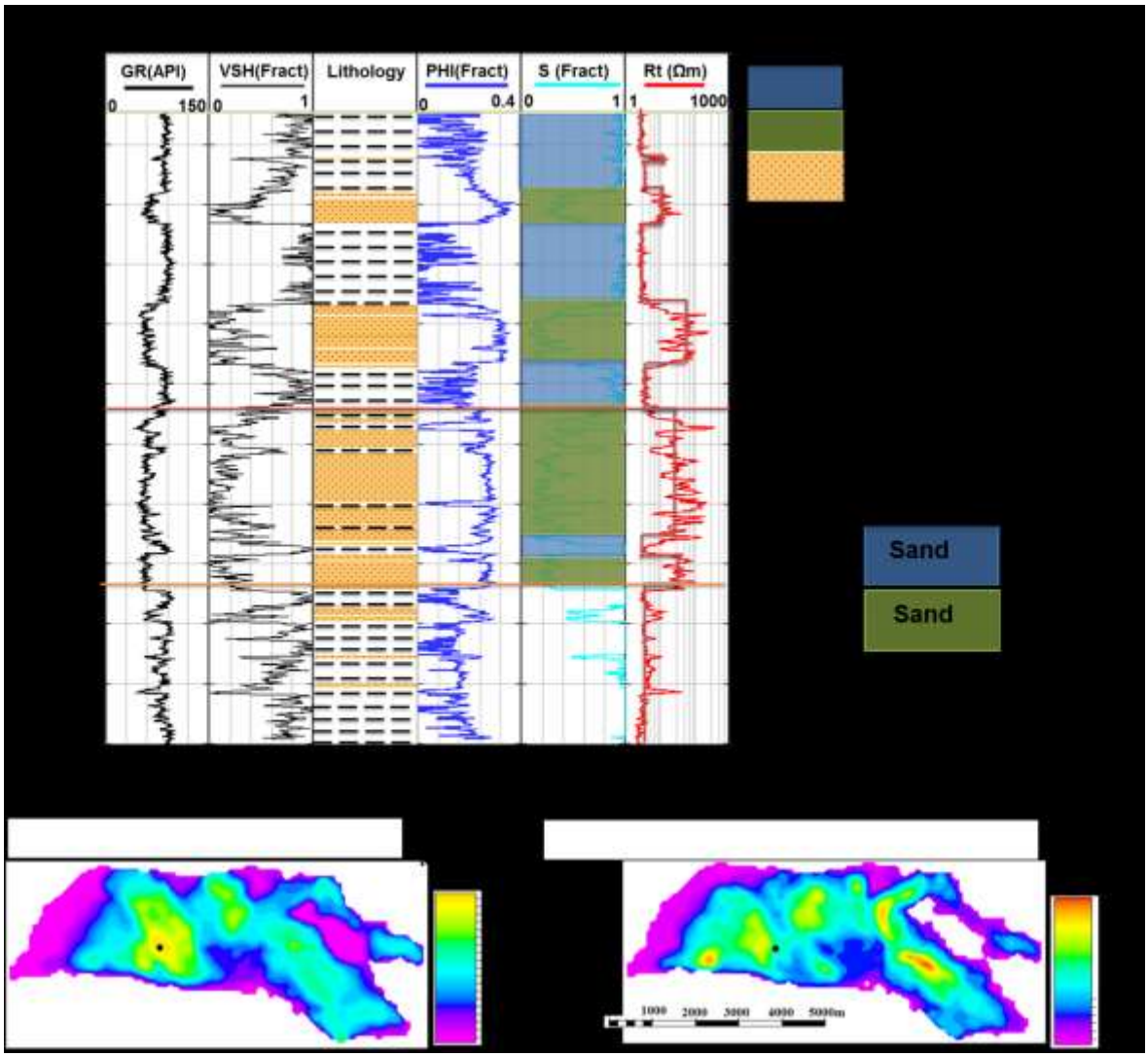

Figure 5.1: *(a) A suite of logs for a North Sea field, from which lithology and fluid conditions are calibrated for the modelling exercise. (b) Calculated baseline average reservoir resistivity map. (c) Map of baseline transverse resistances for the baseline. The calculated field average resistivity of the reservoir is calibrated and correlated with the resistivity log value at the same depth location. The baseline transverse resistance shows areas of elevated values where the EM response is expected to be high. The black dot indicates the x-y location where pseudo-resistivity-depth profiles were taken for the reconnaissance determination of optimum frequency-offset-signal combination.*

For the impedance modelling, several parameters supplied by the field operators were considered. These include the gas-oil ratio (GOR) of 340scf/stb; bubble point pressure (P_b) of 2824psia at 1.87km below the mean sea level; reservoir pressure (P_{res}) of 2907psia; average oil density of 0.8gcm^{-3} at 25°API; oil and water viscosities of 3.5cp and 0.5cp respectively at the formation temperature of 58°C; and the oil formation volume factor (B_o) of 1.16 rb/stb. Usually in monitoring, water injection and hydrocarbon production are considered only in terms of change in saturation and change in pressure. Temperature and salinity are not given much consideration in most cases of sea water injection, except for steam injection where differential temperature is of utmost importance. Thus, we first assume constant temperature of 58°C and salinity of 18,000ppm in this model. Our major aim here is to track changes in water saturation, changes in the reservoir pressure, and cumulative gas liberated from solution using both repeat seismic and CSEM modelled data. Temperature and salinity tracking in time-lapse CSEM is addressed in Chapter 6. The resistivity and impedance models are generated for the desired time-steps both in the Matlab format for further forward modelling of CSEM and seismic data, and in the Petrel format for visualization at the rock physics domain.

5.3 EM modelling and interpretation of modelled data

For the CSEM modelling, the sea water depth - resistivity profile shown in Figure 4.11b (red curve) and the background resistivity structure in Figure 4.12b are used. For each *x*-*y* cell location in the reservoir, a resistivity – depth trace is considered for the 1D dipole modeling of the CSEM response. Several of these 1D responses are then mapped together to produce 2D distribution of CSEM response of the field. In the case of pinch-out sections within the reservoir simulator, a depth of 0.00001m is added to separate two similar depth positions with similar resistivity, in order to allow the dipole 1D code to run. The transmitter dipole is towed 25m above the seafloor and parallel to the receiver dipole fixed on the seafloor. The transmitter – receiver spacing increases by 500m from zero up to 15km total offset. Sixteen transmitting frequencies at equal logarithmic interval between 0.01 to 10Hz inclusive are used. Similar reconnaissance measure as done for the synthetic case, to determine suitable acquisition parameters (frequency-offset-signal combination) is first

performed. Here, we examined the timelapse CSEM responses to the changing resistivity profiles through a chosen simulator cell (black dot in Figure 5.1b and c) after one year, five years and ten years of production and injection activities. The resistivity – depth profiles in Figure 5.2a, b and c show progressive increase in the separation between the baseline and the monitor resistivities curves, thus moving up the oil-water-contact (the red curve) as water replaces oil. These resistivity profiles were forward modelled into CSEM signals and corresponding time-lapse amplitude changes versus frequency and offset is shown in Figure 5.3. It is observed that the magnitude of time lapse EM amplitude increases as a measure of increasing magnitude change in resistivity, progressively from a lower time step to the higher time step with respect to the base resistivity profile. This is an indication of water replacing oil as injection and production activities progress respectively.

The peak timelapse anomaly could be observed at 7km offset and 0.1Hz frequency (Figure 5.3). These acquisition parameters are then used to produce 2D maps of CSEM responses for the entire simulation cells for the timelapse intervals 2004 – 1998 (six years), 2006 – 1998 (eight years) and 2008 – 1998 (ten years). The field-wide CSEM modelling results are presented as time – lapse percentage amplitude anomalies for the inline electric, vertical electric, crossline magnetic fields, and as time – lapse phase difference for the vertical electric field as shown in Figures 5.4, 5.5, 5.6 and 5.7 respectively. In the synthetic modelling in Chapter 4, it has been established that it is desirable to relate the change in CSEM amplitude directly with change in depth-averaged scaled water saturation, (which involves the NTG, porosity and unit thichness) as against the change in transverse resistance. Thus, by visualizing and correlating time-lapse CSEM maps (each of the Figures 5.4, 5.5, 5.6 and 5.7) with the maps of depth-averaged change in water saturation shown in Figure 5.8; areas of the reservoir, in which the water saturation is changing as production and injection activities progress, are clearly seen.

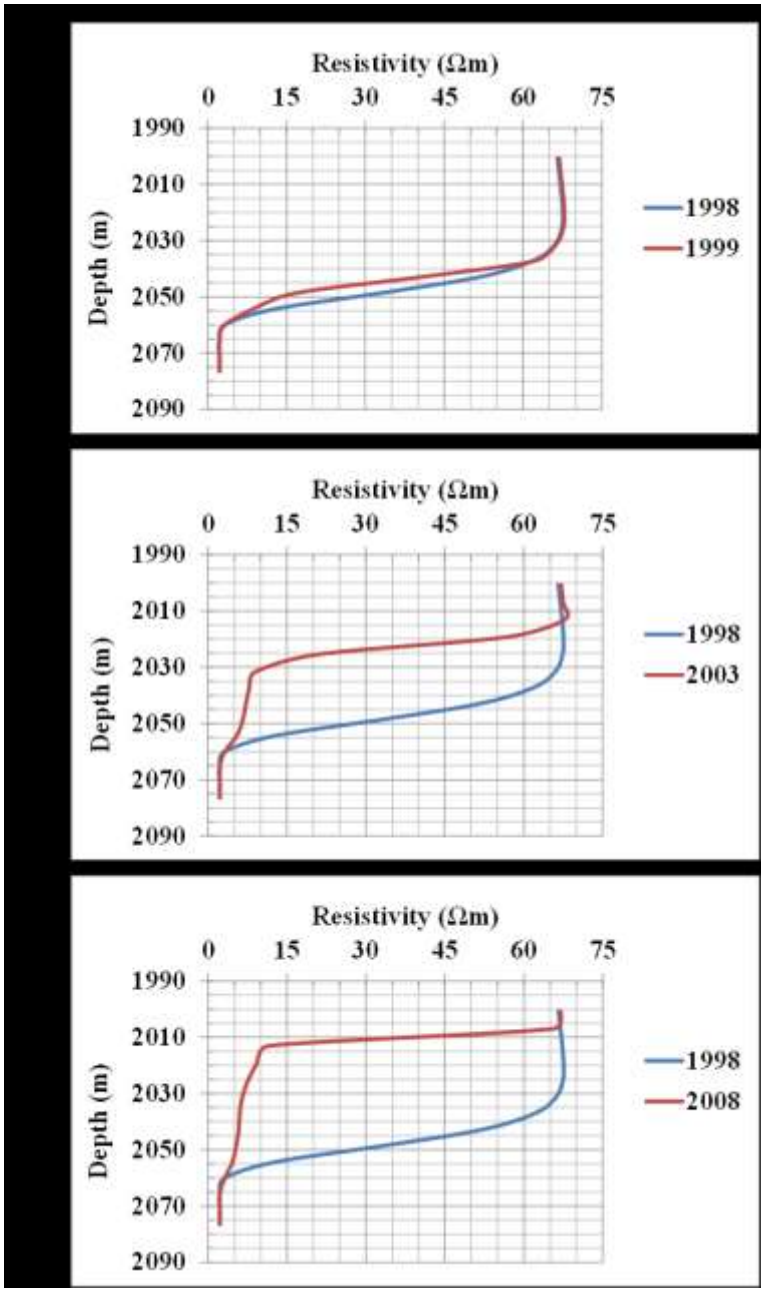

Figure 5.2: *Pre-production (baseline, in blue colour) and post-production (monitors, in red colour) resistivity-depth profiles at the chosen surface location indicated in Figure 5.1. Oil-water contact movement after: (a) one year; (b) five years; and (c) ten years of production and injection activities.*

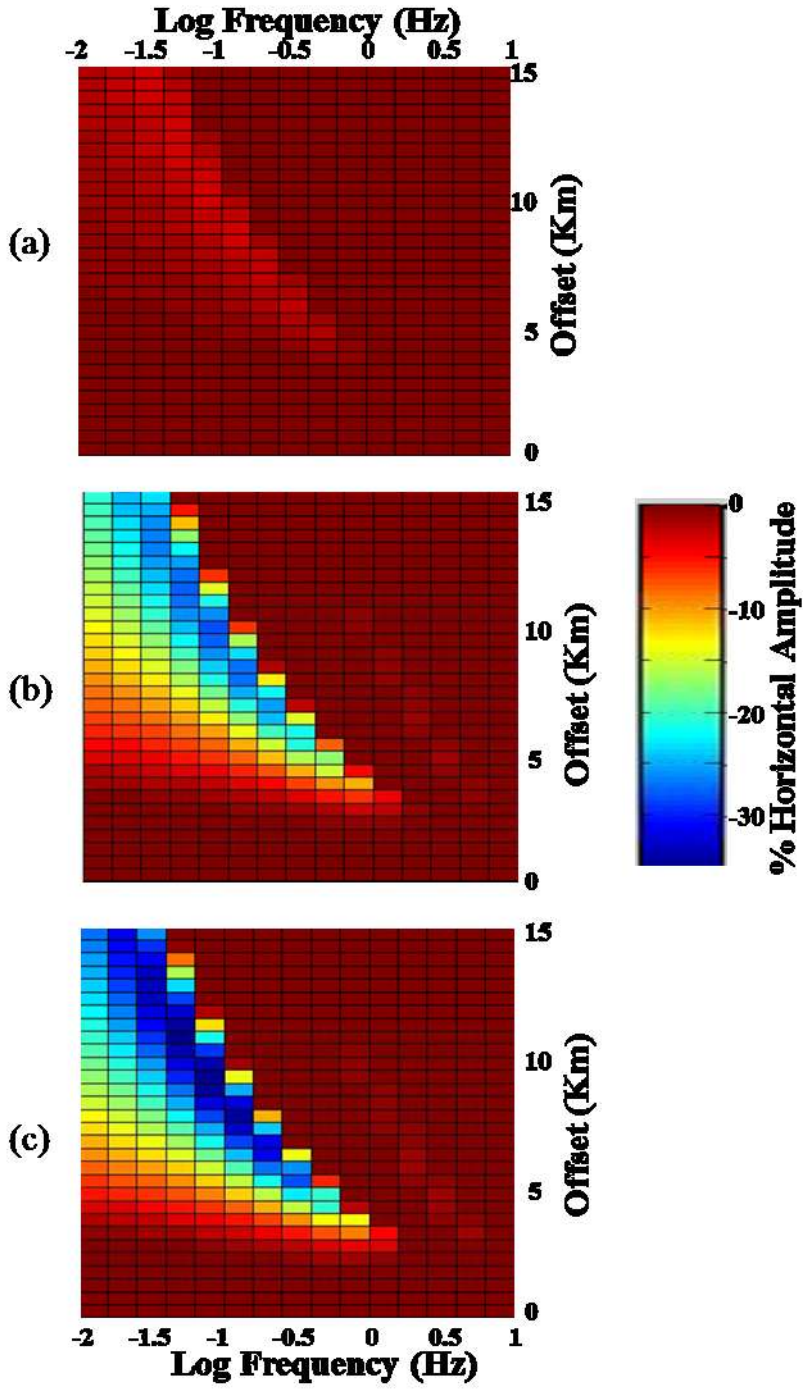

Figure 5.3: *Percentage time - lapse change in CSEM amplitude (inline electric field component) plotted as a function of the survey offset and the frequency for (a) one year; (b) five years; and (c) ten years after production and injection activities.*

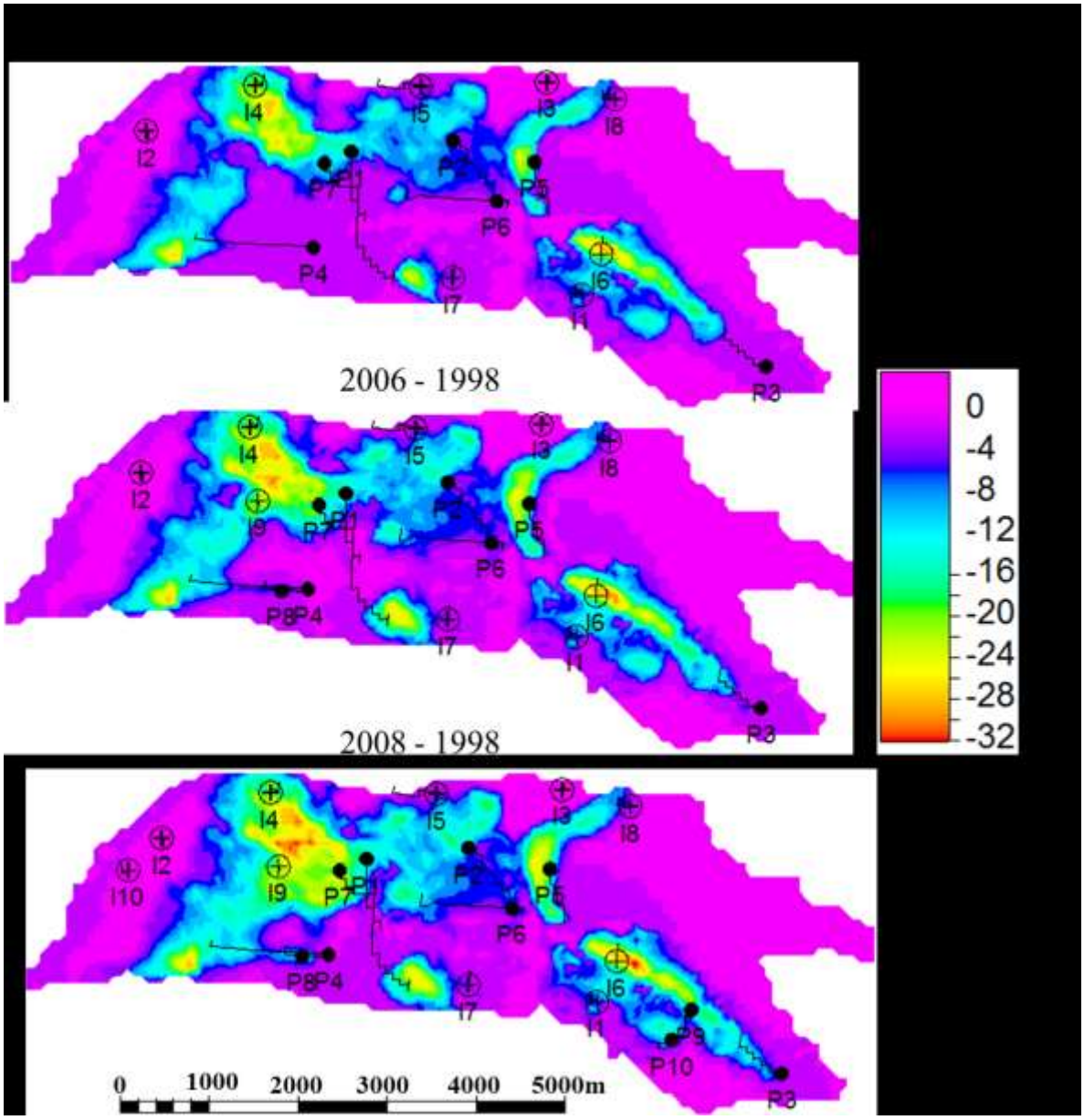

Figure 5.4: *Percentage time – lapse change in CSEM amplitude for the inline electric field component at 7km offset and 0.1Hz frequency for six years (2004 – 1998), eight years (2006 – 1998) and ten years (2008 – 1998) of production and injection activities. Note that the water injectors and oil producers are indicated at the time they started to be operated.*

Qualitatively, they all show the water flooding front. This is helpful in terms of providing early warning of water encroachment onto production well. The results also indicate zero time lapse CSEM signal for the parts of the reservoir where there are no dynamic changes in the reservoir model.

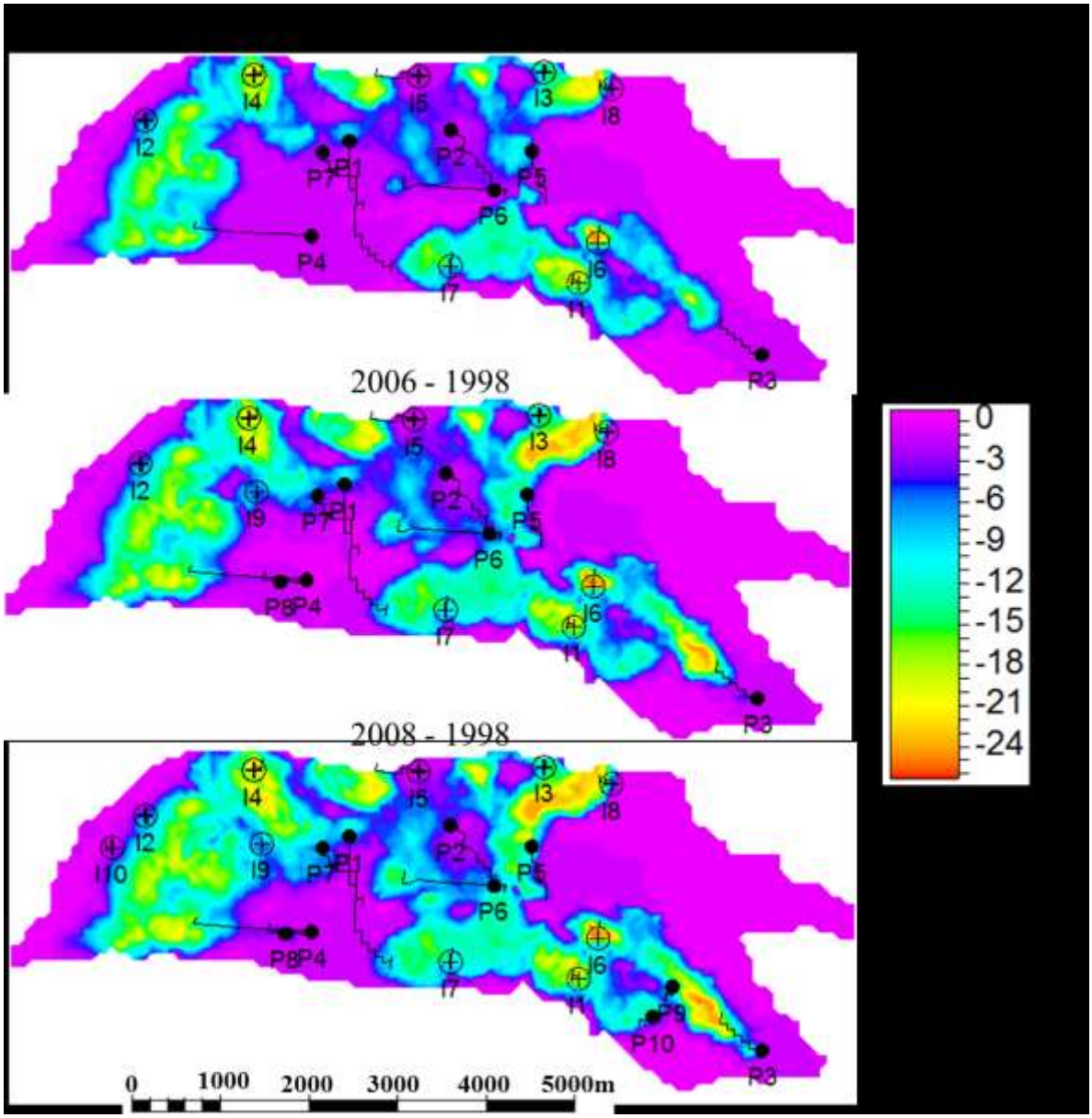

Figure 5.5: *Percentage change in normalized amplitude of the vertical electric field component of CSEM measurements at 7km offset, and 0.1Hz frequency for six years (2004 – 1998), eight years (2006 – 1998) and ten years (2008 – 1998) of production and injection activities. Note that the water injectors and oil producers are indicated at the time they started to be operated.*

Although the zero time lapse CSEM signal in these areas of the reservoir clearly suggests that the reservoir is not changing, but it does not in itself indicates whether these portions of the reservoir are water or hydrocarbon charged unless the initial conditions of the reservoir are known. Calibration to well activities, here referred to as *dynamic well tie*, is therefore very important.

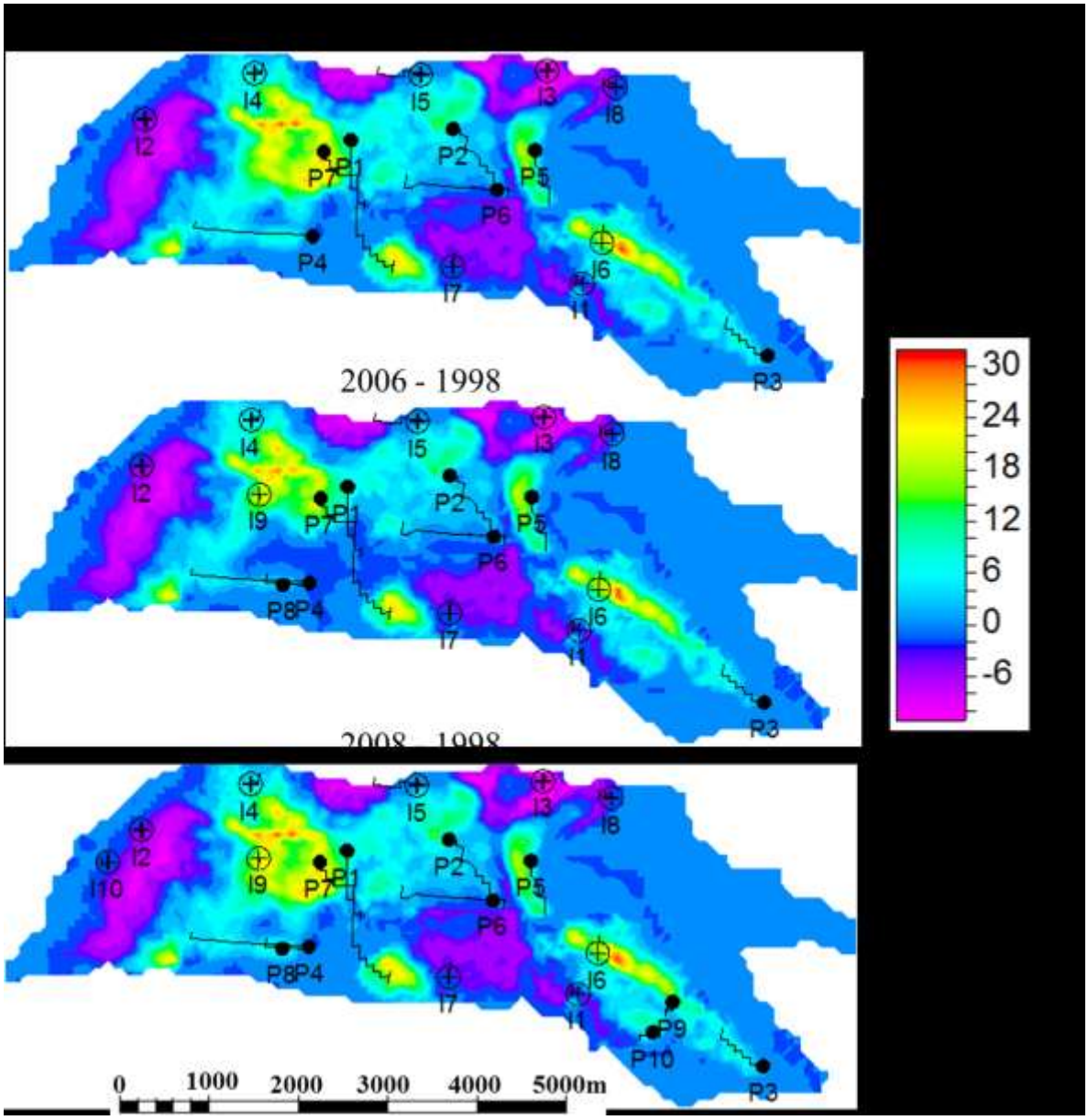

Figure 5.6: *Percentage change in normalized amplitude of the cross-line magnetic field component of CSEM measurements at 7km offset, and 0.1Hz frequency for six years (2004 – 1998), eight years (2006 – 1998) and ten years (2008 – 1998) of production and injection activities. Note that the water injectors and oil producers are indicated at the time they started to be operated.*

For instance, the production wells P4 (in the three maps) and P8 (in the last two monitors) at the bottom centre of the reservoir shows that this area is charged with hydrocarbon, despite the fact that we have zero – valued change in CSEM. Similarly for the injection wells I2 and I10 (in the last monitor) at the left hand corner of the reservoir which shows

that this area is water charged. We would not have been able to determine this without these wells.

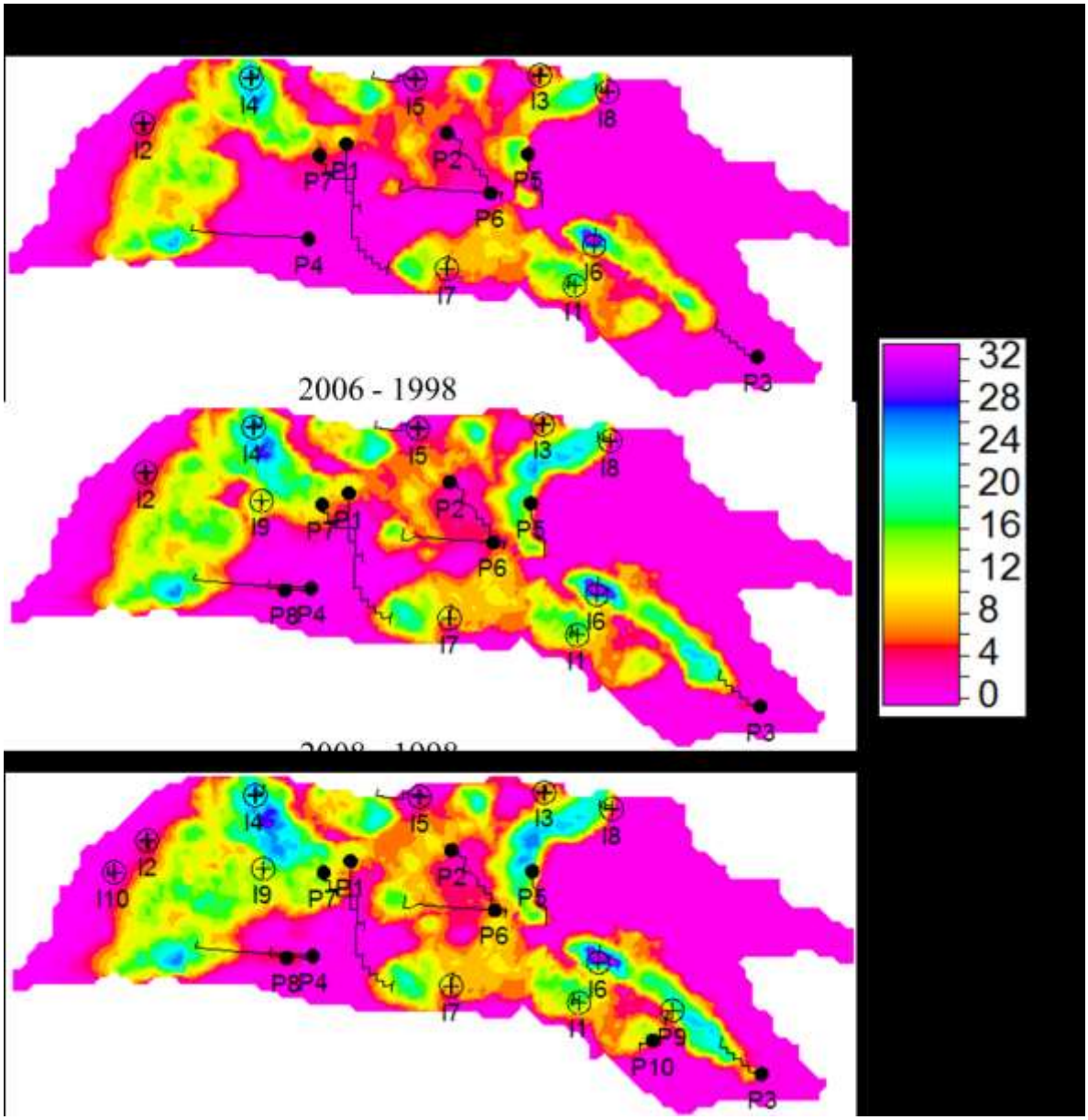

Figure 5.7: *Phase change in the vertical electric field component of CSEM measurements at 7km offset, and 0.1Hz frequency for six years (2004 – 1998), eight years (2006 – 1998) and ten years (2008 – 1998) of production and injection activities. Note that the water injectors and oil producers are indicated at the time they started to be operated.*

We also observe that the repeated CSEM signatures are more pronounced in the vicinity of the injector rather than the producer wells. This is because fluid substitution is more active around the injectors than around the producer, as expected.

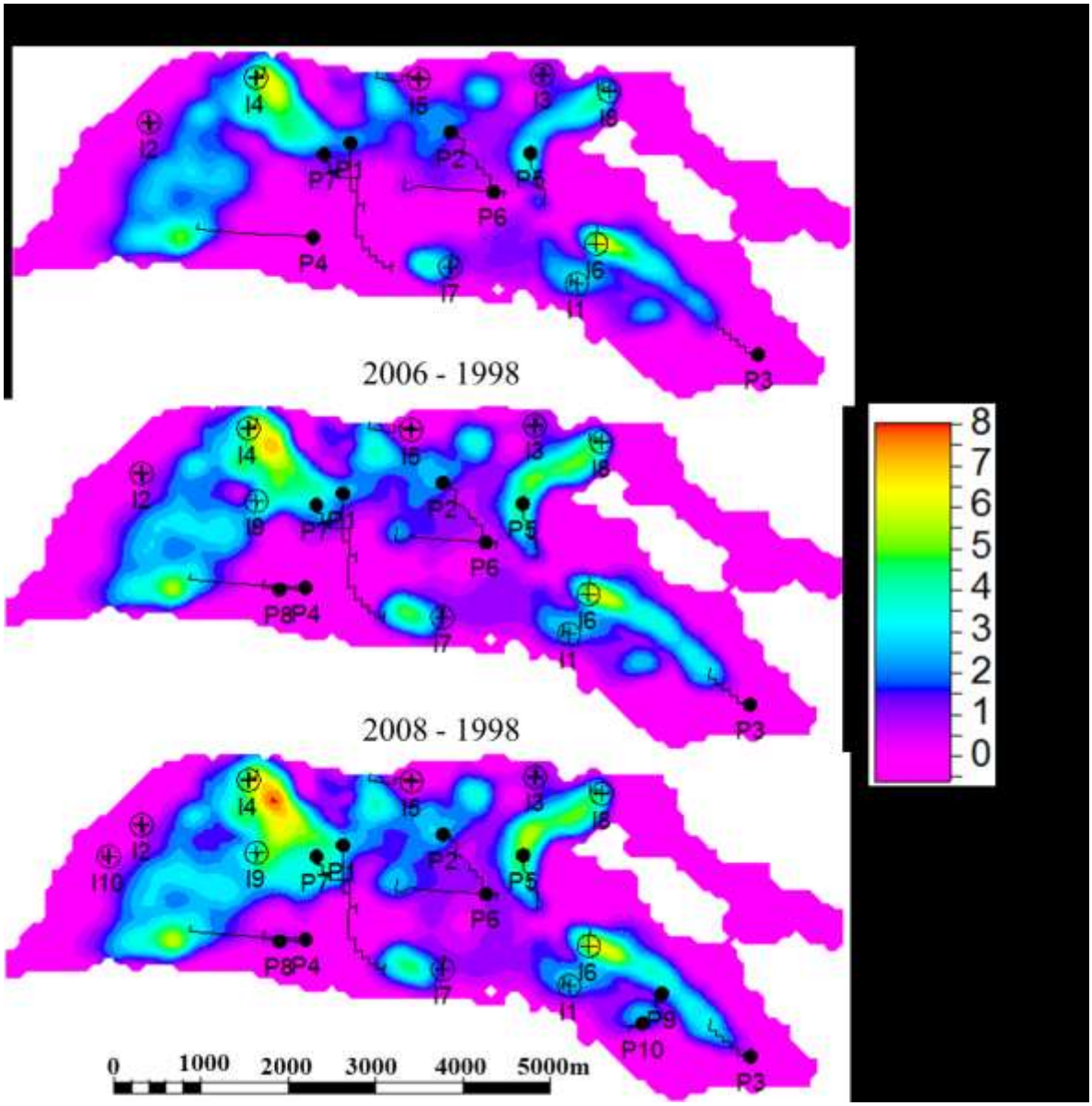

Figure 5.8: *Time lapse change in depth-averaged water saturation for six years (2004 – 1998), eight years (2006 – 1998) and ten years (2008 – 1998) of production and injection activities. Note that the water injectors and oil producers are indicated at the time they started to be operated.*

For each of the CSEM surveys (not shown here), the measured signal ranges between 7.2 x 10^{-14} and 12.1 x 10^{-14} V/Am^2, which is above the noise floor we expect to see for this water depth and overburden thickness (somewhere between 10^{-15} and 10^{-14} V/Am^2). The signal difference is at most minus 4 x 10^{-14} V/Am^2, which constitutes a time lapse CSEM magnitude of -32% amplitude change and 32° phase difference, which are above the

absolute 5% amplitude change and 5° phase difference possible noise floor. Although 1D responses are calculated, we would expect this to be a best case scenario. When higher dimensional effects are taken into account, it is likely that the changes will be smaller. The 3D modelling is described in Chapter 7. However, qualitatively, it can be observed that changes in the water saturation can be mapped by taking the time lapse electromagnetic measurements at different calendar times.

Investigation also showed that the static reservoir properties (NTG, porosity and the reservoir unit thickness) are important scaling factors to establish the linear relationship between the time – lapse CSEM and change in water saturation. Using cross – plots in Figure 5.9, it is shown that time lapse CSEM is a combination of the spatially varying reservoir petrophysical parameters and the dynamically varying water saturation, rather than just the dynamic change in water saturation alone. Thus, initial knowledge of the distribution of these variables is important in constraining the direct measurement of change in water saturation from the time lapse CSEM, even though contraining some of these variables (like NTG) come with some uncertainties, which add up to the uncertainties involved in time – lapse CSEM application.

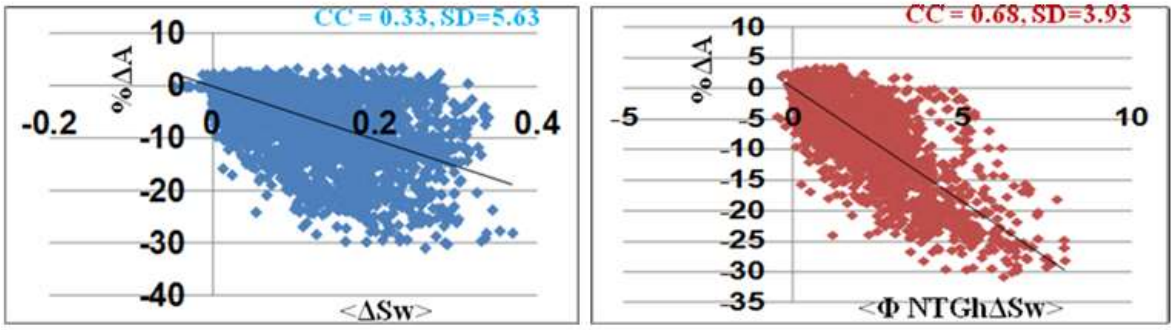

Figure 5.9: *The cross-plots of time-lapse CSEM inline electric field amplitude against the reservoir variables for ten years period of production and injection activities (2008 -1998). On the left – only change in water saturation, and on the right – a combination of spatial variation of net-to-gross, porosity, thickness and change in water saturation). CC is the correlation coefficient, and SD is standard deviation.*

5.4 Comparison of time-lapse seismic and time-lapse CSEM sensitivities to change in water saturation

Having established a fairly good correlation between the time lapse CSEM responses and the change in water saturation scaled with other static reservoir variables, time-lapse seismic modelling is then carried out using the results of simulator to impedance modelling. This modelling includes all the dynamic changes in the reservoir, involving pressure changes, gas coming out of solution and water saturation changes. This enables comparison to be made between the sensitivities of time – lapse CSEM and 4D seismic modelled data to change in water saturation for similar time lapse intervals, considering the various events happening in the reservoir during production and injection activities. Here, the sum of negative amplitudes is used in the time-lapse seismic analysis. This seismic attribute has been previously identified, by the field operator, to be appropriate for this North Sea oilfield.

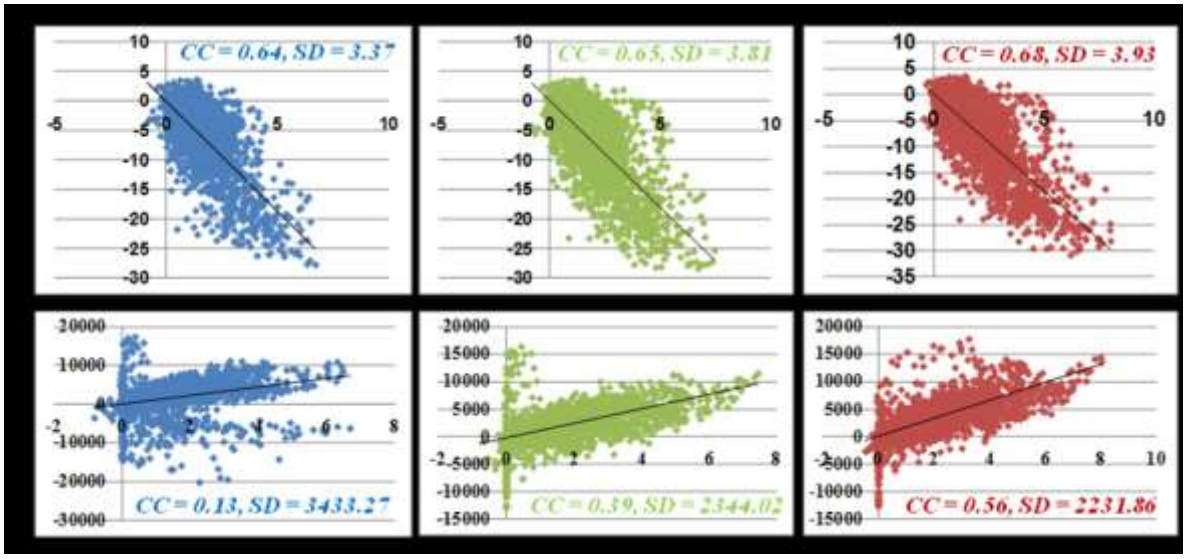

Figure 5.10: *Comparison of time – lapse CSEM and Seismic on the basis of their sensitivities to the change in water saturation. Top and bottom rows show the graphs of time-lapse CSEM and 4D seismic amplitudes cross-plotted against the reservoir depth averaged variables (combination of spatial variation of net-to-gross, porosity, thickness and change in water saturation) respectively. CC is the correlation coefficient, and SD is standard deviation.*

It could be observed in Figure 5.10 that the CSEM is more sensitive and consistently more linearly related to the change in water saturation than the seismic. This is not surprising

because seismic is sensitive to both saturation and pressure changes. Therefore, in line with Falahat et al. (2011) for the 4D seismic case, Equations (4.3) and (4.4) are proposed. The equations show that time-lapse change in CSEM amplitude (ΔA), and the phase differences ($\Delta\phi$) are linearly related to the dynamic and spatial change in water saturation (ΔS_w); and that the relationship is scaled with the spatially varying effective porosity $(\Phi NTG)_w$ and unit thickness $(h)_w$:

$$\Delta A = c(\Phi NTG)_w h_w \Delta S_w ; \qquad (4.3)$$

and

$$\Delta\phi = d(\Phi NTG)_w h_w \Delta S_w ; \qquad (4.4)$$

constants 'c' and 'd' are geologically driven coefficients, which are field specific.

5.5 Coupled interpretation of time – lapse CSEM and 4D seismic modelled data

As stated at the beginging of this chapter, the full story of time-lapse CSEM could only be told whenever we can jointly obtain and interpret repeat CSEM dataset with the repeat seismic dataset for reservoir monitoring. However, a foundation for coupled interpretation can be laid here, since the two datasets can be modelled from the same simulator platform. I proceeded by calibrating the geophysical amplitude events with the well activities using the simulation model as the control. A kind of *dynamic well tie* as done for time-lapse CSEM interpretation in section 5.3. Thus, the maps of time-lapse seismic attribute (sum of negative amplitude) in Figure 5.11, and the maps of depth averaged – scaled time-lapse change in pressure in Figures 5.12 are generated. These are done for the same periods as for the maps of time-lapse CSEM amplitude in Figures 5.4 and maps of depth averaged scaled time-lapse change in water saturation in Figures 5.8. For all the maps, the water injectors and oil producers are indicated at the time they started to be operated.

The following are some of the interpretations which highlight the complimentary roles that time-lapse CSEM can play in 4D seismic reservoir characterisation:

i. Away from the water injector I4 (operational between 2001 and 2008): Seismic hardening observed in 2004 (blue colour, in Figure 5.11) indicates increased water

saturation, ΔS_w, (Figure 5.8) leads the increased pressure, ΔP, (Figure 5.12) during water injection. In 2006, when ΔP rises above that of 2004, hardening persists because there is a corresponding further rise in ΔSw. In 2008, the drop in ΔP below that of 2006, coupled with increased ΔS_w over that of 2006, increases the magnitude of seismic amplitude hardening. At the edges (e.g. top right hand corner), away from injector 4, where pressure diffusion (with increased ΔP) has gone ahead of water flooding front, softening (red colour signal) is consistently observed.

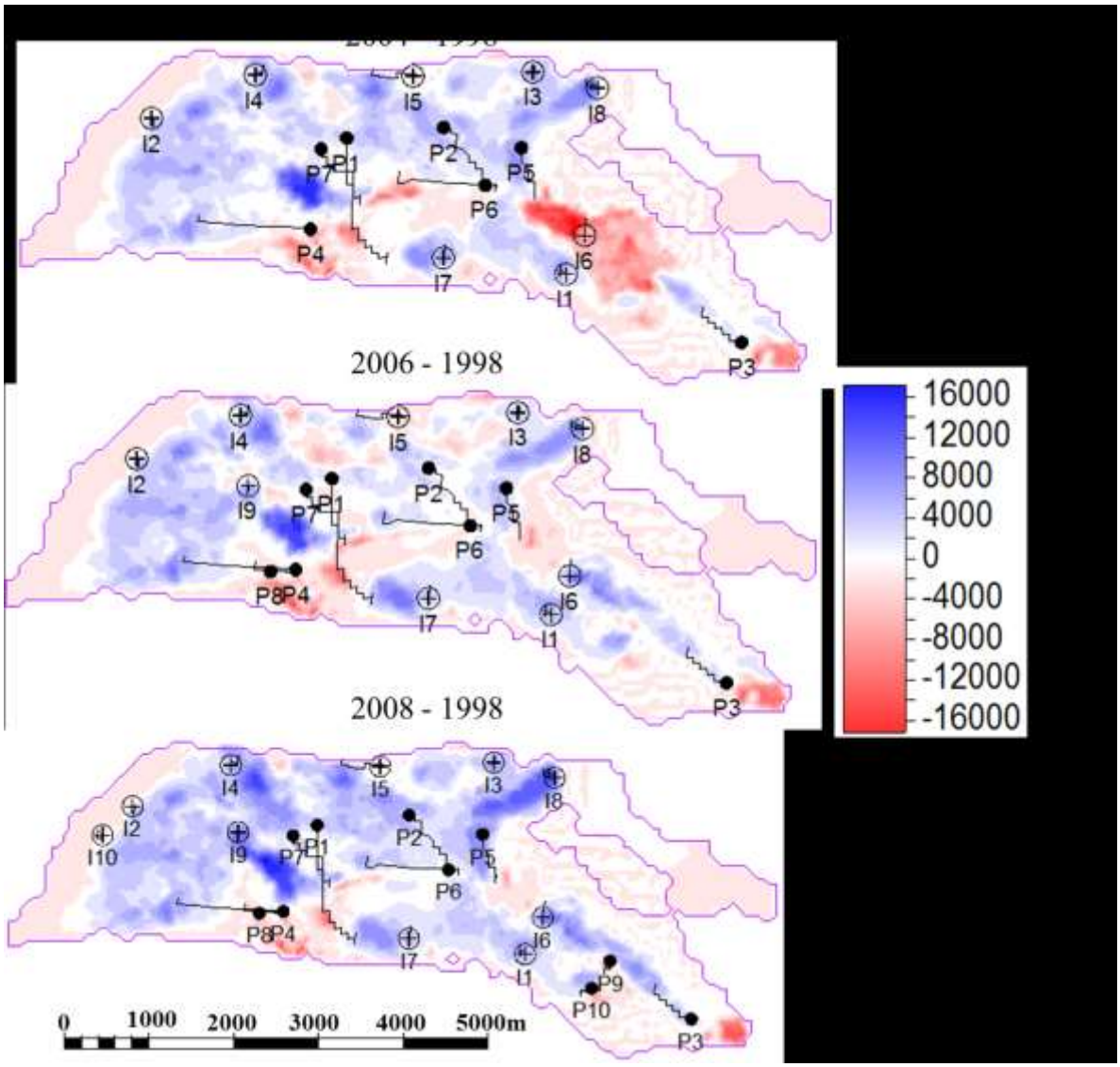

Figure 5.11: *Time lapse change in the sum of negative seismic amplitude for six years (2004 – 1998), eight years (2006 – 1998) and ten years (2008 – 1998) of production and injection activities.*

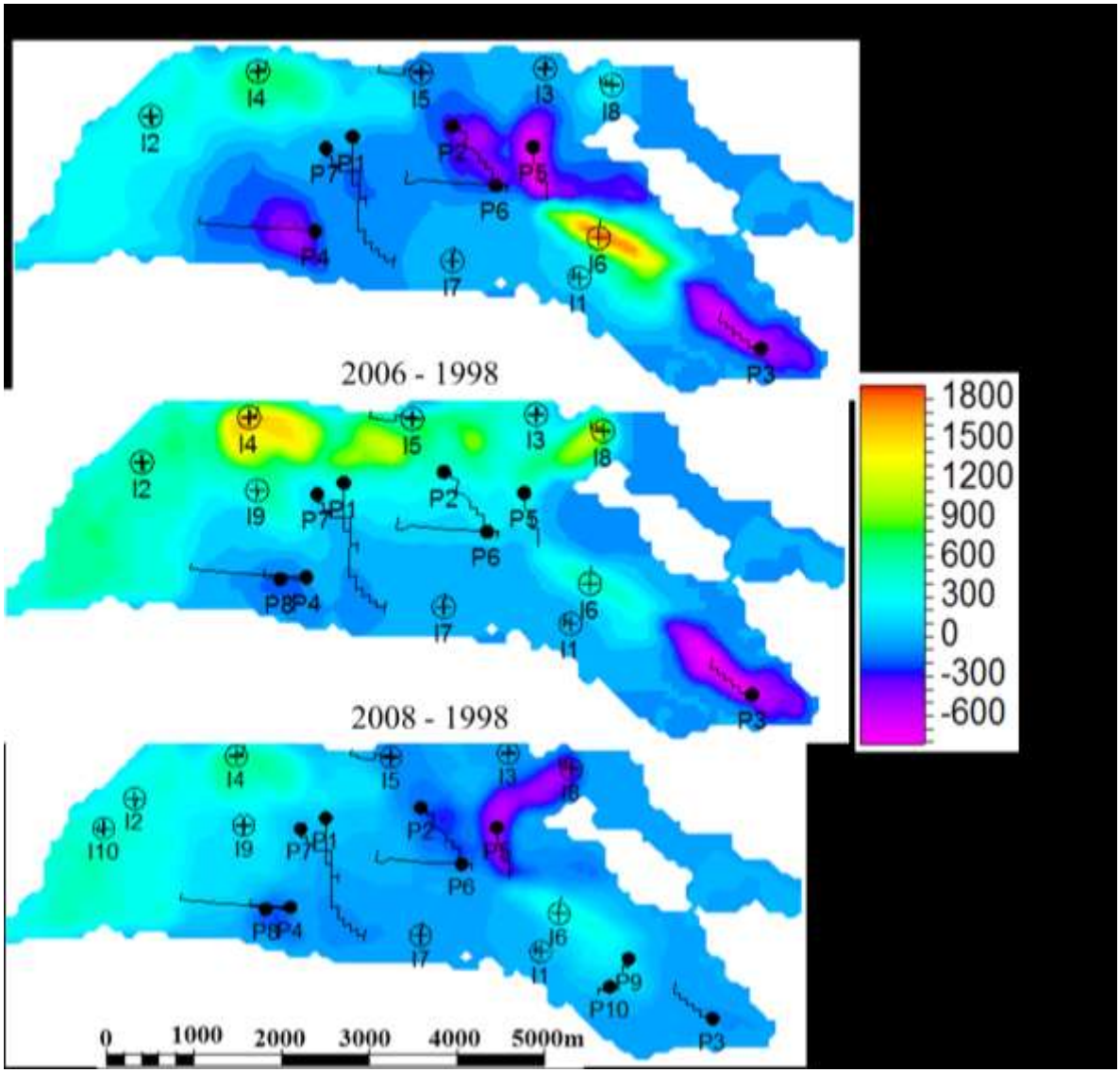

Figure 5.12: *Maps of depth – averaged scaled time-lapse change in pressure for six years (2004 – 1998), eight years (2006 – 1998) and ten years (2008 – 1998) of production and injection activities.*

However, the spreading of high negative amplitude changes in the time-lapse CSEM (Figure 5.4), for the three time intervals, indicates hardening due to continuous rise in ΔSw and spreading of the water flooding fronts. This interpretation is better observed with large – scaled maps as shown in Figure 5.13. Here, the increased saturation effect has hidden the increased pressure effect in the time – lapse seismic. Time – lapse CSEM may provide constraint for quantitative separation of these counteracting effects between 2004 and 2006, along the water flooding front (Figure 5.13).

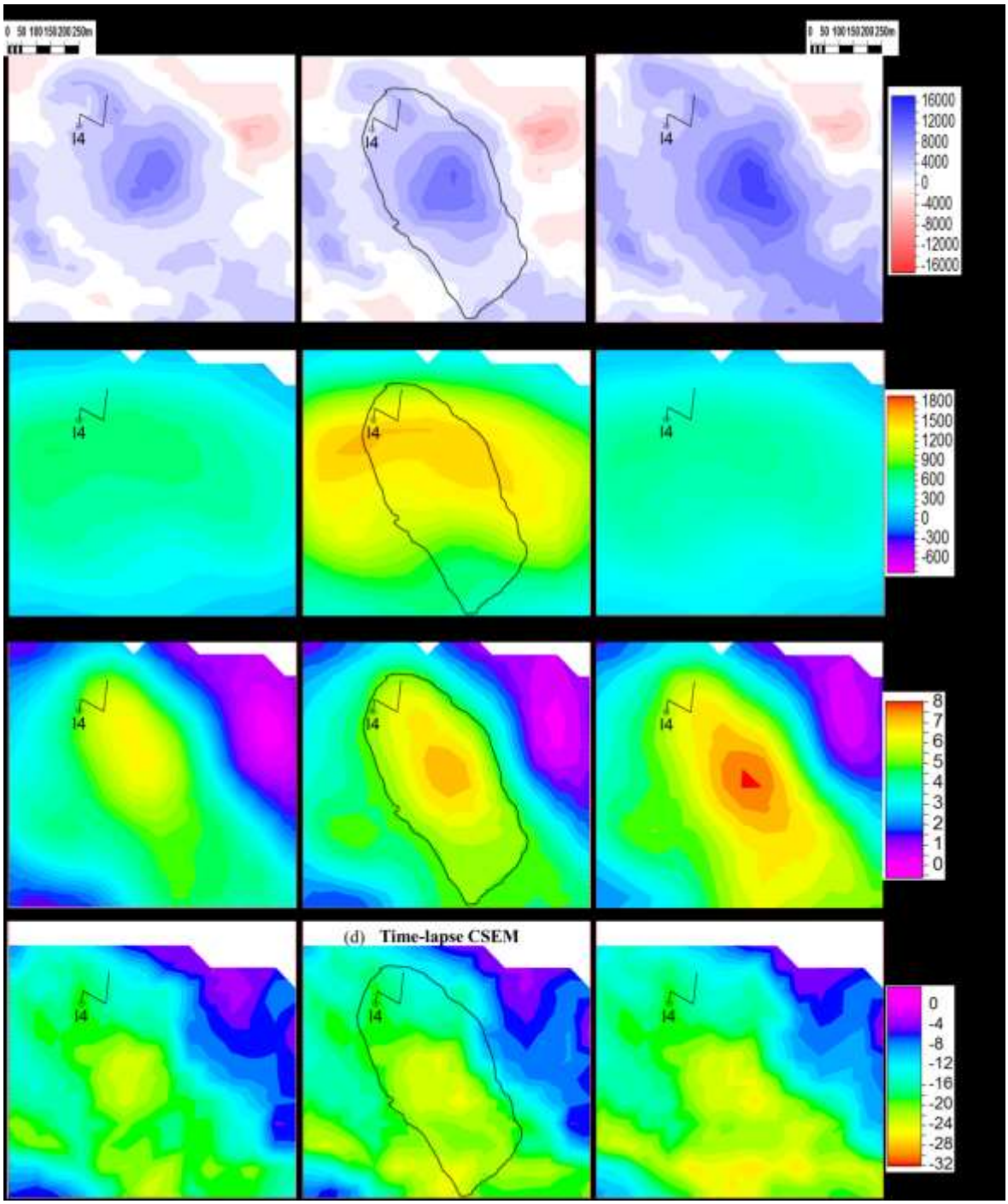

Figure 5.13: *Interpretation away from water injector 4 (water leg), at a larger scale, for six years (2004 – 1998), eight years (2006 – 1998) and ten years (2008 – 1998) of production and injection activities: (a) Time-lapse seismic; (b) Change in pressure; (c) Change in saturation; and (d) Time-lapse CSEM.*

ii. Around the water injector I6 (operational between 2003 and 2008): Seismic softening indicates that the elevated ΔP leads increased ΔS_w between 1998 and 2004 (Figure 5.14a, b and c).

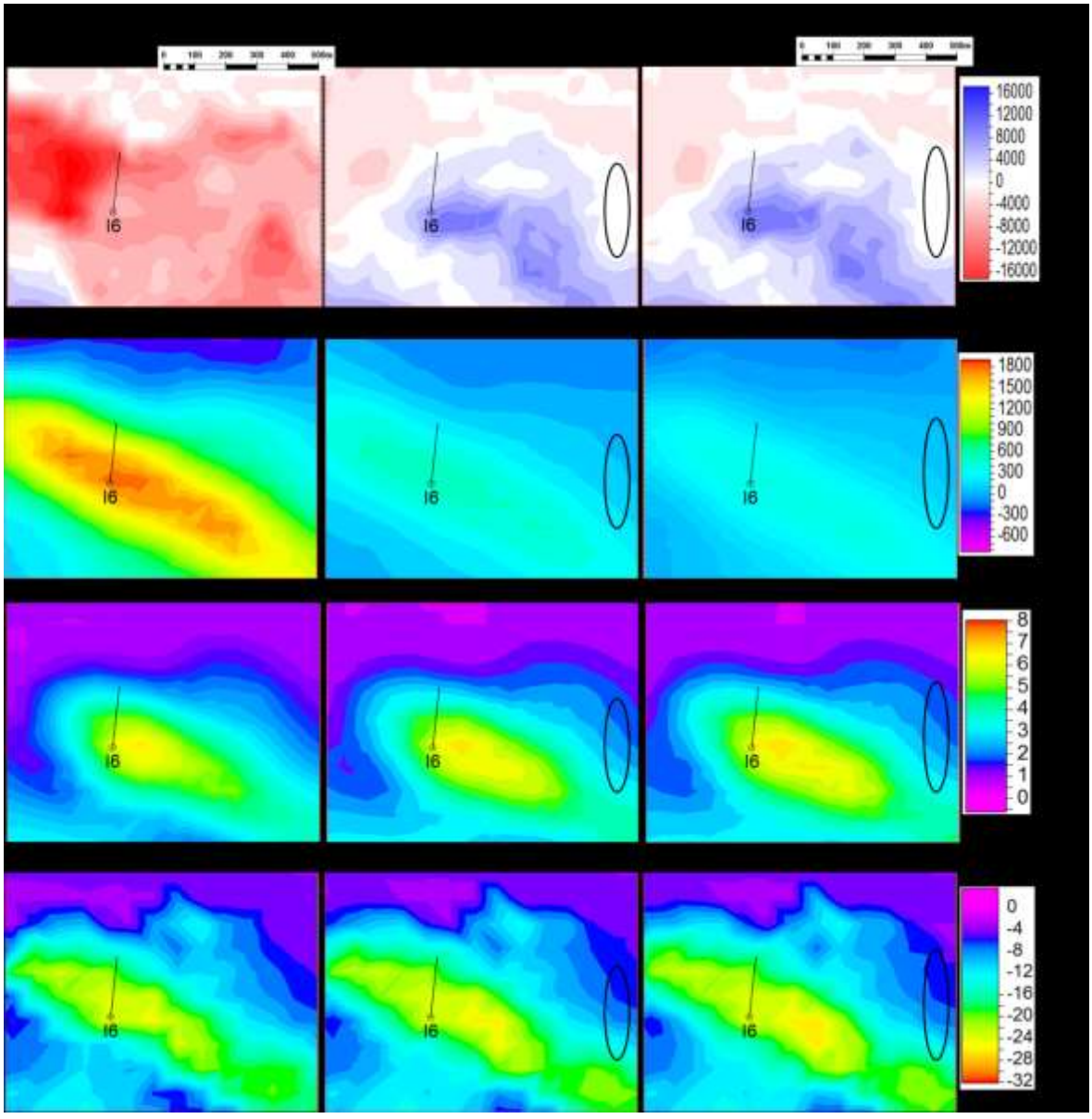

Figure 5.14: *Interpretation around water injector 6 at a larger scale, for six years (2004 – 1998), eight years (2006 – 1998) and ten years (2008 – 1998) of production and injection activities: (a) Time-lapse seismic; (b) Change in pressure; (c) Change in saturation; and (d) Time-lapse CSEM.*

However, as soon as pressure drops in 2006 and in 2008, significantly below the value for 2004, there is seismic hardening. This seemingly indicates that ΔS_w now leads ΔP for these later intervals. Now, the high amplitude change in the CSEM

response is almost consistent for all the three monitor periods considered. This indicates constant hardening, as the magnitude of ΔS_w with respect to the baseline is almost the same for all the time intervals (Figure 5.14c and d). At later time intervals 2006 and 2008, reduced pressure could not support water flooding and there is very little or no change in ΔS_w. Therefore, the seismic hardening signal in 2006 and 2008 is actually due to drop in pressure drop from 2004, and not increase in water saturation. The time – lapse CSEM response confirms this because there is very little or no increase in amplitude change.

Also, at these late intervals, the area indicated by oval shape at the right hand corner shows that the slight increase in ΔP (which should ordinarily produce seismic softening) and the slight increase in ΔS_w (which should ordinarily produce seismic hardening) have both cancelled out each other in the time-lapse seismic maps. Whereas, the slight increase in ΔS_w is captured by the time-lapse CSEM maps. Similar to the interpretation around injector I4 (in Figure 5.13). Interpretation here also point to the fact that time-lapse CSEM is helpful in separating pressure and saturation effects in 4D seismic especially when both effects indicates no 4D seismic signal.

iii. Along the channel connecting water injector I6 (operational between 2003 and 2008) to producer P3 (operational between 1999 and 2007): The time-lapse CSEM maps clearly illuminate the time progression of the water flooding front from injector I6 towards producer P3 until there is a water-breakthrough at the producer in 2008. This means, we can have early warning of water breakthrough from time-lapse CSEM interpretation. The maps also indicate that, within the previously flooded area, there is no significant change in water saturation from one period to the next. This could be diagnostic of efficient water flooding as the front progresses, and it shows that time-lapse CSEM can be a tool of choice in this case (Figure 5.15d and e). Interpretation of time-lapse seismic maps (Figure 5.15a) is not this straightforward due to the complicating effects of changes in water saturation, changes in pressure and the gas coming out of solution.

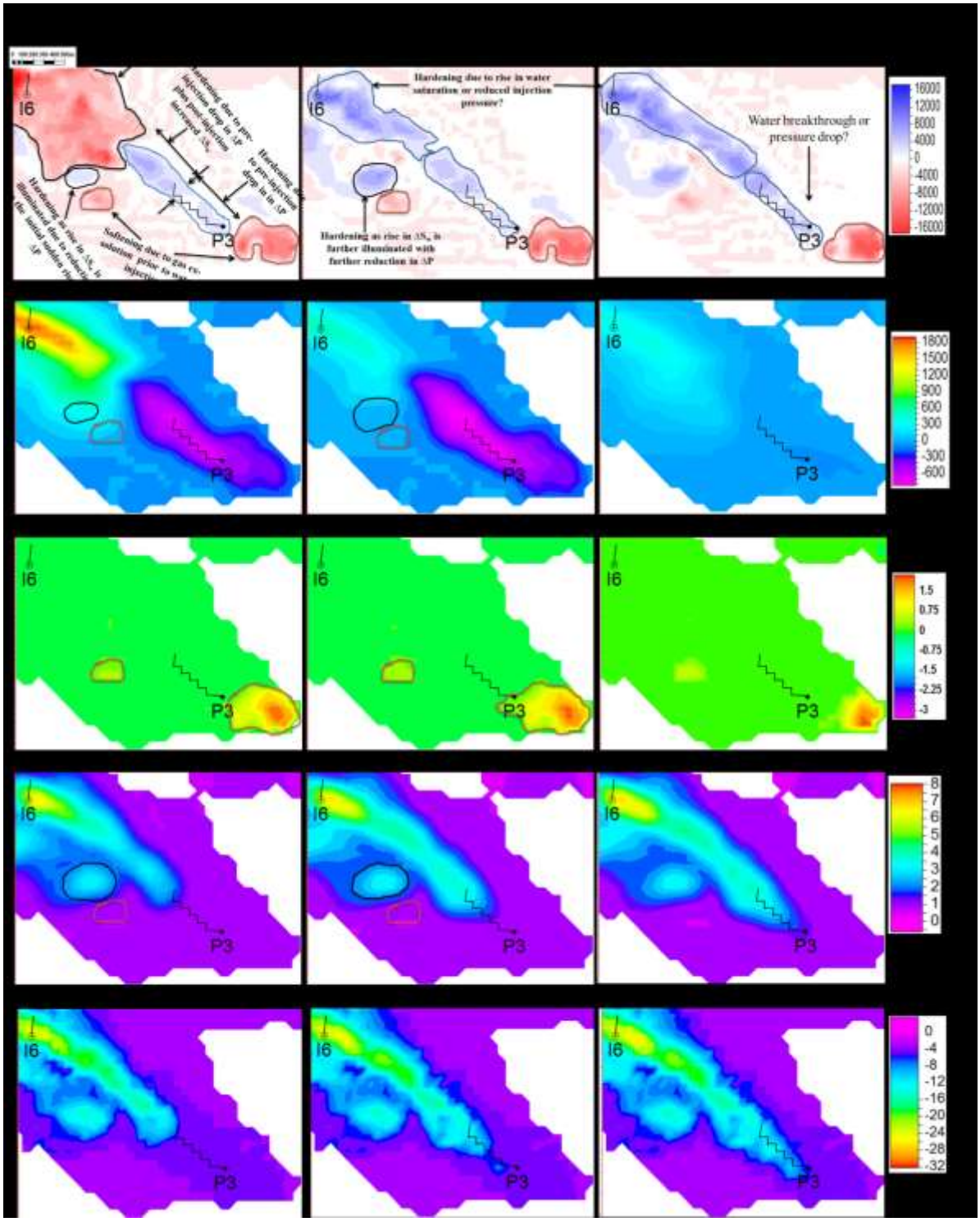

Figure 5.15: *Interpretation along the channel connecting water injector I6 to producer P3, at a larger scale, for six years (2004 – 1998), eight years (2006 – 1998) and ten years (2008 – 1998) of production and injection activities: (a) Time-lapse seismic; (b) Change in pressure; (c) Gas liberation; (d) Change in saturation; and (e) Time-lapse CSEM.*

At the onset of water injection at I6 (in 2004, less than one year since injection started), we know seismic softening near the injector is due to the sudden increase in ΔP (as already highlighted in ii above). The softening signal has a much more higher effect than required to compensate for the hardening due to increased water saturation. Therefore, it is difficult to determine water flooding front in this situation, because the image of seismic softening signal replicates the image of pressure diffusion rather than that of water movement (Figure 5.15a, b and d). Time-lapse CSEM (Figure 5.15e) is definitely helpful in this case, as it illuminates the water flooding front (Figure 5.15d).

Behind the producer P3 to the right hand side (Figure 5.15), for all the time-lapse periods considered, we know seismic softening is almost certainly due to gas liberation as a result of pressure drop below the bubble point pressure. Here, the gas effect is much more than enough to compensate for the hardening effect of pressure drop (in 2004 and 2006). Even when ΔP = 0 in 2008, the gas has not been completely forced back into solution, thus seismic softening is still observed (Figure 5.15a, b and c). The smaller circular – shaped seismic softening effect (smallest region between injector and producer) is difficult to interpret. It could be, errorneously, related to slightly elevated pressure rather than gas effect from pressure drop below the bubble point pressure. However, the slight pressure elevation is not compartmentalized from the bigger pressure elevation (Figure 5.15b). Whereas the smaller area of seismic softening is detached from the bigger one near the injector. Moreover, the maps in Figure 5.15c consistently indicates that there is gas liberation at this location for all the time intervals. This means there is a large scale pressure drop away from the producer (which has been producing since 1999) prior to water injection in 2003, and this is why little traces of gas are still been illuminated by seismic responses all over the mapped area. What we now see is the post- and syn- injection effects with imprints of pre-injection effect. Time-lapse CSEM is completely blind to gas effect, thus it can not provide any help in this case. The small circular – shaped area slight seismic hardening just below the initial softening (in 2004) can be interpreted as the illumination of originally hidden rise in ΔS_w as initial rise in ΔP reduces spatially away from the injector. The

hardening signal becomes stronger in 2006 and 2008 with varying diameter as ΔP further reduces. Seismic, unlike CSEM, in this case does not offer exact diameter of the compartimentalized hardening signal (see Figure 5.15a, d and e). Similarly, in 2006 and 2008, the upper elongated seismic hardening event is mainly an illumination of originally hidden rise in ΔS_w as initial rise in ΔP reduces away from the injector. This also shows the water flooding front. So, while the time-lapse CSEM indicates the water flooding front from the onset of injection in 2004, time-lapse seismic only shows the same from 2006.

The enlongated – shaped seismic hardening, between the two softening signals (in 2004) looks like a continuous water flooding front and could be erroneously interpreted as water breakthrough at the producer, but actually the section can be divided into two events. The upper part (with slightly higher signal strength) being a combination of pre-injection drop in ΔP and post- or syn- injection increase in ΔS_w. While the lower part being mainly pre-injection drop in ΔP. Similar interpretation follows in 2006 for the elongated hardening near the producer. In 2008, the same seismic hardening feature could now be fully interpreted as water flooding front breaking through the producer because ΔP = 0. Without the pressure and water saturation maps, one could errorneously interpret this 4D seismic hardening as water breaking through at the producer P3 from 2004. The time-lapse CSEM, on the other hand clearly indicates time progression of water flooding front which is yet to break through at the producer in 2004. So, in reality, time-lapse CSEM can be a definite tool to monitor water flooding front, and to obtain warning for an early water breakthrough at the producer.

iv. Around producer P5 (operational between 2000 and 2007, and then from 2009) and injector I8 operational (between 2004 and 2009) along the channel: In all the three periods, both the hardening signal on the 4D seismic maps and the time – lapse CSEM maps clearly show the water flooding front along the channel.

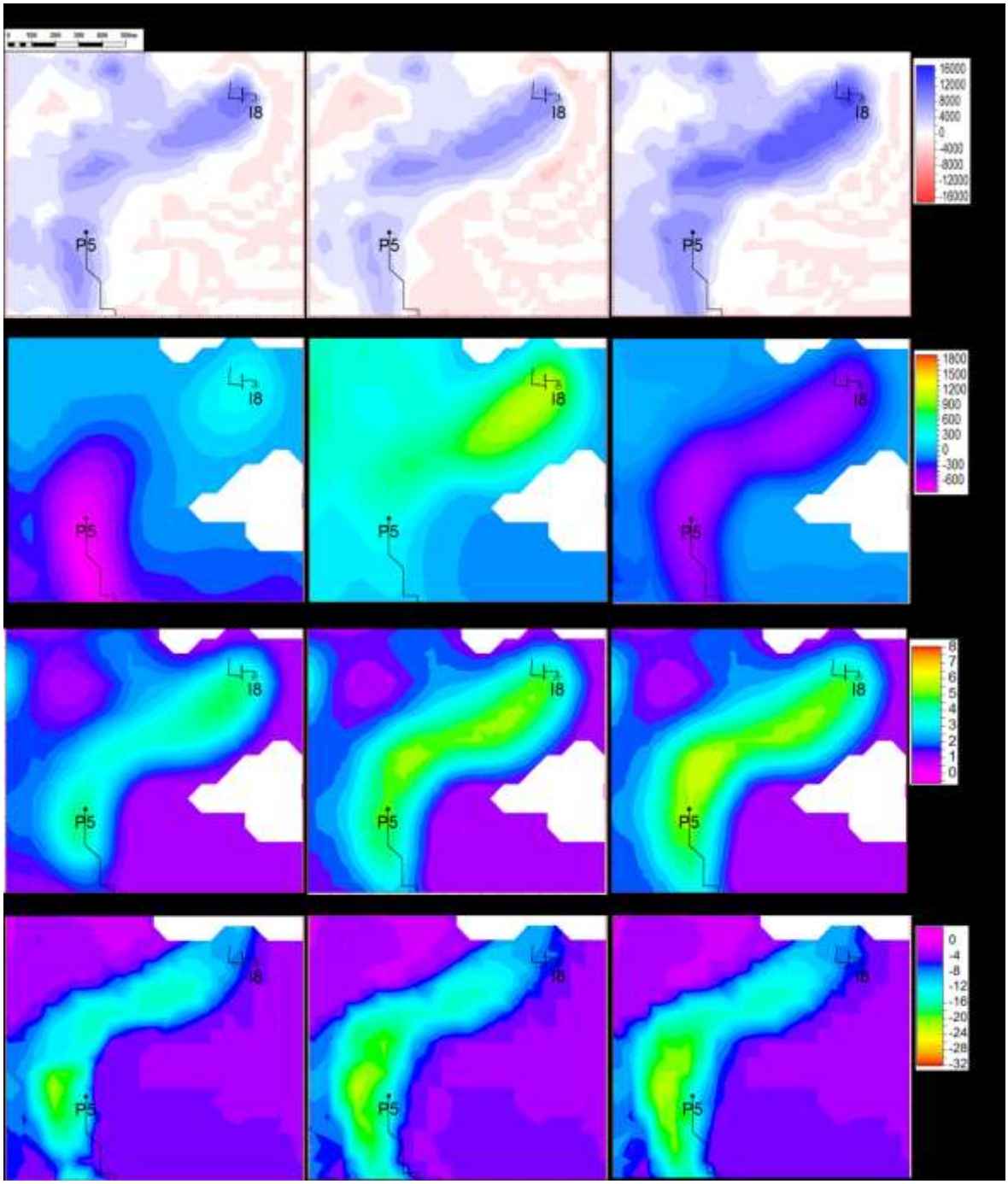

Figure 5.16: *Interpretation along the channel connecting water injector I8 to producer P5, at a larger scale, for six years (2004 – 1998), eight years (2006 – 1998) and ten years (2008 – 1998) of production and injection activities: (a) Time-lapse seismic; (b) Change in pressure; (c) Change in saturation; and (d) Time-lapse CSEM.*

They also indicate water breakthrough at the producer P5 (Figure 5.16a, c and d). However, at 2004 or prior to 2004, pressure had dropped at producer P5 which

probably necessitated injector I8 in 2004. The injection at this time has introduced increased ΔS_w along the channel down to P5, but the pressure introduced at I8 is too small and not enough to raise the pressure at P5. Therefore, the 4D seismic hardening at P5 in 2004 is a combination of both injection induced rise in ΔS_w and pre-injection drop in ΔP. In 2006, increased pressure at I8 has raised ΔP at P5 from negative to zero, thus 4D seismic hardening persists at P5 but now, as expected, with lower magnitude because the earlier additive effect of pressure drop has been removed.

However, the increased pressure at I8 has little or no effect on the seismic hardening. The water effect has already taken the lead. As at 2007, P5 had been shut down due to water breakthrough, but I8 was still supplying water till 2008, thus pressure had dropped along the channel. This raises the magnitude of 4D seismic hardening in 2008 compared to 2006 with respect to the baseline (1998). Time-lapse CSEM has the potential of helping 4D seismic to resolve the two reinforcing effects of changes in water saturation and pressure.

Table 5.1 gives summary of these interpretation which shows that time – lapse CSEM can:

(a) Assist in constraining quantitative separation of ΔS_w from ΔP in time – lapse seismic, either when high positive ΔP is hidden under high positive ΔS_w as seismic hardening (left and middle panels, Figure 5.13) or when high positive ΔS_w is hidden under high positive ΔP as seismic softening (left panel, Figure 5.14). The time – lapse CSEM will show hardening response to high positive ΔS_w in both cases.

(b) Unmask the water flooding front and its dimension whenever positive ΔS_w is masked under positive ΔP as time – lapse seismic softening (e.g. left panel, Figure 5.14). The time – lapse CSEM will show hardening response along the water flooding front.

(c) Help confirm constant ΔS_w between two monitor periods, in which drop in ΔP is captured as time – lapse seismic hardening. In this case, time-lapse CSEM with respect to the baseline for these two monitor periods will be almost constant. In other words, CSEM can serve as a proxy to confirm pressure drop (e.g. Figure 5.14, between 2004 and 2006, and between 2006 and 2008).

Well location and time	Reservoir activities		Time lapse geophysical amplitude change		Interpretation
	ΔSw	ΔP	ΔA Seismic	ΔA CSEM	
Away from I4 (2004)			+ve Moderate (Hardening)	-ve High (Hardening)	In 2004 and 2008, ΔSw leads ΔP. Seismic and CSEM show the water flooding front. Hardening increases progressively with increasing Sw, even in 2006 when ΔP = +ve higher than in 2004. CSEM can help constrain separation of ΔSw from ΔP in seismic.
Away from I4 (2006)			+ve Moderate (Hardening)	-ve High (Hardening)	
Away from I4 (2008)			+ve High (Hardening)	-ve High (Hardening)	
Around I6 (2004)			- ve High (Softening)	-ve High (Hardening)	In 2004, ΔP leads ΔSw. CSEM illuminates the water flooding front. In 2006 and 2008, ΔSw leads ΔP and seismic now illuminates the water front. CSEM can help constrain separation of ΔSw from ΔP in seismic.
Around I6 (2006 and 2008)			+ve Moderate (Hardening)	-ve High (Hardening)	
Far right of I6 (2006 and 2008)			Zero	-ve Small (Hardening)	No seismic signal as ΔP effect cancels ΔSw effect. CSEM illuminates the slight increase in Sw
Behind P3 (2004, 2006)	Zero		- ve High (Softening)	Zero	In 2004 and 2006, ΔP = -ve high. Gas is liberated, thus seismic softening. Softening persists in 2008 even when ΔP=0 because liberated gas has not been force to solution completely. ΔSw = 0. CSEM has no use.
Behind P3 (2008)	Zero	Zero	- ve High (Softening)	Zero	
Lower elongated section between I6 and P3 (2004 and 2006)	 Zero		Continuous +ve Moderate (Hardening)	-ve High (Hardening) close to 16, Zero close to P3	Seismic hardening near the injector merges with hardening near producer. Could be erroneously interpreted as water break through at the producer. CSEM shows the extent of the water front from the injector, and zero response near the producer.
I8 and P5 along the channel (2008)			+ve high (Hardening)	-ve High (Hardening)	Seismic hardening is a combination of drop in ΔP and rise in ΔSw with respect to the baseline. CSEM hardening is mainly due to rise in ΔSw. CSEM can help constrain separation of ΔSw from ΔP in seismic.

Table 5.1*: Summary of interpretations shown in Figures 5.13, 5.14, 5.15 and 5.16 near selected well locations.*

(d) Help illuminate areas with slight positive ΔS_w, where the effects of slight positive ΔS_w and slight positive ΔP have cancelled out each other to yield zero time – lapse seismic amplitude. Time – lapse CSEM will show little hardening response to slight positive ΔS_w (e.g. oval shaped area on the right of Figure 5.14).

(e) Help confirm – the warning of possible water breakthrough by illuminating water flooding figering towards the producer. Whenever pre-injection drop in pressure near the producer is connecting and reinforcing the water flooding front towards the producer, from the injector, seismic hardening signal becomes continuous and will not be able to separate the two events. CSEM will separate the two events as it will give zero signal to the pre-injection drop in pressure near the producer, thereby confirming the figering extent of the water front (e.g. lower enlongated section between I6 and P3 in Figure 5.16 for monitors 2004 and 2006)

These are some of the scenarios whereby time-lapse CSEM, which is a definite water indicator, can play a complimentary role to 4D seismic in reservoir monitoring. This is especially important when we do not have reliable production data or we need to update the simulation model or we require more geophysical inputs to make reservior management decision. CSEM can not discriminate gas from oil, thus blind to gas exsolution, just as it is also blind to pressure changes. This limitation is a *blessing* because it helps in confirming seismic events. Therefore, CSEM is not a substitute to seismic in reservoir monitoring, but it is, potentially, a good complimetary tool that could help resolve ambiguities involved in time lapse seismic interpretation. Thus, integration of time lapse CSEM with 4D seismic is desirable.

5.6 Summary

Comparison of time-lapse CSEM and seismic amplitudes on the basis of their sensitivities to change in water saturation within a producing reservoir where other dynamic events are taking place showed that the CSEM is more linearly related to the change in water saturation than the seismic. This is not surprising since seismic amplitude change is not just a response to change in water saturation, but to a combination of changes in pressure, gas and water saturations. Coupled interpretation of the modelled time-lapse CSEM and seismic maps further revealed that the time-lapse CSEM has a great potential to reduce interpretational ambiguities in time-lapse seismic, especially when there are subtraction or addition of signals due to different combinations of changes in pressure and water saturation both in time and space. This CSEM potential is also reinforced with the fact that time-lapse CSEM is blind to separating gas from oil, thus offering seismic a good

confirmation of situation when pressure drop below the bubble point has caused gas ex-solution, and there is need for an engineer to build up pressure through injection.

However it should be noted that the CSEM modelling method here employed Dipole 1D, which is expected to produce the best possible dataset required to interpret for detailed information about the small dynamic changes within the reservoir. This is why high quality dataset is of utmost importance. 4D seismic data acquisition technology has progressed over the years with a lot of improvements, and for time-lapse CSEM interpretation to become a reality, efforts on its acquisition technology should take a great leap to the level whereby joint 3D and 4D dedicated CSEM and seismic data acquisition would be possible. This is when the best of the complimentary roles of the CSEM to the seismic, particularly in reservoir monitoring, will be revealed. Dedicated 4D joint acquisition will not only save money, but will also enhance frequent reservoir monitoring. In this chapter, it has been shown that coupled qualitative interpretation of time-lapse CSEM and seismic dataset is possible, but high quality dataset will be required to make this a reality.

CHAPTER 6

THE EFFECTS OF TEMPERATURE AND SALINITY IN TIME – LAPSE CSEM

"Then, water is not water" – Colin MacBeth

6.0 Introduction

In Chapter 5, an assumption of similar temperature and salinity conditions for both the injected and the formation waters was made in order to assess the interpretation of time-lapse CSEM in terms of change in water saturation. The assumption facilitated comparison of time-lapse seismic and CSEM in terms of their sensitivities to change in water saturation in the presence of change in pressure. It also enhanced coupled interpretation of time-lapse CSEM and seismic modelled data for qualitative separation of change in water saturation from the change in pressure and gas ex-solution and the attendant management issue. This means '*water is assumed as water*', irrespective of which type of injected water (IW) is involved, and whether the *in situ* water is connate water (CW) or aquifer water (AW) or mixture of two or three of these waters. The production scenario in Chapter 5 is then tantamount to re-injection of produced water at the later stage of oilfield production.

However, we know that production engineers normally want to produce a high volume of oil with a very little amount of water by avoiding or delaying water breakthrough at the producer wells. Even when there is water breakthrough, the produced water is never enough to replace the produced fluids (oil and water) in the reservoir, and extra volume of water is usually sourced elsewhere in order to meet the volume of water required to sustain injection process and keep the material balance. Thus, in all forms of water injection scenarios, either mainly aimed for secondary recovery or tertiary recovery or in form of enhanced oil recovery involving water, there will always be an introduction of dissolved chemical and isotopic compounds into the native reservoir waters (CW, and/or AW). These introduced compounds are usually different from those of the *in situ* waters in terms of, among others, salinities and ionic constituents which could mix together somewhere within the reservoir with a resultant effective (mixed reservoir – water) salinity (S_e). Also, these

waters have different temperature conditions. In particular, we expect the IW, say sea water, to have lower temperature than the subsurface in situ CW or AW. Thus, the injection process is associated with cooling effect with resultant effective temperature (T_e). Therefore, both salinity and temperature conditions of the reservoir are directly impacted during the production and injection activities, and this has implication on the spatial and dynamic value of effective resistivity (R_{we}) of mixed-water within the reservoir, which then impacts on the true resistivity of the fluid-saturated reservoir (R_t), and in turn the CSEM electric and magnetic field responses. Invariable then, '*water is not water*', and this fact is recognized in Chapter 3 where the engineering consistent rock physics is expressed to cater for effective mixed-water properties in the reservoir (see equations 3.17 and 3.18).

The dynamic variations in salinity and temperature in terms of injected fluid versus the in situ fluid are usually tracked as tracers in the reservoir fluid flow simulator. Therefore, in terms of time-lapse CSEM monitoring of water flooding, the fact that '*water is not water*' could either require us to cater for the variation in resultant effective R_{we} while interpreting for the change in water saturation in the repeat CSEM data or in the inversion for change in reservoir resistivity. We might equally just be tracking for different brines for better reservoir management and dynamic reserve estimation of the producing field. As we know, injected water could either mix with the connate water in the oil leg or mix with the aquifer water in the water leg, depending on the injection strategy (e.g. at which part of the reservoir is the injection taking place), see Figure 2.10 in Chapter 2. Therefore, interpretation of time-lapse CSEM for the purpose of tracking water injection will require prior knowledge of the production engineering strategy in the field including the nature of the IW, which could either be sea water, river water, low salinity water, subsurface aquifer water or mixture of any of these with the produced water.

Understanding of the native and the injected waters chemical compositions and how they mix together is also important in terms of the production related issues like corrosion and formation of chemical scales after water breakthrough (Sorbie & Mackay, 2000). For instance, whenever injected sea water, rich in Sulphate (SO^{-4}) ions, mixes with the connate or aquifer water, rich in Barium (Ba^{+2}) ions; solid $BaSO_4$ scale is either precipitated within the reservoir or in the aquifer, which could reduce the porosity and/or permeability of the

reservoir at that location. The $BaSO_4$ could equally be deposited at the producer well, and may block the pipe. These have detrimental effects on production. However, the effects depend on fluids displacement mechanism and the spatial location where fluids mixing are taking place. Numerical modelling of brine displacement and mixing within the reservoir, chemical analysis of produced water or formation water obtained from repeat formation testers (RFT) and drill-stem test, and scale tendency prediction are some of the engineering techniques used in understanding mixing of IW, CW and AW and scale precipitation. Scale inhibiting chemicals are also been added to sea water prior to injection. These methods have their limitations and uncertainty, they are either model-based or mostly restricted to well location, nevertheless they enhance early detection of scaling and the design of preventive measures to avoid its consequences. Repeat CSEM surveys may find proxy application in this respect. Although, CSEM may not be able to detect the solid $BaSO_4$ scale directly, but could possibly detect the resultant effective R_{we} of the mixing brine which should be different from the R_w of individual constituent waters (i.e. IW, CW and AW). If the brine mixing location, where mineral scale may be deposited, is known; then remediation measures to prevent its detrimental effect could properly be targeted at such location. Thus, the initial boundary conditions should be such that there is a significant contrast among the various R_w values for different waters involved. The differences in the salinities and temperatures will play significant roles in this. The salinity of a fluid or a mixture of fluids is the resultant effect of different ionic constituents, expressed in part per million of *NaCl* equivalent.

Sorbie & Mackay (2000) described different scenarios of fluid displacement processes and water mixing mechanisms as shown in Figure 6.1. Their description is here modified with recognition to how R_w value might change in space and time within the reservoir as production and injection activities evolve. In the vertical profile in Figure 6.1a, the producer is perforated in the first four layers, as resistive oil is originally present in these layers, before production and injection activities started. The water injector is perforated in the five layers, including the aquifer. Layer 1 is still producing oil, thus the CSEM measurement should identify the resistive oil distinctively from the conductive water behind it.

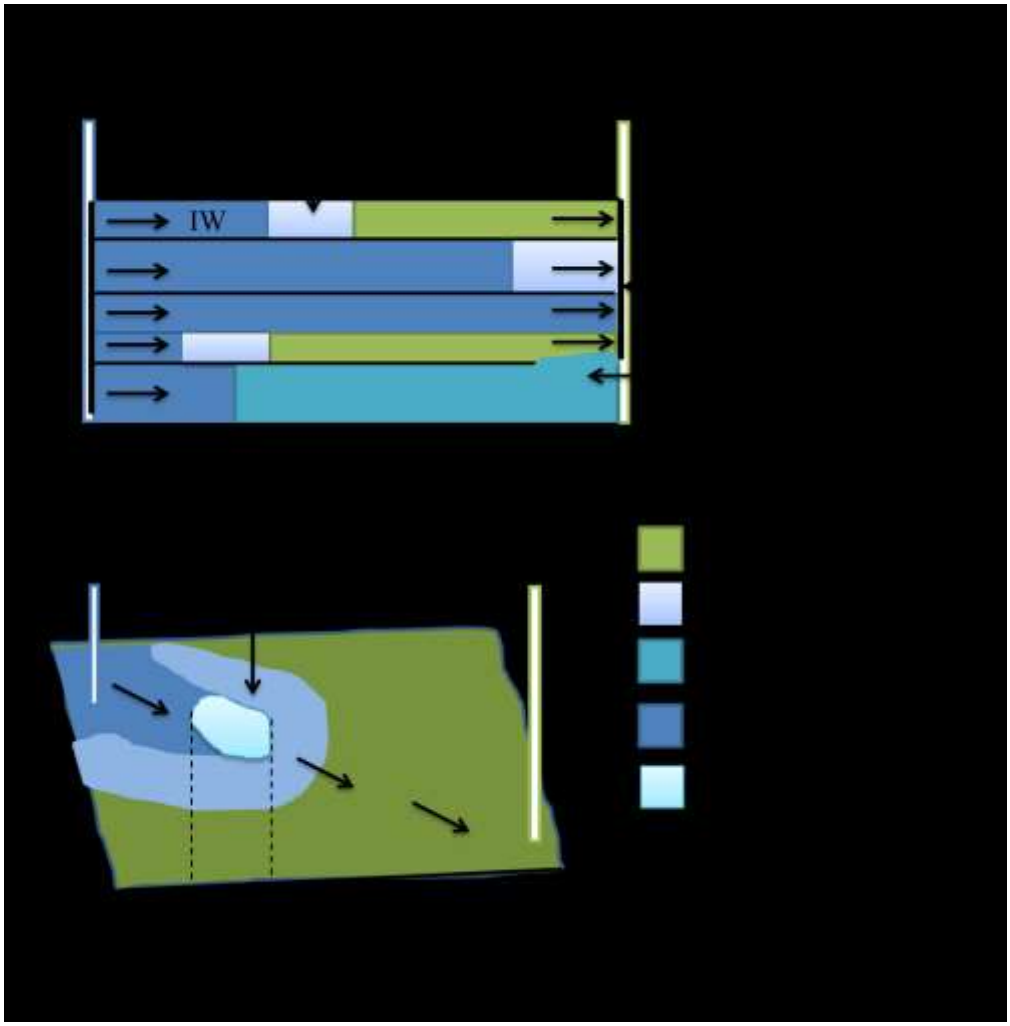

Figure 6.1: *(a) Schematic of 2D fluid displacement processes that are possible, in a vertical cross-section of heterogeneous reservoirs depending on where the injector and/or producer are perforated. Different R_w values are possible at different frontal position within a layer. (b) Schematic of water injection process showing areal flooding pattern involving displacement and mixing of fluids (modified from Sorbie & Mackay 2000).*

So, one might not bother to know the difference between the two types of waters coming behind the oil, and that is when 'water is water'. In layers 2 and 3, the oil has been produced completely, and we now have the connate and injected waters respectively breaking through at the producer. Here, scaling might occur in the well, in which case the CSEM measurements might not be able to detect. However, it could be hypothesized that repeat CSEM measurements should be able to differentiate the waters within the reservoir, and then offer information about the early water breakthrough at the producer. Similarly,

the upward coning of the aquifer water, driven by injected water in layer 5 and lithological continuity between layers 4 and 5, could be detected before it breaks-through into the producer perforated in Layer 4. In any case, the intra-reservoir contacts between the various waters in any of the five layers should be detectable if there exists measurable contrast in R_w, say for layer 1, between the IW with R_{iw} and the CW with R_{cw}. Such contrast will help to identify connate water banking between the injected water and the oil column, which could help in reservoir management. The areal 2D water flooding in Figure 6.1b shows the mobile 'banked' CW and the mixing zone of IW and CW. Here, we are less concerned about the immobile (irreducible) low saturation CW in the oil leg, because even when the mobile CW displaces more oil and mixes with the left over irreducible CW, there might neither be scaling nor even change in R_w value, and if at all, it will be negligible. Our concerns, therefore, are to determine spatial and time change in R_w along the streamlines from the IW near the injector, to the mixing zone, to the 'banked' CW, and to the resistive oil near the producer. And as a proxy to scaling, we might be able to use CSEM to determine the size of the mixing zone (l) based on R_w variation.

Apart from the differing conditions between the injected water and the native water; there might also be spatial variations in the native formation waters (CW or AW) in terms of ionic make-up, salinity, temperature, and thus water resistivity. These variations could be on a small scale across a chosen field, either within the same formation (say within a reservoir) or between two formations (say, between two reservoir sections overlying each other). It could also be on a large scale across a region, either within the same formation or between two different formations (Warren & Smalley 1993). The variations are driven by syn-depositional and post-depositional geological events involving waters (e.g. sea water, meteoric water, subsurface water etc) and chemical interactions with the host sedimentary rocks. For instance, Glasmann et al. (1989), while studying the history of diagenesis and fluid migration across Heather Field within the Middle Jurassic Brent Group, using geochemical evidences including the formation-water chemistry; reported R_w variation ranging between 0.443Ωm to 0.074Ωm, which is equivalent of salinity between 14,000ppm to 100,000ppm respectively. This order of 6 times variation in R_w, shown in Figure 6.2, is significant in terms of calculating water saturation distribution across the field; hence oil saturation, using electric rock physics. Therefore, studies by Glasmann, et al. (1989) is not only important to the understanding of digenetic history and quality of the reservoir, but

also critical to the estimation of static hydrocarbon saturation as discussed in the literatures (e.g. Worthington & Johnson, 1991). It is worth-mentioning that the R_w variation is not just a function of salinity variation; in situ variation in temperature, especially, as a function of depth, and also with the thermal conductivity of the lithologic make-up of the reservoir either laterally or vertically, is also responsible for the variation in R_w.

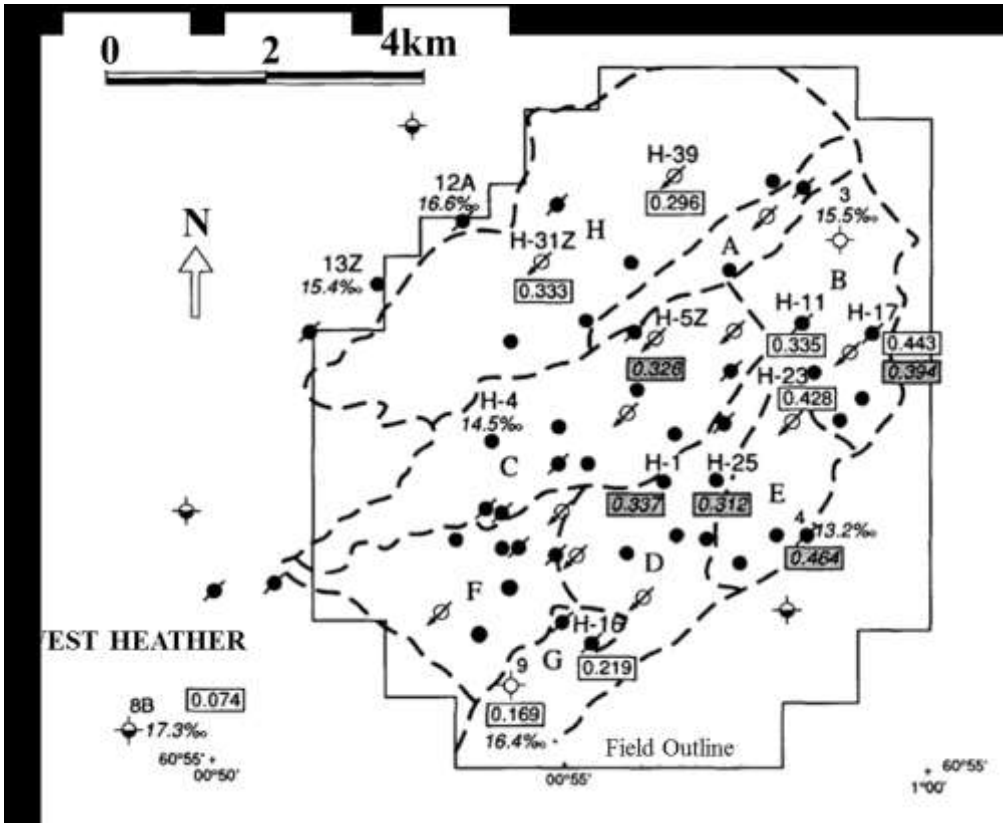

Figure 6.2: *Example of varying water resistivity (at 15°C temperature) distribution across Heather Field (originally from Glasmann et al. 1989, reproduced from Warren & Smalley 1993). Shaded values are for formation water with 15% sea water contamination.*

Based on the foregoing, therefore, the assumption of a single or average value of R_w at a well location as it is usually done in petro-physics, even in the same reservoir horizon, is not valid in reservoir simulation modelling involving both the in situ lateral and vertical variations in lithology, salinity and temperature. Unfortunately, unlike the porosity, permeability, NTG and other static parameters that could be specified for each grid cell in the simulation model to reflect their heterogeneities; geologically – consistent field heterogeneities in reservoir temperature and formation water salinity are not usually considered on cell by cell basis. I presume one major reason for this to be the lack of field

wide temperature and salinity dataset. These data are mainly obtained, either from the produced water-chemistry, or at well locations mainly in terms of R_w. Information about field distribution of R_w is scarce in the literatures and the few available ones are only found in journals that are least suspected, for instance, in diagenesis journals (Warren & Smalley, 1993). Single static average values of these parameters are then assigned for the entire simulation cells.

The potential of CSEM to delineate in situ variation in temperature and salinity was inadvertently recognized by MacGregor et al. (2001), when they interpreted a low resistivity anomaly from marine CSEM survey as diagnostic of the hot and saline fluids penetrating the crust at a site of extensive hydrothermal activity in the Valu Fa Ridge at the Lau Basin. They suspected that the low resistivity anomaly could not have emanated from the high porosity since such hypothesis is not consistent with the seismic information available (high velocity). Now, for the time-lapse application, we first have to identify different sources of injected waters and their relative differences in salinity and temperature with respect to the formation water. We need to understand the science of S_e and T_e in respect to fluid – fluid and/or fluid – rock interactions during water injection. We also need to examine individual effects of S_e and T_e or their combined effect as R_{we} on the time-lapse CSEM responses for a common case of sea water injection using the North Sea field example available. Then, we need to identify different practical scenarios of injected and formation waters with varying salinity-temperature boundary conditions, and how time-lapse CSEM might be interpreted in tracking such water.

6.1 Different sources of injected water

Water is normally injected in order to provide pressure support for the reservoir, and to help sweep and displace hydrocarbon towards the producer wells. It could also be, mainly, to raise the recovery factor and maintain the production rate for a long period of time. In order to set the initial boundary condition for the numerical simulation of water injection process, it is important to know the source and the nature of injected water (IW). IW could be obtained from different sources based on availability and other factors like chosen EOR mechanism. Each of these sources of water have temperature and salinity regimes that are very much different from the native temperature and salinity of the formation water. Thus,

they have different impacts on the electrical properties of the reservoir, which we attempt to determine with CSEM measurement.

These sources include:

(a) **Sea water**: it is the most convenient source of water to drive offshore hydrocarbon production. It is usually taken from sufficient depth in order to reduce algae concentration. Filtering, deoxygenating and biociding are required processes to make the sea water suitable for injection. The temperature condition of injected water is assumed as the seasonal surface temperature at the injector well head, not necessarily, the water-depth temperature, where the water is acquired. The salinity value may vary depending on many factors, some of which are described in Chapter 4. The dissolved salts in the sea is mostly made up of about 30.6% of Sodium (Na^{+}) and about 55% Chloride (Cl^{-}) ions. Magnesium (Mg^{+2}), Calcium (Ca^{+2}), Potassium (K^{+}) and Sulphate (SO_4^{-2}) are the other main components which together account for about 13.65%. Other minor dissolved salts account for 0.75%as shown in Figure 6.3 (University of Rhode Island 2014). The sea water salinity, in equivalent NaCl part per million, is about 30,000 to 35,000 (e.g. in Rider & Kennedy 2013).

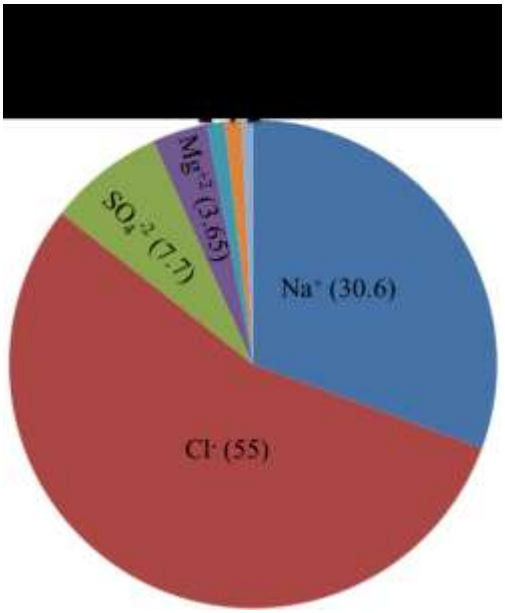

Figure 6.3: *Typical dissolved salts in % – constituents of the sea water (University of Rhode Island 2014).*

(b) **River water**: it is more suitable for onshore production. It also requires filtering, deoxygenation and biociding before injection. It is usually less saline than the sea water, and its temperature is the value measured at the well-head.

(c) **Aquifer water**: it is the subsurface water obtained from water bearing formations other than the oil reservoir. It is usually taken from either the same structure or a nearby structure from the reservoir, and it is considerably pure. While the salinity of the aquifer water might not necessarily be higher than that of the sea water, its temperature is expected to be higher.

(d) **Low salinity water (LoSal)**: this injected water is intentionally made to be of substantially low salinity. While other waters are injected mainly for secondary recovery; low salinity water, on the other hand, is injected for enhanced oil recovery of oil-wet reservoirs. The salinity value of LoSal water may be as low as 500ppm and usually not more than 2,000ppm depending on the clay content of the reservoir, as very low salinity, almost tending to pure water could cause clay swelling. Lager et al. (2011), among other examples in the literatures, presented evidence of enhanced oil recovery using this type of water injection, which is a relatively new technology championed by BP Exploration & Production company.

(e) **Produced water**: this is simply re-injection of produced water. It helps to reduce potential formation damage due to incompatible fluids. Removal of hydrocarbon and solid contaminants in an environmental friendly manner is required before re-injection, and this could make the process as costly as other types of water injection. Also, produced water volume is never sufficient to replace all the produced volumes (oil, gas and water), thus additional 'make-up' water from a different source are usually needed, which may increase the risk of scaling.

Table 6.1 shows the vast variation in the salinities, temperatures and electrical resistivities of injected and formation waters around the world.

Fluid type		Example of oilfield/province	Temperature (°C)	Salinity (ppm of NaCl)	Resistivity, R_w, (Ω-m)	Comment
Formation water		[1]Simpson sd, Oklahoma	-	298,497	0.0001575	
		[2]Saudi Arabia (Arab - D)	93	150,000 - 200,000	0.018 - 0.022	
		[1]Burgan, Kuwait	-	154,388	0.053	Rw calculated at 24°C
		[1]US average	-	94,000	0.08	
		[1]Woodbine, E, Texas	-	68,964	0.1	
		[3]Endicott/Alaska	100	20,000	0.13	
		[7]Niger Delta/Nigeria	54	20,000	0.19	
		[5]Schiehallion/North Sea	57	18,000	0.2	
		California petroleum basins	-	30,000 - 35,000	0.19 - 0.22	Rw calculated at 24°C
		[4]Daquing Field, China	45	5,000 to 7,000	0.55 - 0.74	
		[1]Laugunillas/Venezuela	-	7,548	0.77	Rw calculated at 24°C
Injected water	[1,5,6]Sea water	Niger Delta/Nigeria	24	30,000 - 35,000	0.19 - 0.22	
		Alaskian (Arctic)	5 to 17	30,000 - 35,000	0.22 - 0.36	
		North Sea	5 to 17	30,000 - 35,000	0.22 - 0.36	Average values used for modelling at Schiehallion field during summer: 15°C; 30,000ppm; 0.27Ω-m
	[2]Subsurface Sandstone aquifer water (Wasia and Biyadh)	Saudi Arabia	37	5, 000 - 20,000	0.24 - 0.82	Injected water sourced from the sandstone aquifer overlying the carbonate reservoir
	River water		5 to 50	5,000 - 14,000	0.26 - 1.73	
	[3]Low salinity water	Endicott	24	500 - 1,500	3.05 - 8.03	For EOR in an oil-wet reservoir. Not lower than 5% of the salinity of formation water to avoid clay swelling. Standard reference temperature
	Produced water	-	-	-	-	Values are function of the in situ conditions and earlier injected water

Table 6.1: *Some typical resistivity properties for formation waters and injected waters used in secondary and tertiary recovery from a range of geographical locations around the world ([1]Rider & Kennedy 2013; [2]Rafie & Youngblood 1987; [2]Youngblood 1980; [3]McGuire et al. 2005; [4]Shehata et al. 2012; [5]Martin and MacDonald 2010; [6]Constable 2013; [7]Batzle & Wang 1992). Examples given here are ranked according to Rw values which are calculated, in some cases, with Crain (1986)'s equation in Chapter 3.*

Figure 6.4 shows five examples of different sources of injected waters and conceptualised relative differences in salinities and temperatures with respect to a formation water.

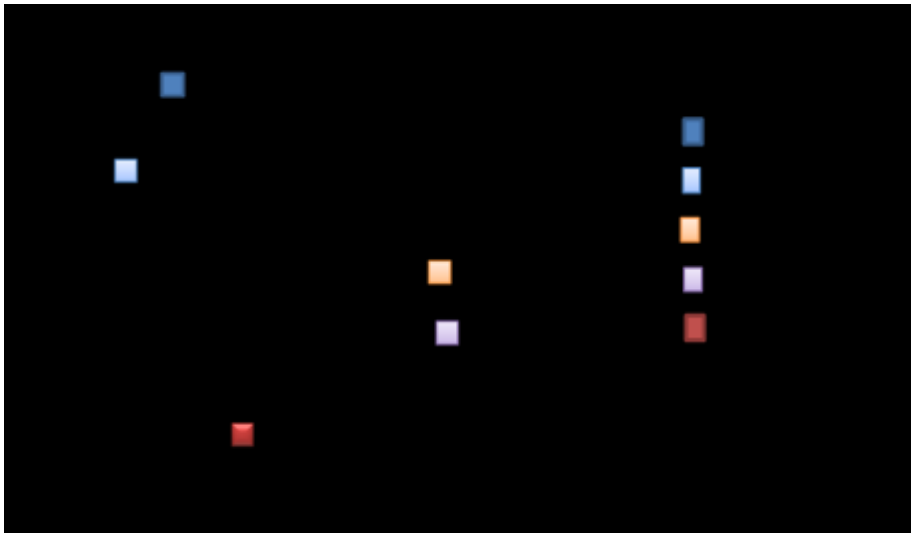

Figure 6.4: *Five examples of sources of injected waters and their probable relative salinities and temperatures with respect to the formation water.*

6.2 Numerical simulation of water injection: Tracking of salinity and temperature

In equations 3.13 and 3.14, resultant effective temperature (T_e) and salinity (S_e) are the main rock physics input parameters to track the injected water, differently from the formation water. These parameters offer the resultant R_{we} of the mixed water. Tracer tracking options are usually set in the fluid flow simulation model to obtain cell-by-cell equivalent values of S_e and T_e, at every time step, as waters with different salinities and temperatures are mixed together. Here, we discuss the science behind the diffusive heat transfer involving the fluids and the reservoir rock, and the diffusive mixing of salinities of injected and formation waters.

(a) Temperature tracking

Thambynayagam (2011) presented an equation of continuity for heat energy conservation in a given region of a medium as:

$$\frac{\partial T_e}{\partial t}(x,y,z,t) = \frac{1}{\rho.c}\left[Q(x,y,z,t) + K\nabla^2 T_e(x,y,z,t)\right] \qquad (6.1)$$

where the term at the left hand side of the equation (6.1) represents the rate of change in temperature 'Te' with respect to change in time 't' over a given volume defined by 'x', 'y' and 'z' dimensions; and on the right hand side, we have 'ρ', 'c', 'Q' and 'K' which are density, and specific heat capacity at reference pressure, heat generated per unit volume per unit time and thermal conductivity respectively. Since we are dealing with a cooling system, it is expected that the heat is transferred, both from the rock and the formation water to the injected water. Fluid-fluid (say, between the injected and formation waters) and rock-fluid interactions are driven more by thermal conduction process than thermal convection as shown in equation 6.1. Both the reservoir and the fluid content lose heat to the injected water. The specific heat are given in terms of mass for fluids, and in terms of volume for rock. The density and the specific heat capacity of the mixed fluid are saturation-scaled linear arithmetic average of the densities and the specific heat capacities of the constitent fluids involved. Thermal conductivity is the aggregate of the thermal conductivities of the rock and the fluids involved. It is assumed that the injected water travels with a high velocity, driven by well-head pressure, such that the geothermal gradient between the surface and the subsurface has a minimal effect on the injected water temperature when delivered into the reservoir. However, the water formation volume has direct effect on the reservoir volume of injected water as against its surface volume. The cooling effects of temperature due to sea water injection is examined in section 6.3.2.

(b) Salinity tracking

Based on recognized analogy between the heat and the mass diffusion, Thambynayagam (2011) modified the heat conduction equation to obtain a mass diffusion equation:

$$\frac{\partial S_e}{\partial t}(x,y,z,t) = \left[M(x,y,z,t) + D\nabla^2 S_e(x,y,z,t)\right] \;; \qquad (6.2)$$

where the term at the left hand side of the equations (6.2) represents the rate of change in salinity (S_e) in part per million of aqueous sodium-chloride (NaCl), with respect to change in time 't' over a given volume defined by 'x', 'y' and 'z' dimensions; and on the right hand side, 'M' is the mass diffusion term, which is the mass generated per unit volume per unit time while 'D' is the diffusion term. The 'D' term is driven, among other parameters,

by transmissibility, water relative permeability and pore volume which are normally defined in the simulation model. Both water density and viscosity are modified in the mixing process involving waters with different salt concentrations (salinities). In addition, for the low salinity injection, the end points water and oil saturations, and their relative permeabilities, including the water-oil capillary pressure are modified by the salinity diffusion.

For numerical simulation purposes, the mass conservation equation for salinity diffusion in a simulator cell, and the viscosity as a function of both changes in temperature and salt concentration are available in commercial simulators. Temperature and brine options, both tracer tracking, in the black oil Eclipse 100 simulator are used to track T_e and S_e for each simulation cell at every iteration time step. In addition to other parameters normally specified in the simulator, specific heat capacities and thermal conductivities of the rock and fluids making up the reservoir are the minimum thermal properties required for temperature tracking. The initial values of temperature and salinity of the formation water and those of the injected water at the injector well-head are defined as the initial boundary conditions at every time step. The initial reservoir temperature and salinity are assumed to be uniform over the entire reservoir section. Although we know these parameters vary within a reservoir layer, and between layers. Notwithstanding, this assumption will help us to determine how they vary dynamically within the reservoir during water injection. Table 6.2 shows some of the parameters used. Apart from the thermal conductivity of water which is specified at 25°C, other reference conditions are for reservoir and injected waters temperatures of 58°C and 15°C respectively, and salinities of 30,000ppm and 18,000ppm respectively. The reference subsurface pressure is 2907psia. Other values are numerically interpolated using these reference conditions.

Item	Specific heat, c, (kJ/kg°K)	Thermal conductivity, K, (W/m/°K)	Density (g/cc)	Volume factor (rb/stb)	Viscosity (cp)
Oil	2.13067	-	0.903	-	3.5
Water	4.1855	0.58	1.011	1.0061	0.5
Reservoir	127.99	1.73	-	-	-
Injected water	4.185	-	0.998	1.0061	0.6

Table 6.2: *Other parameters used in the numerical simulation (Martin & MacDonald 2010; Rider & Kennedy 2013 and various other sources)*

Three production settings are now identified as examples, with their different initial boundary conditions as shown in Figure 6.5, involving different kinds of injected waters. They are: (a) Sea water injection, such as being done to drive oil production in Schiehallion oilfields, in the UK Continental Shelf (Martin & MacDonald 2010); (b) LoSal water injection, such as been successfully recorded for Endicott field in Alaska, USA, where BP had their pilot test for the emerging LoSal EOR technology (McGuire, et al. 2005; State of Alaska, 2011). The LoSal water is manufactured by de-salinizing the seawater, hence the values of salinity and temperature; (c) Aquifer water injection, such as the drive production in Saudi Arabia oilfields, where water evolution and fluid contact movement are important to the calculation of remaining oil saturation, ROS (Rafie & Youngblood 1987; Youngblood, 1980). The potential of using time – lapse CSEM to monitor each of these injection scenarios is assessed in sections 6.3, 6.4 and 6.5.

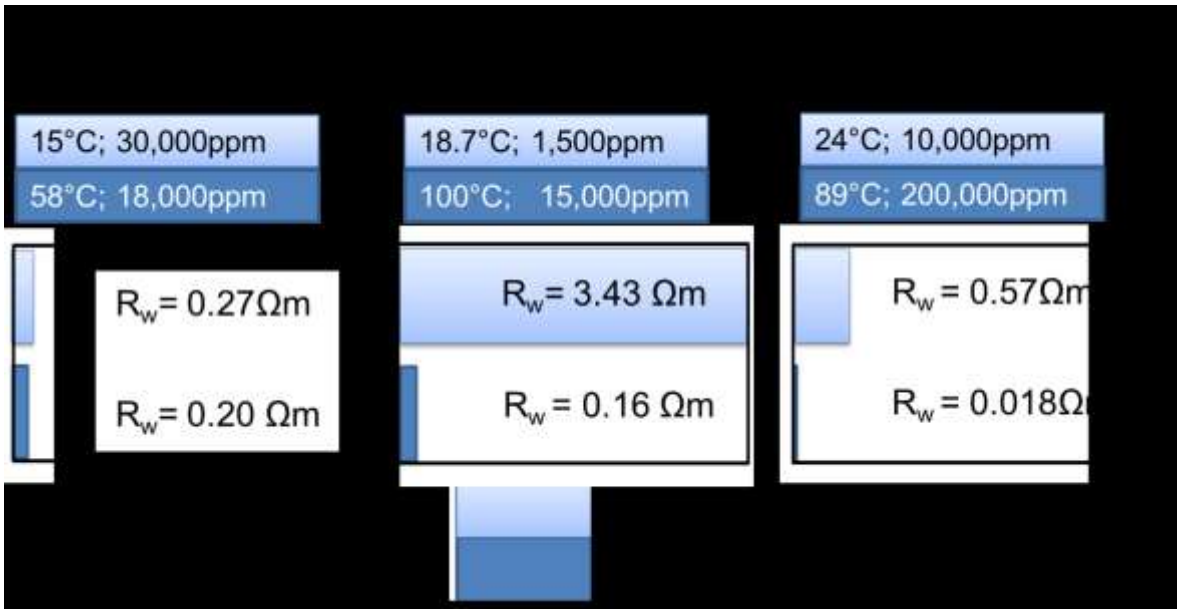

Figure 6.5: *Examples of different water injection scenarios for the reservoir models under consideration, using Crain (1986)'s equation and the literature values of temperatures and salinities for each scenarios : (a) Sea water injection; (b) Low salinity water injection; and (c) Aquifer water injection (see Table 6.1 for references).*

6.3 Example of the North Sea cold water injection

The initial boundary condition is such that seawater with temperature of 15°C, and salinity of 30,000ppm is injected into a reservoir with formation water of 58°C temperature and 18,000ppm salinity (see Figure 6.5a). These values are specified in the simulation model. Figure 6.5a shows that, for this scenario, the value of R_w of the formation water is 0.2Ωm at the initial reservoir temperature and salinity condition, while that of the injected water is 0.27Ωm. At face value, we might say we are increasing the native reservoir R_w value as we inject cold (*cooling*) and more saline water to drive oil production, and the limiting value of R_w between the two initial boundary conditions is $0.2 <= R_w <= 0.27$ (about 1.35 times difference), just at the start of the injection process (before the simulation). However, the mixing mechanism is not this straigthforward. There could as well be reduction in the value of R_w, just as the increase, such that new limiting values may exist for the effective mixed water resistivity R_{we} at a given time and space within the reservoir as injection and production proceed. The new limiting values depend on which process is leading between "*cooling*" and "*salinization*". Intuitively, as shown in Table 6.3, if the salinization process leads the cooling process, R_{we} may tend to 0.13Ωm; whereas if the cooling process leads the salinization process, we might expect R_{we} tending to 0.42Ωm. Therefore, R_{we} value is expected to vary spatially and dynamically across the field but can neither be less than 0.13Ωm, nor greater than 0.42Ωm. In order words, we should expect a mixed water resistivity to be within the limiting range of $0.13 < R_{we} < 0.42$ (less than 3.2 times difference), between a producer well and an injector well at any time step.

Item	Temperature (°C)	Salinity (ppm of NaCl)	Resistivity (Ωm)	Comment
Injected water	15	30,000	0.27	Injected water at the injector well-head
Formation water	58	18,000	0.2	Formation water at the original reservoir condition
Limiting end point values for the mixed water	58	30,000	0.13	Injected water salinity combined with formation water temperature
	15	18,000	0.42	Injected water temperature combined with formation water salinity

Table 6.3: *Limiting boundary values of R_{we} for mixed reservoir water indicated in yellow.*

6.3.1 Assessing the impact of R_{we} on CSEM sensitivity to change in water saturation

Cold saline sea water injection is simulated for a North Sea reservoir using the initial boundary conditions stated above. Before examining the sensitivity of repeat CSEM measurements to the mixing of injected saline cold water and the formation water, let us first look at how R_{we} varies spatially and dynamically. Here, we consider time periods between the pre-injection baseline (1998), and the monitors – three years (2001), six year (2004) and ten years (2008) after water injection on a larger time scale, and every three months between August 1998 and August 2000 on a smaller time scale. Figure 6.6 shows how the value of R_{we} varies over time for the larger time scale. As hypothesized earlier, the limiting value of mixed water resistivity within the reservoir undergoing cooling and salinization is actually observed to be within the range of $0.16 <= R_{we} <= 0.31$ (about 1.94 times difference). This range is larger than the range of initial boundary values. Also, it is observed that the cooling process, which suddenly raises the value of R_{we} by a magnitude of as high as 0.11Ωm, dominates at first arrival of injected water into the reservoir. The effect is restricted within the proximity of the injectors. On the other hand, the salinization process, which gradually reduces the value of R_{we} by a magnitude of as high as 0.045Ωm, lags behind on arrival; it later dominates away from the injectors.

Now using injector I1 as the pivotal reference, and taking an intersection on both sides of the injector; we can examine these effects further with a profile of R_{we} value versus horizontal distance for the time-lapse periods. Looking at the profile shown in Figure 6.7; it is evident that the cooling effect is restricted to a narrow range, about 550m to 650m on the left and right hand sides of the injector respectively. Comparatively, the salinization effect spreads out to about 1,000m to 1,050m on the left and right hand sides of the injector respectively. This means the salinization effect moves faster, almost about twice, than the cooling effect. Also the difference in the magnitude of R_{we} profile on both sides of the injector, especially for time periods 2004 and 2008, is an indication of varying reservoir heterogeneity. The left hand section shows more variation. It is also observed that, as the mixture salinity increases and the cooling effect reduces away from the injector, the R_{we} value decreases, dropping below the original value for the formation water. However, as the

injected water front reaches it limits, the salinity effect becomes less significant while the temperature begin to rise to the original reservoir temperature, thus R_w rises again to the original value close to the producer.

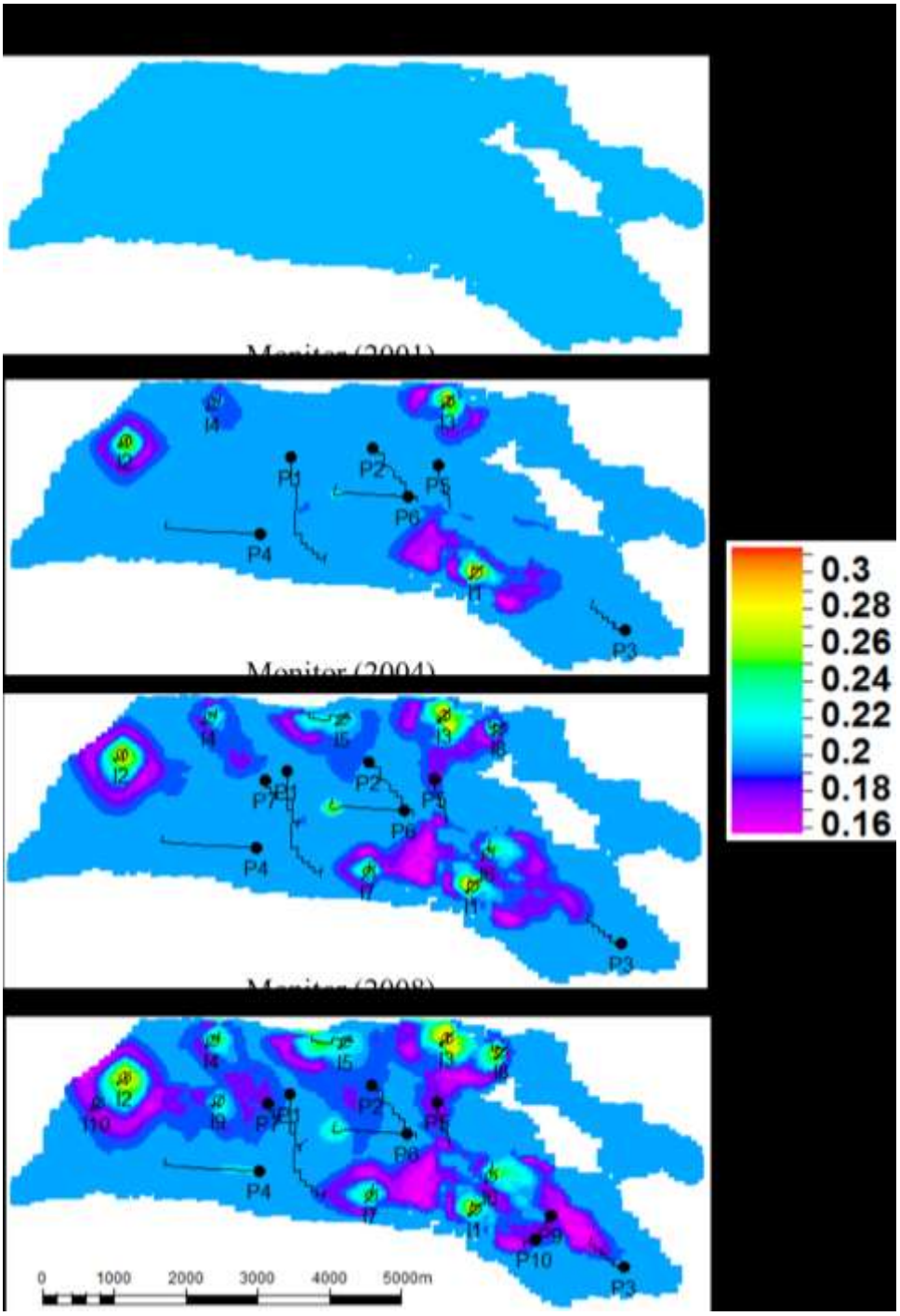

Figure 6.6*: Maps of water resistivity pre-injection and the mixed water resistivity for three, six and ten years after water injection and oil production activities.*

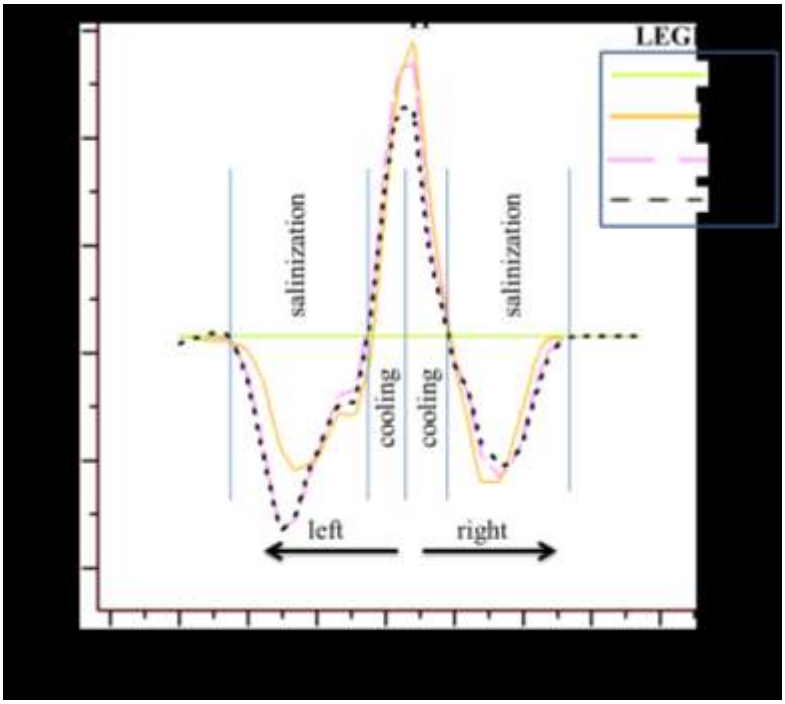

Figure 6.7: *Profile of effective mixed water reservoir resistivity R_{we} value versus horizontal distance, showing the salinization and cooling effects, away from both sides of injector I1 (indicated in the Figure 6.6).*

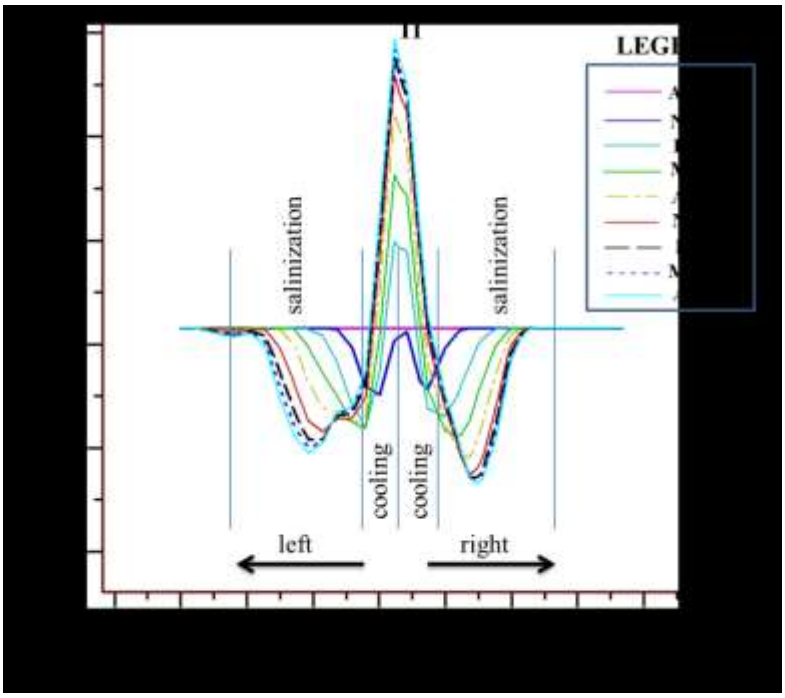

Figure 6.8: *Profile of effective mixed water reservoir resistivity R_{we} value versus horizontal distance, showing the salinization and cooling effects, away from both sides of injector I1 (indicated in the Figure 6.6) for finer time scale (3months interval)*

The three monitor surveys considered here show fairly similar trend, which indicates that the entire system has become stabilized over a period of three years. This means, in this particular field example, it might be worthwhile to examine how this process had evolved over a smaller period of time. Thus, Figure 6.8 shows results for the finer time scale of three months interval. The two effects are now more glaring within the first fifteen months of water injection and thereafter they become stabilised. At the onset of injection, there is a repeated but localised cooling effect as water injection proceeds. This cooling effect surpasses the effect due to increase in salinity around the injector. While the salinity effect, which is mainly due to mass or concentration mixing of the injected and formation waters, spreads out along the water front; the temperature effect is more restricted because both fluid and rock thermal properties are involved.

It is now established that R_{we} changes spatially away from the injector, and it stabilises over time, depending on the duration and rate of water injection. Invariably then, we expect the time-lapse change in CSEM amplitude to be a function of change in water saturation and change in water resistivity. In summary, we know that a change in the CSEM amplitude is a function of change in the true reservoir resistivity between two time periods.

$$\Delta A_{EM} = f(\Delta R_t) \; ; \tag{6.3}$$

Now, for a non compacting reservoir, we have change in resistivity to be:

$$\Delta R_t = \frac{\partial R_t}{\partial S_w} \Delta S_w + \frac{\partial R_t}{\partial R_w} \Delta R_{we}; \tag{6.4}$$

where the magnitude of change in effective water resistivity is a function of salinization or desalinization (salinity change, ΔS_e) and cooling or heating (temperature change, ΔT_e). That is:

$$\Delta R_{we} = \frac{\partial R_{we}}{\partial S_e} \Delta S_e + \frac{\partial R_{we}}{\partial T_e} \Delta T_e \; ; \tag{6.5}$$

Now we want to examine the partial contribution of effective water resistivity (R_{we}) in equation (6.4) to the time-lapse CSEM measurements and interpretation for change in water

saturation. In doing this, the workflow and the CSEM acquisition parameters described earlier in Chapter 5 are used. The results, percentage inline amplitude change (%ΔA) are as shown in Figure 6.9 for the time lapse intervals 2004 – 1998 (six years), 2004 – 1998 (eight years) and 2008 – 1998 (ten years).

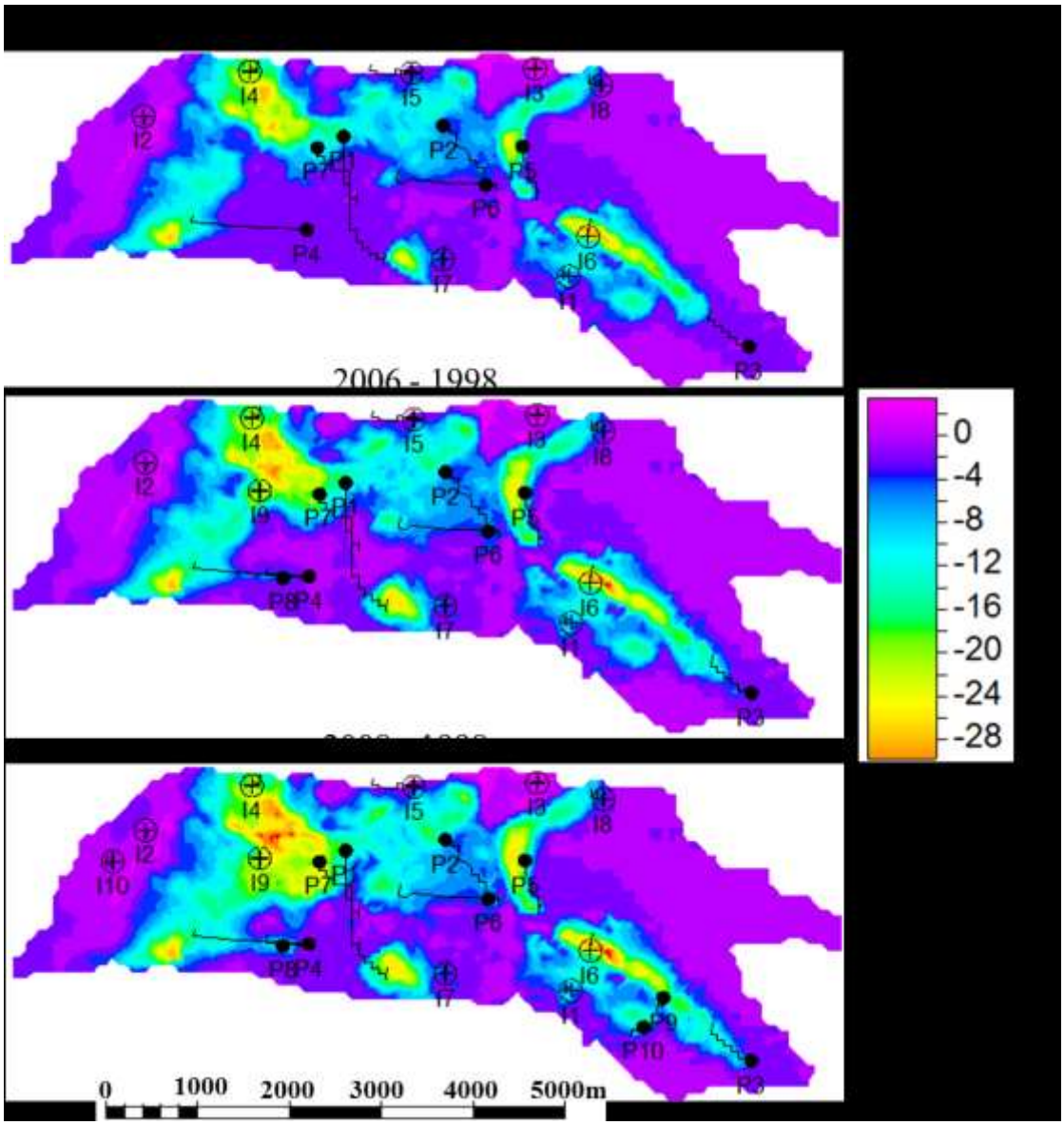

Figure 6.9: *Percentage time – lapse change in CSEM amplitude for the inline electric field component at 7km offset, and 0.1Hz frequency for six years (2004 – 1998), eight years (2006 – 1998) and ten years (2008 – 1998) of production and injection activities, with consideration for effective R_{we}. Note that the water injectors and oil producers are indicated at the time of they started to be operated. Compare this with Figure 5.4 (in which sea water is not tracked) in terms of interpreting for change in water saturation as shown in Figure 5.8.*

The results here are then compared with the results obtained earlier in Chapter 5, where dynamic variation in water resistivity was not considered. It could be observed that there is hardly any visible difference with respect to their sensitivity to change in water saturation (Figure 5.8).

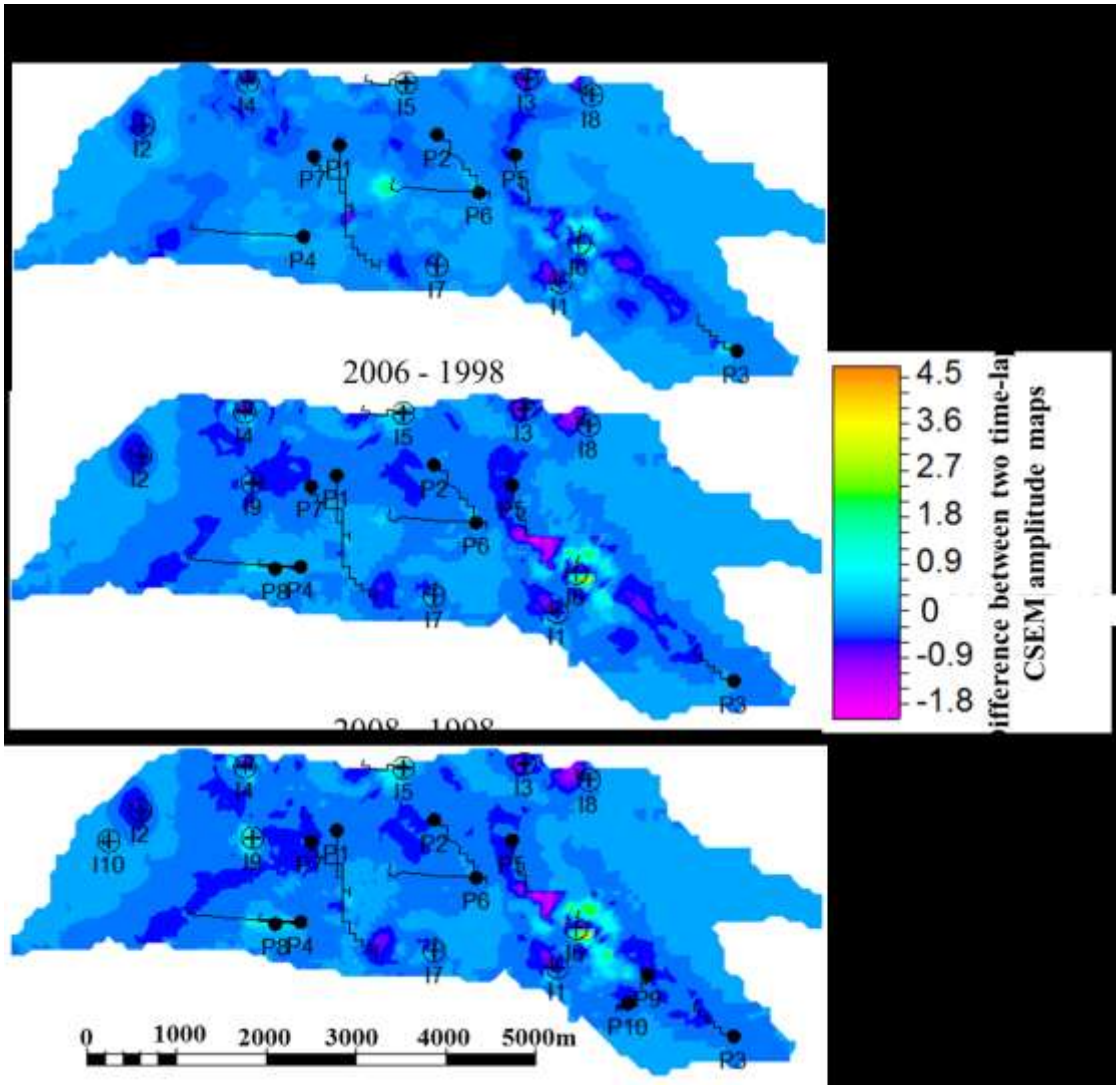

Figure 6.10: *Maps of direct difference between the two time-lapse CSEM maps. The time-lapse CSEM for the case with constant Rw value (see Figure 5.4) is subtracted from the time-lapse CSEM for the case with dynamic effective R_{we}, value (see Figure 6.9). The different ΔCSEM amplitude maps yield very small magnitude, below the 5% noise level expected for current CSEM acquisition technology.*

Quantitatively, direct subtraction of the time-lapse CSEM map with fixed R_w (Figure 5.4) from the time-lapse CSEM map with effective dynamic R_{we} (Figure 6.9) yields a very small

magnitude difference as shown in Figure 6.10. The highest difference (4.5%) is observed at the injectors within the oil leg, where we have highest changes in water saturation; but this is still very much below the practical 5% noise level with the present CSEM acquisition technology (Constable, 2010), despite that the linear difference is an over-estimation of the non-linear relationship that exists between the two cases that produced the maps in Figure 6.10. Therefore, the variation in R_{we} across the field, in this example, is too small to produce measurable magnitude difference in time lapse CSEM. This implies that the variation in R_{we} due to cold saline water injection in this field has negligible impact on the time-lapse CSEM interpretation of change in water saturation. At best, the effect of changing R_{we} could be accounted for, during CSEM inversion to reservoir resistivity (R_t).

Now, we know that there should not be any time-lapse change in either temperature or salinity except for change in water saturation as a result of water injection. However, equation 6.5 requires that we model the partial contributory effect of each of the changes in temperature and salinity, as elements of the changes in R_{we}, to the time-lapse CSEM response. In order words, can we monitor either of temperature or salinity change assuming there is no change in the other, and water saturation is only spatially varying. This will offer us information as to which of the two water elements is more important, especially if we have to decouple or cater for the R_{we} effect in the CSEM responses for interpretation purpose.

6.3.2 The physical effects of temperature

Sensitivity of time-lapse CSEM to the change in temperature is examined here, keeping reservoir salinity (single value) constant, and with only spatially varying water saturation. Figure 6.11 shows the sensitivity of the time lapse amplitude of the three components of CSEM, namely horizontal electric field ($\%E_y$), vertical electric field ($\%E_z$) and cross-line magnetic field ($\%B_x$) to the change in temperature, as the only dynamic property, for time lapse intervals 2001 – 1998 (three years) and 2004 – 1998 (six years). The cooling effect around the injectors clearly confirms that the temperature effect is restricted to the vicinity of the injector. This effect hardly produces measurable response. The best response was obtained within the oil leg where in situ water saturation is originally low with attendant

high temperature of the reservoir (rock and fluid). Although it is assumed that the saturation is not changing dynamically, but it can be implied that as the cold temperature progresses away from the injector, it quickly becomes hot (by the rock and fluid heat capacities and thermal conductivities) and it soon attains the equilibrium formation temperature before it reaches the producers, thus the effect is not felt around the producers.

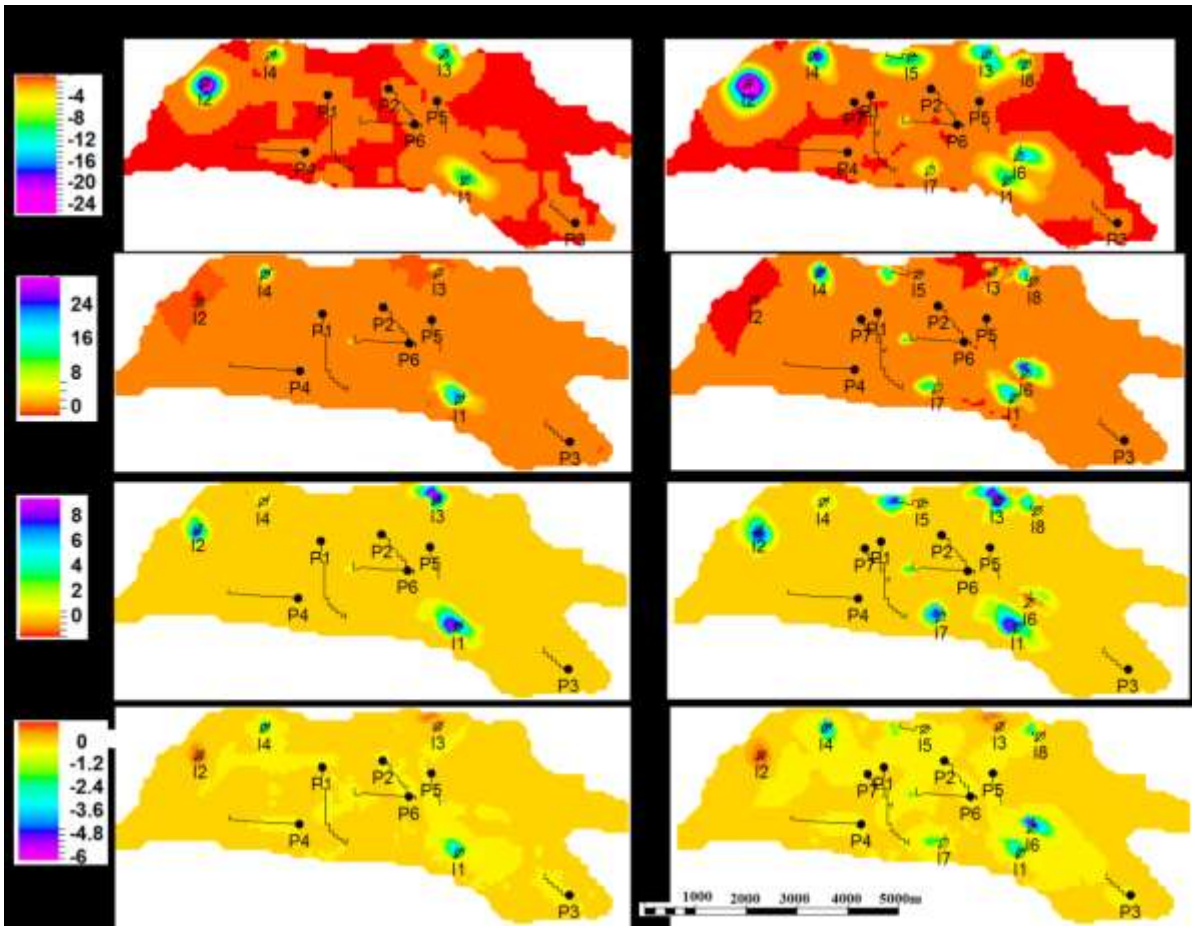

Figure 6.11:*Time-lapse CSEM sensitivity to change in temperature. Topmost row images show the time-lapse maps for change in temperature. Rows two, three and four show the percentage time – lapse changes in EM amplitudes for horizontal electric (%E_y), vertical electric (%E_z) and cross-line magnetic (%B_x) fields respectively.*

The equilibrium temperature is attained just within 1km from a chosen injector I1 after 12months of water injection as shown in Figure 6.12.

(a)

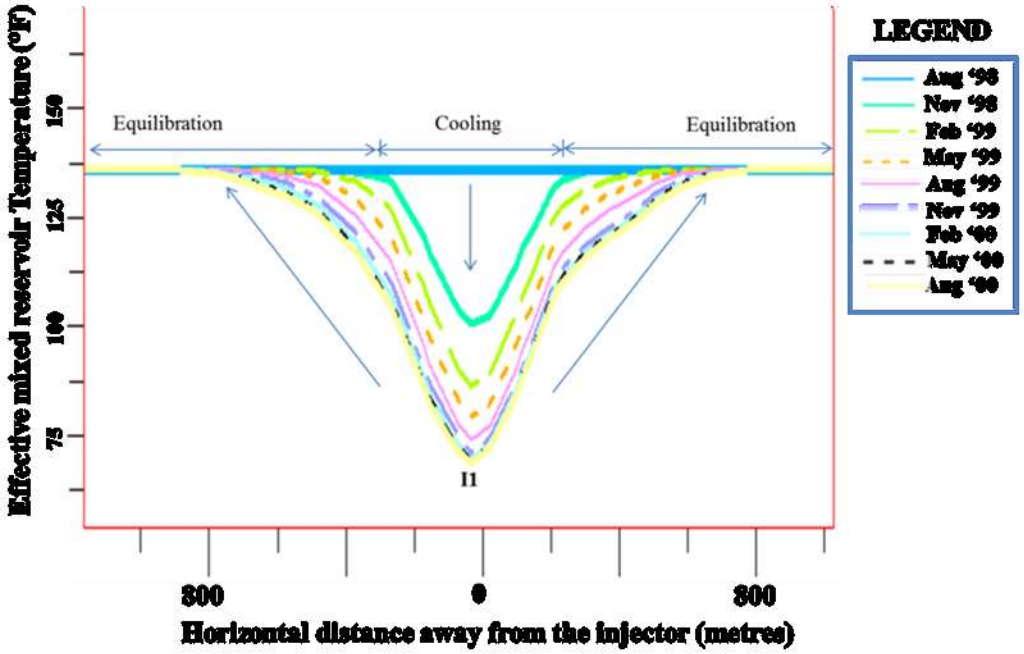

(b)

Velocity of mixed reservoir temperature along the water injection profile

$$\frac{T_e^{\,2} - T_e^{\,1}}{h_2 - h_1}$$ (in °F/m)

Injection time periods		Velocity
3	Nov '98	0.103
6	Feb '99	0.097
9	May '99	0.098
12	Aug '99	0.098
15	Nov '99	0.098
18	Feb '00	0.091
21	May '00	0.091
24	Aug '00	0.091

Figure 6.12*:(a) Profile of effective mixed Temperature T_e (°F) value versus horizontal distance, showing the cooling effect and equilibration, away from both sides of injector I1 (indicated in the Figure 6.11) for finer time scale (3months interval). (b) The cooling velocity (in °F/m) along the water injection profile.*

6.3.3 The physical effects of salinity

Similarly, sensitivity of time-lapse CSEM to the change in salinity is examined. It is observed that the CSEM sensitivity to the change in salinity is more significant than that of either the change in temperature or the change in R_w. The %Ez maps (3rd row, Figure 6.13) clearly replicate the salinity maps, thus vertical electric field offers the best qualitative interpretation, as it provides images of salinity changes.

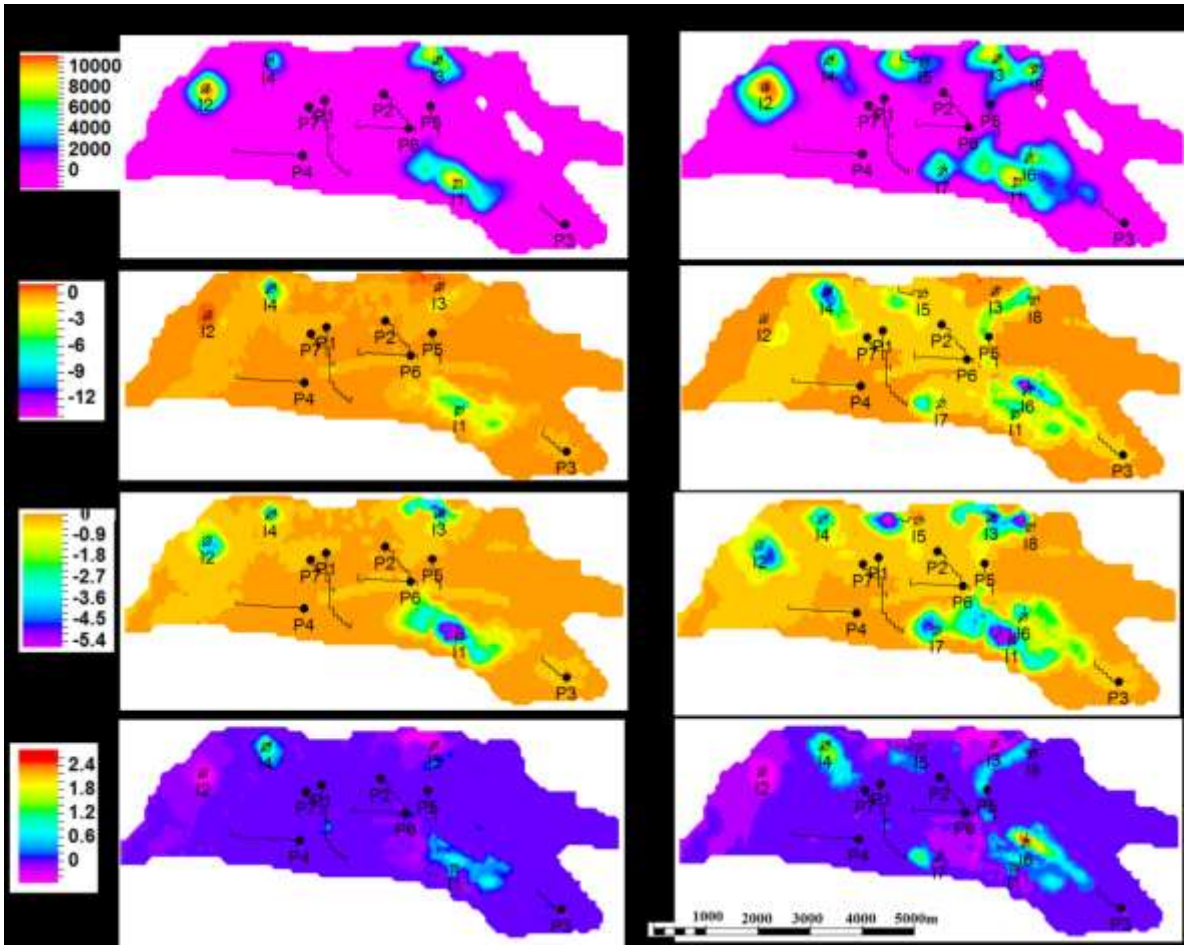

Figure 6.13: *Time-lapse CSEM sensitivity to change in salinity. Topmost row images show the time-lapse maps for change in salinity. Rows two, three and four show the percentage time – lapse changes in EM amplitudes for inline electric (%E_y), vertical electric (%E_z) and cross-line magnetic (%B_x) fields respectively.*

Unfortunately, it produces a lesser amplitude change than 5% noise floor. The horizontal electric field, %Ey maps (2nd row, Figure 6.13) is the only component that produces measurable amplitude changes, particularly within the oil leg where we have low initial value of spatial water saturation with an original salinity of 18,000ppm prior to injection of 30,000ppm salinity. Cross-line magnetic field component is the worst component in this model example. Ordinarily, the salinity and water saturation effects could not be easily decoupled, so one expects that inclusion of dynamic water saturation variation in this example should produce stronger responses for all the three components, especially within the oil leg where we have a large volume of injected water replacing more of the hydrocarbon than connate water. Nonetheless, the amplitude changes are more pronounced within the vicinity of injector, where there is a repeated and irreversible increase in salinity, as expected.

Some inferences from these sensitivity studies are:

(i) Sea water injection in this field model does not impact much on the dynamic value of R_w, thus it does not affect our ability to monitor change in water saturation as seen in Figures 6.9 and 6.10. Although the effect of R_w in this case is below the 5% noise floor and could be considered negligible, but future CSEM field data interpretation or inversion may require compensating for the dynamic variation in R_w due to injection of water with temperature and salinity conditions different from those of the formation water.

(ii) As the injected cold water progressively mixes-up with the formation water; it becomes quickly heated up to assume native equilibrium temperature (Figure 6.15). The highest percentage of temperature change is restricted to the vicinity of injector where the cooling effect is most felt (Figure 6.16c). This is due to the combined specific heat effects of the reservoir rock and the in situ fluids. Thus, the temperature change does not travel far (with attendant low velocity) before it becomes stabilized to the original *in situ* value (Figure 6.12).

(iii) On the other hand, the salinity effect spreads across the reservoir following the injected water closely behind along the flooding front (Figure 6.16a and b). The highest percentage change in salinity is also within the vicinity of water injector and it spreads out evenly along the flooding front (Figure 6.16b).

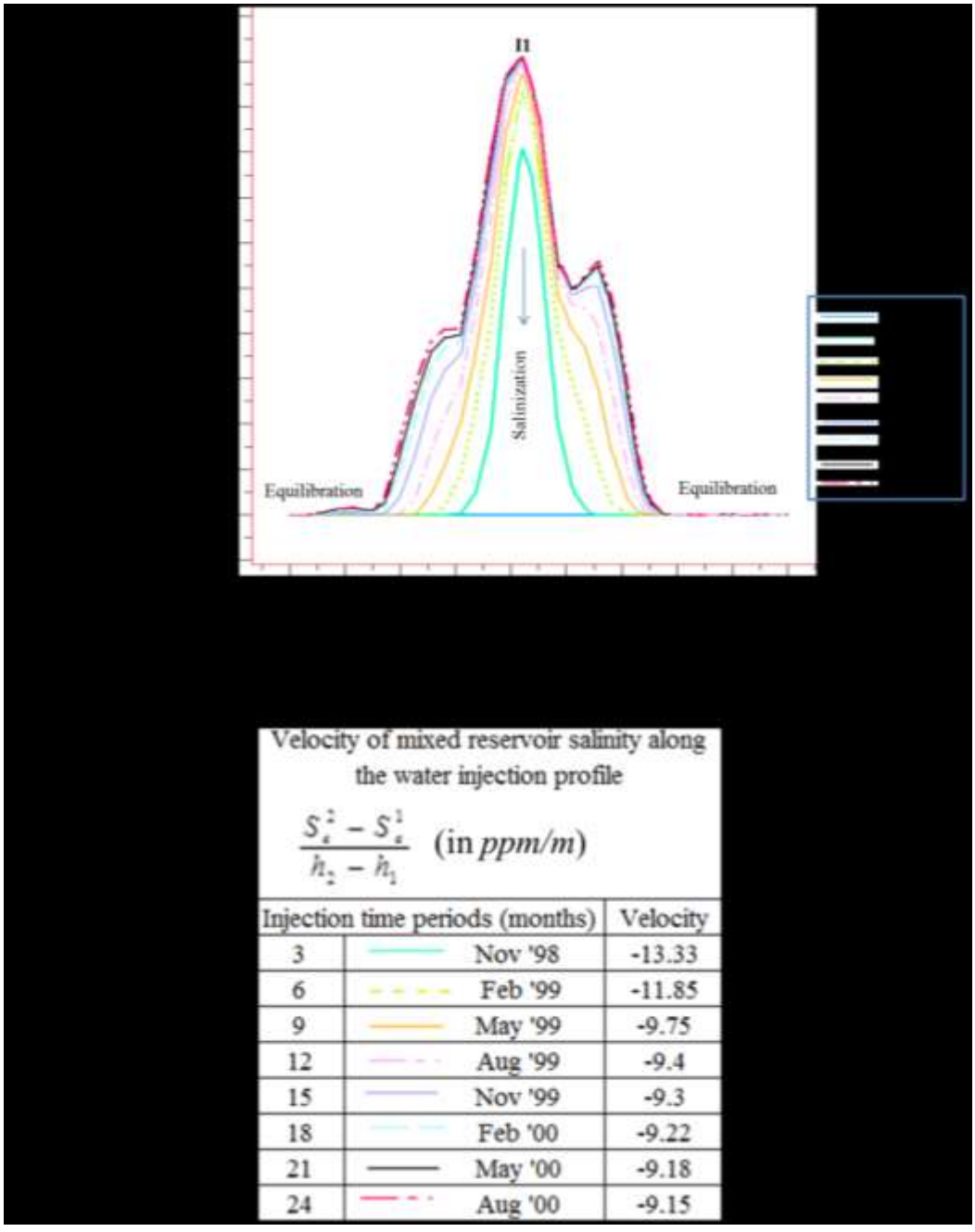

Velocity of mixed reservoir salinity along the water injection profile

$$\frac{S_s^2 - S_s^1}{h_2 - h_1} \quad (\text{in } ppm/m)$$

Injection time periods (months)		Velocity
3	Nov '98	-13.33
6	Feb '99	-11.85
9	May '99	-9.75
12	Aug '99	-9.4
15	Nov '99	-9.3
18	Feb '00	-9.22
21	May '00	-9.18
24	Aug '00	-9.15

Figure 6.14*: Profile of effective mixed salinity (ppm) value versus horizontal distance, showing the salinization effect and equilibration, away from both sides of injector I1 (indicated in the Figure 6.13) for finer time scale (3months interval). (b) The salinization velocity (in ppm/m) along the water injection profile.*

It travels with higher velocity than temperature (Figure 6.14 compared with Figure 6.12). Salinization has an opposing effect of lowering water resistivity while cooling raising water resistivity (Figure 6.15; Figure 6.16b and c). Close to the injector, the cooling effect leads the salinization effect. About 250m away, both effects cancel out each other. Beyond this level, salinization (salinity effect) has over-taken the cooling (temperature effect). The overall R_{we} is now driven by the change in salinity, as the temperature value is more or less the original in situ value at this spatial position (Figure 6.16d)

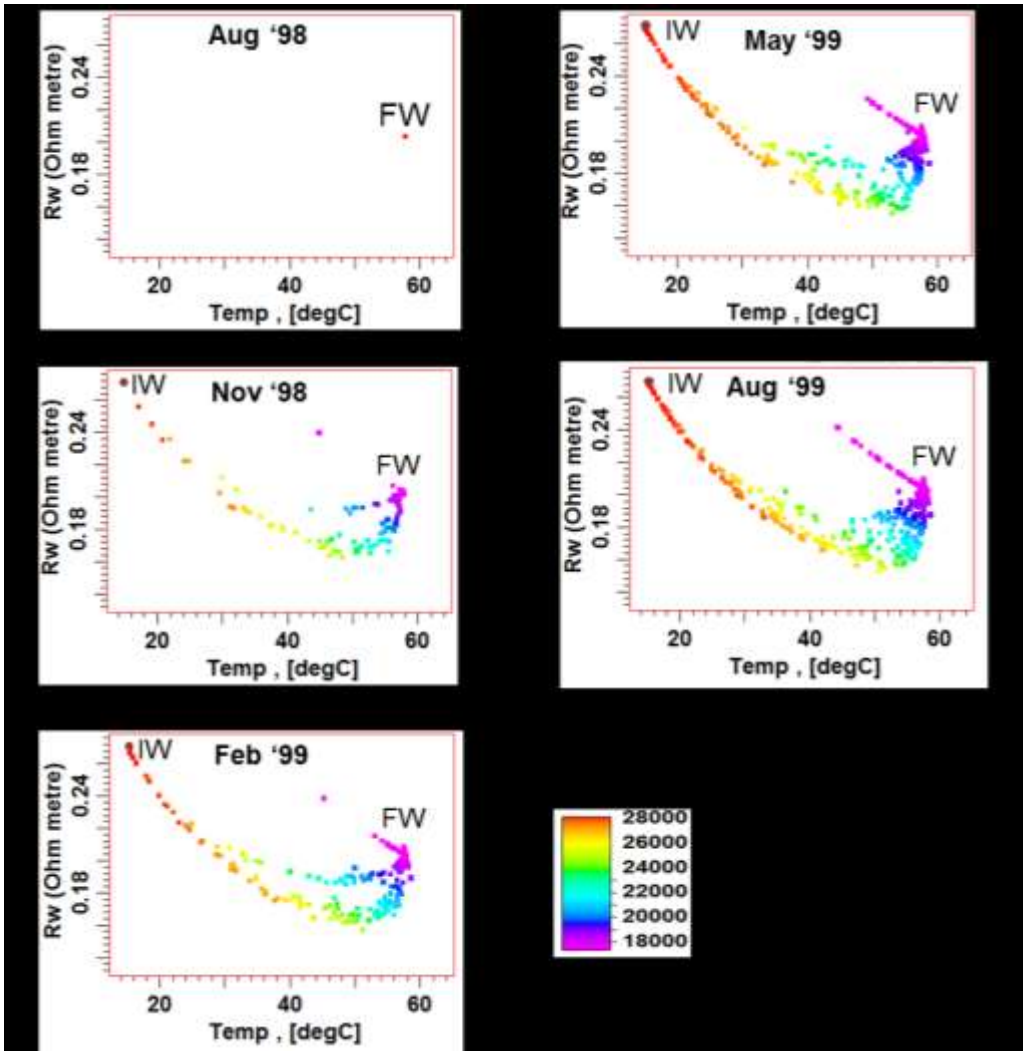

Figure 6.15: *Evolution of effective mixed water resistivity (R_{we} in Ωm) as a function of effective temperature (T_e in °C) and effective salinity (S_e in ppm) at every three months of injection starting from pre-injection (Aug '98).*

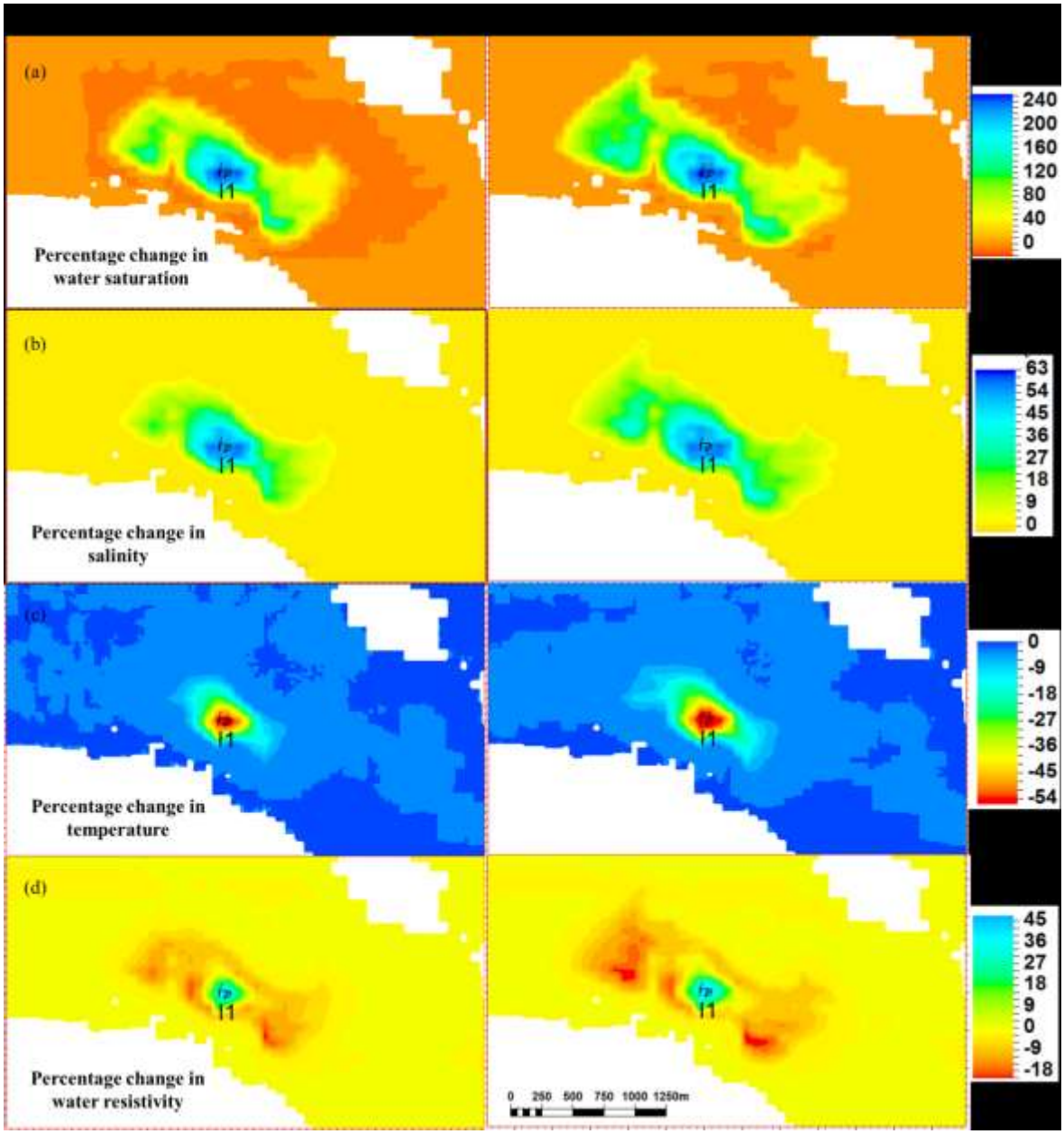

Figure 6.16: *Evolution of percentage changes in the fluid properties away from the injector: (a) Water saturation; (b) Water salinity; (c) Temperature; (d) Water resistivity, for 1 year and 2 years after injection.*

6.4 Potential of CSEM in monitoring Low Salinity (LoSal) water injection: Analogue of Endicott field Alaska, USA

Now, let us investigate this further with another practical example of water – related recovery, which is the low salinity enhanced oil recovery, popularly called *LoSal* – EOR.

Typical field application of this relatively emerging technology is successfully recorded by BP in their pilot test at Endicott field in Alaska, USA, where low salinity water (1,500*ppm* equivalent *NaCl* solution and temperature of 18.7°C) is injected into a reservoir containing formation water with salinity of 15,000ppm and temperature of 100°C (McGuire et al. 2005; State of Alaska 2011). The low salinity water is manufactured from the sea water. This scenario is as shown in Figure 6.5b.

6.4.1 Motivation

The main motivation, as shown in Figure 6.5b, is based on the fact that there is a significant contrast between the resistivities of injected low salinity water (3.43Ωm) and the saline formation water (0.16 Ωm). This 21 times difference in resistivity is considered to be large enough to possibly produce measurable time-lapse CSEM amplitude change between the two waters, apart from the contrast between either of the waters and the highly resistive oil. If this is possible, it will enable us to understand water evolution process during water flooding. In particular, knowledge of how the low salinity water distributes amongst the other fluids would be desirable to determine its efficiency. This is important, as *LoSal* water may not flow through the reservoir in the same way as the higher salinity water in conventional waterflooding. To address this objective, the CSEM responses are modelled to determine the likely potential of monitoring such a waterflood. The same North Sea reservoir model and CSEM acquisition parameters are used, but the salinity and temperature boundary conditions (formation and injected water) for Endicott field in Alaska, USA are utilised for this sensitivity analysis. The benefits, mechanisms, and the simulation of *LoSal* water injection are described in Appendix 2.

6.4.2 Interpretation of CSEM modelled results

Having simulated *LoSal* water injection as described in Appendix 2 (section A2.1); the CSEM responses are modelled for the baseline, and the monitors – three and six years after production. In order to proceed with the interpretation as shown in Figure 6.17, let us compare the maps of the CSEM time-lapse responses for the inline electric ($\%\Delta E_y$), the vertical electric ($\%\Delta E_z$) and crossline magnetic ($\%\Delta B_x$) field components in the last three

rows respectively; with the maps of changes in water saturation and changes in salinity in the first and the second rows respectively.

For the electric field components (E_y and E_z), a very high negative timelapse anomaly (deep blue colour) indicates areas of the reservoir away from the injectors, toward producers (e.g. away from injectors I2 and I4 towards producers P4 and P1 respectively), where the formation water (with a low resistivity of 0.16Ωm) has displaced highly resistive oil (oil - saturated reservoir with resistivity of about 60Ωm). There is a reduced anomaly (light blue colour) within the areas of high initial oil saturation (e.g. right hand corner of the reservoir), where a large portion of the injected low salinity water (with a resistivity of 3.43Ωm, higher than that of the formation water) mixed with some portion of low resistivity formation water has displaced highly resistive oil (e.g. around injectors I1, I6, I7 and producers P3, P5, P6). Close to the injectors, where injected low salinity – low temperature water displaces formation water, a typical connate – water banking phenomenon, we observe a positive time-lapse response (red colour). In this 1D analysis, the magnitude of the mapped amplitudes varies directly with the volumetric proportion of replacement. In this case, $\%\Delta E_y$ ranges between 27% and -27%. Whereas, for injected water, where the salinity is assumed to be the same as that of the formation water, the $\%\Delta E_y$ ranges between 0% and -32% (Figure 5.4). This shows that time-lapse CSEM is sensitive to change in salinity and could potentially be used to monitor low salinity water injection. Whenever we inject water into the reservoir, our main intention is to drive the oil towards the production wells while avoiding water breakthrough. However, in the process, the injected water mixes with the native formation water and they jointly replace the oil. In this circumstance, we wish to distinguish the injected low salinity water from the native formation water in order to examine the efficiency of the former.

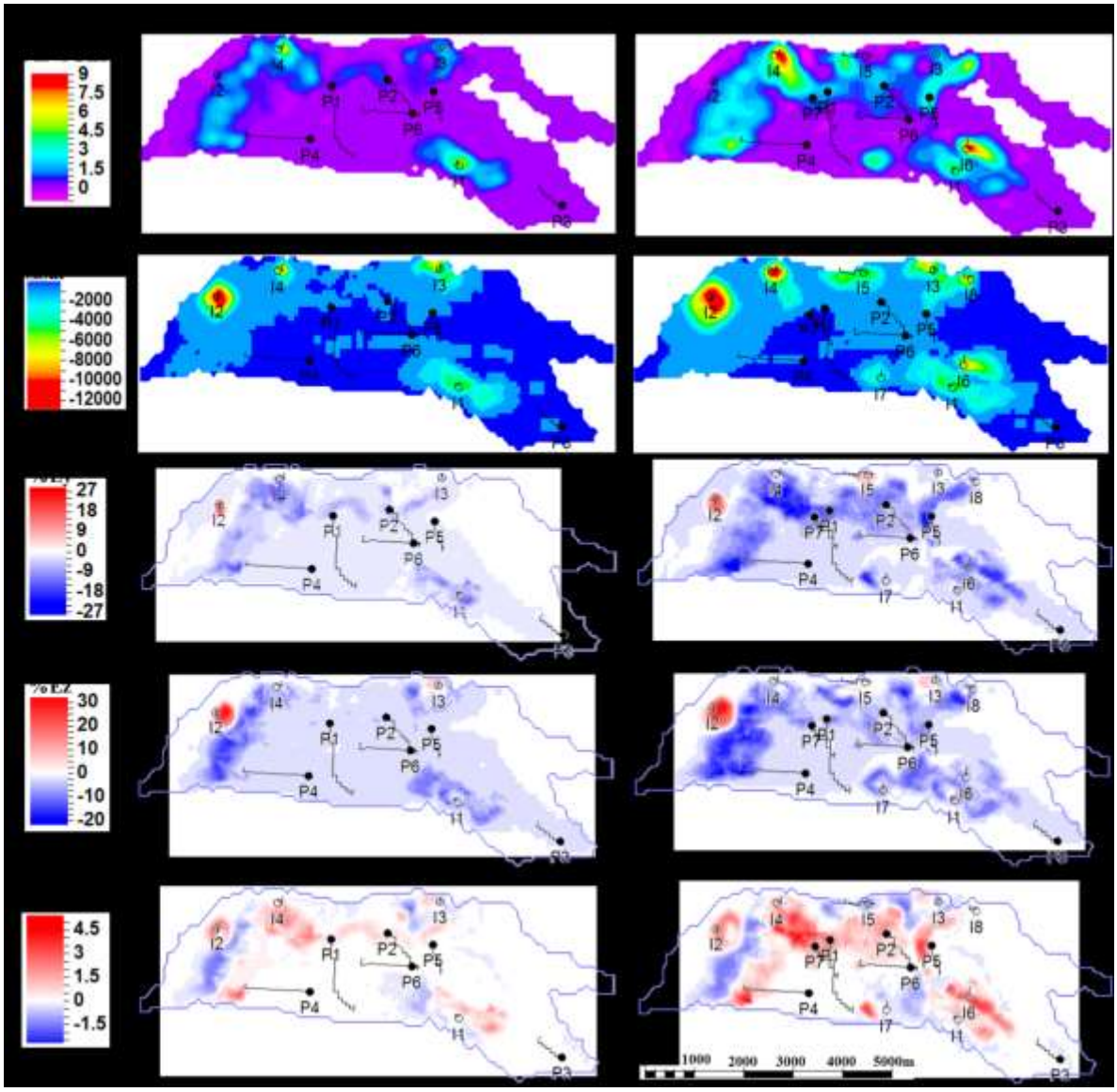

Figure 6.17: *Qualitative interpretation of time – lapse EM amplitude for a producing reservoir undergoing low salinity water injection. Top row images show the maps of time-lapse changes in reservoir – variable scaled water saturation between the various monitor models and the baseline model. The second row images show the maps of change in salinity. The last three rows are the corresponding time-lapse CSEM amplitudes maps, for the horizontal electric, vertical electric and cross-line magnetic field components respectively, for 3 and 6 years interval respectively.*

Therefore, if we inject within the water leg, where the native water saturation is higher than the oil saturation; oil is driven by the banked formation water mixed with a little amount of low salinity water. This result into the highest possible reduced signal (deep blue in the E_y and E_z maps, Figure 6.17), which is still lower than what was obtained with only high

salinity formation water or sea water replacing oil. I term this lowering of electric field EM signal as the *dimming effect of low salinity* due to reduced resistivity. Moving away from the injector, the effect of low salinity injected water reduces, just as the mixture of the two waters tends to give salinity value closer to that of the high salinity formation water than to the injected low salinity water. Now, injecting low salinity water within the oil leg, where the original formation water saturation is much lower than the oil saturation, will lead to more of the injected low salinity water driving the oil. This means oil is been replaced with a mixture of a large portion of the low salinity water and a little portion of high salinity native water. In this case the CSEM signal is much lower than what is obtainable in a situation where the oil is replaced by only formation water (light blue on the bottom right corner of the E_y and E_z maps, Figure 6.16). Thus, the *dimming effect of low salinity* is much more observed within the oil leg where reduction in resistivity is higher, than within the water leg. This has a good implication about evaluating the efficiency of the low salinity water injection. One other possibility is injection within the aquifer, where the low salinity water is pushing the formation water thus producing positive time-lapse CSEM signal (red colour on the left hand corner). This *brightening effect of low salinity* may not be desirable in terms of *LoSal - EOR* objectives.

Table 6.4: *Resistivity distribution of fluids involved in the replacement process, and the corresponding relative magnitudes in the electric and magnetic fields* responses.

All of these phenomina are true for the cross-line magnetic field (B_x) maps (on the last row of Figure 6.16) and similar interpretations follow, but with polarity reversal. Tables 6.4 shows the possible fluid replacement scenarios, the expected corresponding changes in

resistivity and the amplitude changes in electric and magnetic fields. This table summarises the interpretation of the time-lapse CSEM maps shown in Figure 6.16.

6.5 Potential of CSEM in monitoring Aquifer water injection: Analogue of Saudi Arabia offshore clastic field

Another production scenarios which shows the practical importance of salinity and temperature effect is the injection of subsurface – derived aquifer water with an average salinity of 10,000*ppm* into an underlying sandstone reservoir containing formation water with average salinity value of 200,000*ppm* and resistivity of 0.018Ωm (Rafle & Youngblood 1987; Youngblood 1980). This is the case with a particular Saudi Arabia oilfield, where production and injection setting has posed challenges to the operator of this field in terms of determining the remaining oil saturation as a result of water evolution resulting into varying values of representative R_{we}. Presently they are using an in-house proprietary neutron – pulsed logging system to determine spatial and dynamic salinity values around the wells in order to enhance calculation of representative R_{we} values to be fed into Archie's equation to calculate dynamic S_w values. This involves logging many wells and interpolating salinity values across the wells. The accuracy of this method depends largely on the number of wells logged over the entire oilfield. Here, the potential of using time lapse CSEM to image this variation in R_{we} is examined. Based on the formation water salinity and resistivity provided, the initial formation water temperature is calculated, using equation 3.17, to be 89°C. Standard temperature of 24°C (75°F) is assumed for the injected aquifer water such that its resistivity is 0.57Ωm (see Figure 6.5c). Other model parameters used to simulate salinity and temperature tracking in this scenario are as described in Table 6.2. However, unlike LoSal simulation, the relative permeability data are not modified in the scenarios (see Appendix 2), since our aim is mainly to track the effect of injected water which has significantly lower salinity value than the formation water. The interpretation simply follows the same line of argument as the LoSal injection. Figure 6.18 shows that changes in salinity within the vicinity of injectors at the water-leg (say, I2) yields change in the CSEM amplitude for the three field components.

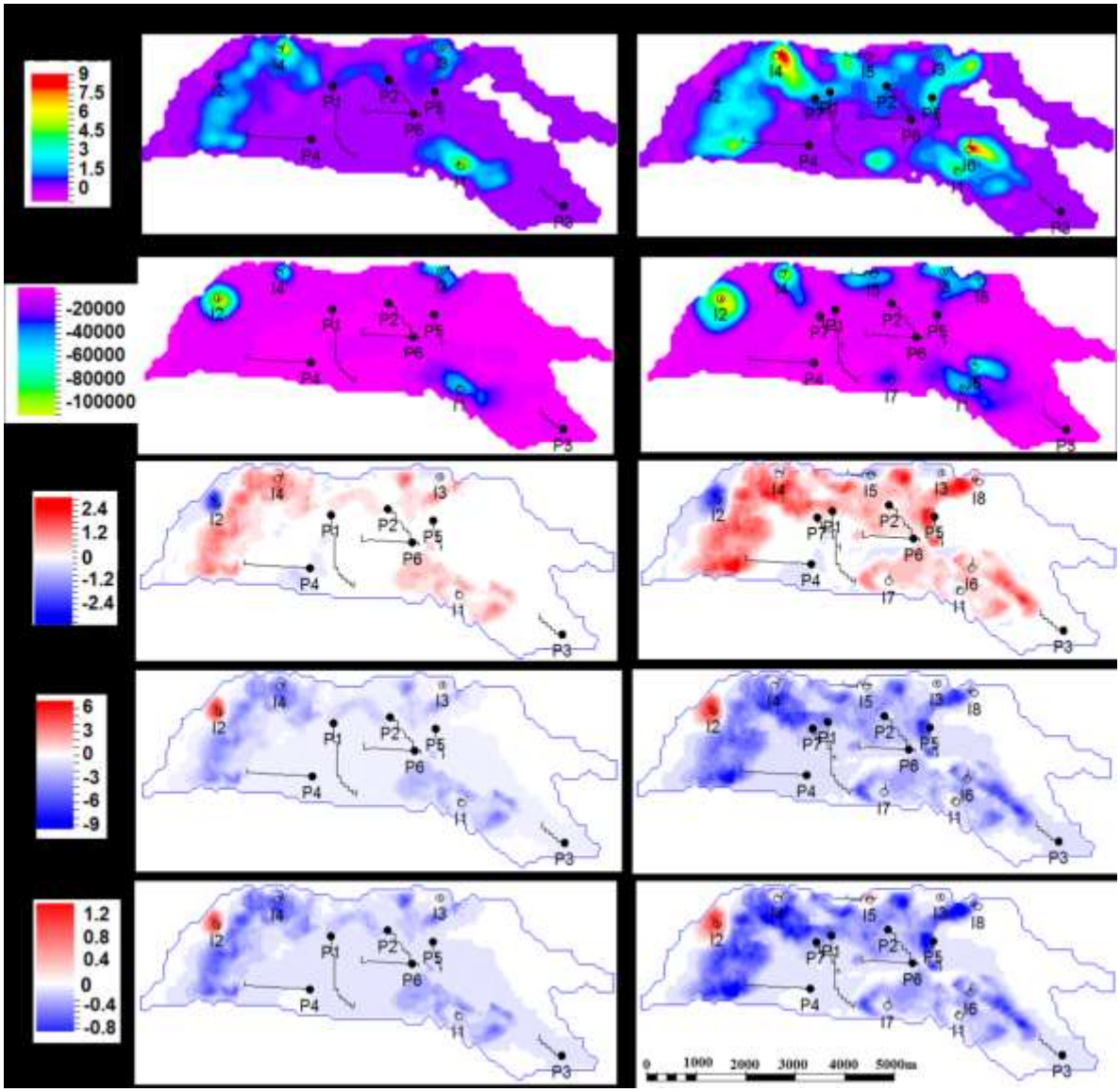

Figure 6.18: *Qualitative interpretation of time – lapse EM amplitude for a producing reservoir undergoing aquifer water injection. Top row images show the maps of time-lapse changes in reservoir – variable scaled water saturation between the various monitor models and the baseline model. The second row images show the maps of change in salinity. The last three rows are the corresponding time-lapse CSEM amplitudes maps, for the horizontal electric field, vertical electric field and cross-line magnetic field components respectively for 3 and 6 years interval respectively.*

Here, injection of aquifer water with lower salinity causes reduced salinity of the reservoir water. Whereas, when high salinity formation is banked between the oil and the injected low salinity aquifer water at the water leg, we see a very conductive water displacing the oil. The signal in this example is generally lower than what we obtained with low salinity water injection (Figure 6.17) because the originally very high salinity of the formation

water (200,000*ppm*) before production means a very low R_w to begin with, which means the resistivity of the fluid-saturated reservoir is lower compared to when the formation water salinity is 15,000*ppm*. So the CSEM signals and the changes are also lower.

6.6 Brine tracking: seismic versus CSEM

Next, let us investigate the three injection scenarios described above, referenced to the scenario with constant brine properties, not only in terms of their normalised percentage time-lapse CSEM amplitude changes but also in terms of their percentage 4D seismic amplitude changes. This is to show the strength of CSEM over seismic in tracking different brines combinations. Let us proceed with the modelling using only one year time-lapse interval, and a single water injector. The static and dynamic properties are similar for all the scenarios, except the salinity and temperature boundary conditions which are as stated earlier for each of the scenarios.

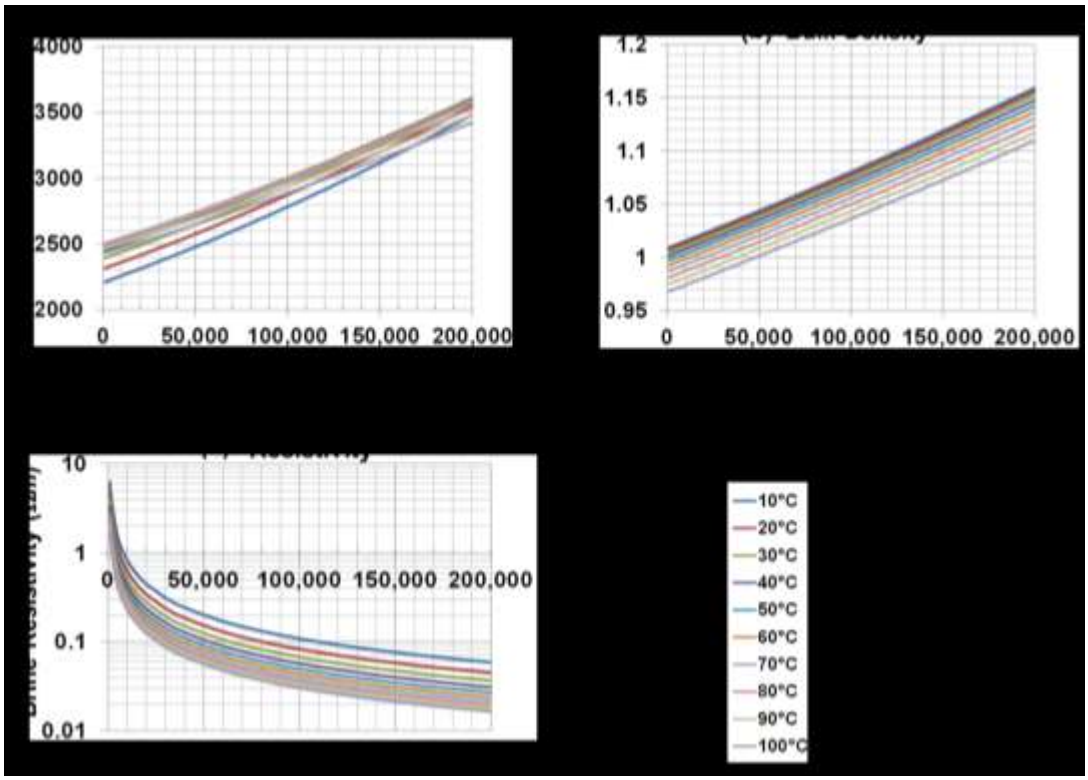

Figure 6.19: *Brine acoustic properties: (a) bulk modulus; and (b) bulk density (Han & Batzle 2000); and electrical property (c) resistivity (Crain 1986) as functions of salinity and temperature.*

First, comparison is made between the fundamental acoustic properties of brine (the bulk density and the bulk modulus) and the electrical property of brine (the resistivity), both as functions of salinity and temperature. It is evident from Figure 6.19 that for a given temperature, brine bulk modulus and bulk density generally increase with increasing brine salinity, but there are some overlapping values in bulk modulus. However, the brine resistivity decreases with increasing salinity at a given temperature. Also, while bulk modulus generally increases with temperature for a given salinity, both bulk density and resistivity decrease with increasing temperature.

Now, the acoustic properties for the three scenarios are compared, similar to Figure 6.5 for the electrical resistivity of brines. Figure 6.20 and Figure 6.21 show the comparison for the brine bulk moduli, and bulk densities respectively for the three scenarios of water injection. Here, oil saturation of 0.8 with connate water saturation of 0.2 is considered. It could be observed from both Figure 6.19 and Figure 6.20 that the variation in bulk moduli is more significant than the variation in bulk densities, comparing the three scenarios with one another.

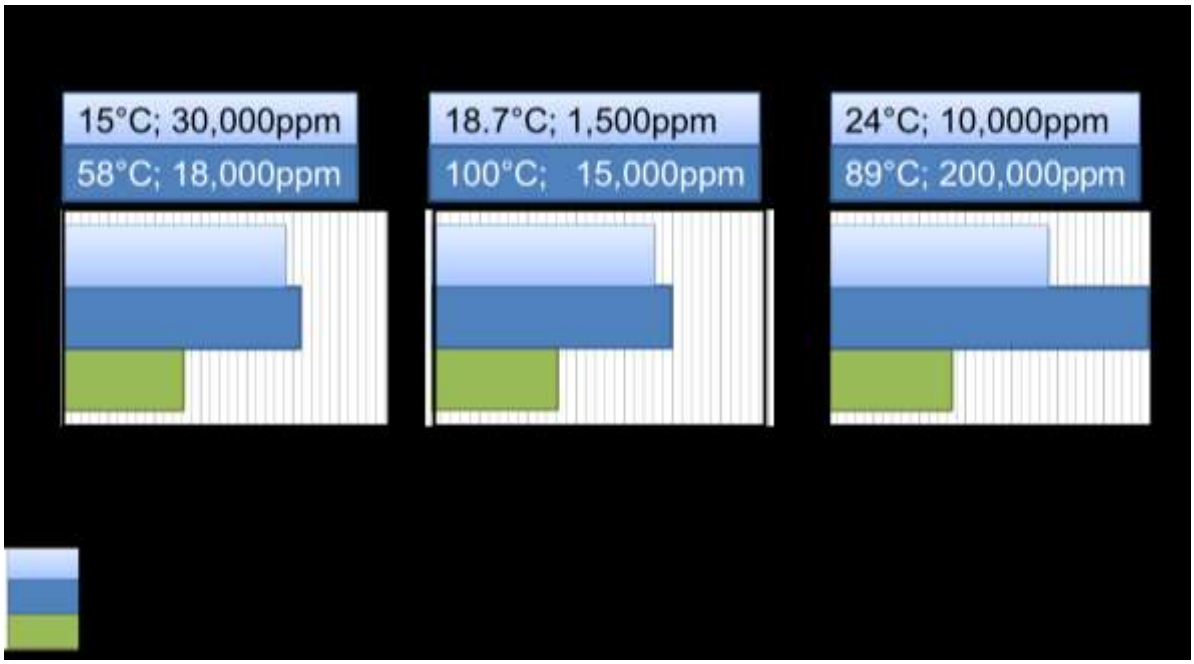

Figure 6.20: *Comparison of brine bulk moduli for different water injection scenarios using Han & Batzle (2000) widget software showing the relationship between bulk modulus, salinity and temperature. The values of temperatures and salinities for each scenarios are obtained from the literature : (a) Sea water injection; (b) Low salinity water injection; and (c) Aquifer water injection.*

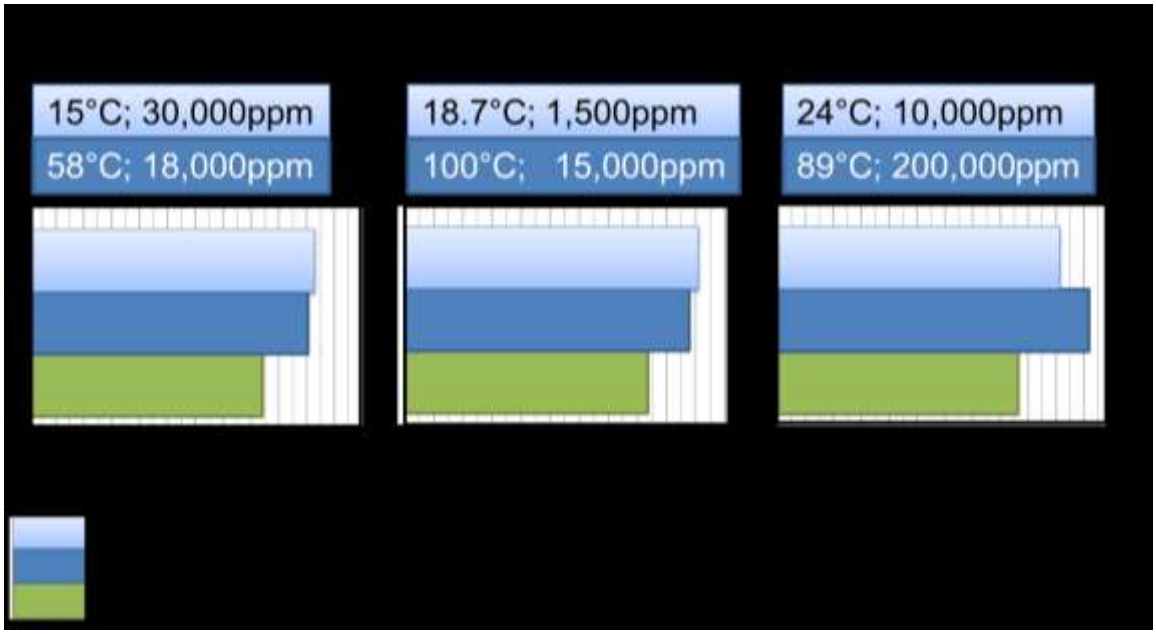

Figure 6.21: *Comparison of brine bulk densities for different water injection scenarios using Han & Batzle (2000) widget software showing the relationship between bulk modelus, salinity and temperature. The values of temperatures and salinities for each scenarios are obtained from the literature : (a) Sea water injection; (b) Low salinity water injection; and (c) Aquifer water injection.*

However, when we compare the variation in bulk moduli with the variation in resistivities in Figure 6.5, we see that resistivity has the highest variation between a set of brines combination to another set. Oil resistivity was not included in Figure 6.5 as this is assumed to be infinitely large, up to $10^6\Omega$m (Crain 1986), which means resistivity is the best property to separate oil from brine. Now, using the coupled seismic and CSEM forward modelling workflow in Figure 4.2, the percentage changes in amplitude normalised with the baseline amplitude for the time-lapse seismic and the time – lapse CSEM is calculated, between 1998 and 1999 for the reference scenario and these three injection scenarios. The results are compared for seismic case in Figure 6.22 and for the CSEM case in Figure 6.23.

For the seismic case, the pressure dominant effect (softening) has been muted out in order to highlight only the change in water saturation, which contain information on the brine properties (salinity and temperature). This also permits comparison of the seismic results with the CSEM results. The three scenarios show deviations from the reference model (Figure 6.22a), with about 0.1% decrease in seismic amplitude change for the sea water injection at Schiehallion (Figure 6.22b); about 3% decrease for the low salinity injection at

Endicott field (Figure 6.22c); and 0.4% increase for subsurface aquifer water injection at a Saudi Arabian oilfield (Figure 6.22d). The bar chart in Figure 6.22e summarises the amplitude deviations from the reference model.

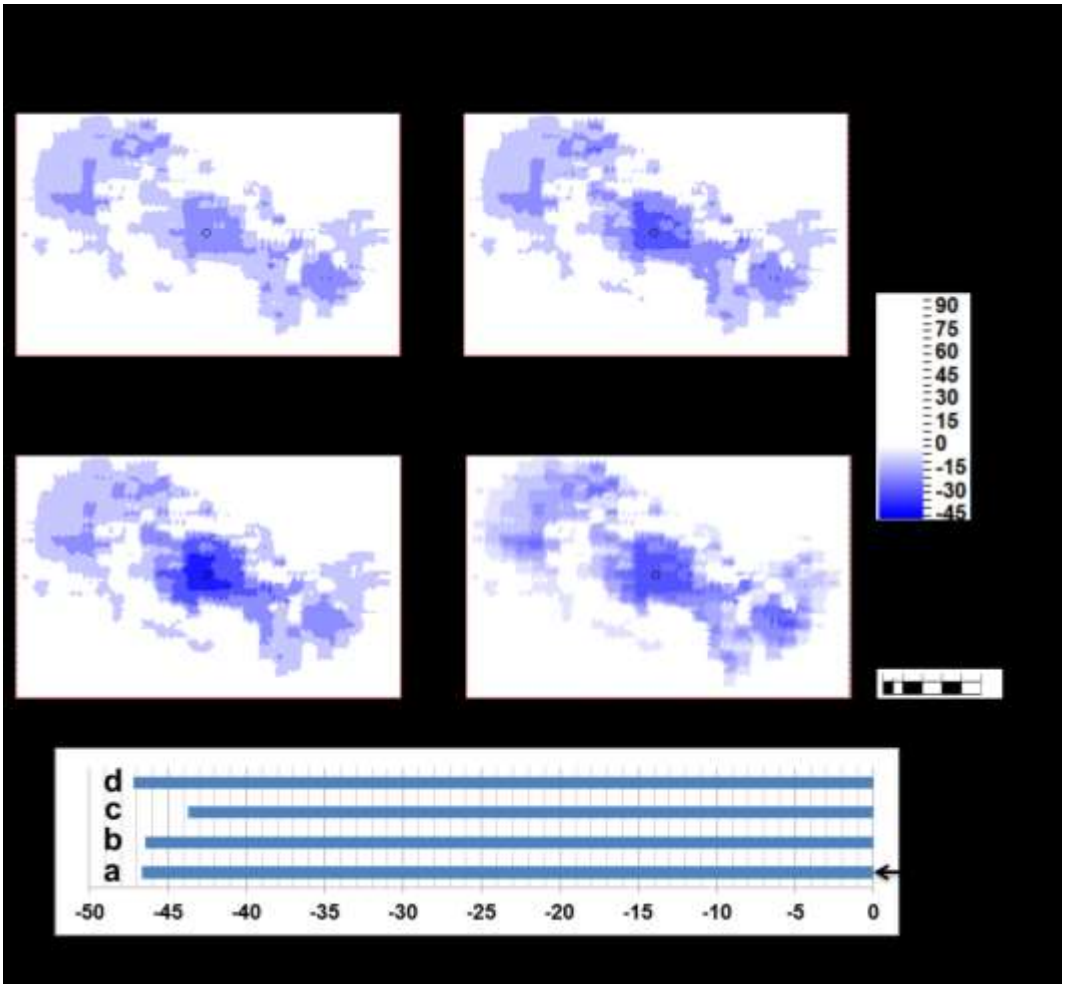

Figure 6.22: *Comparison of percentage amplitude changes in the 4D seismic modelled results for different water injection scenarios with differing combinations of brines: (a) reference scenario with constant brine properties: (b) Sea water injection; (c) Low salinity water injection; (d) Aquifer water injection; and (e) the bar chart showing amplitude change deviations from the reference scenario.*

This means different brine properties combinations produce differing time-lapse seismic amplitude signals with reference to the constant brine properties. The variation is however small, with the highest deviation being 3% for the low salinity water flooding. Generally speaking, the impact of the injected brine is felt within the proximity of injector. The signal

seen away from the injector is related to the brine mixing, and the signal seen further away is the effect of formation water replacing oil (light blue signal).

For the CSEM case, the three scenarios show deviations from the reference model. The salinity and temperature effects are competing against each other and this is why we see the bipolarity amplitude changes, especially for aquifer – water injection and low salinity water flooding in Figure 6.23c and d.

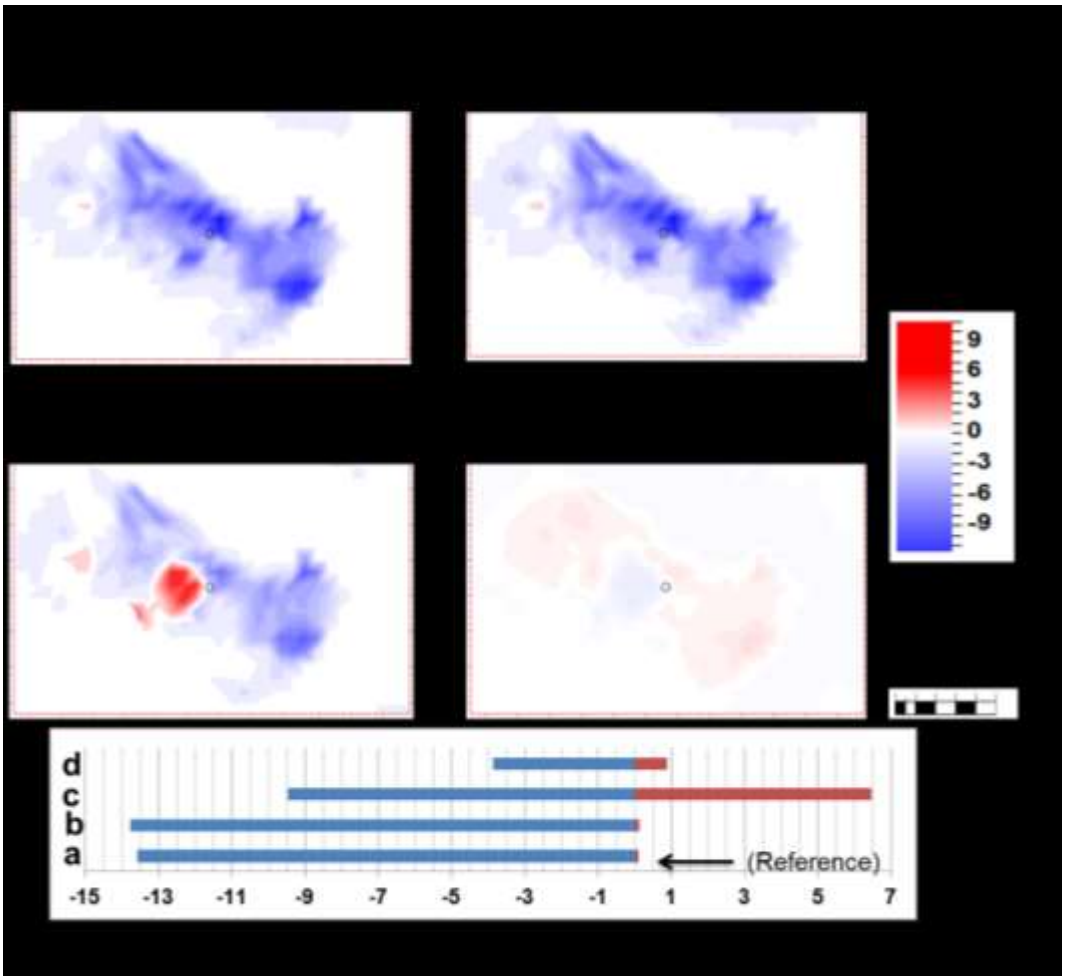

Figure 6.23: *Comparison of percentage amplitude changes in the time-lapse CSEM modelled results for different water injection scenarios with differing combinations of brines: (a) reference scenario with constant brine properties: (b) Sea water injection; (c) Low salinity water injection; (d) Aquifer water injection; and (e) the bar chart showing amplitude change deviations from the reference scenario.*

With respect to the reference model we observe: (a) 0.1% decrease in time-lapse CSEM amplitude change for the sea water injected into Schiehallion reservoir with almost similar value of brine resistivity; (b) 1% total decrease for the low salinity injection. Here we see a central effect of combined low salinity and low temperature of the injected brine reinforcing each other to produce signal due to high resistivity injected brine replacing the low resistivity formation brine around the injector; (c) 12.1% absolute decrease in time-lapse CSEM amplitude change for subsurface aquifer water injected into very saline reservoir water. Here, the resistivity difference between the injected and formation brine is very high such that there is dimming effect for signal around and away from the injector. The bar chart in Figure 6.22e summarises different CSEM signals for different combinations of brine properties with reference to the constant brine properties.

Figure 6.24 shows that, although time-lapse amplitude changes in seismic are significant higher than those of the time – lapse CSEM. However, the deviations in the time-lapse CSEM modelled scenarios from the reference model are bigger than we see in seismic.

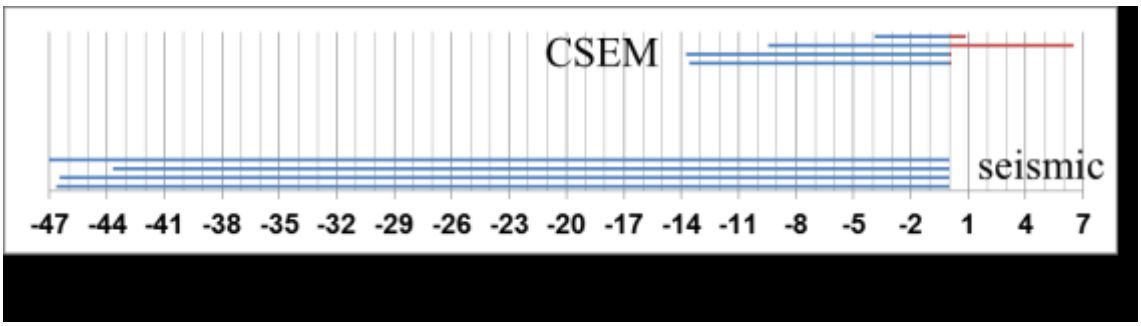

Figure 6.24: *The bar chart showing amplitude change deviations from the reference scenario in which both CSEM and seismic changes are compared.*

6.7 Summary

It has been shown that time – lapse CSEM can distinguish different injected waters from the *in situ* formation water, based on the resistivity anomaly between them, and might potentially be useful in monitoring some selected water flooding systems. This is because the resistivity of the mixed water during injection and fluid replacement is a function of

salinity and temperature differences. Considering cold sea water injection, while temperature effect is restricted to the vicinity of injector, the salinity effect on the other hand effect travels further away from the injector along the water front. Although the latter is smaller in magnitude but its effect have some practical consequences. For instance, in terms of determining the efficiency of *LoSal* water injection for EOR purpose, and in determining the remaining oil in place behind the water flooding front, especially in production scenarios involving significant difference in salinity between the injected water and the formation water.

Modelling of seismic and CSEM sensitivities to different combinations of salinity and temperature, in different secondary and enhanced oil recovery mechanisms, over a period of one year shows the importance of brine chemistry in time-lapse reservoir monitoring for a variety of reasons. Water-flooding directly into the hydrocarbon reservoir (both in the water and oil legs) is potentially visible to both the seismic and CSEM methods. However, seismic has problems associated with mainly pressure effects. EM has problems with salinity and temperature effects competing against each other. When water is injected into the aquifer, seismic might not see it but EM might. Whilst seismic can distinguish between different brines at different chemical conditions due to mass flows in the ocean, distinguishing even quite contrasting formation and injected waters in the reservoir has not yet been reported. EM is quite responsive to brine chemistry, and it appears theoretically possible to distinguish extremes in the subsurface hydrocarbon reservoir. Low salinity injection is easily visible, so also aquifer water injection.

CHAPTER 7

3D CSEM MODELLING AND TIME – LAPSE ANALYSIS

7.0 Introduction

As stated in Chapter 2, good quality repeat datasets are required for geophysical monitoring of changes in the hydrocarbon producing reservoir. This is because the reservoir changes we seek to measure are very small and so also the geophysical signal will be small and only good quality, high resolution data could provide interpretable information we desire. In Chapters 4, 5 and 6, Dipole 1D modelling of CSEM data presents an idealistic and best possible quality and interpretable repeat EM data. However, unlike seismic where 1D convolutional modelling could to a large extent represent the real field data; the Dipole 1D CSEM modelling represents an over-simplified electromagnetic response of the earth. This is because, while seismic is sensitive to the earth's layer density and velocity and to the changes in these properties between layers, thus making it possible to delineate layer boundaries within the earth volume. CSEM, on the other hand, is sensitive to the bulk resistivity of a 3D volume of the earth, and in the context of hydrocarbon reservoirs to the transverse resistance (the vertically integrated resistivity). Therefore, we would expect the Dipole 1D modelling done in Chapters 4, 5 and 6 as schematically described in Figure 7.1a, to be the best case scenario. This 1D modelling only requires pseudo-log extraction of traces of resistivity-depth profiles from the reservoir simulator at every surface location, and no consideration is given to the higher order dimensions. When other dimensional effects, shown in Figure 7.1b, are taken into account in 3D modelling, it is likely that the changes will be smaller. In this Chapter, full 3D frequency domain, electromagnetic responses of CSEM surveys are numerically forward modelled from the 3D resistive (reservoir) structures embedded in horizontally layered background earth model, using the 3D integral equation (IE) method to solve the Maxwell's EM equations.

The main limitation of the IE method is the assumption of horizontally homogeneous background model (Dmitriev 1969, in Zhdanov 2009). This is such that the background

resistivity structure is still here represented with the 1D resistivity logs measurement as described in Chapter 4.

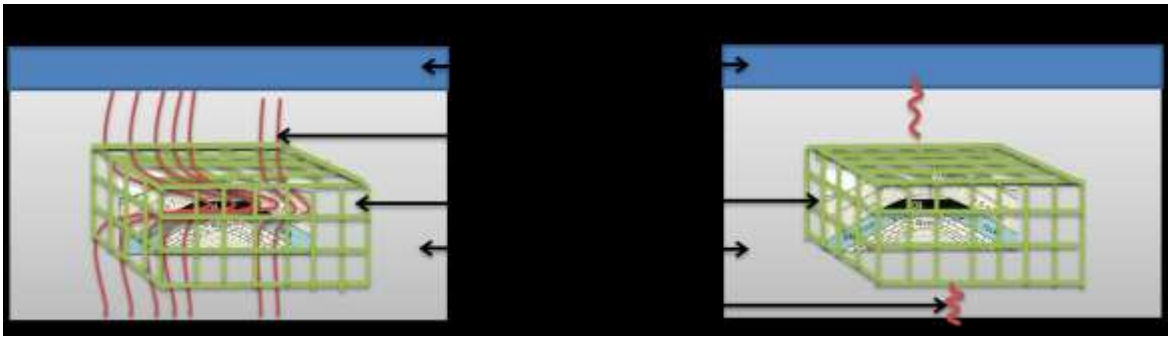

Figure 7.1: *Schematics comparison of (a) 1D and (b) 3D CSEM modelling of a 3D reservoir model. See text for description.*

Also in this method, the conductivity, 'σ' (which is the reciprocal of resistivity), is considered to be distributed into two forms, namely the background conductivity (σ_b) which is employed for electromagnetic Green's function calculation; and the anomalous conductivity (σ_a) which lies within the domain of integration. Therefore, the assumption of simple background structure allows the electromagnetic Green's function calculation to be performed easily and in timely manner. Moreover, such horizontally homogeneous background layers have been commonly used in EM exploration and any deviation from the 1D background model is considered to be anomalous conductivity (Zhdanov 2009). Now, this is consistent with a non-compacting reservoir, where time-lapse difference in the measured EM signal is only associated with the changes in the anomalous conductivity ($\Delta\sigma_a$) within the hydrocarbon producing reservoir.

Another method that could be used to forward model the EM response is the differential equation (DE) method, whereby the differential forms of the Maxwell's equations are numerically solved directly. This could either be in form of finite difference (e.g. Maao, 2007) or finite element (e.g. Key & Ovall, 2011). DE has an advantage of grid flexibility, such that discretization of model parameters could be done using differential methods. The downside of this method is the requirement for the discretization of the whole model, both the background and anomalous domains. Whereas for the IE method, discretization is only

required in the anomalous domain. Although the DE method is widely used to handle models of complicated geological structure, it is however more computationally time consuming than the IE method due to the requirement to discretize the background domain (Zhdanov 2009). For time-lapse measurements involving overburden changes, the DE method could be more appropriate than the IE method. For a non-compacting reservoir, it would be more time-efficient to use the IE method, moreover that the DE method is not likely to provide any additional accuracy over the IE method. Even for a typical reservoir model of 96,000 cells used here, it takes about 36 hours to simulate the EM response using the IE method.

Details about the physical and mathematical description of the IE method are available in the open literature (e.g. Hursan & Zhdanov 2002; Zhdanov 2009). Here, we are more concerned with the application of this method in modelling surface changes in the electromagnetic fields that could be related to subsurface changes in the reservoir, due to hydrocarbon production and water injection activities. We proceeded with various hypothetical examples, and then show a fluid flow engineering simulator – driven example. The algorithm used is supplied by the Rock Solid Images (RSI). It is a FORTRAN version of the original MATLAB programme by Hursan et al. (2006). This is employed for the resistivity – to – EM modelling, in which both the 3D grid (x-, y-, and z- dimensions) are discretized into regular-sized cells, and the corresponding resistivity distribution for all the cells of the resistive anomalous body are extracted into the EM calculator, without having to do pseudo-log extraction.

7.1 Hypothetical homogeneous 3D resistivity to repeat 3D electromagnetic modelling

Let us build our understanding from repeat 3D EM modelling of a hypothetical homogeneous 3D resistivity model. Here, our objectives are to examine different scenarios of model and survey parameters and how they impact on the measured time-lapse signals. The model scenarios are conceptualized in line with different practical field situations.

7.1.1 Signal strength as a function of the size of the anomalous conductive body

The objective here is to examine the effects of an expanding conductor inserted into a resistive body. We consider the model and the survey parameters shown in Table 7.1.

		Parameter	Value
Model	**Sea water**	Depth	400m
		Resistivity	0.33Ωm
	Background structure	Overburden Thickness	1990m
		Average resistivity (7 layers)	3Ωm
	Target Anomalous Body	Baseline resistivity	60Ωm
		Dimension	10 by 10 by 0.05km
		Cell size	100 by 100 by 5m
		Number of cells	100 by 100 by 10
X-directed survey array	**Source**	Length of array (Sx)	20km (-10 to 10)
		Source interval	400m
		Number of Sources	51
	Receiver	Length of array (Rx)	22km (-11 to 11)
		Receiver interval	200m
		Number of Receivers	111
	Field	Transmission Frequency	0.1Hz
		Component measured	In-line electric field

Table 7.1: *Initial model and survey parameters for the modelling*

The model is a mimic of a particular North Sea field. These parameters are kept constant except for the perturbation of the target anomalous body in the monitor models as shown schematically on the plan view in Figure 7.2. Since transmission frequency depends largely on the overburden structure (e.g. in MacGregor & Tomlinson 2014), and because the overburden structure for the 1D modelling is retained for the 3D modelling, then the same transmission frequency (0.1Hz) used in 1D modelling (see Figure 4.15) is used in 3D modelling.

The target anomaly is originally considered to be resistive 'hydrocarbon saturated' body with resistivity of 60Ωm. The perturbation in the monitor surveys, which is effected with the insertion of a conductive body of 5Ωm, is considered to be similar to 'water injection'. The size of the inserted conductor increases like an '*advancing water-front.*' For Monitor 1, the size of the conductor is 2 x 2 x 0.05km; for Monitor 2, 4 x 4 x 0.05km; while for

Monitor 3, 6 x 6 x 0.05km. This means we are invariably looking at lateral flooding system. Thus, we expect some time-lapse anomalies in the monitors with respect to the original baseline model. Each cell shown in Figure 7.2 is further sub-divided into ten cells. The acquisition geometry is arranged such that the towline is x-directed at the centre of the baseline body, thus the sources are traversed parallel to the receivers placed along the x-axis (West – East) direction. No measurement is made along the y-axis (South – North) direction.

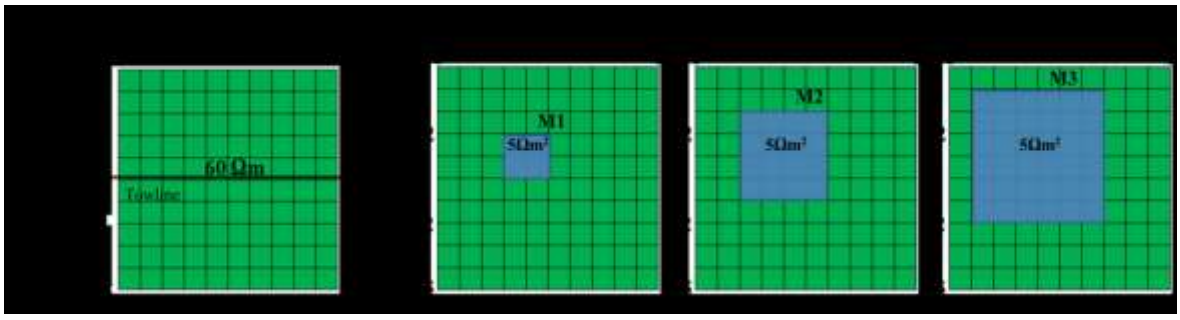

Figure 7.2: *Schematics diagram of baseline and three monitor anomalous models (from left to right) showing the perturbation. See text for description.*

The modelling results are as shown in Figure 7.3. The percentage changes in the in-line CSEM amplitude (ΔM1, ΔM2, ΔM3) are calculated using Equation 4.1 in Chapter 4. Figure 7.3a is a plot of in-line CSEM amplitude changes along the x-directed towline, showing the position and extent of the inserted conductor as it expands from one monitor to the other. As expected, the bigger the inserted conductor (likened to injected water), the larger the CSEM amplitude changes. This anomalous change in amplitude is not symmetrical about the centre of the towline (x = 0) because the inserted conductors are also not symmetrical.

If we define range (r) as a function of source position (S_x) and receiver position (R_x) as:

$$r = \sqrt{(S_x - R_x)^2} \quad ; \tag{7.1}$$

Then, a plot of CSEM amplitude changes as a function of source-receiver range (r) and distance along the towline also reveals the visual increase in the amplitude as a function of expanding conductor inside the resistor as shown in Figure 7.3b.

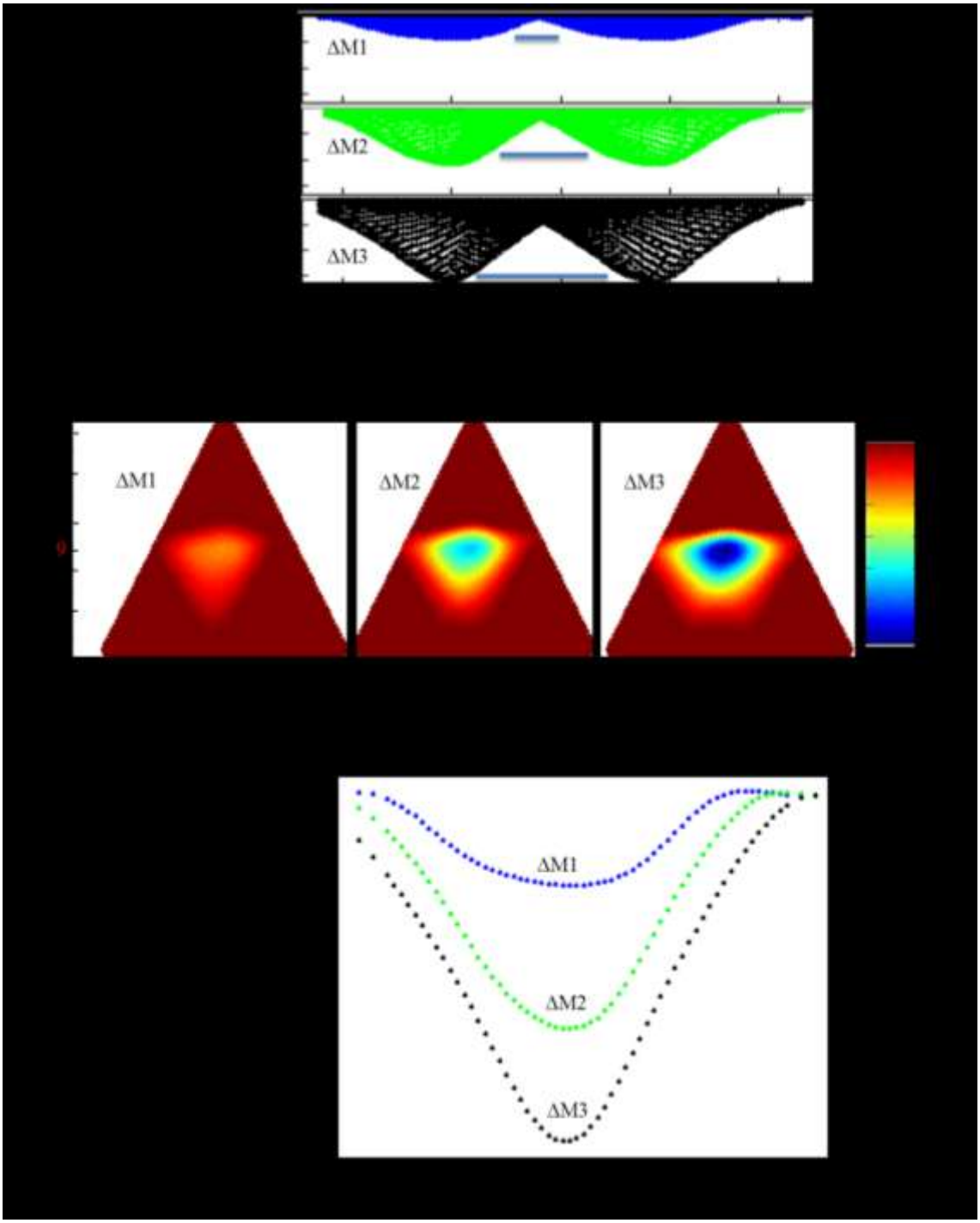

Figure 7.3: *Modelling results displayingin-line CSEM: (a) amplitude changes with respect to the baseline plotted along the x-directed towline; (b) amplitude changes with respect to the baseline as a function of source-receiver range (r) and distance along the towline; and (c) peak amplitude change with respect to the baseline as a function of common midpoint.*

It is also observed that the peak signal occurs at the range around 9km ±100m, thus for source-receiver midpoint offset along the towline, (*mpx*), defined as:

$$mpx = 0.5(S_x + R_x) \quad ; \tag{7.2}$$

A plot of changes in the in-line CSEM amplitude against the source-receiver common midpoint in Figure 7.3c also reveals the amplitude increase as a function of expanding conductor. Thus as expected, the signal strength increases with the size of anomalous conductive body. However, while this exercise cannot show us the size and shape of the inserted conductor, we expect that the ratio of the signals should be proportional to the ratio of the sizes of the expanding conductor, at least for the peak amplitude. This is not directly so, because the signal ratio is about 1:3:4, whereas the ratio of the area coverage of the anomalous conductor is 1:4:9. This means we cannot yet look at the time-lapse CSEM from the quantitative perspective.

7.1.2 The importance of a prior knowledge of the anomalous body in repeat CSEM survey design

The focus here is to examine how our prior knowledge of possible position of the expected anomaly could enhance optimum repeat CSEM survey design. To do this, we consider Monitor 1 model in Section 7.1.1 for the symmetrical and asymmetrical cases as shown in Figure 7.4, and keeping the acquisition geometry the same, that is assuming good repeatability of survey geometry, we produce the inline CSEM amplitude changes as shown in Figure 7.5.

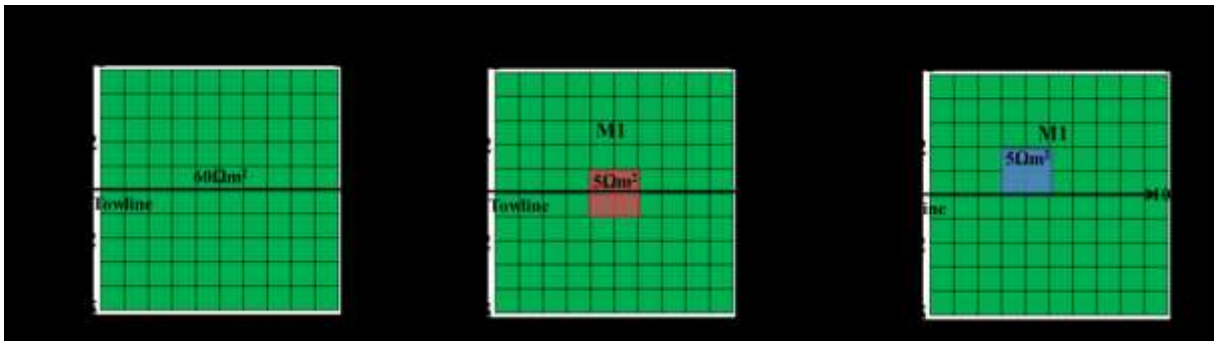

Figure 7.4: *Schematics diagram of the model of the baseline (left), symmetrical anomaly in red colour (middle) and asymmetrical anomaly in blue colour (right) monitor models, with the towlines indicated. See text for description.*

The results show that the signal magnitude is larger for the symmetrical case than for the asymmetrical case, despite that the two anomalous conductors are of equal size. This is simply due to the geometrical positioning of acquisition parameters relative to the anomalous bodies. This is similar to the classical '*edge-effect*' in CSEM exploration. This could be avoided in time-lapse CSEM measurement with a prior knowledge of the suspected anomalous body, and putting such knowledge into the survey design for repeat measurements. Although engineering simulator has its uncertainty and that is why its predictions is always updated as more information are available, but it could also be helpful in providing prior knowledge useful in planning repeat CSEM surveys for optimum signal strength.

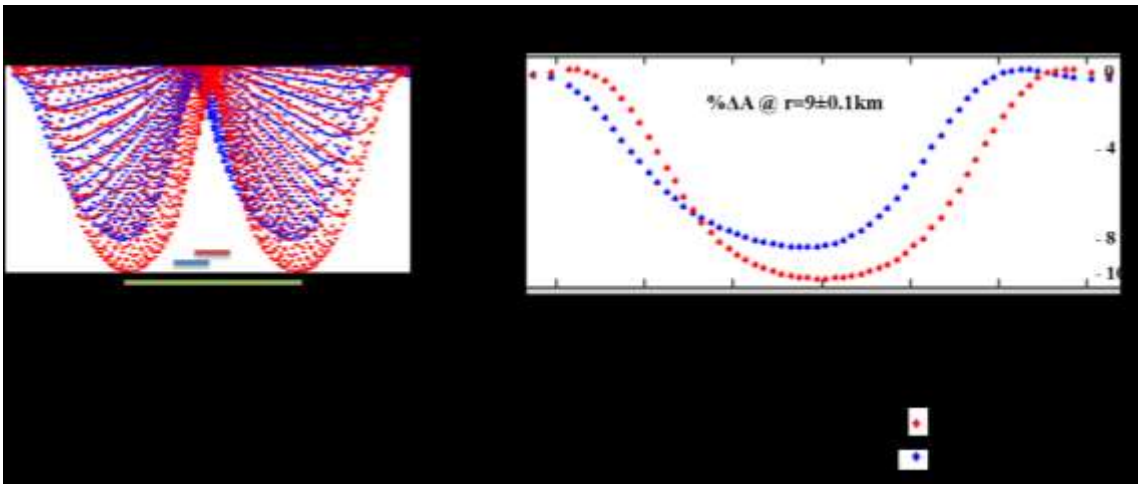

Figure 7.5: *Modelling results showing symmetrical (in red) and asymmetrical anomaly (in blue) displaying in-line CSEM: (a) percentage amplitude changes with respect to the baseline plotted along the x-directed towline, showing the position of the two conductors relative to the resistor; (b) peak percentage amplitude change with respect to the baseline at range 9km±100m, with respect to common midpoint offset.*

7.1.3 Repeat EM amplitude measurements for decreasing dimension of a resistive model along and perpendicular to the towline direction

Following on from the fact established in section 7.1.2, let us examine how the EM amplitude changes as we reduce the dimension of the resistive body along and perpendicular to the towline. The objectives here are to define the extent of the anomalous change in the resistive model. In this instance, we use a rectangular model with dimension

4 x 6 x 0.06km and the grid cell size 40 x 60 x 6m, making 100 x 100 x 10 number of cells. Figure 7.6 shows the schematic representation of the resistive model with respect to the background structure.

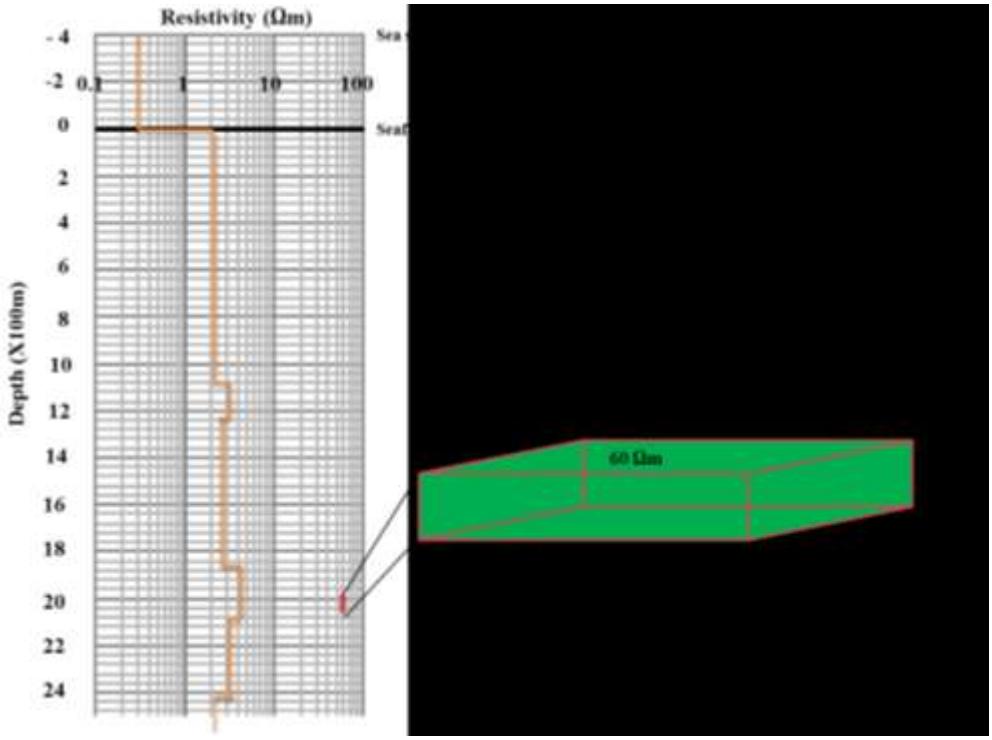

Figure 7.6: *Schematic representation of 3D resistive model with respect to the 1D background resistivity structure, similar to the model information in Table 7.1 except for the smaller model dimension.*

Here, we utilise an array of 9 towlines running south-north direction from -10km to 10km. The towlines are spaced from one another 1km apart, in the west – east direction from -4km to 4km. There are 11 receivers, separated 1km apart from one another, along each towline between -5km and 5km. Thus we have a total of 99 receivers for the entire array as shown in Figure 7.7. So, the array covers and extends far beyond the *x*-*y* dimension of the subsurface resistor - buried baseline target model (the green coloured outline in Figure 7.7). We use 0.1Hz source transmission frequency as the overburden structure is still maintained.

The CSEM amplitude response for the baseline resistive model is normalized with the conductive background response. Normalised amplitude responses are obtained at 16 different source-receiver offsets between 3km and 11km at 0.5km interval. For each offset,

magnitudes of normalised amplitude were measured at 9 spatial positions on the model, expressed by the coordinates shown in Figure 7.8a. These magnitude values are then plotted as a function of the 16 source-receiver offsets for each of the 9 spatial positions as shown in Figure 7.8b.

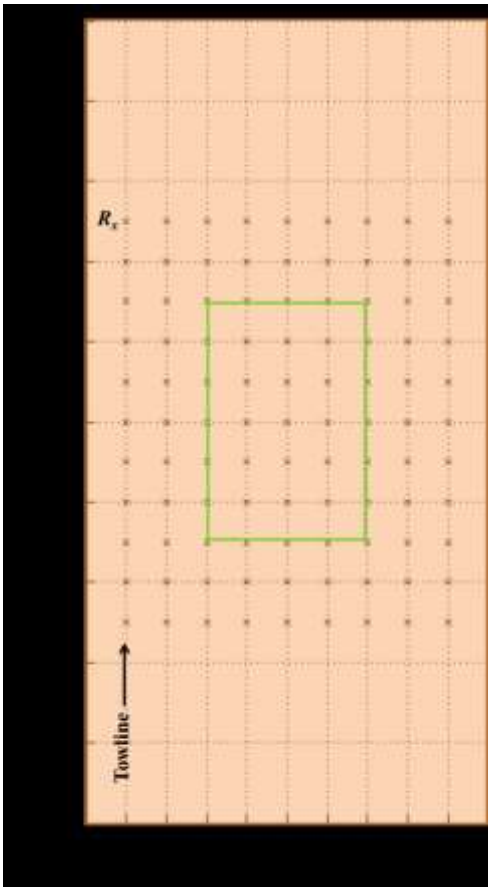

Figure 7.7: *Schematic representation of survey array showing the towlines along the northing direction. The receiver positions are shown with crosses. The baseline outline of the anomalous body is shown with green colour.*

It could be seen that the anomaly strength varies across the structural outline of the body with the peak normalized amplitude magnitude of 22% obtained at the central position (coordinate, x=0; y=0) of the body. The anomaly is low at the edge positions. Figure 7.8b shows that the peak anomaly for all spatial positions is observed at 8.5km offset. Beyond 10km offset, there is a flip in the sign of anomaly values. This is attributable to the classical air interaction with the anomaly.

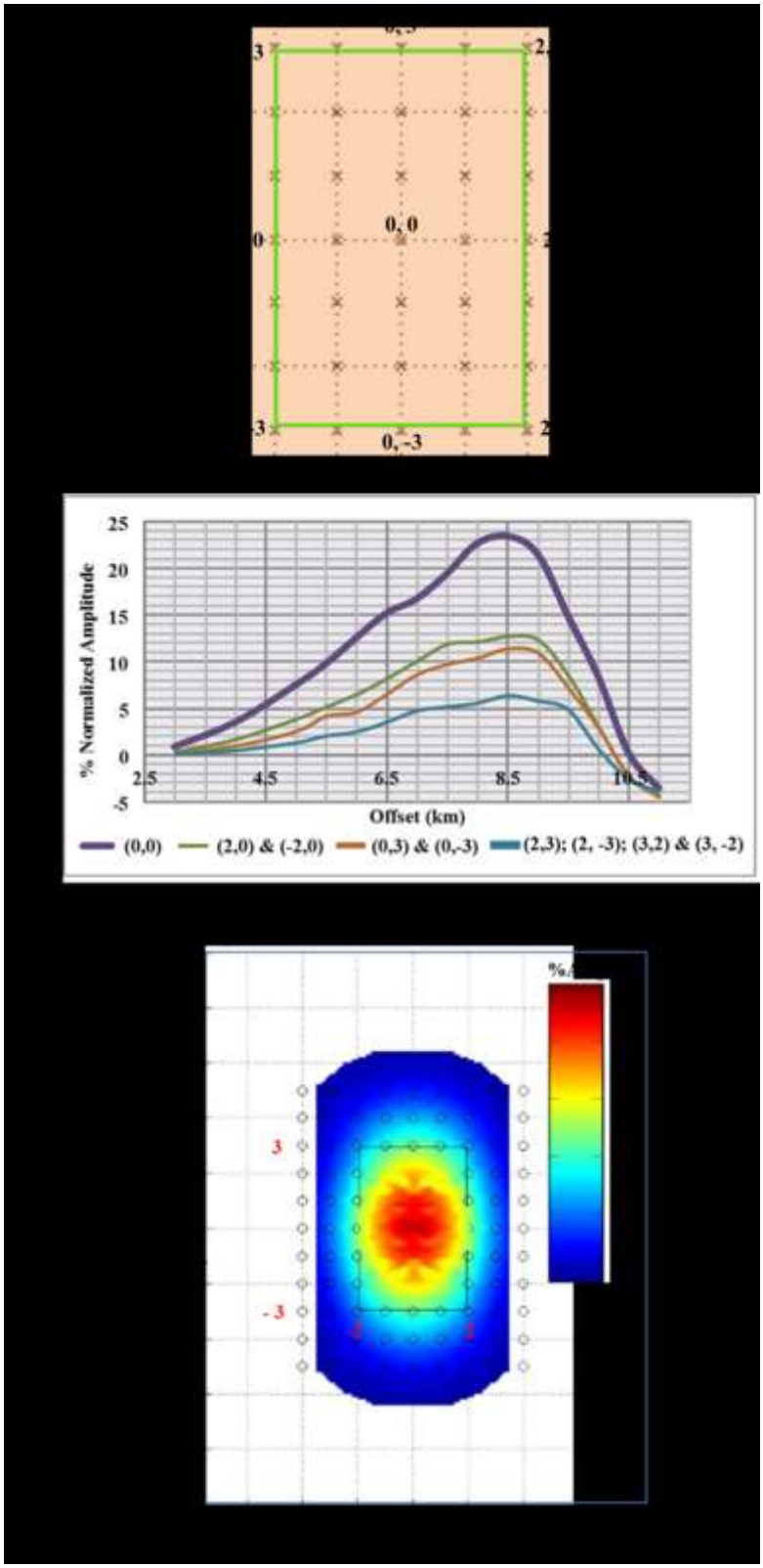

Figure 7.8: *Baseline survey: (a) 9 spatial positions where magnitudes of normalized amplitude response were measured; (b) Measured magnitudes plotted as a function of source – receiver offset; (c) Common source – receiver map of the normalized amplitude at 8.5km offset for peak anomaly.*

Using 8.5km offset for peak anomaly, we obtain the common source – receiver offset map of the baseline normalised amplitude as shown in Figure 7.8c. The 3D resistive body produced a significant 2D anomaly with respect to the background structure. However, the rectangular (4km by 6km) shape of the body cannot be exactly reproduced on the EM modelled result. This is due to the intrinsic structural resolution problem of electromagnetic methods.

Let us now reduce the size of the base model on the *y* – axis by 1km, and 2km to obtain monitors 1 and 2 models respectively (Figure 7.9a). This mimics replacement of resistive 'hydrocarbon' with the background 'water'. Before we do the 4D analysis of repeat EM measurements of these models, it is important to know the optimum amplitude and offset suitable for the chosen transmission frequency of 0.1Hz.

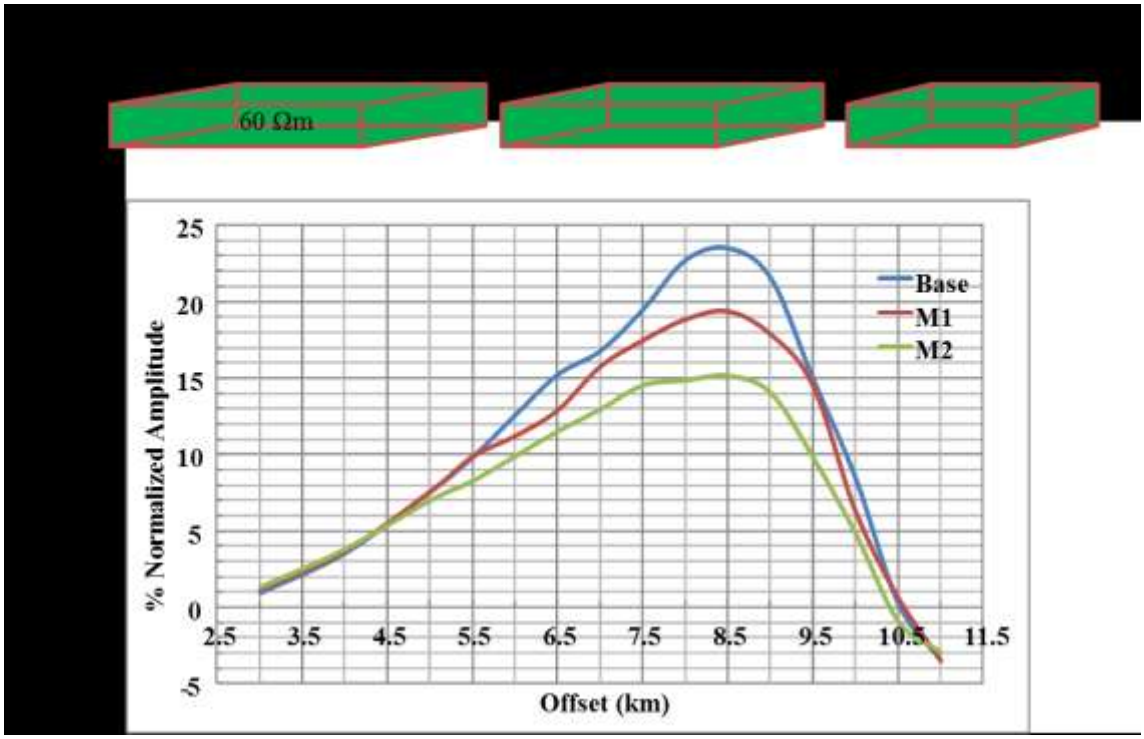

Figure 7.9: *(a) Baseline and monitor models, with similar resistivity value but with progressive reduction in the y-dimension. (b) Normalized amplitudes with respect to the background at the central position of the anomalous bodies (coordinates, 0, 0) plotted against source – receiver offsets for the baseline and monitor models*

Therefore, the anomalous amplitudes at the central coodinate of each of these varying dimensions of the 3D bodies were plotted for different offset. It is observed that the highest normalised anomalous amplitude with respect to the background is still at 8.5km offset as shown in Figure 7.9b. This offset is then taken for further analysis.

Next, we reduce further the dimension of the 3D anomalous body along the y – axis by 3km, 4km and 5km to obtain M3, M4 and M5 respectively. Then we calculate the normalized amplitude maps for the baseline and the five monitor models with respect to the background response as shown in Figure 7.10a. The percentage difference anomaly maps for the monitors with respect to the baseline are shown in Figure 7.10b. The largest difference signal in Figure 7.10b, as expected, is observed on the far right. It is the difference between the largest (Baseline with 4km x 6km x 0.06km volume) and the smallest (monitor with 4km x 1km x 0.06km volume) sized 3D body.

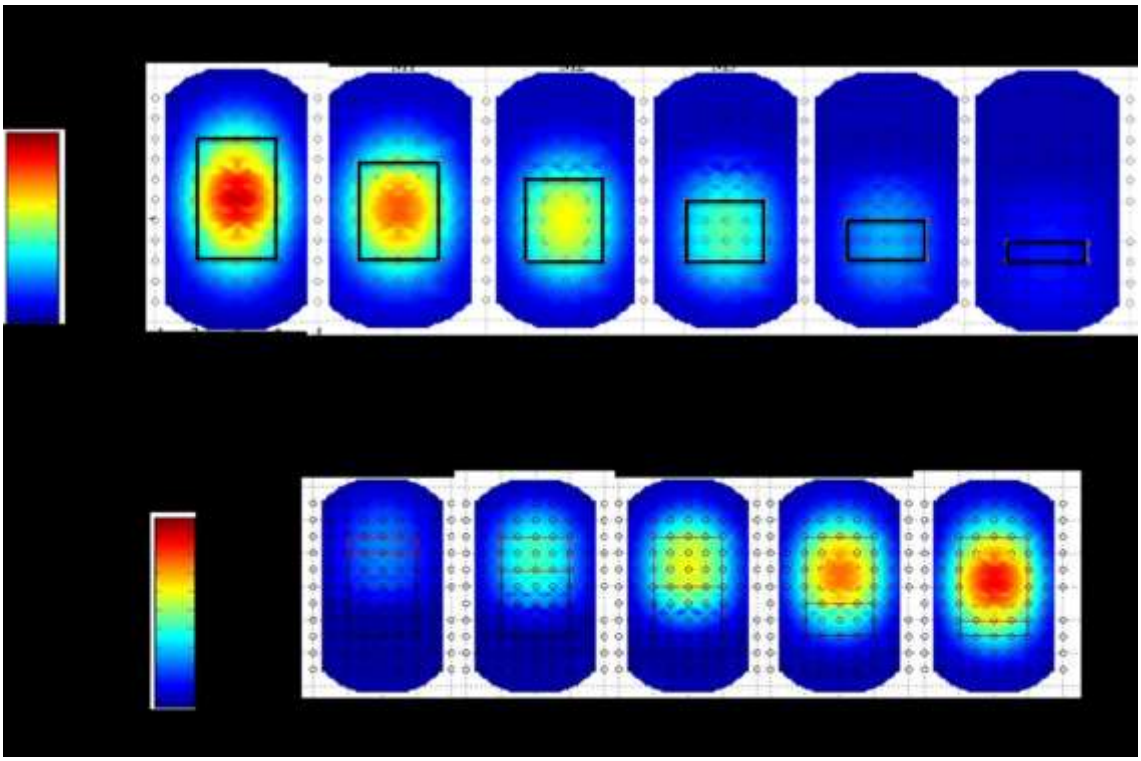

Figure 7.10: *CSEM amplitude analysis at 8.5kn offset, for dimensional reduction along the towline: (a) Normalized amplitude maps for the baseline and the five monitor models with respect to the background response. (b) The percentage difference anomaly maps for the monitors with respect to the baseline. See text for detail.*

We obtain up to 20% amplitude differences. These maps were calculated at 8.5km offset, which produces the optimum amplitude. While the difference maps offers information as to the possible area extent of the anomalous zone where the resistive bodies have been replaced with the background, the resolution is expectedly poor.

A similar effect is observed for the decreasing dimension along the x – axis, perpendicular to the towlines direction (see Figure 7.11).

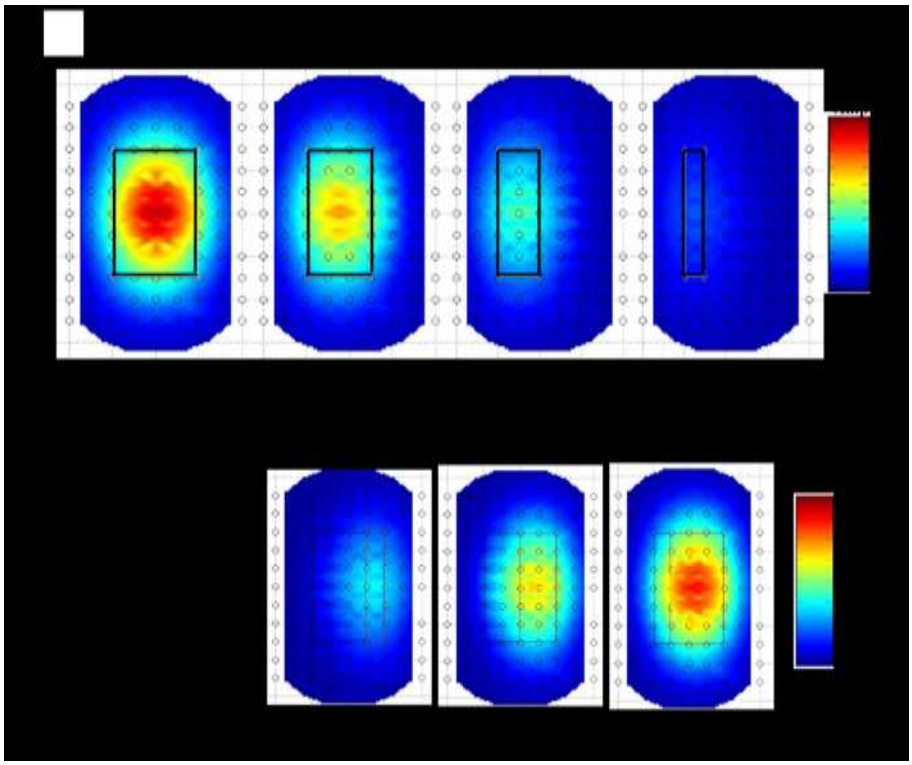

Figure 7.11: *CSEM amplitude change at 8.5km offset, for dimensional reduction perpendicular to the towline: (a) Normalized amplitude maps for the baseline and the three monitor models with respect to the background response. (b) The percentage difference anomaly maps for the monitors with respect to the baseline. See text for detail.*

Here, the x – axis is reduced progressively by 1km from the right hand side for monitors 1, 2 and 3. Both analyses are tantamount to lateral water flooding, whereby the conductive water (similar to background condition) replaces the resistive oil (similar to the resistive model). It is either we analyse several individual static maps for the baseline and the monitors, to understand where-else do we have resistive oil highlighted with amplitude

maps normalised with the background response, or we calculate dynamic difference maps normalized with the baseline response to highlight the flooded areas and then assume the other portion is where we have resistive oil remaining to tap. The latter option could be misleading; as such area could equally be saturated with conductive water, as it will give similar time-lapse difference signal. So, it is better to combine the two analysis methods for better understanding, especially when there is no flow fluid simulation model to calibrate the time-lapse signals with activities at the well locations. Comparing Figure 7.10 with Figure 7.11, it can be seen that the dynamic anomalies are better resolved when they are parallel to the towlines than when they are perpendicular to the towline, this is because they are better sampled along the towlines than across the towlines.

7.1.4 Repeated EM measurements due to changing subsurface resistive body

Here we assume that, rather than replacement with background low resistivity value as depicted by reduction in the dimension of the resistive model, the resistivity of the model has reduced but geometrical dimension is still the same.

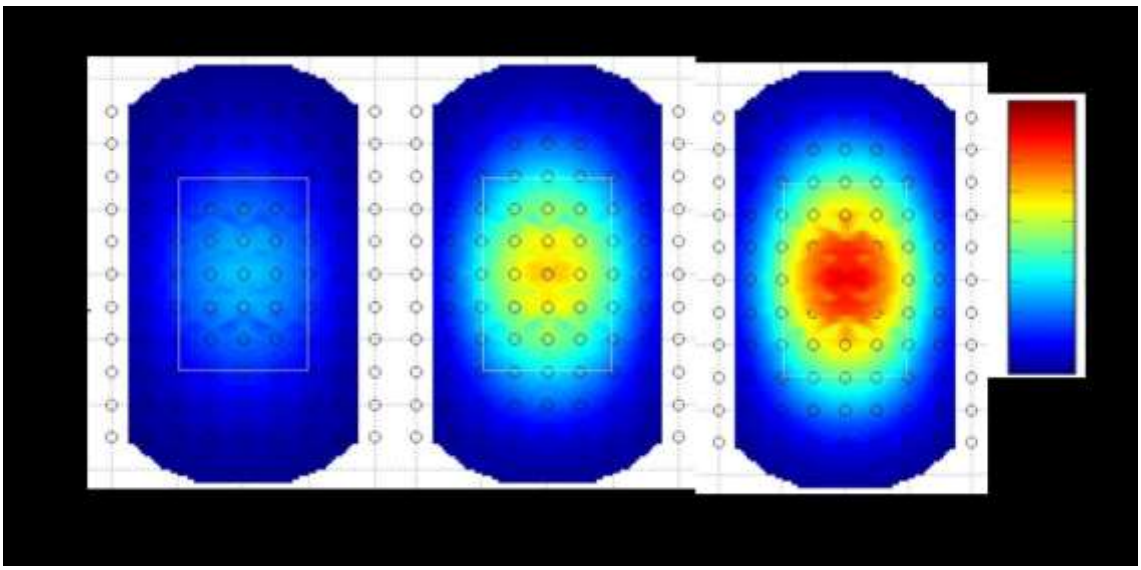

Figure 7.12: *CSEM percentage difference anomaly maps for the monitors with respect to the baselineat 8.5kn offset, for reducing resistivity of the resistive body. See text for detail.*

This is similar to reduced hydrocarbon saturation as we produce the reservoir. Of course, this means increased water saturation. If the baseline resistivity is reduced from 60Ωm to 40Ωm, 20Ωm and 10Ωm respectively for monitors 1, 2 and 3; then we have difference CSEM amplitude maps as shown in Figure 7.12. For ΔM1 with 33% decrease in resistivity from the baseline, we observe a 7% change in CSEM amplitude; similarly for ΔM2 with 67% drop in resistivity produces about 12% change in CSEM amplitude, while ΔM3 with 83% drop in resistivity produces approximately 18% change in amplitude. All observations are made at the centre of the anomalies, but a similar trend is observed at the edges. It could be deduced that there is a ratio of almost 5 to 1 between the percentage reduction in resistivity and the corresponding percentage change in CSEM dynamic amplitude with respect to the baseline.

7.1.5 Repeated EM measurements due to an expanding square of a conductor inserted into a subsurface resistive body

Next, let us insert a 5 Ωm square conductor into the resistive model. We start from conductor with dimension 1km by 1km for monitor 1, and then steadily expand the conductor to 2km by 2km for monitor 2 and finally to 3km by 3km for monitor 3. This is to mimic a water injector drilled and completed within an oil leg, where water pushes away the oil towards the producer somewhere else. Our aim is see how the EM signals changes as the square conductor expands, similar to how a water front expands around the injector. It could be observed that the wider the inserted square hole, the lesser the detectable amplitude with respect to the background in Figure 7.13a, thus we have increasing time-lapse amplitude responses Figure 7.13b.

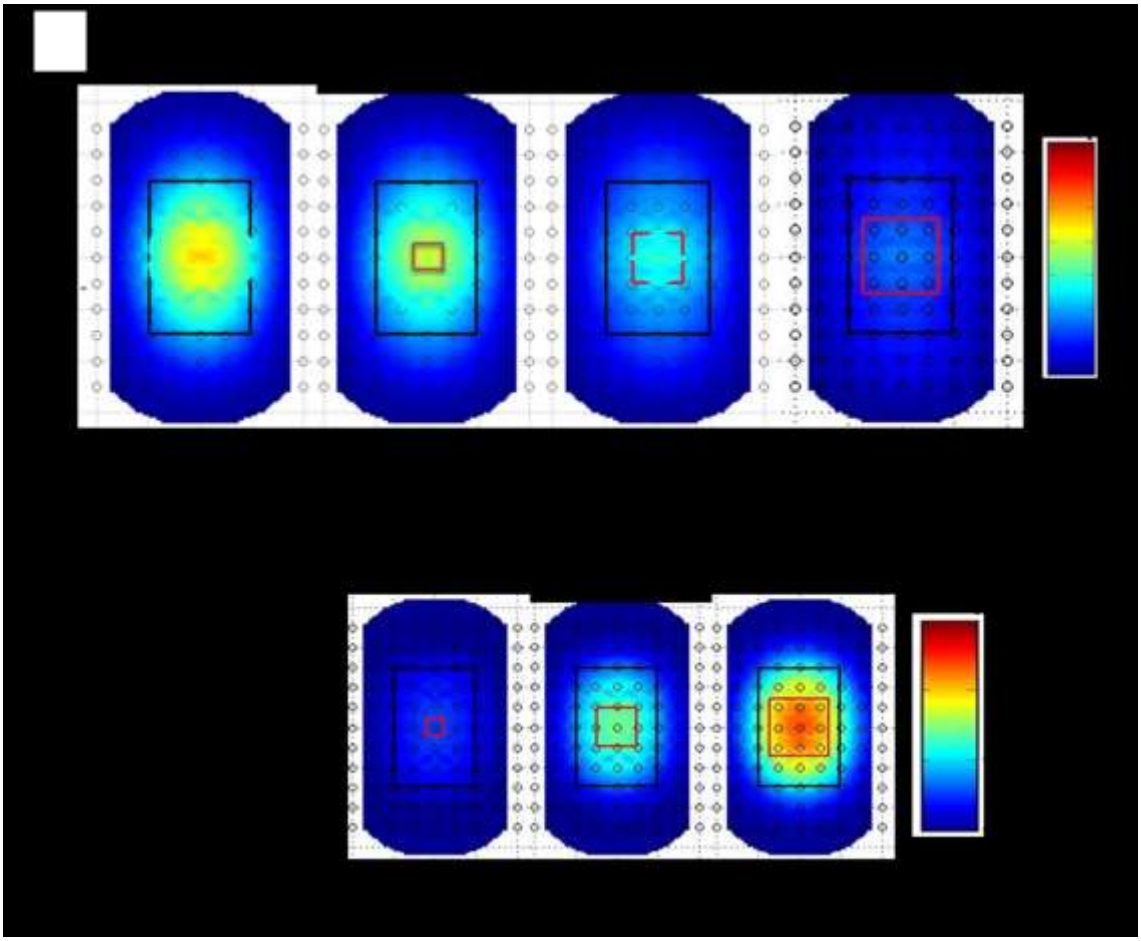

Figure 7.13: *CSEM amplitude change at 8.5km offset, for expanding square conductors inside the resistive body: (a) Normalized amplitude maps for the baseline and the three monitor models with respect to the background response. (b) The percentage difference anomaly maps for the monitors with respect to the baseline. See text for detail.*

7.1.6 Effect of overburden thickness on repeat EM measurements

Here we look at the effect of overburden thickness, that is, the burial depth of the resistor on the repeat EM measurements of the changes in the resistor. We consider, in turn, two other cases of burial depths; 250 m (i.e. interval 1740 m to 1800 m), and 500 m (i.e. interval 1490 m to 1550 m) shallower than the 1900m depth (i.e. 1990 m to 2050 m) as shown in Figure 7.14 for a resistor with similar dimension.

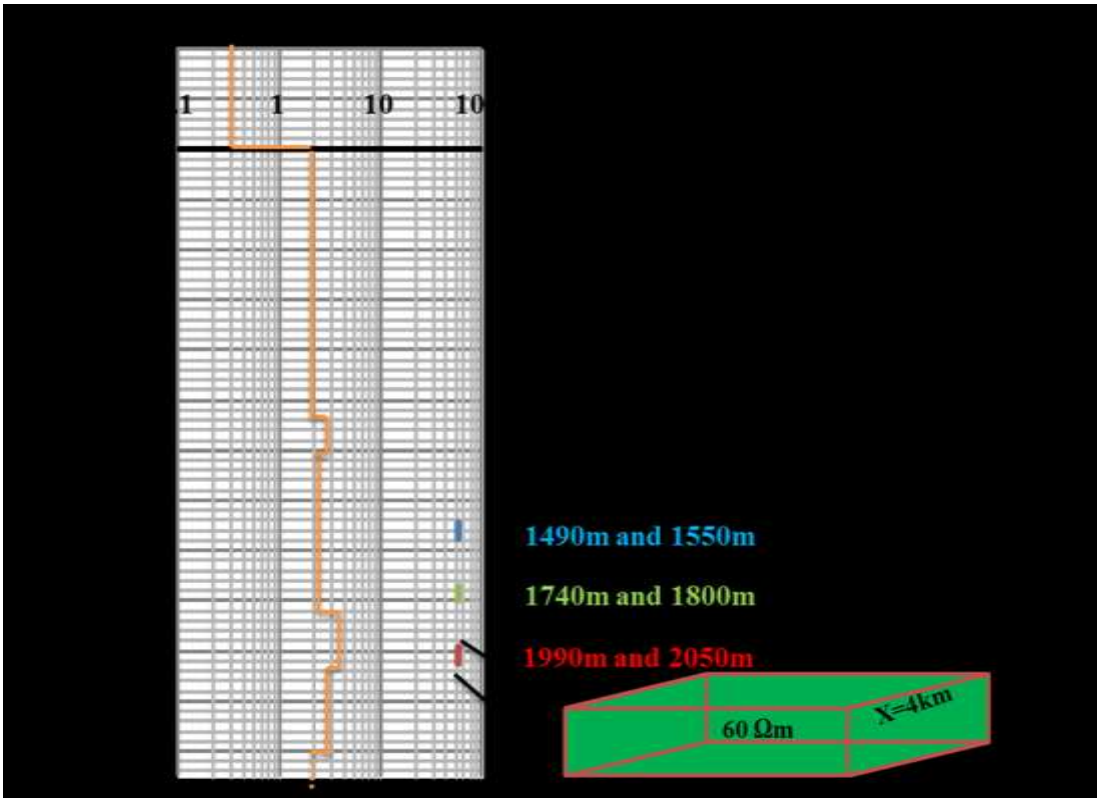

Figure 7.14: *3D resistive body indicated at different burial depths: original depth, 250m and 500m shallower depths.*

Figure 7.15a shows the 1D CSEM amplitude responses as a function of frequency and offset for the three cases of burial depths, each amplitude measurement is normalised with its background response. Different signal contents are observed for similar frequency – offset combination. For better comparison, we use 0.1 Hz and 8.5 km as reference frequency and offset respectively, as indicated with small circle in Figure 7.15a, to model 3D responses for the three cases of burial depths, each normalised with individual background response. It is observed that even though the resistive target model is of equal size, the normalised EM amplitude increases with the shallowness of the burial depth.

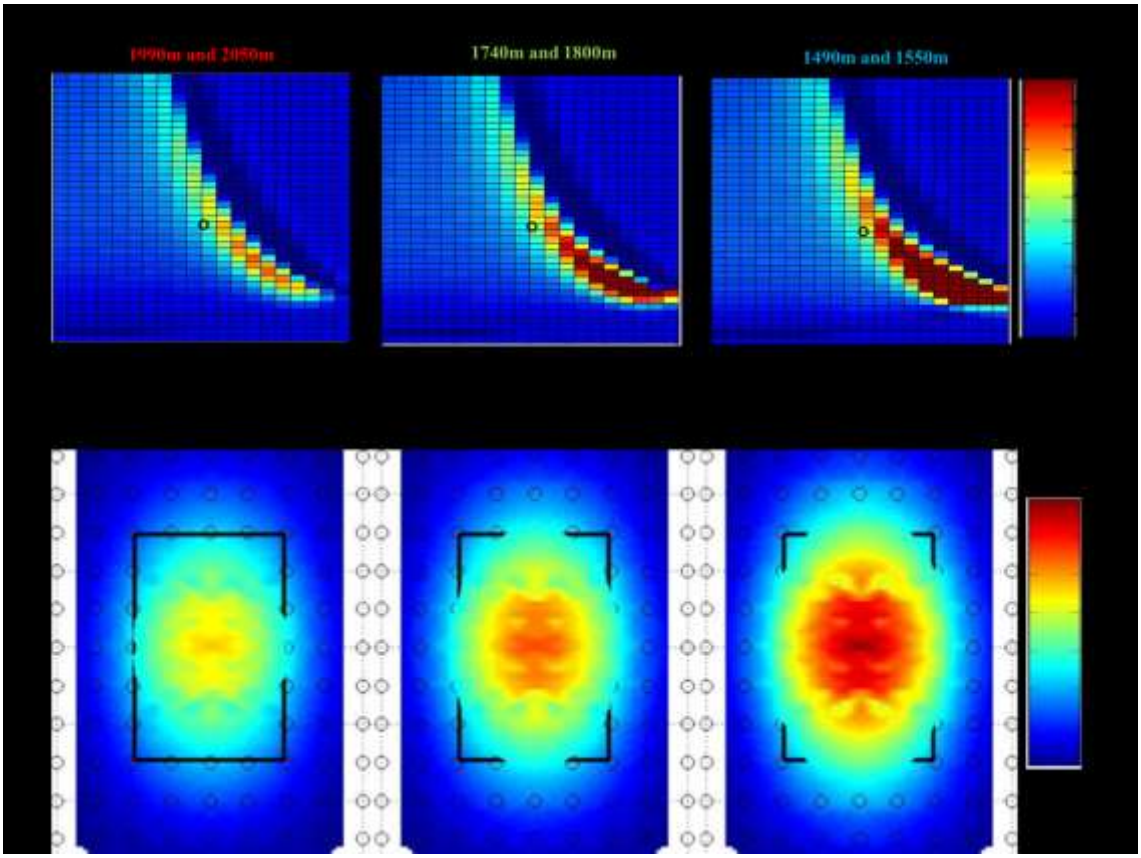

Figure 7.15: *Baseline CSEM measurements for resistive body placed at different burial depths: (a) 1D Frequency – offset – signal plot. (b) 3D modelled results at a chosen offset of 8.5km and frequency 0.1Hz indicated with small circle in (a). See text for detail.*

Next, the resistive target model is perturbed, for each case of burial depth, and the respective EM amplitude changes with respect to individual baselines, at the centre of the anomaly are plotted against the offsets as shown in Figure 7.16, similar observation is made. The shallower the resistive model, the higher the repeat EM amplitude change. Of course, this is a general phenomenon in geophysics.

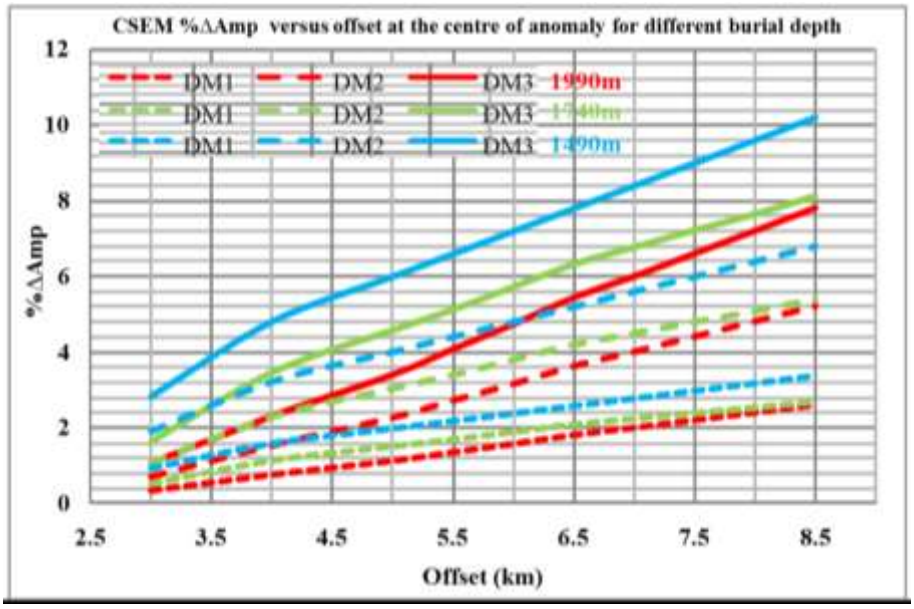

Figure 7.16: *A plot of repeat EM amplitude changes with respect to individual baselines, at the centre of the anomaly, against the offset for different depths to the top of anomalous resistive model as indicated.*

7.1.7 Effect of background resistivity on repeat EM measurements

Most of the time, especially during exploration, we do not have information about the background resistivity structure. In this case, we examine the impact of the background structure by doubling the original values. This resulted in about 70% reduction in the amplitude response of the 3D body with respect to the background structure (see Figure 7.17a and b).This means the more resistive the background; the less our ability to detect the resistive anomalous subsurface target. Even in time-lapse measurements, information between well locations is limited. The repeat EM response is also reduced by similar amount for the same perturbation (see Figure 7.18). This shows the importance of the background information in CSEM modelling and interpretation. The appropriate question to ask then is what production phenomenon can cause time-lapse change in background resistivity?

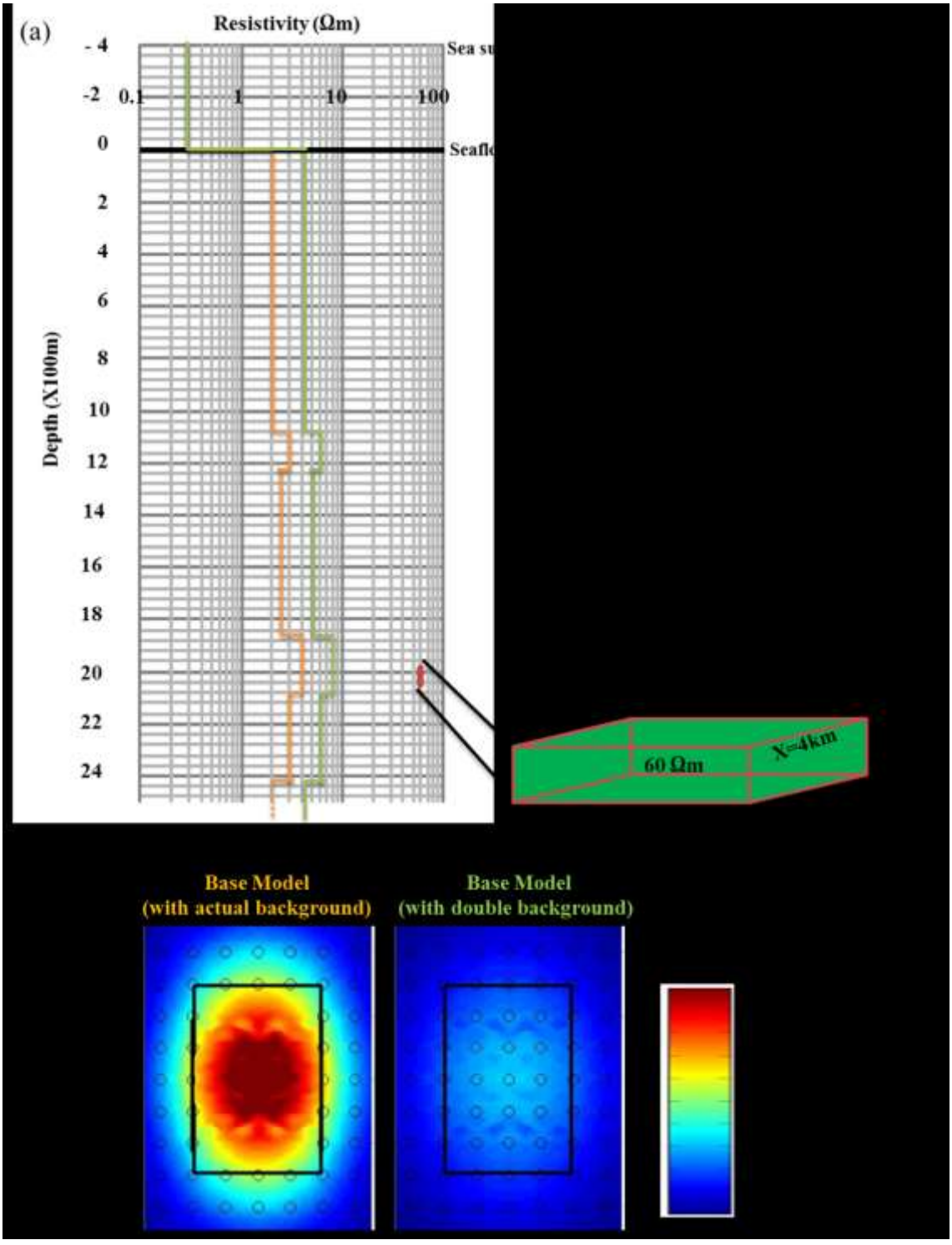

Figure 7.17: *Effect of background resistivity: (a) schematic of double background resistivity with respect to the target model; (b) Normalized EM amplitude for the base model of the two cases.*

For compacting reservoirs, where young and unconsolidated overburden sediments become more compacted as we produce from the underlying reservoir, thus decreasing the porosity

in the overburden and possibly in the reservoir for further production. This condition could increase the resistivity, and would deem the time-lapse response for oil – water replacement.

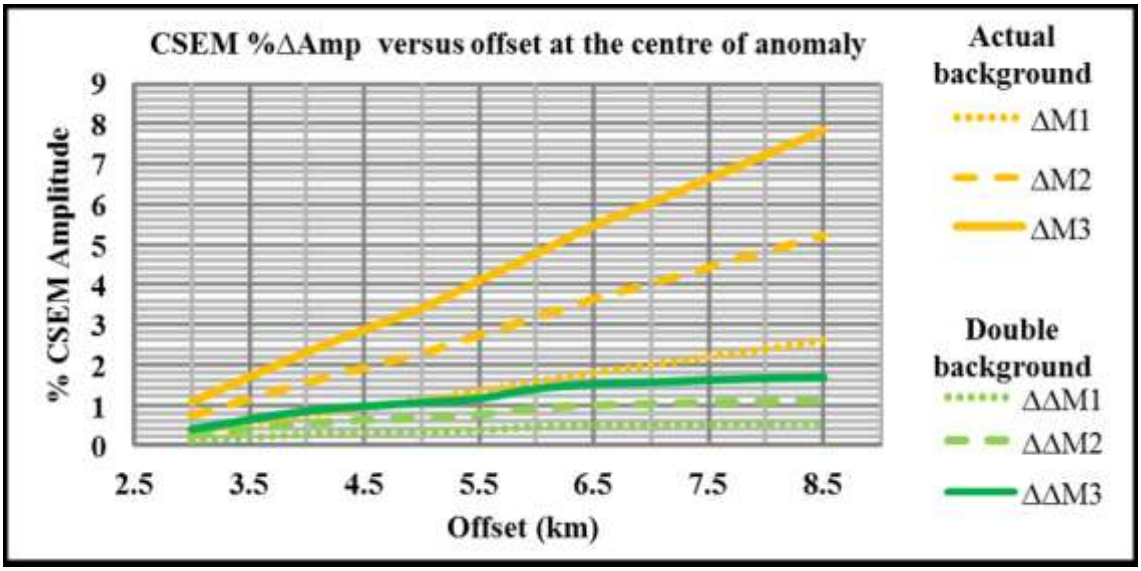

Figure 7.18: *Effect of background resistivity: Repeat EM measurements for the two cases of background resistivity structure. See text for details.*

Also, if we have near surface salt water intrusion into the overburden, there could be reduction in the resistivity which should produce reversed EM response to the above phenomenon. This could constitute geologically – induced 4D noise, rather than desirable engineering – induced 4D signal. However, a case of this nature is not likely, except for reservoirs near a mobile salt dome. For non-compacting reservoir where there is no near surface salt intrusion, there is no other feasible scenario that could increase or decrease the overburden resistivity structure.

7.1.8 Effect of overlying shallow resistor on repeat EM measurements of the underlying resistor

Usually, we tend to have more than one reservoir section in a field. Thus, we model the effect of an overlying smaller resistor (20m) on the main resistive target (60m) as schematically described in Figure 7.19a. The overlying resistor produces an 'add-up' EM

amplitude effect on the underlying resistor. Thus, we have higher baseline amplitude response with respect to the 1D background structure for the case with shallower resistor than for the case with no shallower resistor, as shown in Figure 7.19b.

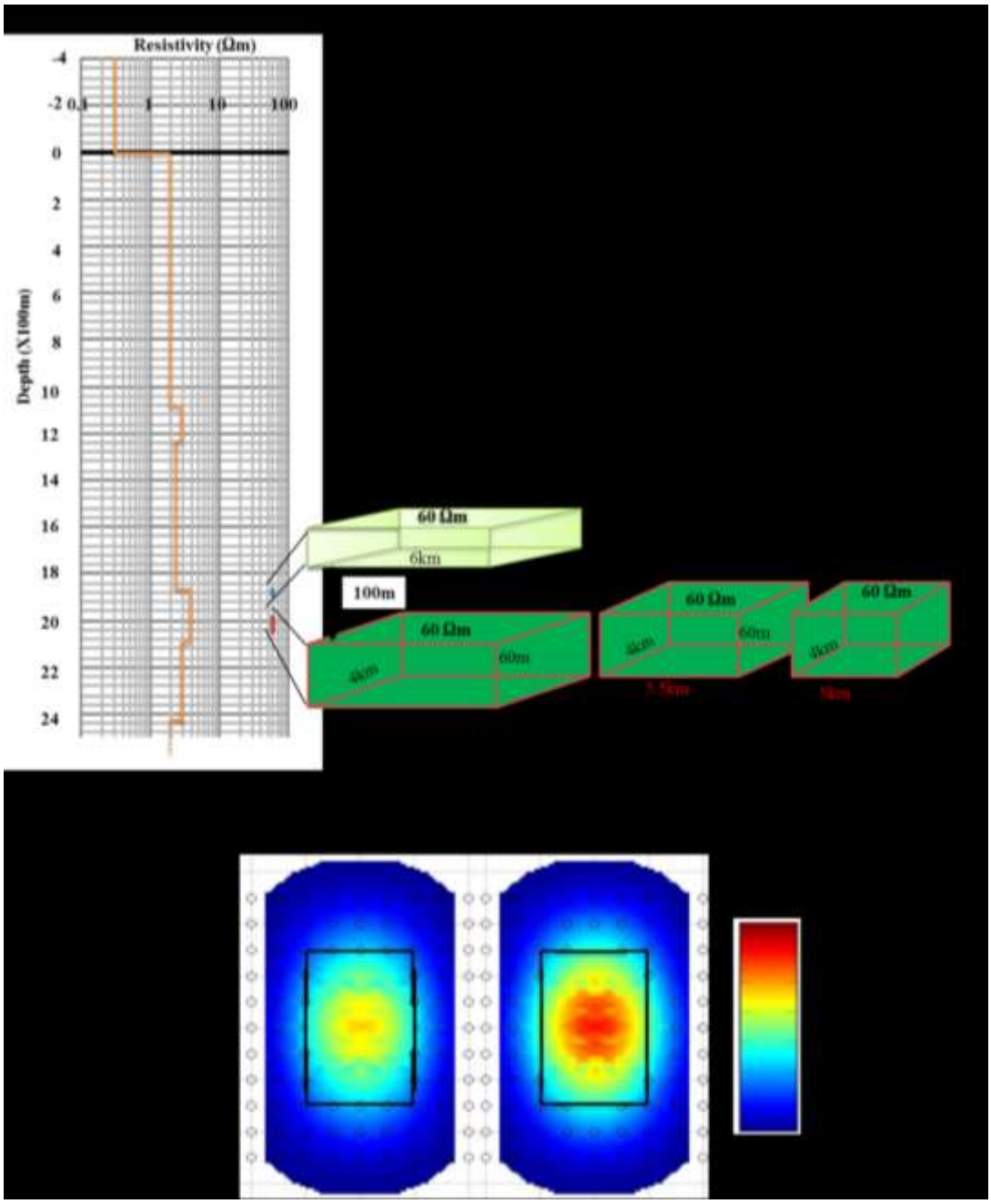

Figure 7.19: *Effect of shallower resistor: (a) Schematic illustration of shallower and thinner resistor overlying the main resistor. The main resistor is subjected to changes the in y-dimension. (b) Baseline EM amplitude responses normalized with similar background response, for the two cases of 'no shallower' and 'with shallower' resistor. See text for details.*

For time-lapse domain, we consider changes only in the deeper resistor with dimensional reduction along the *y*-axis by 0.5km for monitor 1; and by 1km for monitor 2. This is done for both cases, with and without shallower resistor. It is observed that the shallower resistor acts to increase the EM amplitude contribution of background structure with respect to the repeat EM difference signal, due to the deeper changing resistor. Therefore, the magnitude of time-lapse signal becomes much smaller for the case when there is a shallower 3D resistor, than for the case when there none, as shown in Figure 7.20.

In reality we can usually identify the producing reservoir, such that we can isolate the effect of the other non-producing reservoir layer. However, the situation can become more challenging if two or more reservoir intervals are perforated and being produced at the same time. In this case, the overall time-lapse EM signals should be decoupled into the component parts in order to interpret for individual resistive layers. This is one area where inversion could be of help.

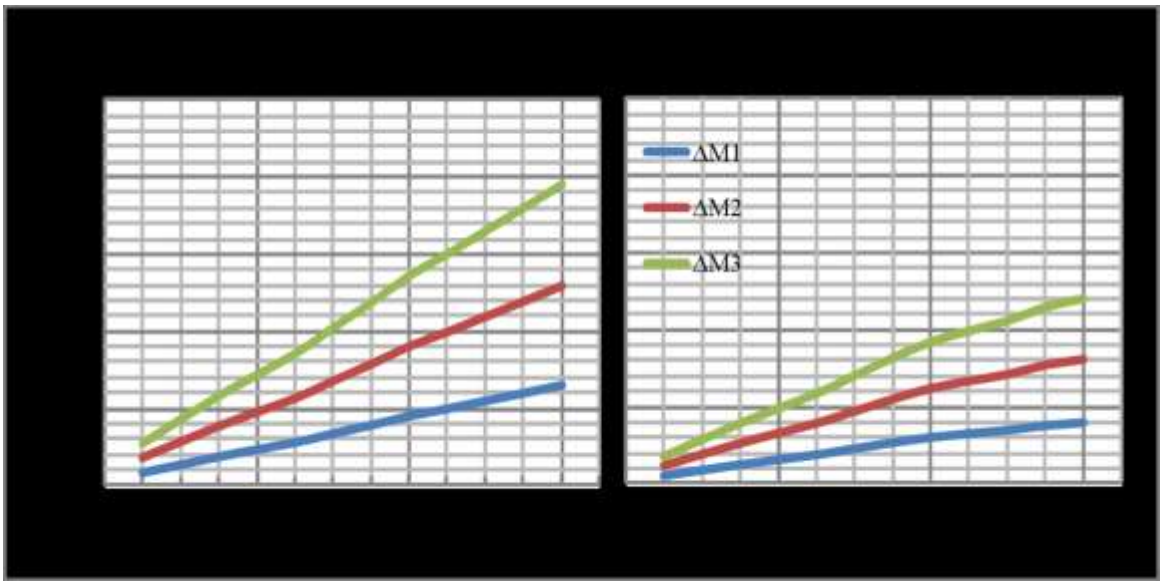

Figure 7.20: *Effect of shallow resistor: Percentage CSEM amplitude measurements normalized by individual baselines, for the two cases without and with shallower resistor. See text for details.*

7.1.9 EM attributes analysis: second derivatives of amplitude with respect to source – receiver range

So far, the major problem with CSEM surveys is anomaly registration within the structural outline. One way that has been identified to mitigate the problem is by taking the second derivatives of the repeat normalized CSEM amplitudes with respect to the source-receiver rangeas shown mathematical in Equation 6.3 (see Andreis & MacGregor 2011).

$$2^{\text{nd}} \text{ Derivatives EM attributes } = \frac{\partial^2 A}{\partial R^2} \quad ; \quad (6.3)$$

where 'A' is the normalized EM amplitude and 'R' is the source – receiver range.

This attribute helps in defining the edges of the anomalous body. Here we implement this idea for the EM responses along the line of instruments with some model examples. For instance, using the EM response for the baseline model in section 7.13 (Figure 7.8c), a plot of stacked 2nd derivatives versus source – receiver positions along the towlines in Figure 7.21 defines the limiting edges (-3km to 3km) of the anomalous body along y – dimension.

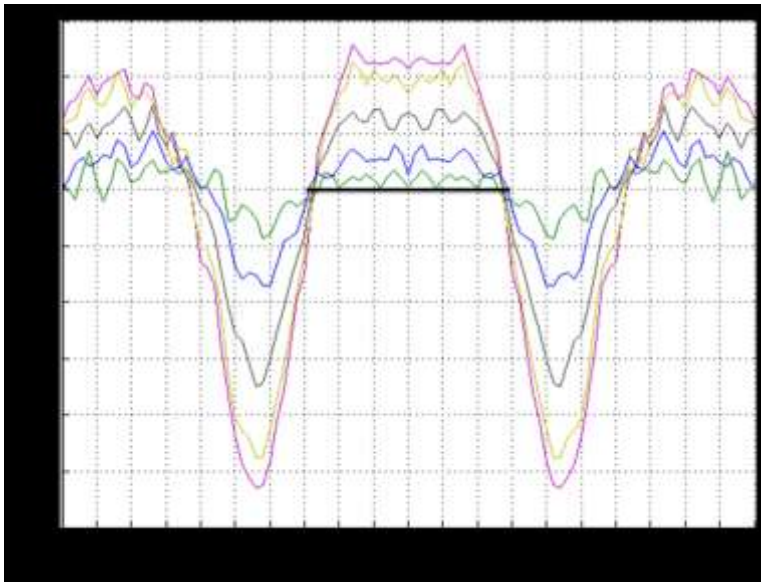

Figure 7.21: *A plot of stacked 2nd derivatives versus source – receiver positions along the towlines.*

Another example is shown in Figure 7.22. Here we rotate the original model by interchanging the *x*– and *y*– axes such that it looks as if the repeat surveys are carried out with *x*-directed tow-lines, even though the survey is *y*-directed. Here, part of the model has been replaced with the background by removing 0.5km, 1km and 1.5km along the *y*-dimension of the model, respectively for monitors 1, 2 and 3. Then, the repeat EM amplitude changes normalized with the baseline are calculated as shown in Figure 7.22a. Without the 'red-colored' frame, it would be difficult for us to identify the areas where we have background resistivity structure replacing the model resistivity.

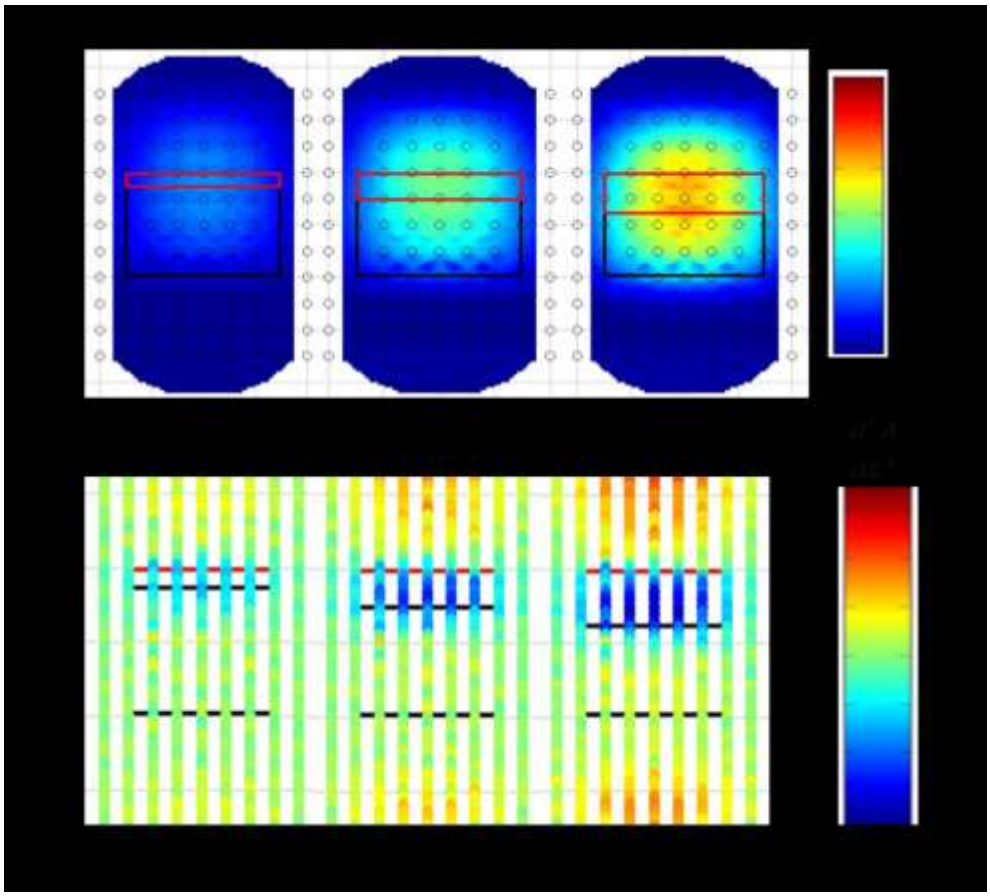

Figure 7.22:*2nd derivatives EM attribute: (a) Repeat EM amplitude changes normalized with the baseline. (b) The corresponding stacked 2nd derivatives maps showing the edges of the anomaly. See text for details.*

However, with the second derivative maps of EM amplitude changes with respect to source – receiver range, presented along the towlines as shown in Figure 7.22b; it could be observed that the section of the base resistive model that has been replaced with conductive

background is properly outlined and the size and intensity of such section increases with the length of replacement.

Another example is considered for the expanding square holes in section 7.1.5; the squares are better defined with the second derivatives attribute as shown in Figure 7.23.

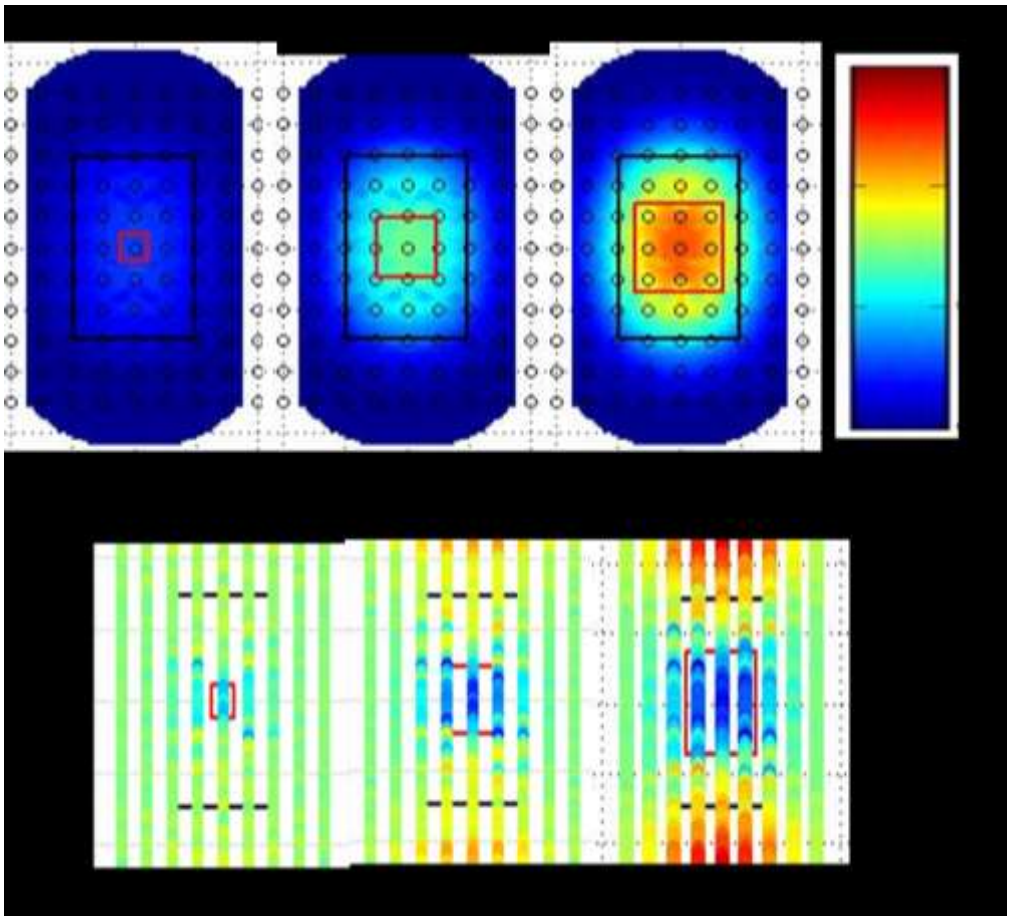

Figure 7.23:*2nd derivatives EM attribute: (a) Repeat EM amplitude changes normalized with the baseline, for expanding square holes. (b) The corresponding stacked 2nd derivatives maps showing the edges of the expanding square anomaly. See text, and section 7.1.5 for more details.*

However, it should be noted that noise has not been incorporated into these example.

7.2 Heterogeneous synthetic reservoir simulation to 3D CSEM modelling: Can we interpret 4D CSEM difference maps qualitatively?

So far we have looked at a homogeneous resistor with regular change in shape, analogous to conductive water replacing resistive oil. Nonetheless, in order to examine how well can we qualitatively interpret repeat 3D EM modelled results in reality; we now consider a heterogeneous synthetic reservoir model. Here, changes in saturation are irregular in shape and realistic water-flooding front, based on engineering simulation model is used.

7.2.1 Direct qualitative interpretation

We use the same reservoir model dimension of 4km *x* 6km *x* 60m,but a slightly different grid cell dimension of size 50m *x* 50m *x* 6m, making up 80 *x* 120 *x* 10 (96,000) number of cells.

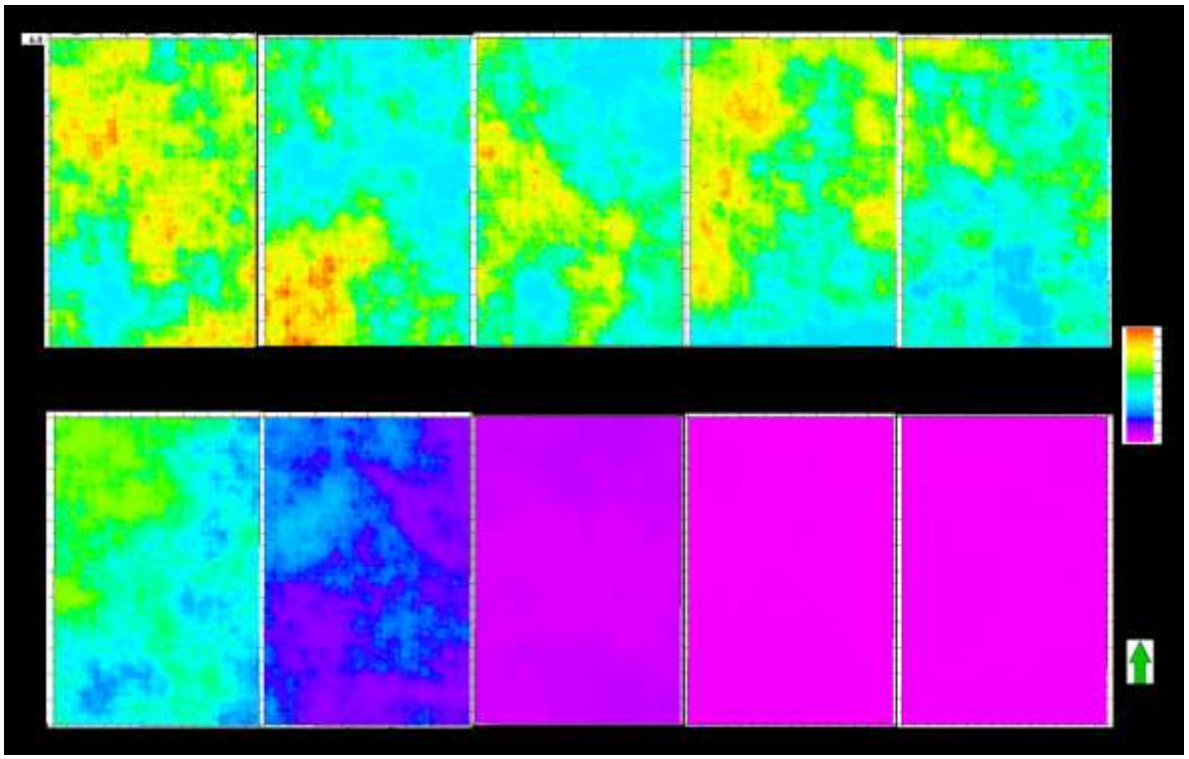

Figure 7.24: *Resistivity slices for the baseline model; layers 1 to 5 (left to right, at the top row) and layers 6 to 10 (left to right, at the bottom row). See text for more description. Layer 1 to 10 represents top to bottom of the reservoir.*

All other survey parameters were maintained, except that the line spacing is now 500m apart, making the number of y-directed towlines to be 17, as against 9 as used previously. The ten layers of the 3D resistivity distribution, calculated using reservoir properties derived from the simulation model are as shown in the resistivity slices in Figure 7.24. The resistivity ranges from 5 Ωm to 45 Ωm. The top layers of the reservoirs have high resistivity values, while the bottom layers have lower resistivity values. These lower values are still greater than the background values of 3Ωm. These layers resistivities are combined together to generate the transverse resistance map for the baseline (left hand side of Figure 7.25). Similarly, monitors 4 and 10 transverse resistances are calculated, middle and right of Figure 7.25 respectively.

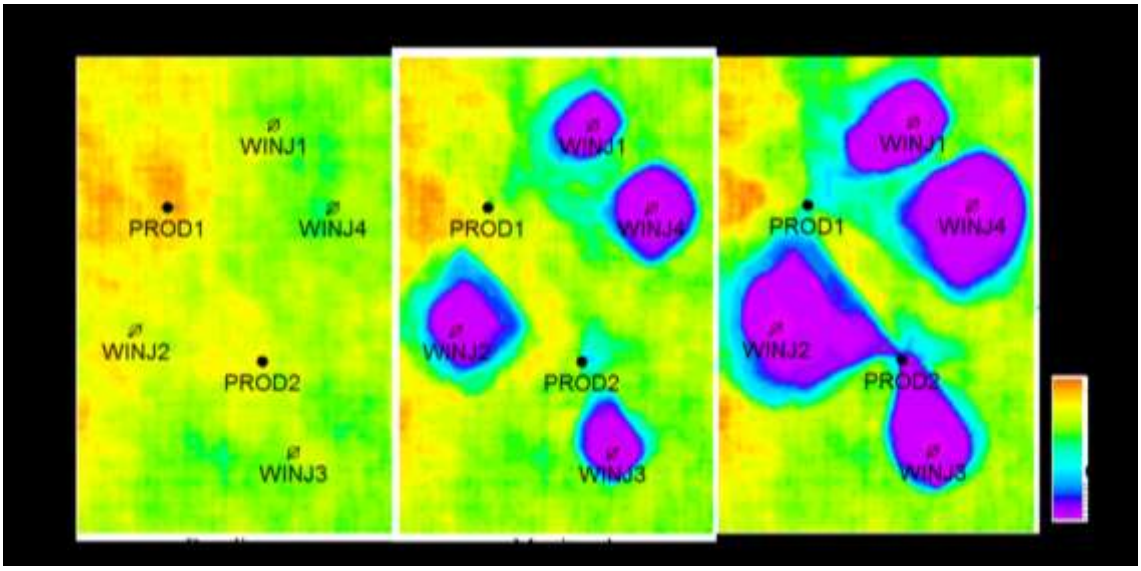

Figure 7.25: *Transverse resistances for the baseline, monitors 4 and 10 from left to right hand side respectively. See text for more description.*

To proceed with this investigation we first examine signal strength versus internal resolution of reservoir modelled properties to determine optimum source-receiver offset for further analysis. Using monitor 4 model for instance, the maps of EM amplitude normalized with background for different offsets are generated as shown in Figure 7.26. It is observed that although signal strength reduces (as indicated in the variously included colour bars, which could not be scaled together) but the resolution improves with decreasing offsets (from 8.5km to 2 km). For offsets 7 km and above, the anomalous body

produced negative normalized amplitude. This indicates increased air interaction with increasing offset. For this heterogeneous reservoir model, therefore, we cannot use the same offset of 8.5 km as used for homogeneous model. Internal heterogeneity in the reservoir model has affected optimum offset. Figure 7.26 shows that 2.2km could be considered optimum offset for good resolution (compare the fourth image from left bottom row in Figure 7.26 with the 9 other images). Resolution is considered of higher priority than signal strength in the case, especially in terms of interpreting for internal reservoir architecture in reality. In any case, even at the onset of relatively good signal resolution (at 5km offset, image on the far right – top row in Figure 7.26), the signal strength is small, just about 5%, which is close to the EM noise floor (mentioned in Chapter 4).

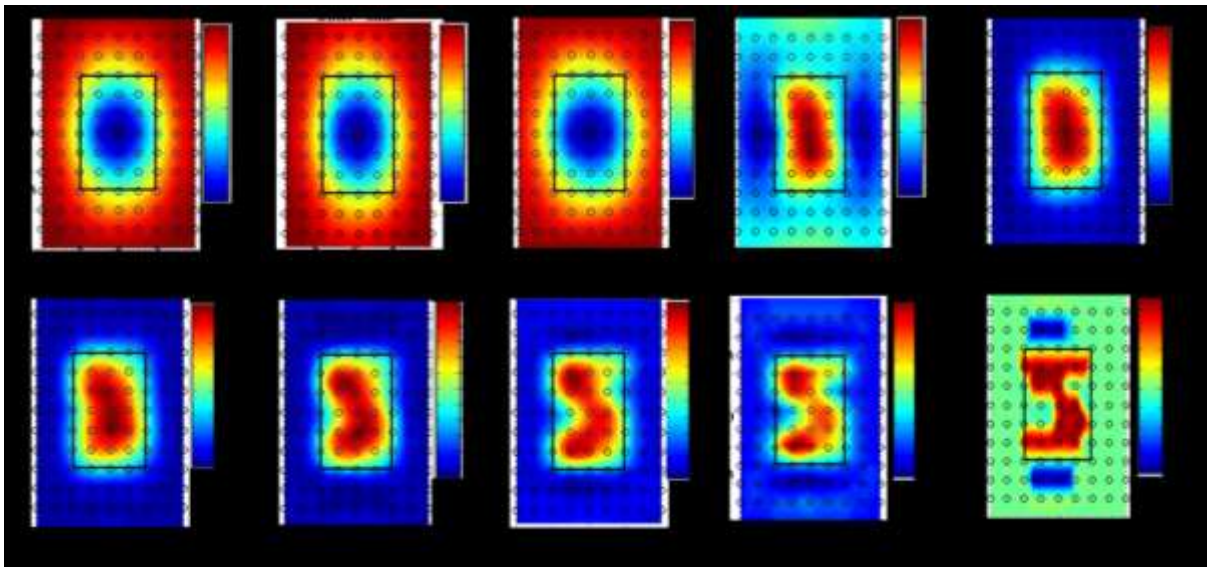

Figure 7.26: *Plots of anomalous EM amplitudes normalized with background showing signal strength versus resolution at different offsets.*

Using this offset, difference maps of the time-lapse transverse resistances of the two monitors with respect to the baseline transverse resistance are visually compared with the respective difference maps of the repeat 3D CSEM modelled responses normalized with the baseline response, as shown in Figures 7.27 with various outlines of water flooding fronts indicated. The CSEM difference maps generally show very low signal, which may require high precision detectors to accurately measure it. There are two major reservoir monitoring issues shown clearly on the maps of transverse resistance (Figure 7.27a), which should guide our interpretation of time-lapse CSEM maps (Figure 7.27b).

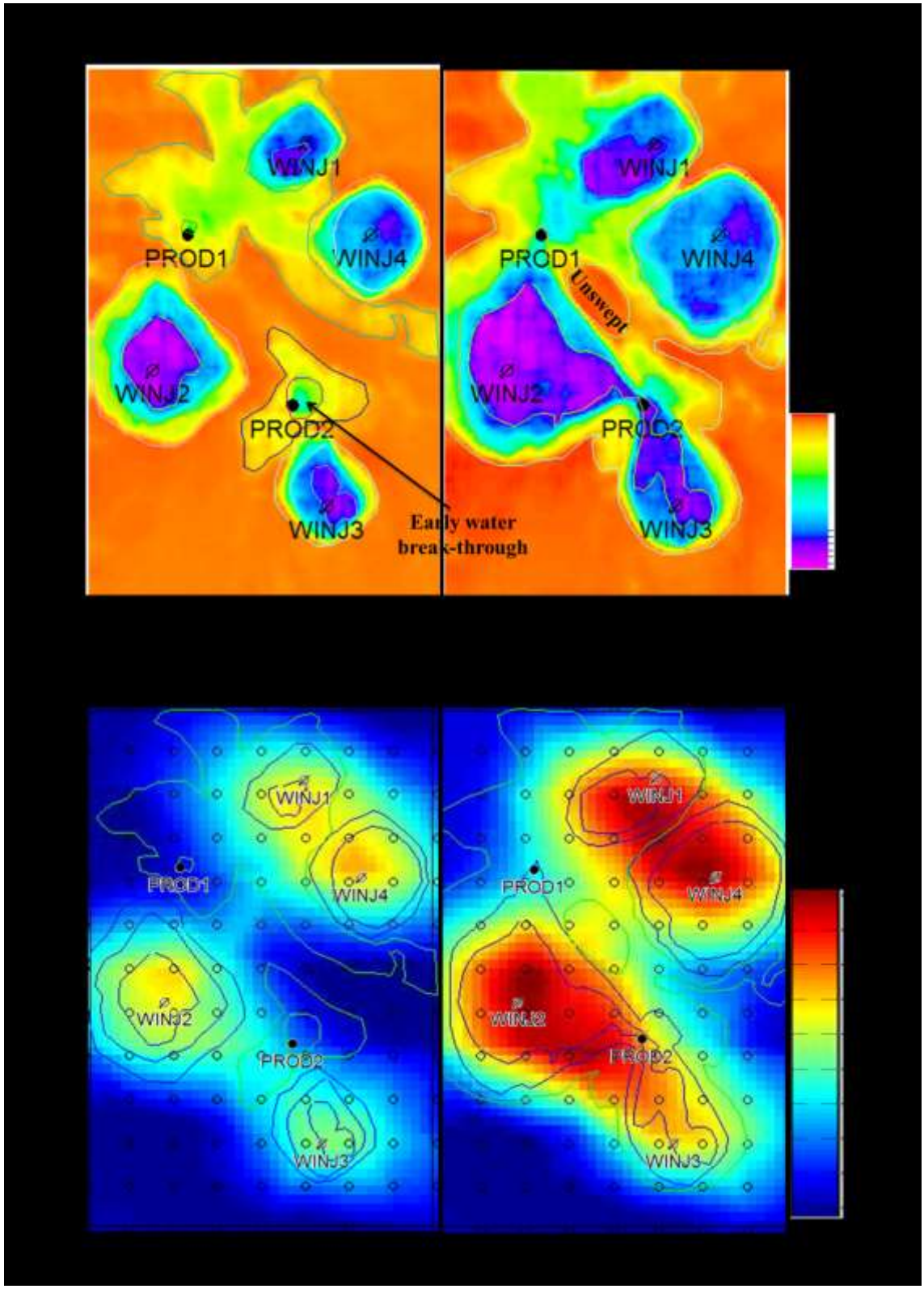

Figure 7.27: *(a) Difference maps of transverse resistances for monitors 4 and 10 with respect to the baseline transverse resistance. (b)The 4D CSEM amplitude difference maps for monitors 4 and 10 with respect to the baseline at 2.2km offset. See text for more description.*

Firstly, the early water break-through both at PROD1 and PROD2 after four years of production as shown in the ΔTR (Monitor 4) map. This could be avoided or managed by adjusting the production and injection prognoses, if it is detectable from the 4D CSEM difference maps. The repeat 3D CSEM difference maps in Figure 7.27b offer us broad definition of the points of water injection and fair understanding of the flooding pattern. However, it unfortunate, though expected, that it is unable to clearly define these two important reservoir monitoring and management features of interest. For instance, the flooding fronts coming from the water injectors WINJ1 and WINJ3 show early water breakthrough at PROD1 and PROD2 respectively, with about 400 Ωm^2 reduction in transverse resistance at both producers (left hand panel of Figure 7.27a), but these are hardly detected with the EM difference maps (left hand panel of Figure 7.27b). The 4D EM only detects reduction in transverse resistance above 700 Ωm^2 within the close proximity to the injectors. This implies that fine detail small changes in transverse resistance away from the injectors, close to the producers, cannot be easily detected directly from the 4D EM difference maps. Notwithstanding, at least we are able to isolate big saturation changes, say a distance above 500 m, away from the injector. This could be useful in situations whereby softening 4D seismic signal due to pressure up has hidden the water flooding signal (see Figure 2.11 in section 2.2).

Secondly, un-swept region with an area of about 0.5 km^2 near PROD1 after ten years of production and injection activities, as shown in the ΔTR (Monitor 10) map. The transverse resistance of this region is about 1400 Ωm^2 (corresponding region on Monitor 10 at the right hand of Figure 7.25). Considering the 60 m vertical thickness of the reservoir model, this region has equivalent resistivity of 24 Ωm, and volume of 0.03 km^3. This could contain commercially saturated amount of hydrocarbon that could be economically tapped through infill drilling. It is expected that the un-swept region, which has zero change in transverse resistance (outline indicated with green-letter on right hand panel of Figure 7.27a), should ordinarily show zero change in the 4D EM amplitude difference map. Contrarily, a relatively significant EM amplitude change is observed in this region (right hand panel of Figure 7.27b). The false-signal is due to the intrinsic diffusivity nature of electromagnetic field. In this case, the real signals due to the water flooding front from injector WINJ2, and

the adjoining front from injectors WINJ1 and WINJ4 have left a combined foot-print of diffused false-signal in this un-swept region.

7.2.2 Improved repeat survey acquisition geometry (rotated model)

Since the changes in the reservoir seems aligned at an angle of 45°, trending Northwest – Southeast, we could then rotate entire survey array 45° anticlockwise such that the towlines run along the four flooding fronts for better illumination of the anomalies. For instance, a towline parallel to a line joining the positions of injectors WINJ1 and WINJ2 in Figure 7.27. This is possible since we shall always have the fluid flow simulation model. It is similar to aligning geophysical acquisition geometry along the geological strike of the outcrop analogue for subsurface exploration target.

However, in order to keep computation time down, it is easier to rotate the model while keeping the lines along the *y*-axis as done earlier. Here we use a similar static model parameters but adjusted the dynamic parameters such that the water injection and oil production processes lead to water flooding fronts running in the North-South direction, parallel to the towlines. This attempt is shown in Figure 7.28 with two producers and two injectors. It resulted into a bigger signal magnitude. Better broad resolution of the big water flooding front is also observed, especially at the left hand side of the model from where the survey commenced. However, fine detail water flooding fronts could still not be resolved. For instance, water breakthrough at producer PROD2 could not be illuminated. The intrinsic diffusion of the EM response is still very much present.

Figure 7.29 shows the result of removing the 'diffusion glow' in the time – lapse EM amplitude signal (from Figure 7.28b), such that there is no EM difference signal outside the outlined water flooding fronts. It is observed that not only the diffused signal is removed; other signals related to change in transverse resistance within the water flooding fronts (inside the outlines) are equally removed. These are the useful but 'insignificant' signals that could not be separated from the diffusion. This has left us with amplitude changes ranging between 0.16% and 0.30%, constituting upper 46% of the time-lapse EM amplitude, which is interpretable for change in transverse resistance. Comparing Figure

7.29 with Figure 7.28a, the upper 46% 'significant' time-lapse EM signal corresponds to change in transverse resistance of between -800 Ωm^2 and -1050 Ωm^2 (equivalent to resistivity reduction of between 13Ωm to 18Ωm).

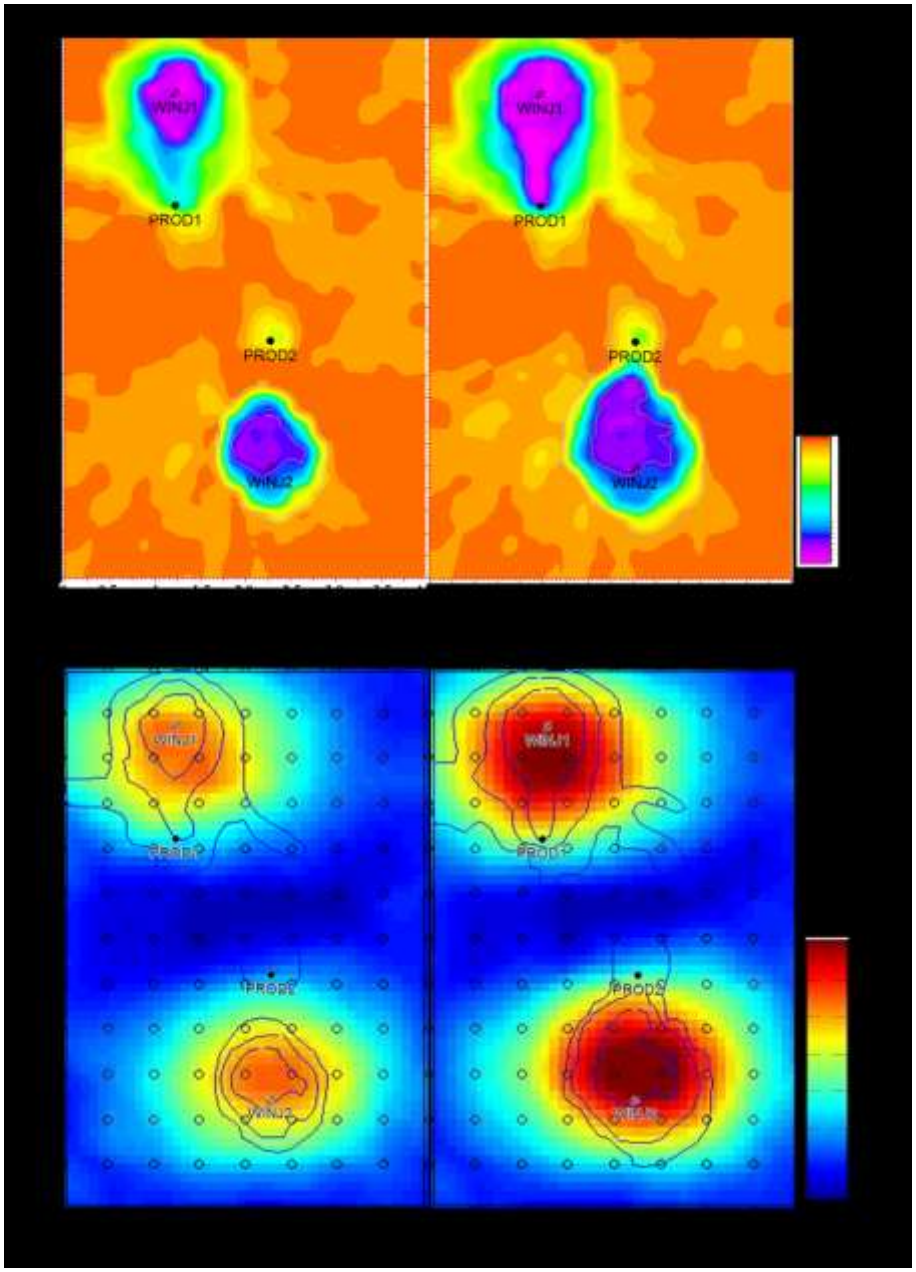

Figure 7.28: *(a) Difference maps of transverse resistances for monitors 4 and 10 with respect to the baseline transverse resistance for a rotated model. (b)The 4D CSEM amplitude difference maps for monitors 4 and 10 with respect to the baseline at 2.2km offset. See text for more description.*

In other words, time – lapse EM signals related to fine detail changes in the water flooding fronts with transverse resistance smaller than this range are neither detectable nor interpretable because they could not be separated from the 'diffusion glow.'

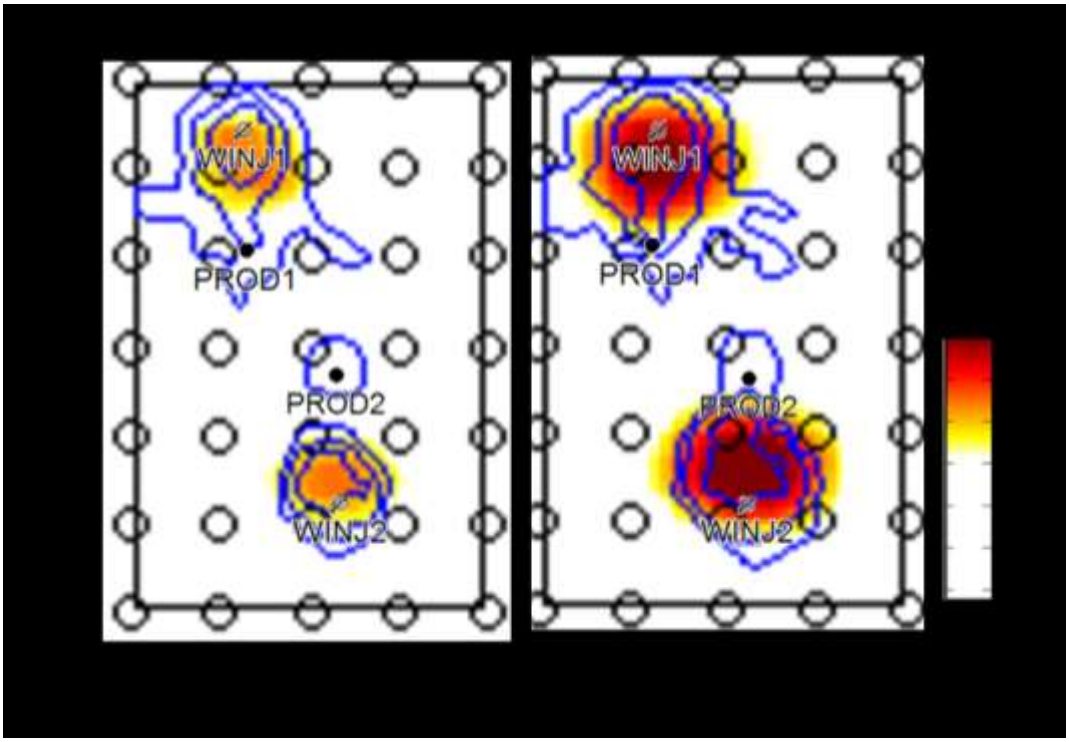

Figure 7.29: *The significant4D CSEM amplitude difference maps for monitors 4 and 10 with respect to the baseline at 2.2km offset. See text for more description.*

7.2.3 Examination of second derivative attribute for the heterogeneous model

One more thing we could do is to examine the second derivative attribute of the difference amplitudes. This is done for both un-rotated and rotated models as shown in Figures 7.30 and 7.31 respectively. Comparing Figures 7.30 and 7.31 to Figures 7.27 and 7.28 respectively; we could hardly see any improvement in the anomaly registration for both cases. This is unlike the improvement we see in Figures 7.22 and 7.23 for the cases of homogeneous model. It seems this attribute is not offering useful information for irregular heterogeneous reservoir condition. Throughout, we have not added noise to the modelled data, yet the results are not clearly interpretable.

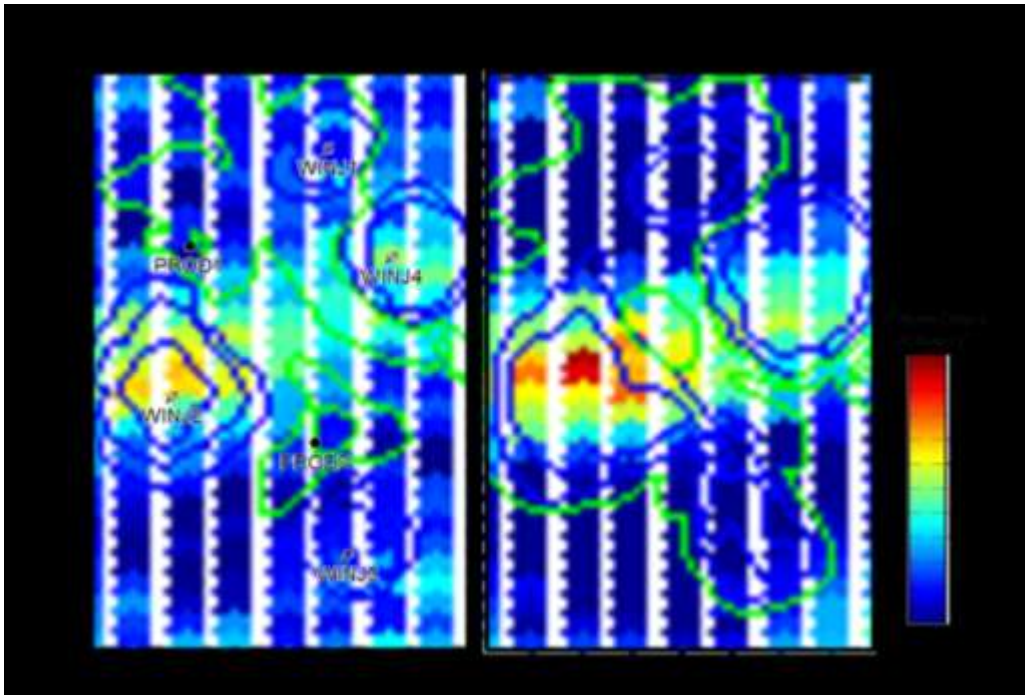

Figure 7.30:*2nd derivatives maps for the un-rotated model results shown in Figure 7.27. See text for more description.*

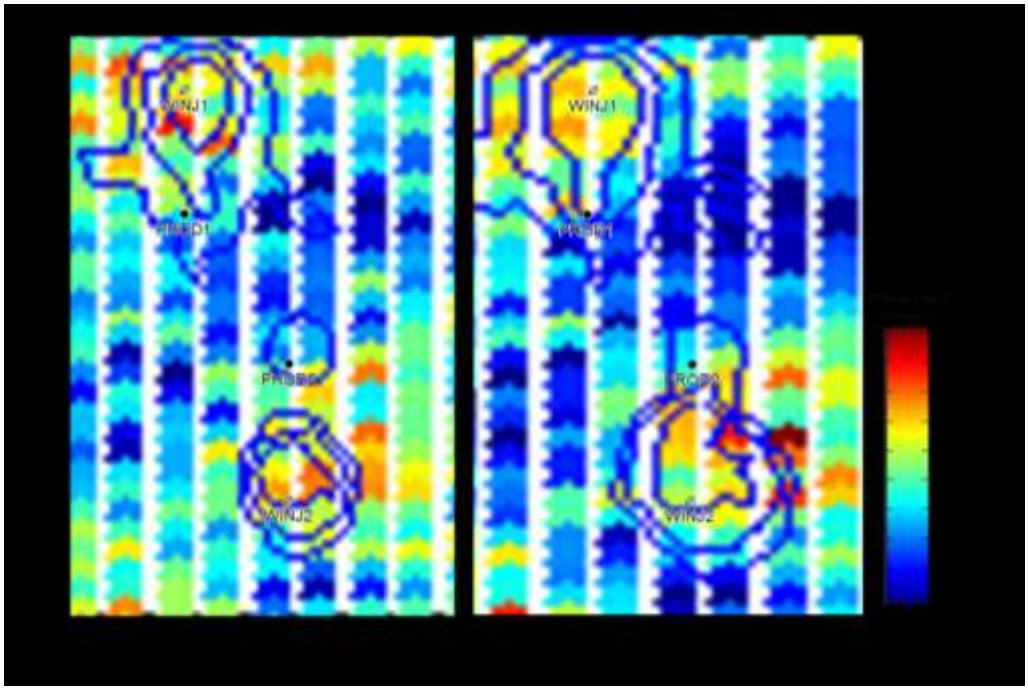

Figure 7.31:*2nd derivatives maps for the rotated model results shown in Figure 7.28. See text for more description.*

7.3 Summary: Discussion of way forward

Despite that the reservoir grid is directly used for the CSEM modelling, without upscaling from the geological model, the resolution of the repeat 3D EM difference signal is still too low for practical quantitative reservoir monitoring. Even with the improved parallel acquisition strategy, the 4D EM maps only offer information about the overall trend of the anomalous zone. The 4D EM difference signal is generally small and will require high precision detector for practical application of 4D CSEM technology in reservoir monitoring. Fine detailed information about the change in transverse resistance, due to fluid saturation change within the proximity of the production wells, seems difficult to detect. For a heterogeneous model with realistic reservoir properties and practical changes in water saturation, the second derivative attribute hardly offers any improvement to resolution unlike the case of the homogeneous model. So, fine details about early water breakthrough at the producers are still elusive, just as the bypassed region could not be isolated. However, 4D CSEM is still generally possible, and the time-lapse anomaly registration is better than static exploratory CSEM anomaly registration. However, unlike 1D time-lapse EM amplitudes, it seems direct interpretation of 4D EM amplitude will be difficult in reality. The highest observed 4D EM modelled signal of about 0.3%, in this study, is far less than the 2% to 5% noise level in CSEM data.

The next logical way forward is to carry out simulator-grid-constrained inversion. We could either do individual 2D inversion of the repeat 3D CSEM modelled data to generate the maps of transverse resistances for the baseline and monitor models. Then calculate the difference maps of transverse resistances, which could then be interpreted for the changes in water saturation. This will largely depend on the level of recovery of the transverse resistances in the inversion process, which in turn is a function of the constraint applied to minimize the non-uniqueness. Or at best, we could do full 3D inversion to reproduce the resistivity slices. This latter option is most desirable for both qualitative and quantitative interpretation, but the current inversion technology is very time consuming. Also recovery of resistivity slices to a very high level of similarity is necessary to interpret the small time-lapse changes in the reservoir. Once we have been able to recover either the 2D transverse resistance or the resistivity slices to a good level of certainty, we could then carry out noise

analysis by adding non-repeatable random noises and a certain percentages of noise floor to the modelled data before the inversion process, this will allow us to determine the amount of noise permissible for 4D time-lapse interpretation.

CHAPTER 8

CONCLUSIONS AND RECOMMENDATIONS FOR FUTURE WORK

8.0 General Summary

The central objective of this thesis is the assessment of time-lapse marine CSEM for reservoir monitoring applications. To place this objective in good context, a review of hydrocarbon production and recovery mechanisms (i.e. primary, secondary and enhanced oil recovery) was presented in Chapter 2 for the benefit of effective communication between the EM community and reservoir engineering community. The potential applications of time-lapse CSEM method, as a complimentary tool to time-lapse seismic, are examined from the eyes of a practical reservoir manager.

Out of the three primary hydrocarbon production mechanisms, only aquifer water drive could be monitored by time-lapse CSEM. This is because the production history involves water replacement of oil within the reservoir or water breakthrough at the producer, both of which could lead to time-lapse change in resistivity as conductive water displaces resistive oil. The other two primary mechanisms for hydrocarbon production: the gas-cap drive and solution gas drive are less likely to produce resistivity contrast between the resistive gas and the displaced resistive oil, thus time-lapse CSEM is not useful in these scenarios (see Table 2.1).

For secondary recovery of hydrocarbon involving water flooding, in the offshore environment, time-lapse CSEM has a great potential application in terms of complimenting time-lapse seismic in discriminating between pressure and saturation effects. Time-lapse CSEM can also help in resolving other reservoir management issues like location of bypassed oil, siting of in-fill producer, determination of water evolution, sweep efficiency and detection of early water breakthrough. Generally speaking, the term EM amplitude hardening is assigned to the condition of increased conductivity (lowered resistivity) due to water driving and replacing oil whenever water is injected into the oil leg of the reservoir.

However, for injection into the aquifer, there may be hardening or softening. This depends on the combination of temperature and salinity contrasts, thus contrast in water resistivity between the injected water and *in situ* water. Hardening occurs if the injected water is more saline and less resistive than the *in situ* water, while softening occurs if the injected water is less saline and in turn more resistive than the *in situ* water. For secondary recovery involving gas reinjection into the water leg either for environmental regulation to prevent gas flaring or for pressure support from the aquifer in driving oil up-dip; softening due to increased resistivity is expected to produce a good measure of time-lapse change in the EM amplitude. Gas reinjection can be done either into the gas-cap to avoid gas-cap decline and to maintain pressure, or into the oil leg to raise pressure and to displace oil laterally or down-dip. In both cases, there may not be any resistivity contrast for EM application (see Table 2.2).

Low-salinity water injection and polymer flooding are identified as enhanced oil recovery mechanisms where time-lapse CSEM can find potential reservoir monitoring applications. Low salinity water injection was further discussed in Chapter 7.

This review was followed by an assessment of a suitable rock physics model that is both geological and fluid flow consistent in Chapter 3. The electrical importance of intra-reservoir shale with respect to the sand components was considered in terms of its effects on the static resistivity of the reservoir. The choice of suitable rock physics model is dependent on the sand – shale arrangement, which could be in parallel or series. For a layered sequence of sand-shale lamination in the turbidite geological model example used, a rock physics model with an arithmetic average of constituents sand and shale resistivities was employed. In this rock physics model, the total estimate of resistivity for a vertically arranged sequence of sand and shale layers is the summation of the product of the volume ratios and resistivities of each of the two lithologies. The value of resistivity was also examined in this Chapter, both at the well log and reservoir scales. In furtherance to the previous knowledge, it was confirmed that change in resistivity is a good measure of change in water saturation that might occur in a producing reservoir undergoing water injection. At well logs scale, resistivity was compared with the elastic properties of the reservoir. It was confirmed that while the elastic properties, especially V_p/V_s ratio, are

much better lithologic discriminators; resistivity on the other hand is a better fluid discriminator than even the P-impedance (a better elastic property than the V_p/V_s for fluid discrimination).

In order to transform the value of resistivity into surface measurements of time-lapse CSEM for successful reservoir monitoring applications, various technical issues involved were assessed in similar fashion as the 4D seismic screening and feasibility studies. Three hydrocarbon provinces, namely West Africa, Gulf of Mexico and the North Sea were selected for the screening exercise involving many indices categorized into reservoir properties, formation water properties, sea water properties, overburden conditions and the electromagnetic survey indices. The West Africa and the Gulf of Mexico provinces scored equal assessment marks for the reservoir properties indices, such as high NTG, high porosity, low cementation factor, and thick reservoir units which mostly characterize relatively young geology (e.g. Tertiary Niger Delta) unlike the relatively old geology of the North Sea provinces which are typically of Permian and Jurassic ages. West Africa showed higher chance of success over the Gulf of Mexico in terms of its deeper water depth, shallower depth to the top reservoir, better optimum frequency, all of which are good for CSEM survey. It was concluded from this assessment (in Figure 3.13) that West Africa province has overall least risk, while the North Sea has least potential. Thus the West Africa province presents itself for the highest technical chance of successful time-lapse EM application, even though the EM survey repeatability, just as seismic still is, presents high risk for the three provinces. Despite this assessment results, subsequent modelling parameterization used the North Sea Oilfield example as the framework.

The review in Chapter 2 showed that time-lapse EM cannot stand alone for reservoir monitoring; it has to be integrated with 4D seismic methods. This integration will only be possible whenever the two dataset are repeatedly acquired simultaneously either by towed streamers, or better by permanent sensors over a producing oilfield, with high level of repeatability. To set foundation for this, two major assumptions were made. First is that we have a good quality repeated EM signal (or its resistivity derivatives through EM inversion), thus we are required to analyze, interpret and examine its values in terms of its complimentary or alternative roles to time-lapse seismic in reservoir monitoring. This best

quality repeat EM data were obtained through Dipole 1D forward modelling. Although this does not represent 3D volumetric EM field of the subsurface, characterized by imprint of field diffusion. However, it presents to us a good quality EM signal, which we hoped for, with improvement in 3D acquisition and processing technology (left hand side of Figure 2.6). The second assumption is that we can eventually acquire repeat EM dataset simultaneously with repeat seismic dataset over the same producing field (topmost element on the left hand side of Figure 2.6), thus we are also required to integrate the two dataset for dynamic reservoir characterization. With this in mind, a fluid flow simulator to electromagnetic modelling (sim2EM) workflow was established in Chapter 4, and it was incorporated into an already available simulator to seismic (sim2seis) workflow. This facilitated forward modelling to generate the two datasets for coupled interpretation. The simulation model provided the common producing oilfield, and it also aided the interpretation of the modelled datasets. This sim2EM workflow was first tested before the couple forward modelling of seismic and EM.

Using 3D reservoir model built with reservoir properties of a North Sea oilfield, and Dipole 1D EM modelling, the time-lapse CSEM feasibility study was carried out to assess the impacts of the sea water resistivity stratification and overburden complications on repeatability in Chapter 4. It was discovered that while the sea-water resistivity profile mainly impacts on the signal strength, the background resistivity distribution are the major causes of poor structural resolution in CSEM measurement. These effects were more pronounced on the static modelled amplitude maps, but they partially cancel out in the time-lapse modelled amplitude maps. Detectability and interpretability were also assessed. Amplitude changes in both the electric and magnetic field components showed good linear correlation coefficient to the changes in transverse resistances. For instance, in the model example in which the water flooding is almost vertically directed, the change in the vertical electric amplitude is about 91% correlated to the change in transverse resistance, similar coefficient was observed in the cross-line magnetic field. Whereas for the time-lapse inline electric field, the correlation coefficient with respect to the change in transverse resistance is low, between 23% and 28%. However, these values were all consistent from one time-lapse period to another. Investigation also revealed that there is a linear correlation of 99% between the transverse resistance and the depth average water saturation. This indicates that

the change in CSEM measurements can be comfortably related with the depth average change in water saturation in order to aid qualitative interpretion, to determine the water flooding front, and to attempt a more direct quantitative estimation of change in water saturation.

A simulation model of a North Sea producing oilfield was then used for a more realistic time-lapse EM modelling and interpretation in Chapter 5. By visualizing and correlating time-lapse CSEM difference maps with the maps of depth-averaged change in water saturation; the CSEM difference maps clearly indicated areas of the reservoir in which the water saturation is changing as production and injection activities progress, thereby providing early warning of water encroachment onto the production wells. The results also indicate zero time lapse CSEM signal for the parts of the reservoir where there are no dynamic changes in the reservoir model. Interpretation proceeded by calibrating the EM amplitude change to well activities at each well location. This is termed *dynamic well-tie.* It was also shown that initial knowledge of the distribution of static reservoir properties is important in constraining the correlation between the change in water saturation and the time lapse CSEM, even though contraining some of these variables (like NTG) come with some uncertainties, which add up to the uncertainties involved in time – lapse CSEM application.

Comparison was then made between the sensitivities of time – lapse CSEM and 4D seismic modelled data to the change in water saturation for similar time lapse intervals with consideration given to the various events happening in the reservoir during production and injection activities. These events included changes in water saturation, changes in pressure, gas coming out of solution. The sum of negative amplitudes, which has been previously identified by the field operator as the appropriate seismic attribute for this oilfield, is used in the time-lapse seismic analysis. It was observed that the CSEM is more sensitive and consistently more linearly related to the change in water saturation than the seismic. This was not suprising since seismic is sensitive to other dynamic events. Chapter 5 ended with coupled interpretation of time-lapse CSEM and 4D seismic modelled data. This revealed that the time-lapse CSEM has a great potential to reduce interpretational ambiguities in time-lapse seismic, especially when there are confounding signals due to increasing

pressure and water saturation. This CSEM potential is also reinforced with the fact that CSEM is blind to separating gas from oil, thus offering seismic a good confirmation of situation when pressure drop below the bubble point has caused gas ex-solution, and there is need for an engineer to build up pressure through injection.

In Chapter 3, engineering consistency was incorporated into the rock physics to cater for the effective salinity and temperature of mixed reservoir water during water injection. This enables the concept of '*water is not just water*' to be examined in Chapter 6. First, different types of injected waters used in the oilfield production were reviewed (e.g., sea water, produced water, low salinity water, river water etc). Then, using an example of cold sea water injection in a North Sea field example, the sensitivities of temperature and salinity changes on time-lapse CSEM responses are examined. It was shown that the cooling effect which tends to slightly increase water resistivity is a function of both the rock and the fluids thermal conditions. It is restricted to the vicinity of injectors, and hardly produces measurable time – lapse CSEM response around the producers. This is because the injected water has gotten mixed with the formation water and has assumed the in situ equilibrium condition as the water travels towards the producers. However, the salinization effect produced an irreversible increase in salinity, and reduced resistivity change. This leads to CSEM amplitude changes which are more pronounced within the vicinity of injector, where there is a repeated salinization. Generally speaking, time – lapse CSEM can distinguish injected water from the in situ formation water, based on the resistivity anomaly between them, and this might potentially be useful in monitoring some selected water flooding system. This was tested on the *LoSal* – EOR mechanism, whereby time-lapse CSEM provided information about water evolution. This was attributable to dimming effect resulting from reduced salinity of the mixed reservoir water, which in turns reduced the time-lapse CSEM signal when compared with a situation whereby there is no salinity difference. Similar results were obtained for aquifer water injection. Chapter 6 ended with a comparison between time – lapse CSEM and time – lapse seismic in terms of their sensitivities to different brine combinations. It is concluded that CSEM is a better brine tracking tool than seismic.

Time-lapse 1D dipole modelling generally proves values of CSEM, but a caution has to be applied as 1D EM is not representative of the real 3D situation. This is why 4D EM modelling was examined in Chapter 7. This enabled several hypothetical scenarios to be examined for both homogenous and heterogeneous cases. These included practical issues of optimum and improved acquisition strategy; varying subsurface conditions such as single versus stacked reservoir; simple versus complex overburden; analytical tools such as first and second derivatives among others. It was observed that prior knowledge of possible *direction of water flooding front* is important. This is because, aligning repeat survey geometry parallel to the expected time-lapse anomaly offered optimum signal response. It was concluded that the 4D EM amplitude difference map produced broad information and direction of water flooding front. However, fine detail information about bypassed oil zone and water encroachment at producers could not be easily mapped due to the static diffusion imprints which are not cancelled-out with repeat measurements. Also, the overall 4D EM amplitude signal (0.18% with respect to the baseline) is small and may require high precision measuring instrument for this technology to be possible. This is more complicated with the fact that only about 46% upper part of this small signal could be useful for dynamic interpretation; the other lower 54% is attributable to diffusion imprint, which could be filtered-out. In the process of filtering out images attributable to diffusion, a large part of informative signals relating to the water flooding front are filtered with it. The interpretable 46% upper part of the time – lapse signal (0.18%) corresponds to change in transverse resistance of about -800Ωm^2 and -1050Ωm^2 (equivalent to resistivity reduction of between 13Ωm to 18Ωm). The very low 4D EM signal underscores the need for addition of noise, because it will of course further render the modelled data un-interpretable. Although the second derivate attributes worked well for homogeneous model, it did not particularly work for the qualitative interpretation of heterogeneous modelled EM data. While the model outline is defined, the intra-reservoir fluid contacts were not defined. Simulator-grid-constrained inversion was suggested as the next logical step forward in this research. If we are able to recover internal heterogeneity in the inverted reservoir resistivity or transverse resistance, then we may be able to qualitatively interpret the data for reservoir monitoring purposes.

8.1 Specific conclusions

This thesis has achieved three main objectives:

(1) It has extended the engineering-driven concept of 4D seismic technology into time-lapse CSEM in order to place the latter in a better perspective for reservoir monitoring application. Now, the CSEM has been presented from the '*eyes of a reservoir manager*.' The thesis has come up with the risk assessment indices to be examined for successful application of time-lapse CSEM.

(2) The possible strengths and weaknesses of time-lapse CSEM in reservoir monitoring have been examined through the review of production mechanism, simulator and rock physics driven 1D EM modelling and feasibility studies. Coupled modelling of time-lapse CSEM and seismic data, and interpretation of modelled data has shown areas where CSEM could play excellent complimentary roles to seismic in reservoir monitoring.

(3) The practical effects of changes in temperature and salinity during secondary and enhanced oil recovery involving brine mixing, on the time-lapse CSEM and 4D seismic have been examined. This highlighted CSEM as a better tool than 4D seismic in brine tracking.

(4) The repeat 3D CSEM modelling has revealed the challenges of 4D CSEM analysis for practical application and provided clear directions for future work. It has also shown the importance of prior information from the simulation model in constraining optimum repeat survey acquisition geometry.

It could be concluded that time – lapse CSEM has a great potential as a tool for reservoir monitoring. It could not standalone but will excellently complement 4D seismic. Specific productions mechanisms where time – lapse application may be possible are: water-flooding (e.g. sea water injection at Schiehallion oilfield, North Sea), low salinity EOR (e.g. At Endicott oilfield, Alaska), subsurface aquifer water injection (e.g. A Middle East

carbonate or clastic oilfield) and other brine related oil recovery processes. However, the practicality of 4D CSEM will be greatly enhanced with joint seismic and CSEM data acquisition in the nearest future. It should be noted that the geological system used as the basis for this work, the layered sands in shales (e.g. in Schiehallion, Gulf Coast, East Africa fields), is typical of a certain type of geological system (deepwater reservoirs) – rather than all geological systems and that the user of the workflow described here should bear this in mind (*caveat emptor*).

Whenever time-lapse CSEM data acquisition becomes practicable, the cost – benefit of the method in the deep water environment will be enormous. For instance, going by the cost of acquiring marine CSEM data, about $2,000,000 (Ridyard & Hesthammer 2011), the benefit will be the success in total dollar revenue of oil recovered (depending on the oil price), less the cost of CSEM survey ($2million) among other costs, especially the very expensive offshore drilling operation. The daily cost of drilling offshore well is between $500,000 and $550,000 (Phillips 2008); this amounts to at least $7,500,000 for a minimum of 15 days it takes to drill a typical offshore well (Diamond Offshore, 2014). Another cost – benefit of time-lapse CSEM data would be a decision made against embarking on drilling an infill well. In this case, the cost – benefit will be cost of drilling offshore well (which is avoided) minus the cost of acquiring repeat CSEM data. In terms of integration of time-lapse CSEM with 4D seismic, the benefits will be focused on the time-lapse effects which 4D seismic could not properly imaged due to pressure effect or simply due to lack of acoustic impedance contrast. For instance brine tracking in low salinity EOR, which 4D seismic might not detect, time-lapse CSEM interpretation could assist in evaluating the efficiency of the EOR mechanism in terms of how much extra oil could be recovered. The cost – benefit of time-lapse CSEM method will especially be significant, whenever repeat CSEM data could be acquired simultaneously with repeat seismic data, as this will reduce the marginal cost of surveying. Therefore the economic worth of time-lapse CSEM depends on many factors such as: the cost of data acquisition, the cost of well drilling offshore, the amount of additional oil recovery and the prevailing oil price, among other factors.

8.2 Recommendations for future work

There are opportunities to take this research forward. Recommendations are made to address some technical issues relating to: (1) Application; (2) 3D Modelling; (3) Inversion, noise analysis, interpretation and better definition of reservoir properties; (4) Possibility of frequent monitoring.

(1) **Applications**: Other possible practical monitoring applications of time-lapse CSEM could be explored with 1D feasibility studies, especially for injection processes involving varying water resistivity as a result of varying temperature and salinity. Attention should be focussed on the EM imaging of waterflood chemistry (that is, salinity and temperature alteration) in reservoir engineering, which involves development of better resistivity models. Salinity changes in polymer flooding could be tracked by time-lapse CSEM, to provide information as to the evolution of different fluids injected. In polymer flooding, low salinity water is first injected to neutralise the high salinity formation water before the polymer solution is applied. Thus feasibility studies could be done in conjunction with 4D seismic, as time-lapse seismic has not been tested for monitoring of producing reservoir undergoing polymer flooding. Polymer injection is an EOR technique used in producing bypassed oil in a high permeability reservoir, where the mobility ratio of water is a lot higher than that of oil, thus making conventional water flooding inefficient. Another possible area of time-lapse CSEM application is the water flooding of medium or heavy oil at deep-offshore environments, such as seen offshore Brazil and China. Here, the injected water and the oil being displaced have similar densities (Manrique & Campanella 2006), thus very small change in elastic properties which may not produce measurable time-lapse seismic signal. However, the resistivity contrasts between the injected water and the medium or heavy oil should lead to measurable time-lapse CSEM. Integrated feasibility will also help highlights the value of time-lapse CSEM.

(2) **3D Modelling**: The 3D CSEM modelling algorithm currently takes regular-sized grid cells. While the industrial fluid flow simulation models are built with corner-

point geometry, containing irregular – sized grid cells, which are more representative of the real field situation. Therefore, efforts should be geared towards improving the EM forward modelling algorithms to take irregular grids from the simulator directly, without having to re-grid the cells into regular size. Also, an average – sized simulation model could contain more than 200,000 cells, and forward modelling this to generate EM data takes a long time to run, if not impractical, with the 3D integral EM algorithm. In this case, upscaling to coarse large-sized cell with reduced number of cells may be required. This has implication on the resolution of details as properties are also distorted and less presentative of the reality. Thus, improvement in the algorithm capacity may be required or other algorithm methods like finite element or finite difference should be used for fine grid size.

(3) **Inversion, noise analysis, interpretation and better definition of reservoir properties**: 2D and 3D inversion of EM modelled data is a definite next step in analysing EM for reservoir monitoring. The inversion has to be constrained with prior information obtainable from the simulation model. The higher the level of confidence in recovering the transverse resistance or resistivity slices, the more reliable the practical reservoir monitoring information derivable from the inverted products. Once this procedure is established, noise analysis can then be done. Certain amount of non-repeatable noise could be added to the modelled data before carrying out the inversion, and then the interpretation is done, and compared with the first interpretation before the noise is added. This process should provide reasonable answers to questions like: how much non-repeated noise is permissible for time-lapse EM data or inverted products to be interpretable? Among others, what amount of efforts should be put into the acquisition strategy? Finally, the combined forward and reverse modelling procedure should be re-applied to different scenarios of hydrocarbon production mechanisms, in order to have better definition of EM reservoir properties (e.g. NTG) and anisotropy features (e.g. Archie constants – a, m and n). This will enhance full examination of the practical applications of 4D CSEM to reservoir monitoring. Inversion could also be of help in resolving two or more reservoir intervals perforated and being produced at the same

time, such that the time-lapse CSEM response will be decoupled into the component parts in order to interpret for individual resistive layers.

(4) **Frequent monitoring**: 4D seismic data acquisition technology has progressed over the years with a lot of improvements. This has made frequent reservoir monitoring and continuous reservoir management possible. Possible reservoir management and business implications for frequent 4D CSEM monitoring could be assessed using frequently repeated 3D forward and reverse modelling.

As stated in Chapter 2, a complete story about time – lapse CSEM will better be told, whenever both the CSEM and seismic data could be simultaneously acquired from a producing field at the same calendar periods, especially with permanent sensors. Therefore, CSEM data acquisition – focussed researches should look into this possibility, but successes in the assessment of time – lapse CSEM for reservoir monitoring could serve as impetus to encouraging researches into simultaneous repeat CSEM/Seismic data acquisition. Other potential improvements in CSEM technology for time-lapse applications are as mentioned in Figure 2.7 (in page 39).

APPENDICES

Appendix 1: Archie's model and reservoir fluid saturation

A1.0 Archie's clean sand resistivity model

Archie (1942) gives the fundamental equation relating resistivity with the petrophysical properties of a reservoir rock. For a clean homogeneous sand reservoir (see Figure 3.1a), the bulk totalresistivity (R_t) of the fluid-saturated rock is emperically related with the rock porosity (Φ), water saturation (S_w) and water resistivity (R_w). The equation is given as:

$$R_t = \frac{aR_w}{\Phi^m S_w^n} \quad ; \tag{A1.1}$$

where '*a'* is the compaction factor, it is otherwise called compaction factor which accommodates any change in the cementation factor, and it is usually assumed to be equal to the value of 1; '*m'* is the cementation/porosity factor, which usually assumes a value of 2 for consolidated sandstone, but could be as low as 1.3 for an unconsolidated sand; '*n'* is the saturation exponent which assumes a value of 2 for clean consolidated water-wet rock, but could range between less than 2 and 8, usually increasing with the degree of oil-wetness of the rock (Donaldson & Siddiqui, 1989). The constants '*a*', '*m*' and '*n*' could be determined empirically from core samples in the laboratory, as they are lithological-dependent and may vary from one geological terrain to the other.

Cementation/porosity factor, '*m'* can also be evaluated for fully water-saturated sand where 'S_w=1*'* and the value of 'R_t*'*, and'Φ' are measured directly from well logs. The value of 'R_t*'* at 'S_w=1*'*is commonly called 'R_o*'*. Usually at a well location, 'R_t*'* is read from deep resistivity logs (e.g. laterologs or induction log); 'Φ' is evaluated using the porosity tools (density, sonic, neutron etc), while 'R_w*'* is usually calculated either from the SP logs at reservoir temperature and salinity, ormeasured directly from theproduced water (sample from the drillstem test), or calculated using any of the emperical equations (described in section 3.1.2) relating reservoir temperature and salinity with water resistivity (e.g. Crain 1986; Tiab & Donaldson, 2004; Schlumberger, 2009).

Any of these parameters could be calculated from Equation (A1.2) assuming the values of others are known from the well logs or from core analysis. Taking the logarithm of both sides of Equation 3.1 for 'S_w=1' yields:

$$\log R_o = \log a + \log R_w - m \log \Phi; \quad \text{(A1.2)}$$

Thus if we assume 'a =1' and we have other parameters as described above, then the value of 'm' could be easily evaluated. This is only a fair approximation, since a single value of 'm' may not properly represent entire reservoir.

A1.1 Reservoir fluid saturation

Archie's equation has been extensively used in the geoscience community to calculate the value of water saturation (S_w) within a reservoir section at a well location, from which oil and gas saturations are evaluated as shown in Equations (3.3a,b, c and d) below:

For two phase oil reservoir (oil and water only), in which oil saturation (S_o) is

$$S_o = 1 - S_w \ ; \quad \text{(A1.3a)}$$

For two phase gas reservoir (gas and water only), in which gas saturation (S_g):

$$S_g = 1 - S_w \ ; \quad \text{(A1.3b)}$$

For three phase reservoir containing hydrocarbon (oil and gas) and water,

$$S_{hc} = 1 - S_w \ ; \quad \text{(A1.3c)}$$

where

$$S_{hc} = S_o + S_g \ ; \quad \text{(A1.3d)}$$

In terms of time-lapse reservoir monitoring using CSEM, we are interested in measuring change in resistivity due to change in water saturation as a result of fluid replacement within the pore spaces. Thus these saturation equations should include the interaction among injected water (e.g. sea water), connate water (irreducible *in situ* water) and/or aquifer water. This is elaborated in section 3.1.2.

Appendix 2: Low salinity water injection

A2.0 Benefits and mechanism of low salinity water injection

Before we model time-lapse CSEM responses for this scenario, it is necessary that we discuss the benefit and the mechanism of *LoSal* water injection, and how it is usually simulated. Recent studies have shown that injecting low salinity water, rather than high salinity water, can improve the benefits of water flooding with an increase in the amount of displaced hydrocarbon, especially in clayey sandstone reservoir. Although there is yet no universally acceptable explanation for this phenomenon, as the precise action of low salinity water is still debatable, but the usually suggested mechanism adduced to this recovery process, is the wettability alteration towards a greater water-wetness of the reservoir rock due to chemical processes (e.g. Tang & Morrow 1997; McGuire et al. 2005; Jerauld et al., 2006; Seccombe, et al. 2010; Gamage & Thyne 2011; Lager et al. 2011 among many others). This alteration tends to allow more hydrocarbon flow for equal volume of injected water. The mechanism suggests that the bound oil (irreducible – residual oil) surrounding the detrital clayey particles between rock grains, which injected high salinity water could hitherto not move, could now be made mobile with injected *LoSal* water, thereby raising oil recovery. Figure A2.1 shows the schematic illustration of the benefit of this emerging technology for an oil-wet clastic reservoir.

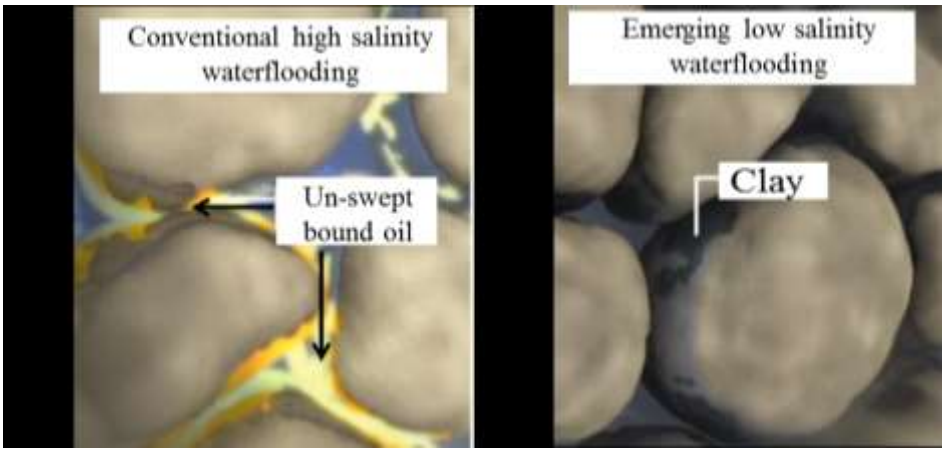

Figure A2.1:*(a) Conventional high salinity water-flooding showing some un-swept bound oil over the clayey matrix. (b) Emerging low salinity water flooding, with initially un-swept oil now been swept away from the clayey matrix (from BP website, 2012).*

A large amount of un-swept oil after high salinity water flooding in Figure A2.1a has now been recovered by the *LoSal* water flooding as shown in Figure A2.1b. This phenomenon has been tested and validated by many scholars mentioned above, using core-flooding, single-well chemical tracers and inter-well field trials.

There are two approaches to the application of *LoSal* water flooding. It could either be for tertiary oil recovery or for secondary oil recovery. For instance, Gamage & Thyne (2011) reported a core flooding experiment in which high salinity water flooding led to 49% oil recovery, but a further injection of low salinity water yielded 1% additional oil. The low salinity water-flooding, in this case, is considered to be for tertiary recovery.

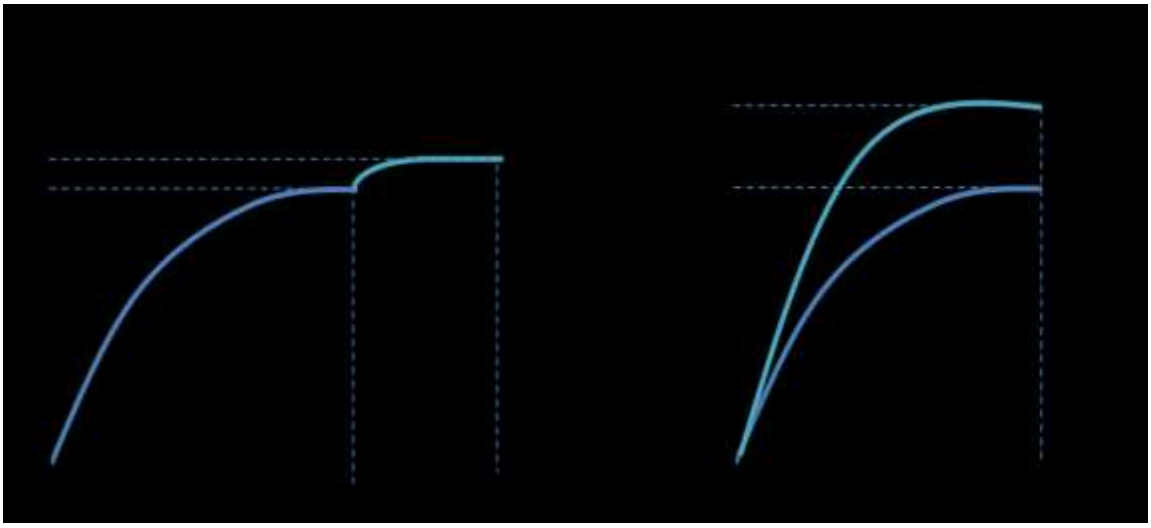

Figure A2.2*:(a) Tertiary recovery by low salinity water flooding. (b) Secondary recovery by low salinity water flooding. Illustration is done using the example given by Gamage & Thyne (2011).*

However, when similar core, with the same oil and rock types was flooding directly with low salinity water, without having to first subject the core to high salinity water flooding, 60.5% of original oil in place (OOIP) was recovered. Here, *LoSal* water injection is considered to be for secondary recovery. Figure A2.2 gives schematic illustration of the two approaches.

Apart from improving the oil recovery, the other potential benefit of low salinity water injection is the reduction in the formation of chemical scale. Low salinity water injection

has also been considered as "inexpensive and environmentally friendly oil recovery method" (Gamage & Thyne2011). For simplicity, we consider the *LoSal* water injection for the secondary oil recovery case.

A2.1 Simulation of LoSal water injection

The main reservoir parameter that changes during low salinity water injection is the relative permeability. Normally, from the mechanism of *LoSal* – EOR, by breaking the bond between the residual oil and clay mineral, and subsequently increasing the volume of mobile oil; the relative permeability curves are effectively shifted to the right. This is such that the reservoir rock has now become more water saturated with lesser residual oil. The original relative permeability data are supplied with the simulation model by the North Sea oilfield operating company. The data are modified for the low salinity water injection with 6% increase in water wetness (i.e. 6% of the residual oil is produced). In order to preserve the shape while changing the end points to obtain new relative permeability curves for the low salinity water injection, we use the empirical Corey model, which describes relative permeability for the oil – water system with power law equations (Reynolds et al. 2004 in Li et al. 2012), as shown in equation A2.1.

$$K_{rw} = a_w \left(\frac{S_w - S_{cw}}{1 - S_{ro} - S_{cw}} \right)^{b_w}; \qquad \text{(A2.1a)}$$

$$K_{ro} = a_o \left(\frac{1 - S_{ro} - S_w}{1 - S_{ro} - S_{cw}} \right)^{b_o}; \qquad \text{(A2.1b)}$$

where K_{rw} and K_{ro} are relative permeabilities of water and oil respectively. a_w is relative permeability of water at $S_w = 1 - S_{ro}$; and a_o is the relative permeability of oil at $S_w = S_{cw}$.S_w is the water saturation; S_{wc} is the connate water saturation; and S_{ro} is the residual oil saturation. b_w and b_o are the exponential factors which define the shape of the relative permeability curves.

Using equations A2.1a and b, and the original relative permeability data, we obtain the values of b_w and b_o. These values are then used with 6% reduction in the original residual

oil saturation to generate new set of relative permeability with similar shape. Figure A2.3 shows permeability curves for the original high salinity water and the modified version for the low salinity water. The increased water wetness has resulted into higher relative permeability for oil and lower relative permeability for water. Looking at the oil relative permeability (the red solid curve) for high salinity water injection, it is observed that the water saturation is about 70% (with residual oil saturation of about 30%) when the oil relative permeability (K_{ro}) is equal zero. Here, the remaining oil is no longer producible by the conventional high salinity water flooding.

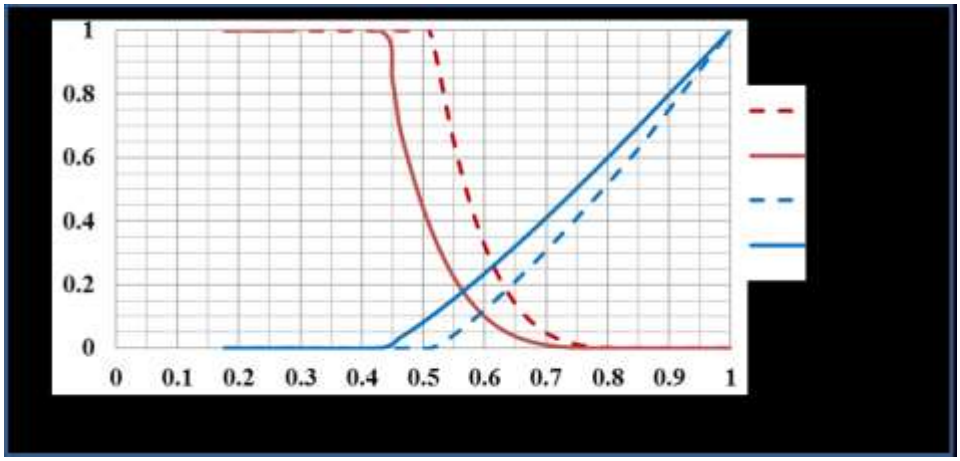

Figure A2.3*: Relative permeability curves. The original curves shown with solid lines are plotted from the data supplied by the North Sea oilfield operator for high salinity water; while the modified curves shown in dash lines are derived with 6% reduction in the residual oil, using the power law equation A2.1 (Reynolds et al. 2004 in Li et al. 2012) to preserve the original shape.*

Now, assuming low salinity water injection has raised oil recovery by 6% volume, the two relative permeability curves have shifted to the right, such that the equilibrium relative permeability (about 0.2) for both fluids is now at about 63% as against the initial 57%. The water saturation has now increased from 44% (solid blue curve) to 50% (blue dotted curve) when the water relative permeability (K_{rw}) is equal zero. Also, the residual oil saturation has reduced from the original 30% (solid red curve) to 24%. This means some initial residual oil has now become mobile and producible.

Comparing the simulated results of the high salinity water injection (20,000*ppm*, equivalent to that of the formation) with the low salinity water (1,000*ppm*) injection, Figure A2.4a

shows downward curve shift (from blue to green) in the field oil remaining in place. This means, a good amount (8MMB) of the initial residual oil (with high salinity water injection) has been produced by low salinity water injection as show by upward curve shift in the total field oil produced in Figure A2.4b. However, this phenomenon is observed to have started at approximately after six years of production. This means, before six year of production, the nature of injected water does not matter as either high or low salinity water injection will lead to similar volume of oil production. Therefore, one can actually begin the tertiary low salinity water injection just about the end of 5 years of production, and this will reduce the cost associated with low salinity water injection in terms of desalination process.

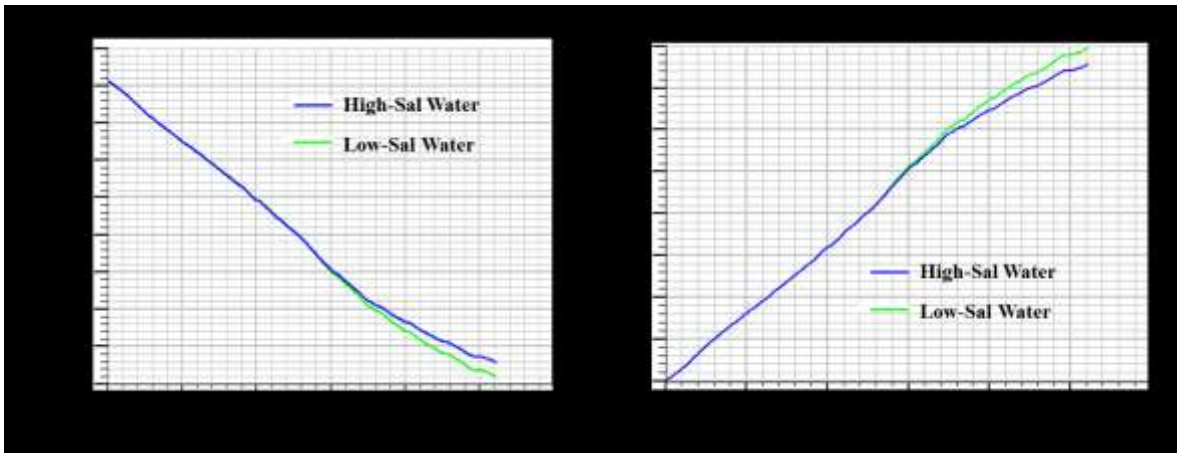

Figure A2.4: *(a) A plot of field oil in place (in billion STB) versus time (in years). (b) A plot of field oil production (in 100 million STB) versus time (in years). Blueand green coloured curves are for the high salinity water and low salinity water injection respectively.*

REFERENCES

Amini, H., Alvarez, E., MacBeth, C., & Shams, A. (2012). Finding a petro-elastic model suitable for sim2seis calculation. Copenhagen: 74th EAGE Conference.

Andreis, D., & MacGregor, L. (2008). Controlled-source electromagnetic sounding in shallow water: Principles and applications. *Geophysics, 73*(1), F21-F32.

Andreis, D., & MacGregor, L. (2011). Using CSEM to monitor production from a complex 3D gas reservoir - A synthetic case study. *The leading Edge*, 1070-1079.

Archie, G. E. (1942). The electrical resistivity log as an aid in determining some reservoir characteristics. *Petroleum Transactions of the AIME, 146*, 54–62.

Baba, K. (2005). Electrical structure in marine tectonic settings. *Surveys in Geophysics, 26*, 701–731.

Bannister, P. R. (1968). Determination of the electrical conductivity of the seabed in shallow waters. *Geophysics, 33*, 995–1003.

Batzle, M., & Wang, Z. (1992). Seismic properties of pore fluids. *Geophysics, 57*(11), 1396-1408.

Becker, K., VonHerzen, R. P., Francis, T. J., Anderson , R. N., Honnorez, J., Adamson, A. C., Alt, J. C., Emmermann, R., Kempton, P. D., Kinoshita, H., Laverne, C., Mottl, M. J., Newmark, R. L. (1982). In situ electrical resistivity and bulk porosity of the oceanic crust Costa Rica Rift. *Nature 300*, 594-598 .

Bertrand, A. (2005). *The impact of seawater velocity variations on time-lapse seismic monitoring* . Edinburgh: Heriot Watt University.

Best, D. L., Gardner, J. S., & Dumanoir, J. L. (1980). A computer-processed wellsite log computation. Houston: Society of Petroleum Engineers (SPE, 9039).

Bhuyian, A. H., Landro, M., & Johansen, S. E. (2012). 3D CSEM modelling and time-lapse sensitivity analysis for subsurface CO2 storage. *Geophysics, 77*(5), E343-E355.

Black, N., & Zhdanov, M. S. (2009). Monitoring of hydrocarbon reservoirs using marine CSEM method. *International Exposition and Annual Meeting.* Houston: SEG .

BP. (2012). *BP* . Retrieved October 12, 2012, from http://www.bp.com/extendedsectiongenericarticle.do?categoryId=9044064&contentId=7077181

Brock-Nannestad, L. (1965). Determination of the electrical conductivity of the seabed in shallow waters with varying conductivity profile. *Electronics Letters, 1*(10), 274–276.

Brown, V., Hoversten, M., Key, K., & Chen, J. (2012). Resolution of reservoir scale electrical anisotropy from marine CSEM data. *Geophysics, 77*(2), E147-E158.

Cagniard, L. (1953). Basic theory of the magnetotelluric method of geophysical prospecting. *Geophysics, 18*, 605–635.

Carstens, H. (2014). Three disappointments in the Barents Sea. *GeoExPro*, 64-66.

Chave, A. D., Constable, S. C., & Edwards, R. N. (1991). Electrical exploration methods for the seafloor, in M. Nabighian, ed., Electromagnetic methods in applied geophysics. *SEG Investigations in Geophysics, 2*(3), 931–966.

Cheesman, S. J., Edwards, R. N., & Law, L. K. (1988). First results of a new short baseline sea floor transient EM system. In 5. A. Meeting (Ed.). (pp. 259–261). SEG Expanded Abstracts.

Clavier, C., Coates, G., & Dumanoir, J. (1984). Theoretical and Experimental Bases for the Dual-Water Model for Interpretation of Shaly Sands. *Society of Petroleum Engineers , 24*(2), 153-168.

Coggon, J. H., & Morrison, H. F. (1970). Electromagnetic investigation of the sea floor. *Geophysics, 35*, 476–489.

Constable, S. (2010). Ten years of marine CSEM for hydrocarbon exploration . *Geophysics, 75*(5), 75A67–75A81.

Constable, S. (2013). Review paper: Instrumentation for marine magnetotelluric and controlled source electromagnetic sounding. *Geophysical Prospecting, 61*(sup 1), 505-532.

Constable, S. C. (1990). Marine electromagnetic induction studies. *Surveys in Geophysics, 11*(2), 303-327.

Constable, S. C. (2004). *Patent No. WO 2004/053528 A1.* World International Property Organisation.

Constable, S., & Srnka, L. J. (2007). An introduction to marine controlled source electromagnetic methods for hydrocarbon exploration. *Geophysics, 2*(72), WA3–WA12.

Constable, S., & Weiss, C. J. (2006). Mapping thin resistors and hydrocarbons with marine EM methods: Insights from 1D modeling. *Geophysics, 71*(2), G43-G51.

Constable, S., Orange, A., Hoversten, G. M., & Morrison, H. F. (1998). Marine magnetotellurics for petroleum exploration: Part 1 —A sea-floor equipment system. *Geophysics, 63*, 816–825.

Corbett, P. M., Mousa, N. I. A. (2010). Petrotype-based Sampling Applied in a Saturation Exponent Screening Study, Nubian Sandstone Formation, Sirt Basin, Libya. *Petrophysics, 51*(4), 264-270.

Cox, C. S. (1980). Electromagnetic induction in the oceans and inferences on the constitution of the earth. *Geophysical Surveys, 4*(1-2), 137-156.

Cox, C. S. (1981). On the electrical conductivity of the oceanic lithosphere. *Physics of the Earth and Planetary Interiors, 25*(3), 196–201.

Cox, C. S., Filloux, J. H., & Larsen, J. C. (1971). Electromagnetic studies of ocean currents and electrical conductivity below the ocean floor. *In A. E. Maxwell, ed., The sea, 4:Wiley*, 637–693.

Craig Jr, F. F., Wilcox, P. J., Ballard, J. R., & Nation, W. R. (1977). Optimized Recovery Through Continuing Interdisciplinary Cooperation . *Journal of Petroleum Technology, 29*(7), 755-760.

Crain, E. R. (1986). *The Log Analysis Handbook.* Tulsa: Pennwell Publishing.

Dasgupta, S. N., & Jervis, M. A. (2009). Results from Passive Seismic Field Trial for Reservoir Monitoring in Saudi Arabia. Amsterdam: 71st EAGE Conference & Exhibition .

Diamond Offshore. (2014). *Diamond Offshore.* Retrieved January 15, 2015, from http://www.diamondoffshore.com/offshore-drilling-basics

Dmitriev, V. I. (1969). Electromagnetic fields in inhomogeneous media. Moscow: Proceeding of computational centre.

Donaldson, E. C., & Siddiqui, T. K. (1989). Relationship Between the Archie Saturation Exponent and Wettability. *SPE Fonnation Evaluation*, 359-362.

Doveton, J. H. (2001). All Models Are Wrong, but Some Models Are Useful: "Solving" the Simandoux Equation. *IAMG 2001 Conference.* Cancún, Mexico: International Association for Mathematical Geology.

Dresser Atlas Inc. (1982). *Well logging and interpretation techniques.* Dresser Industries.

Drysdale, C. V. (1924). The distribution of the magnetic field and return current around a submarine cable carrying alternating current—Part I. *Philosophical Transactions of the Royal Society, A224*, 95–140.

EAGE. (2014). PGS does first simultaneous EM and 2D seismic survey. *First Break, 32*(1), 39.

Edwards, R. N. (1997). On the resource evaluation of marine gas hydrate deposits using sea-floor transient electric dipole-dipole methods. *Geophysics, 62*, 63–74.

Edwards, R. N., & Chave, A. D. (1986). A transient dipole-dipole method for mapping the conductivity of the seafloor. *Geophysics, 51*, 984–987.

Edwards, R. N., Law, L. K., Wolfgram, P. A., Nobes, D. C., Bone, M. N., Trigg, D. F., DeLaurier, J. M. (1985). First results of the MOSES experiment: Sea sediment conductivity and thickness determination, Bute Inlet, British Columbia, by magnetometric offshore electrical sounding. *Geophysics, 50*, 153-161.

Eidesmo, T., Ellingsrud, S., MacGregor, L. M., Constable, S., Sinha, M. C., Johanson, S., Kong, F. N., Westerdahl, H. (2002). Sea bed logging (SBL), a new method for remote and direct identification of hydrocarbon filled layers in deepwater areas. *First Break, 20*, 144–152.

Ellingsrud, S., Eidesmo, T., Jonansen, S., Sinha, M. C., MacGregor, L. M., & Constable, S. (2002). Remote sensing of hydrocarbon layers by seabed logging (SBL): Results from a cruise offshore Angola. *The Leading Edge, 21*, 972–982.

Ellis, M., & Keirstead, R. (2011). Geological Parameters Effecting Controlled-Source Electromagnetic Feasibility: A North Sea Sand Reservoir Example. San Antonio: SEG Annual Meeting.

Evans, R L; Webb, S C; Team, RIFT-UMC. (2002). Crustal resistivity structure at 9.5°N on the East Pacific Rise: Results of an electromagnetic survey. *Geophysical Research Letters, 29*, 1082.

Evans, R. L., Constable, S. C., Sinha, M. C., & Cox, C. S. (1991). Upper crustal resistivity structure of the East Pacific Rise near 13°N. *Geophysical Research Letters, 18*, 1917–1920.

Falahat, R., Shams, A., & MacBeth, C. (2011). Adaptive engineering-based scaling for enhanced dynamic interpretation of 4D Seismic. In 7. E. Conference (Ed.). Vienna: 73rd EAGE Conference.

Fanchi, J. R. (2006). *Principles of Applied Reservoir Simulation* (3rd ed.). Oxford: Elsevier.

Filloux, J. H. (1967). An ocean bottom, D component magnetometer. *Geophysics, 32*, 978–987.

Fonarev, G. A. (1982). Electromagnetic research in the ocean. *Geophysical Surveys, 4*(4), 501–508.

Gallardo, L. A., & Meju, M. A. (2003). Characterization of heterogeneous near-surface materials by joint 2D inversion of dc resistivity and seismic data. *Geophysical Research Letter, 30*(13, 1658), 1-1 to 1-4.

Gamage, P., & Thyne, G. (2011). Comparison of Oil Recovery by Low Salinity Waterflooding in Secondary and Tertiary Recovery Modes. Denver: Society of Petroleum Engineers.

Gassmann, F. (1951). Über die Elastizität poröser Medien [On elasticity of porous media]. *Vierteljahrsschrift der Naturforschenden Gesellschaft, 96*, 1-23.

Glasmann, J. R., Lundegard, P. D., Clark, R. A., Penny, B. K., & Collins, I. D. (1989). Geochemical Evidence for the History of Diagenesis and Fluid Migration: Brent Sandstone, Heather Field, North Sea. *Clay Minerals, 24*, 255 - 284.

Grude, S., Dvorkin, J., Clark, A., Vanorio, T., & Landro, M. (2013). Pressure effects caused by CO2 injection in the Snohvit Field. *First break, 31*(12), 99-101.

Han, D., & Batzle, M. (2000). Velocity, density and modulus of hydrocarbon. *SEG Technical Program Expanded* (pp. 1892–1866). Tulsa: Society of Exploration Geophysicists.

Harris, P. E., & MacGregor, L. M. (2006). Determination of reservoir properties from the integration of CSEM and seismic data. *First Break, 24*(11), 53-59.

Hesthammer, J., Stefatos, A., & Sperrevik, S. (2012). CSEM efficiency - evaluation of recent drilling results. *First Break, 30*(6), 47-55.

Hoversten, G. M., Cassassuce, F., Gasperikova, E., Newman, G. A., Chen, J., Rubin, Y., Zhangshuan, H., Vasco, D. (2006). Direct reservoir parameter estimation using joint inversion or marine seismic AVA and CSEM data. *Geophysics, 71*(3), C1-C13.

Hoversten, G. M., Morrison, H. F., & Constable, S. (1998). Marine magnetotellurics for petroleum exploration: Part 2—Numerical analysis of subsalt resolution. *Geophysics, 63*, 826–840.

Hursan, G., & Zhdanov, M. S. (2002). Contraction integral equation method in three-dimensional electromagnetic modeling. *Radio Science, 37*(6), 1-13.

Hursan, G., Ueda, T., & Zhdanov, M. (2006). *3D Electromagnetic modelling based on the method of Integral equations.* Utah: Consortium for Electromagnetic Modelling and Inversion University of Utah.

Iqbal, G., & Satter, A. (2010). *Fundamentals of reservoir engineering, in D.H. Johnston (2013), Practical applications of time-lapse seismic data, Chapter 2: Reservoir engineering and reservoir management* (Series no. 16 ed.). Tulsa: SEG Distinguished Instructor Short Course.

Jack, I. (1998). *Time-Lapse Seismic in Reservoir Management.* Tulsa: First Annual SEG Distinguished Instructor Short Course.

Jerauld, G. R., Lin, C. Y., Webb, K. J., & Seccombe, J. C. (2006). Modeling Low-Salinity Waterflooding. San Antonio: Society of Petroleum Engineers.

Johnston, D. H. (2013). *Making a Difference with 4D: Practical Applications of Time-Lapse Seismic Data.* Tulsa: SEG Distinguished Instructor Short Course.

Key, K. (2009). 1D inversion of multicomponent, multifrequency marine CSEM data: Methodology and synthetic studies for resolving thin resistive layers. *Geophysics, 74*(2), F9-F20.

Key, K., & Ovall, J. (2011). A parallel goal-oriented adaptive finite element method for 2.5-D electromagnetic modelling. *Geophysical Journal International, 186*, 137-154.

Key, K., Constable, S., & Weiss, C. J. (2006). Mapping 3D salt using the 2D marine magnetotelluric method: Case study from Gemini Prospect, Gulf of Mexico. *Geophysics, 71*(1), B17–B27.

Killough, J. E. (1995). Ninth SPE Comparative Solution Project: A Reexamination of Black-Oil Simulation. San Antonio: Society of Petroleum Engineers.

Kjølhamar, B., Serch, C. S., Pedersen, C. B., & Myklebust, R. (2014). The Hoop Basin. *GEOExPro*, 36-40.

Klein, J. D. (1993). Induction Log Anisotropy Corrections. *The Log Analyst, 34*, 18-27.

Lager, A., Webb, K., & Seccombe, J. (2011). Low Salinity Waterflood, Endicott, Alaska: Geochemical Study & Field Evidence of Multicomponent Ion Exchange. Cambridge: 16th European Symposium on Improved Oil Recovery.

Landro, M. (2001). Discrimination between pressure and fluid saturation. *Geophyscis, 66*(3), 836-844.

Li, H., Chen, S., Yang, D., & Tontiwachwuthikul, P. (2012). Etimation of relative permeability by assited history matching using the Ensemble-Kalman-filter method. *Journal of Canadian Petroleum Technology , SPE 156027*, 205-214.

Liang, A., Abubakar, A., & Habashy, T. M. (2011). Feasibility study of marine CSEM for reservoir monitoring using joint 3D EM modeling and fluid flow simulator. Vienna: 73rd EAGE Conference.

Liang, L., Abubakar, A., & Habashy, T. M. (2012). Joint inversion of controlled-source electromagnetic and production data for reservoir monitoring. *Geophysics, 77*(5), ID9-ID22.

Lien, M. (2013). Simultaneous joint inversion of amplitude-versus-offset and controlled-source electromagnetic data by implicit representation of common parameter structure. *Geophysics, 78*(4), ID15-ID27.

Lien, M., & Mannseth, T. (2008). Sensitivity study of marine CSEM data for reservoir production monitoring. *Geophysics, 73*(4), F151-F163.

Lumley, D. E. (2004, November). Business and technology challenges for 4D seismic reservoir. *The Leading Edge, 23*, 1166-1168.

Lumley, D. E., Behrens, R. A., & Wang, Z. (1997). Assessing the technical risk of a 4-D seismic project. *The Leading Edge, 16*(9), 1287-1292.

Maao, F. A. (2007). Fast finite-difference time-domain modeling for marine-subsurface electromagnetic problems. *Geophysics, 72*(2), A19-A23.

MacBeth, C., Floricich, M., & Soldo, J. (2006). Going quantitative with 4D seismic analysis. *Geophysical Prospecting, 54*(3), 303-317.

MacBeth, C., Floricich, M., & Soldo, J. (2006). Going quantitative with 4D seismic analysis. *Geophysical Prospecting, 54*, 303-317.

MacBeth, C., Stephen, K. D., & McInally, A. (2005). The 4D seismic signature of oil–water contact movement due to natural production in a stacked turbidite reservoir . *Geophysical Prospecting, 53*(2), 183-203.

MacGregor, L. (2011). Integrating Well Log, Seismic, and CSEM Data for Reservoir Characterization. *SEG Europe Honorary Lecture*.

MacGregor, L. M., Constable, S., & Sinha, M. C. (1998). The RAMESSES experiment III: Controlled source electromagnetic sounding of the Reykjanes Ridge at 57°45'N. *Geophysical Journal International, 135*, 773–789.

MacGregor, L., & Cooper, R. (2010). Unlocking the value of CSEM. *First Break, 28*(5), 49-52.

MacGregor, L., & Tomlinson, J. (2014). Marine Controlled Source Electromagnetic Methods in the hydrocarbon industry: a tutorial on methods and practice. *SEG Interprepation (accepted for publication)*.

MacGregor, L., Bouchrara, S., Tomlinson, J., Strecker, U., Fan, J., Ran, X., Yu, G. (2012). Integrated analysis of CSEM, seismic and well log data for prospect appraisal: a case study from West Africa. *First Break, 30*(4), 77-82.

MacGregor, L., Sinha, M., & Constable, S. (2001). Electrical resistivity structure of the Valu Fa Ridge, Lau Basin, from marine controlled-source electromagnetic sounding. *Geophysical Journal International, 146*, 217-236.

Manrique, E., & Campanella, J. (2006). *EOR Returns to Mainstream Recovery.* Concordia, Kansas: The American Oil and Gas Reporter.

Marsala, A. F., Al-Buali, M., Ali, Z., Ma, S. M., He, Z., Biyan, T., He, T., Zhao, G. (2011). First Pilot of Borehole to Surface Electromagnetic in Saudi Arabia - A New Technology to Enhance Reservoir Mapping & Monitoring . Vienna: 73rd EAGE Conference & Exhibition incorporating SPE EUROPEC.

Marsh, J. M., Whitcombe, D. N., Raikes, S. A., Parr, R. S., & Nash, T. (2003). BP's increasing systematic use of time-lapse seismic technology. *Petroleum Geoscience, 9*(1), 7-13.

Martin, K., & MacDonald, C. (2010). The Schiehallion Field: Applying a geobody modelling approach to piece together a complex turbidite field. Aberdeen: Devex.

Mavko, G., Mukerji, T., & Dvorkin, J. (1998). *The Rock Physics Handbook.* Cambridge: Cambridge University Press.

Maxwell, J. C. (1954). *A treatise on electricity and magnetism.* New York: Dover Publications (unabridged and unaltered republication of the third edition of 1891), pp. 506.

McGuire, P. L., Chatham, J. R., Paskvan, F. K., Sommer, D. M., & Carini, F. H. (2005). Low salinity oil recovery: An exciting new EOR opportunity for Alaska's North Slope. Irvine: SPE.

Meadows, M., Adams, D., Wright, R., Tura, A., Cole, S., & Lumley, D. (2005). Rock physics analysis for time-lapse seismic at Schiehallion Field, North Sea. *Geophysical Prospecting, 53*, 205-213.

Mieles, L., Darnet, M., Van Popta, J., Singh, M., Wilt , M., & Levesque, C. (2009). Experience with Crosswell Electromagnetics (EM) for Waterflood Management in Oman. Doha: International Petroleum Technology Conference.

Moser, J., Poupon, M., Meyer, H., Wojcik, C., Rosenquist, M., Adejonwo, A., Smith, D. (2006). Integration of electromagnetic and seismic data to assess residual gas risk in the toe-trust belt of deepwater Niger Delta. *The Leading Edge, 25*(8), 977-982.

Orange, A., Key, K., & Constable, S. (2009). The feasibility of reservoir monitoring using time-lapse marine CSEM. *Geophysics, 74*(2), F21-F29.

Palshin, N. A. (1996). Oceanic electromagnetic studies: A review. *Surveys in Geophysics, 17*(4), 455-491.

Perkin, R. G., & Walker, E. R. (1972). Salinity calculations from in situ measurements. *Journal of Geophysical Research, 77*, 6618-6621.

Phillips, D. (2008). *Cost of Offshore Drilling Rising as Fast as Oil Prices.* MONEYWATCH.

Poupon, A., & Levaux, J. (1971). Evaluation of water saturation in shaly formations. *SPWLA 12th Annual Logging Symposium.* Dallas: Society of Petrophysicists and Well-Log Analysts.

Rafle, M. Y., & Youngblood, W. E. (1987). Advances in Quantitative Reservoir Description and Monitoring in Saudi Arabia. *12th World Petroleum Congress.* Houston, USA: World Petroleum Congress.

Ramananjaona, C., MacGregor, L., & Andreis, D. (2011). Sensitivity and inversion of marine electromagnetic data in a vertically anisotropic stratified earth. *Geophysical Prospecting, 59*(2), 341-360.

Reynolds, A. C., Li, R., & Oliver, D. S. (2004). Simultaneous Estimation of Absolute and Relative Permeability by Automatic History Matching of Three-Phase Flow Production Data. *J Can Pet Technol, 43*(3), 37-46.

Rider, M., & Kennedy, M. (2013). *The Geological Interpretation of Well Logs* (Third ed.). Glasgow: Rider-French Consulting Limited.

Ridyard, D., & Hesthammer, J. (2011). Value creation using electromagnetic imaging. *World Oil*, 51-54.

Salako, O., MacBeth, C., & MacGregor, L. (2012). Towards joint interpretation of CSEM Surveys with 4D Seismic for Reservoir Monitoring. Copenhagen: 74th EAGE Conference.

Salako, O., MacBeth, C., MacGregor, L., & Mackay, E. (2013). Potential Applications of Time-lapse Marine CSEM to Reservoir Monitoring. London: 75th EAGE Conference & Exhibition incorporating SPE EUROPEC.

Satter, A., Varnon, J. E., & Hoang, M. T. (1994). Integrated Reservoir Management. *Journal of Petroleum Technology, 46*(12), 1057-1064.

Schlumberger. (2009). Retrieved December 06, 2012, from http://www.slb.com/~/media/PremiumContent/resources/books/log_charts/chartbook.pdf

Seccombe, J., Lager, A., Jerauld, G., Jhaveri, B., Buikema, T., Bassler, S., Dennis, J., Webb, K., Cockin, A., Fueg, E. (2010). Demonstration of Low-Salinity EOR at Interwell Scale, Endicott Field, Alaska. Tulsa: Society of Petroleum Engineers.

Shahin, A., Key, K., Stoffa, P. L., & Tatham, R. H. (2010). Time-lapse CSEM analysis of shaly sandstone simulated by comprehensive petro-electric modeling. Denver: SEG Expanded Abstracts.

Shahin, A., Key, K., Stoffa, P., & Tatham, R. (2012). Petro-electric modeling for CSEM reservoir characterization and monitoring. *Geophysics, 77*(1), E9-E20.

Sharma, M. M., Garrouch, A., & Dunlap, H. F. (1991). Effects of wettability, pore geometry, and stress on electrical conduction in fluid-saturated rocks. *The Log Analyst, 32*, 511-526.

Shehata, A. M., Ghatas, A., Kamel, M., Aly, A., & Hassan, A. (2012). Overview of Polymer Flooding (EOR) in North Africa Fields - Elements of Designing a New Polymer/Surfactant Flood Offshore (Case Study). Cairo: Society of Petroleum Engineers 151952.

Simandoux, P. (1963). Dielectric measurements on porous media application to the measurement of water saturations: study of the behaviour of argillaceous formations. *Revue de l'Institut Francais du Petrole 18*, (pp. 193-215).

Sinha, M. C., Patel, P. D., Unsworth, M. J., Owen, T. R., & MacCormack, M. R. (1990). An active source EM sounding system for marine use. *Marine Geophysical Research, 12*, 59–68.

Society of Exploration of Exploration Geophysicists. (1996-2013). *SEG*. Retrieved July 2013, from http://library.seg.org/action/doSearch?displaySummary=true&target=default&text1=Marine+CSEM&field1=AllField&logicalOpe1=AND&text2=&field2=AllField&logicalOpe2=AND&text3=&field3=AllField&logicalOpe3=AND&text4=&field4=AllField&logicalOpe4=AND&text5=&field5=

Sorbie, K. S., & Mackay, E. J. (2000). Mixing of injected, connate and aquifer brines in waterflooding and its relevance to oilfield scaling. *Elsevier, 27*, 85-106.

Staple 2006 in MacBeth, C. (2013). Example of hidden water saturation signal in a 4D seismic attaribute difference cube. Institute of Petroleum Engineering, Heriot Watt University.

State of Alaska. (2011). *Alaska Oil and Gas Conversation Commission*. Retrieved 2014, from http://doa.alaska.gov/ogc/annual/current/18_Oil_Pools/Endicott%20-%20Oil/Endicott,%20Ivishak%20Oil/1_Oil_1.htm

Strack, K. M. (2004). *Patent No. US 6,739,165 B1.* United States of America.

Tabanou, J. R., Anderson, B., Bruce, S., Bomemann, T., Hodenfield, K., & Wu, P. (1999). Which resistivity should be used to evaluate thinly bedded reservoirs in high-angle wells? Oslo: SPWLA 40th Annual Logging Symposium.

Tang, G. Q., & Morrow, N. R. (1997). Salinity, Temperature, Oil Composition, and Oil Recovery by Waterflooding. *SPE Reservoir Engineering, 12*(4), 269-276.

Thakur, G. C. (1996). What Is Reservoir Management? *Journal Petroleum Technology*, 520-525.

Thambynayagam, R. K. (2011). *The Diffusion Handbook: Applied Solutions for Engineers* (1st ed.). New York: McGraw-Hill Companies.

Thyne, G. (2011). Evaluation Of The Effect Of Low Salinity Waterflooding For 26 Fields In Wyoming. Denver: Society of Petroleum Engineers.

Tiab, D., & Donaldson, E. C. (2004). *Theory and Practice of Measuring Reservoir Rock and Fluid Transport Properties* (Second ed.). Oxford: Gulf Professional Publishing.

Toinet, S. (2004). 4D Feasibility and Calibration Using 3D Seismic Modeling of Reservoir Models. Abu Dhabi: Society of Petroleum Engineers 88783.

Tsili, W., & Sheng, F. (2001). 3D electromagnetic modelling using finite differences. *Geophysics, 66*(5), 1386-1398.

University of Rhode Island. (2014). *University of Rhode Island*. Retrieved May 26, 2014, from http://omp.gso.uri.edu/ompweb/doee/science/physical/chsal1.htm

Vozoff, K. (1972). The magnetotelluric method in the exploration of sedimentary basins. *Geophysics, 37*, 98–141.

Warren, E. A., & Smalley, P. C. (1993). The chemical composition of North Sea formation waters: a review of their heterogeneity and potential applications. In P. J.R (Ed.), *Petroleum Geology of Northwest Europe: Proceedings of the 4th Conference* (pp. 1347-1352). London: The Geological Society.

Warren, E. A., & Smalley, P. C. (1994). *North Sea Formation Waters Atlas* (Memoir No. 15 ed.). London: The Geological Society.

Waxman, M. H., & Smits, L. J. (1968). Electrical Conductivities in Oil-Bearing Shaly Sands. *Society of Petroleum Engineers, 8*(2), 107-122.

Webb, K. J., Black, C. J., & Al-Ajeel, H. (2004). Low Salinity Oil Recovery - Log-Inject-Log. Tulsa: Society of Petroleum Engineers.

Weitemeyer, K., Constable, S., & Key , K. (2006). Marine EM techniques for gas-hydrate detection and hazard mitigation. *The Leading Edge*, 629 - 632.

Wilt, M., Little, J., Zhang, P., Chen, J., & Morea, M. (2005). Using Crosswell EM to Track Waterflooding at the Lost Hills Oil field. Houston: SEG Technical Program Expanded Abstracts.

Wirianto, M., Mulder, W. A., & Slob, E. C. (2010). A Feasibility Study of Land CSEM Reservoir Monitoring: The Effect of the Airwave. *PIERS ONLINE, 6*(5), 440-444.

Worthington, P. F. (1985). The evolution of shaly-sand concepts in reservoir evaluation. *THE LOG ANALYST*, 23-40.

Worthington, P. F., & Johnson, P. W. (1991). Quantitative Evaluation of Hydrocarbon Saturation in Shaly Freshwater Reservoirs. *The Log Analyst*, 358-370.

Youngblood, W. E. (1980). The application of pulsed neutron decay time logs to minotor waterfloods with changing salinity. *SPE*, 957-963.

Zach, J. J., Frenkel, M. A., Ridyard, D., Hincapie, J., Dubois, B., & Morten, J. P. (2009). Marine CSEM time-lapse repeatability for hydrocarbon field monitoring. Houston: SEG International Exposition and Annual Meeting.

Zhdanov, M. S. (2009). *Geophysical Electromagnetic Theory and Methods* (First ed.). Oxford: Elsevier.

Zhdanov, M. S., Endo, M., Black, N., Spangler, L., Fairweather, S., Hibbs, A., Eiskamp, G. A., Will, R. (2013). Electromagnetic monitoring of CO2 sequestration in deep reservoirs. *First Break, 31*(2), 85-92.

Ziolkowski, A., Parr, R., Wright, D., Nockles, V., Limond, C., Morris, E., Linfoot, J. (2010). Multi-transient electromagnetic repeatability experiment over the North Sea Harding field. *Geophysical Prospecting, 58*(6), 1159-1176.